# Applications of Coulomb Crystals in Cold Chemistry

Alexander D. Gingell

Merton College, University of Oxford

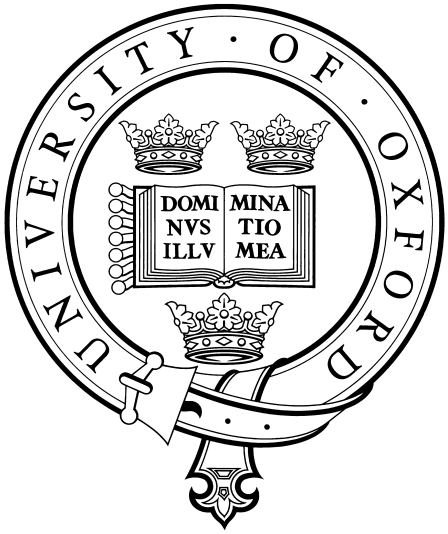


A thesis submitted for the degree of Doctor of Philosophy

Hilary Term, 2010

# Applications of Coulomb Crystals in Cold Chemistry

Alexander D. Gingell, Merton College, Hilary Term, 2010

A thesis submitted in partial fulfilment of the requirements for the degree of Doctor of Philosophy of the University of Oxford

## Abstract

This thesis describes the study of a range of ion-molecule reactions at very low collision energies using a newly developed experimental technique which involves the reaction of velocity-selected beams of translationally cold neutral molecules with very low kinetic energy ion ensembles. These studies have been enabled by the construction of a new apparatus for trapping and laser-cooling gas phase atomic ions ($^{40}Ca^+$). The laser-cooling process results in the formation of ordered, low kinetic energy, lattice-like ion structures, also known as "Coulomb crystals". The properties of single and multicomponent Coulomb crystals (which may also involve molecular ions), and their manipulation via modulation of the applied fields, are explored experimentally and with the use of molecular dynamics simulations. Variations in the laser-cooling parameters are shown to result in different steady-state populations of the electronic states of $^{40}Ca^+$ involved with the laser cooling cycle, and these are modelled within an appropriate theoretical framework.

The imaging of $^{40}Ca^+$ fluorescence as a function of time allows the study of various ion-molecule reactions at collision energies around 300 K, with single ion sensitivity. These reaction studies are extended to low-temperature (collision energies close to 1 K), by combination of the ion trap apparatus with a bent quadrupole guide velocity-selector. Ion-molecule collision energies are shown to be variable over a short range through a change in the quadrupole guide voltage, or the ion trapping parameters; the effect of these modulations on the rate constant is explored for $Ca^+ + CH_3F$.

Bimolecular rate constants for the reactions of $^{40}Ca^+$ with $CH_3F$, $CH_2F_2$ and $CH_3Cl$ have been determined for a range of $^{40}Ca^+$ state populations, allowing resolution of the global rate contributions from the ground and combined excited states. These results are analysed in the context of capture theories and *ab initio* electronic structure calculations. In each case, suppression of the ground state rate constant is explained by the presence of either a submerged or real barrier on the ground state potential surface. Rates of reaction from the combined excited states are generally found to be in line with capture theories, and in some cases variation is found between the high and low collision energy regimes. Molecular product ions generated in these experiments have been shown to be sympathetically-cooled into the crystal structure, and subsequently identified through resonance-excitation mass spectrometry. Molecular ions were also produced by multiphoton laser ionisation of a thermal background gas of OCS molecules. An ion-molecule reaction involving a molecular ion, that of charge transfer between $OCS^+$ and $ND_3$, has been studied at a collision energy near 1 K for the first time using sympathetically-cooled $OCS^+$ and velocity-selected $ND_3$. These experiments illustrate the generality of the techniques described herein, and should lead to many possibilities for future studies.

To my parents

# Acknowledgements

I would like to express my deepest gratitude to my Supervisor Tim Softley, not just for his copious support and guidance over the "DPhil years", but for all of his help and good humour during the entirety of my ten years at Oxford. No matter what our official relationship at the time or how busy he was, Tim invariably made himself accessible to me and always went out of his way to help me with whatever problem I had, no matter how insignificant. For his friendship and ever-present support I thank him gratefully. I will look back very fondly at my time in Oxford and Tim will be a big part of that.

While on the subject of tutors, I would also like to thank Veronique Gouverneur, Mike Laidlaw, Helen Cruse and Grant Ritchie for the time they invested teaching me the various aspects of the undergraduate chemistry course. In particular I would like to thank Grant Ritchie for his truly excellent physical chemistry tutorials during my 2nd and 3rd years. His cheerful demeanour, enthusiasm and upbeat attitude were infectious and contributed greatly to both my success in finals and my decision to specialise in physical chemistry.

During my DPhil I was extremely lucky to be working with Stefan Willitsch. Stefan is not only a tremendous scientist, but an excellent human being — one who appreciates good movies (obviously you're not a golfer!) and is not afraid to tell you when you're not working hard enough! Without Stefan this DPhil would most definitely not exist. Thank you for working with me and teaching me what it really means to do a good job on something. Catch you later on down the trail...

I want to thank Martin Bell for the huge amount of help given to me during different aspects of this work, and for always pushing me to do better (even if he wasn't always successful!). A valued friend, Martin's insight and assistance in and out of the laboratory were often crucial. In the same vein I want to thank James Oldham for his many helpful contributions, both in the laboratory and to the molecular dynamics simulations. To put it briefly, working with James and Martin has been a pleasure. Now, tell me a joke...

The staff of the electrical and mechanical workshops deserve a special mention for their invaluable contributions to all of the projects I have worked on here. Phil, Keith, Andy, John, Kevin, Charlie, Les, Howard, Roger — thank you for all that you have done for me and for putting up with the increasing frequency of the jobs that needed doing urgently and at short notice!

I would like to thank all the other members of the Softley group present during my tenure for making it such a friendly and pleasant place in which to work (and special thanks to Elin for all of the green tea!). Thanks must also go to my friends outside Oxford for providing me with enough distraction (and roast dinners) to keep me sane and for giving me an outlet away from academia. Al W, Becky, Dan and Han (and Spike!), John Philip Bastiaan Koch, Henry, Fleur, Mikey, Jo - thanks for everything!

I feel very lucky to have the support of a wonderful family, led by the best parents anyone could hope for. They have given me all the love and support I have ever needed and more in reserve. This thesis is dedicated to them and in particular to my Mum and Dad, Lesley and David, without whose tireless devotion nothing I do would be possible.

# Contents

# Chapter 1

# Introduction

In recent decades, a great deal of progress in the field of cold matter has enabled the production of atoms and molecules with ever-decreasing translational and internal energies. Such developments have bolstered research in a number of exciting areas in chemical physics, and particularly fascinating from a chemical perspective is the study of chemical processes in the low temperature regime. Ranging in scope from bimolecular reactions and inelastic scattering through to processes such as Bose-Einstein condensation, the interaction of chemical species at very low energies can give rise to phenomena that deviate markedly from expectations based on higher energy observations and experience. Therefore, low temperature reaction studies represent a unique opportunity to gain fundamental insights into the behaviour and interaction of matter, as well as other physical phenomena.

At higher energies, chemical species have a characteristically broad population distribution over their internal rotational and vibrational quantum states. Additionally, bimolecular collisions occur over a wider range of angular momentum states, as more energy is available to surmount centrifugal barriers. This means that a wider range of quantum states contribute to the rates of higher energy chemical processes, and this increased averaging can obscure some of the more subtle

aspects of the reaction dynamics (*e.g.*, reactive resonances). However, as the energy is lowered, the population of the internal states must collapse into the lowest available states, and reactive collisions are ultimately restricted to the lowest angular momentum state (which is the regime of s-wave scattering). Investigation of the intricate details of low-energy state-resolved reaction dynamics can in the end only afford us an increased understanding of processes at higher energies, where thermal averaging will be more prevalent.

Key features of low energy chemical dynamics, which are expected to become dominant in the ultracold regime, are the quantum phenomena that emerge when the de Broglie wavelengths ($\lambda = h/p$) associated with interacting chemical species become comparable in size to the range of the forces governing their interaction. In nuclear physics, this criterion was reached for collisions of sub-atomic particles such as protons or neutrons many decades ago; even at very high kinetic energies the associated de Broglie wavelengths of these particles exceed the extremely short range of the nuclear forces*. Thus quantum phenomena such as s-wave scattering, resonances and tunnelling became major features in the landscape of nuclear physics as far back as the early twentieth century. However, the forces that govern the interactions between atoms and molecules are very much longer range than the nuclear forces, typically operating at distances measured in Angstroms. This, in conjunction with their larger masses, means that atoms and molecules must be cooled to very low energies in order for their de Broglie wavelengths to exceed these distances (*e.g.* , the de Broglie wavelength of a $CH_3F$ molecule is 0.3 Å at 300 K but 30 Å at 30 mK). It is only in recent years that advancements in experimental techniques have allowed the production of atoms and molecules at kinetic energies low enough to facilitate investigation of these same phenomena at the atomic and

*For example, in collisions between protons and neutrons at ∼1 MeV or $10^{10}$ K, the associated de Broglie wavelengths are in the region of $\sim 30\times10^{-13}$ cm, whereas the strong nuclear force becomes non-negligible only at separations less than about $\sim 2\text{–}2.5\times10^{-13}$ cm [1].

molecular levels.

In this thesis, we adopt the conventions of the cold matter field, within which the term "cold" has come to represent temperatures ranging from around 10 K down to about 1 mK, and sub-millikelvin temperatures are described as "ultracold". To put these temperatures in perspective, consider that the coldest naturally occurring region in the observable universe is the so-called Boomerang nebula, which at its coldest has a temperature of $\sim$1 K [2]. The low temperature stems from an extremely fast adiabatic expansion of gas (164 km/s), driven by a large rate of mass-loss from the dying central star. A thick outer envelope of CO absorbs microwave radiation at 3 K, shielding the inner adiabatic expansion from thermalisation to the microwave background temperature [2]. Thus, this structure is the only known example of a naturally occurring region at a temperature lower than the 2.728 K of the cosmic microwave background. In contrast, temperatures increase somewhat inside the giant interstellar clouds of dust particles and gas molecules that constitute about 10% of the matter in the Milky Way galaxy. Typical conditions in these clouds range from number densities $n \approx 10^2$–$10^3$ cm$^{-3}$ and temperatures of 50–100 K in the more diffuse areas, to $n \approx 10^4$ cm$^{-3}$ and temperatures of 5–10 K in the cold dense cores of more concentrated aggregates [3]. Despite the very low densities in these regions, collisional processes do occur on the very long timescales of the astrophysical medium. Temperatures between 100–200 K can occur in the upper atmosphere of Earth, or in the atmospheres of other planets such as Saturn's moon Titan. Thus, in so far as is known, temperatures less than approximately 1 K are the sole preserve of the laboratory.

Despite the somewhat artificial nature of laboratory experiments involving cold and ultracold atomic and molecular collisions, there remain many examples of naturally occurring chemical processes where an improved understanding may be

dependent on such work. An intriguing example of a poorly understood process in the cold regime, which occurs outside our everyday experience in the upper atmosphere and in interstellar chemistry, involves the behaviour of acids such as HCl in nanoenvironments at very low temperatures (as opposed to their behaviour in bulk water at room-temperature). HCl dissociation and the subsequent solvation of the charged fragments has recently been studied at 0.37 K using helium nanodroplets, and this work illustrated the requirement of no fewer than four $H_2O$ molecules for complete dissociation [4]. This seemingly esoteric cold chemistry could have significant implications for our understanding of how chlorine-containing compounds damage the ozone layer in the upper atmosphere. In the 10–25 K temperature range, barrierless ion-molecule reactions involving many polar and non-polar neutral molecules dominate the chemistry of cold interstellar gas[†], and are crucial in driving processes such as star formation [3]. While computer modelling of these clouds requires knowledge of the rate constants for the relevant reactions at these temperatures, the vast majority have not been measured experimentally at present [6]. In the absence of these data, a strong theoretical understanding is paramount in making rational predictions of these values, and experimental studies remain the proving ground of theory. Similarly, a better understanding of chemical reactivity at still higher temperatures would be invaluable in the research of processes in the atmosphere such as OH[‡]radical chemistry [8], and in the atmospheric evolution of Earth and other stellar bodies. For example, the atmosphere of Saturn's moon Titan[§], which ranges in temperature between 94–200 K, is widely considered a natural laboratory in which to understand the early atmospheric development of Earth [9].

[†]More recently the significance of neutral and radical reactions has also been recognised [5].

[‡]Recently, cold matter techniques involving Stark deceleration and electrostatic trapping (covered later) were used to directly measure the radiative lifetimes of the Meinel system of OH [7].

[§]Titan is the only body in the solar system besides Earth and Venus with a thick atmosphere and solid surface.

As well as providing a strong test of our fundamental understanding of chemical dynamics, access to the cold and ultracold regimes is an enabling factor for progress in a host of other fields. For example a single laser-cooled ion confined in an ion trap closely approximates the spectroscopic ideal of a particle at rest in a perturbation-free environment. High resolution spectroscopic studies benefit from the reduced Doppler broadening of measured linewidths, and longer observation times which mitigate transit-time broadening [10]. In frequency metrology such systems are very promising for the realisation of optical clocks, with accuracies around two orders of magnitude higher than current microwave primary standards [11, 12]. Increases in measurement precision have prompted investigations into the possible time variation of physical constants [13, 14] as well as the search for an electric dipole moment of the electron [15]. Attempts are also being made to detect very small parity-violating energy differences ($\sim 10^{-11}$ J mol$^{-1}$ or 100 aeV) between different enantiomeric forms that occur on account of the electroweak interaction [16]. The advancement of research into quantum information processing has relied heavily on ultracold systems such as a string of trapped laser-cooled ions, and there has been recent interest regarding the use of dipolar molecules trapped in optical lattices [17, 18]. As an example, the first experimentally-demonstrated quantum byte relied on a string of eight laser-cooled $^{40}Ca^{+}$ atoms in a linear Paul trap, a system very much like that used for the work in this thesis [19]. Systems involving quantum degenerate gases may be used in the study of many-body quantum effects [20–22], and in the exploration of condensed matter physics [23, 24].

## 1.1 Production of cold atoms and molecules

Techniques for cooling atoms rely heavily on laser-based methods such as Doppler cooling or the optical molasses technique, which can provide a pathway to the

ultracold regime. Generally, achieving temperatures in the microkelvin regime and below requires additional methods such as the evaporative cooling of atoms in magnetic traps, which involves slowly reducing the depth of the potential well and gradually losing the highest energy atoms in the ensemble. Techniques for loading atoms into magnetic traps for the purpose of evaporative cooling involve either buffer gas cooling [25], or Zeeman-slowing followed by magneto-optical trapping and subsequent transfer to a magnetic trap [26]. Evaporative cooling has allowed the cooling of atomic ensembles into the nanokelvin regime and allowed practical demonstration of Bose-Einstein condensation (BEC) in a large number of atomic samples [27–29]. These quantum degenerate gases, first predicted in work by Bose and Einstein in 1924–5 [30, 31], are a celebrated example of the dominance of quantum phenomena in atomic or molecular samples at very low energy.

Molecules are a much more difficult proposition than atoms for direct laser-cooling, chiefly due to the complexity of their energy level structures and the related difficulty of establishing a closed cooling cycle. This difficulty arises because electronic excitation usually results in spontaneous decay to a plethora of rovibrational states, with branching ratios that depend on Franck-Condon factors and dipole selection rules. According to the total angular momentum selection rule $\Delta J = 0, \pm 1, J = 0 \nleftrightarrow 0$, up to three repumping lasers would be required per vibrational level (assuming no hyperfine structure), and depending on the Franck-Condon factors there may be decays to a wide range of vibrational levels (poor vibrational selectivity is usually the dominant problem). Despite such factors, recent proposals have shown that certain simpler molecules may be amenable to laser-cooling, as favourable Franck-Condon factors suppress certain decay routes [32, 33]. Therefore, certain molecules (in either the ground state or a metastable excited state), may require a lower and therefore practically achievable number of repumping lasers. Molecules such as TiO and TiS, which have no hyperfine struc-

ture, optimal Franck-Condon factors, and only one allowed decay route per vibrational level have been singled out as excellent candidates for direct laser-cooling with the use of pulsed electric fields to nonadiabatically remix the ground-state magnetic sublevels [32]. Simulations performed for TiO suggest the viability of this approach in the creation of a magneto-optical trap for certain polar molecules [32]. In a similar vein, Demille *et al.* have recently demonstrated the optical cycling and deflection of a beam of SrF molecules using one main pump laser, one vibrational repumping beam, and with a magnetic field employed to remix the ground Zeeman sub-levels [34]. It is envisaged that the straightforward addition of a second vibrational repumping laser could enable direct laser-cooling, through an increase in the photon scattering rate from $\sim$150 to $10^5$ photons/s.

To mitigate the difficulty of implementing a closed cooling cycle, a number of broadband laser cooling schemes have been suggested [35–37]. These generally involve the sequential redistribution of the vibrational and/or rotational populations into the ground states through application of a suitable multiple single frequency laser system or a shaped mode-locked femtosecond laser.

Laser-based methods have also been proposed that do not require any repumping lasers. For example, in the case of the OH radical, Robicheaux has proposed driving a two-photon stimulated Raman transition in the terahertz regime using high-finesse cavities to drastically reduce the decay times under vacuum [38]. A magnetic field acts on the change in magnetic moment when the internal state changes in order to remove a substantial amount of energy with the absorption of relatively few photons.

The coldest molecules produced to date have been formed by the association of already-ultracold laser-cooled alkali metal atoms via three-body collisions, photoassociation or magnetic Feshbach resonance tuning. Indeed this latter technique,

which involves the sweeping of magnetic field strength such that free ultracold atoms are made isoenergetic with weakly-bound molecular states, has allowed the recent formation of molecular BECs [39–41]. However, these techniques are not widely applicable due to the initial requirement of a conveniently laser-coolable atomic species. Alternative methods have been developed that do not involve Doppler laser-cooling, but rather make use of electric or magnetic fields to slow molecules. These include Stark, Zeeman and optical deceleration [42–44], which can be used to decelerate molecules into the millikelvin temperature range, and which depend on the electric or magnetic dipole moment or polarisibility of the molecule. Stark deceleration in particular is discussed further in Section 4.2.3. Lasers may however be employed to optically pump certain molecules and facilitate magnetic trapping after a period of electrostatic deceleration. Such an optical pumping scheme has been demonstrated experimentally for NH [45], opening up the possibility of accumulating the NH radicals in a magnetic trap. Electric fields may also be employed to filter out the pre-existing slower moving molecules in a thermal gas sample [46]. This is termed velocity-selection, and is discussed in detail in Section 4.2.2.

A number of methods make use of collisions or atomic/molecular interactions to remove molecular kinetic energy. Kinematic cooling involves inelastic scattering between the species in two crossed supersonic molecular beams, where each beam has a narrow well-defined velocity distribution. A subset of the collisions involve scattering angles and recoil velocities that cancel out the velocity vector of one of the collision partners in the laboratory frame [47, 48]. Alternatively, molecules can be cooled through collisions with a colder species. In buffer gas cooling, repeated collisions with a low temperature gas (usually helium) rapidly cool all the available degrees of freedom of a molecule. This is a reasonably general technique, requiring only that the species in question survives multiple collisions with the buffer gas.

However, separation from the buffer gas requires molecular confinement while the buffer gas is pumped away *e.g.*, via magnetic field trapping, and often the challenge is to remove the buffer gas efficiently. Molecular ions may also be translationally cooled through their Coulomb interaction with a laser-cooled atomic ion ensemble within an ion trap; this is known as sympathetic-cooling [49–54], and forms the basis for the reaction experiments described in Chapter 7.

Thus, methods for the production of cold molecules can be broadly separated into two categories. Indirect methods, such as photoassociation and Feshbach tuning, produce molecules at the lowest temperatures, but are restricted to a very limited number of species (typically alkali dimers). Direct methods (the remaining examples) can be applied to a more chemically diverse range of molecules, but are at present restricted to temperatures in the millikelvin regime and higher. A detailed description of the techniques available for this purpose is beyond the scope of this thesis; the interested reader is referred to a number of adroit review articles [55, 56]. Those methods employed in the current work are outlined in more detail in later sections.

Despite the large amount of progress made in recent years in the development of techniques for cooling atoms and molecules, their application to chemical problems in the cold and ultracold domains has been comparatively rare. In part, this is due to the relatively low molecular fluxes produced by many of the methods outlined in this section, and a marked lack of generality with regard to the identity of the species they produce. Lower reactant number densities result in fewer collisions and therefore a low rate of product generation; this creates difficulties with regard to the detection of the products. Many of these problems may be mitigated by studying ion-molecule systems, which offer a number of advantages in this regard. Firstly, ion-molecular reactions are frequently barrierless, and therefore occur with

relatively large rate constants at low energy. Additionally, ions may be robustly trapped with the use of electric fields, allowing a long interaction time. Thus trapped-ion systems are sensitive to even very low molecular fluxes, and product ions can be detected at a single particle level. This would be of little use if the products could not accumulate, but it is in fact possible to trap the product ions generated in these reactions, assuming the trap depth is greater than the nascent kinetic energy of the product ions. The strong confinement possible for charged species means that typical trap depths are large enough to successfully confine the product ions for even rather exothermic reactions. Lastly, sensitive detection methods such as *in situ* mass spectrometry allow the accurate identification of trapped atomic or molecular ions.

The work presented in this thesis makes use of the combination (for the first time) of a laser-cooled trapped-ion apparatus with a quadrupole guide velocity-selector for cold neutrals, and details the study of a range of ion-molecule chemical reactions in the cold regime. In light of the fact that ion-neutral molecule reactions are the subject of the experimental studies later in this thesis, where appropriate, further discussion in this chapter will be oriented towards ion-molecule systems.

## 1.2 Gas phase chemical reactions at low temperatures

For a great many chemical reactions, a positive-energy saddle point in the reaction potential energy hypersurface separates the reactants from the products. In this case, the reactants require an activation energy to surmount the potential barrier and form the products, and this energy can arise from thermal fluctuations given a high enough temperature. However, as the temperature falls, less energy is available for scaling the barrier and consequently fewer collisions result in reaction.

Ultimately, even for small barriers, the rate constants for these types of reaction become negligible in the limit of very low temperatures[¶]. This Arrhenius-like dependence on the temperature is well explained by a variety of transition-state theories (TST) [57].

Whereas the rates of chemical reactions involving an activation barrier may become vanishingly small as the temperature is lowered, certain classes of reaction remain fast even into the cold regime, and in fact their rates can exhibit an inverse temperature dependence. These so-called "barrierless" reactions dominate the landscape of fast low-temperature reactions. Examples include radical-radical, radical-neutral and ion-neutral molecule reactions, as well as certain unimolecular decompositions, reactions of electronically/vibronically excited molecules (including Rydberg states) and even some atom-molecule reactions [55]. As discussed previously, these types of barrierless reactions are predominant in both the high atmosphere, particularly the lower stratosphere where temperatures are around 200 K, and in interstellar gas clouds where they occur at temperatures between about 5 and 25 K.

In the low temperature limit, the long-range region of the intermolecular potential exerts a large influence on chemical reactivity; the reactants are travelling more slowly and thus sample this region for an increased length of time. Significantly, it is this part of the potential which controls the orientation of the approaching reactants [58, 59], and investigation of these influences on reactivity is facilitated at lower energies. Also, these long-range interactions are relatively weak in comparison to the effect of externally applied electric and magnetic fields, suggesting that such applied fields can provide an extra degree of control over the rate and outcome of chemical processes in this regime. The shifting of molecular energy

[¶]Quantum mechanical tunnelling through the reaction barrier provides some exceptions, particularly for light atoms.

levels with external magnetic or electric fields could allow an excited bound level of the reactive complex to be brought into or out of resonance with the collision energy leading to enhancement or suppression of the reaction efficiency. Moreover, external fields can mix states so that forbidden electronic transitions become allowed to a controllable degree; in this way the reaction rate may be controlled by the field strength (for examples see [60] and references therein). Also, the ability to trap slow moving atoms or molecules may provide us with the chance to study reactions with increased sensitivity, given the potential for interaction times in vast excess of those available through traditional molecular beam techniques. This is especially true in the case of ion-molecule reactions where the product ions may be accumulated in the trap and measured over a period of minutes or even hours. However, trapping may be less advantageous in this regard for neutral molecules which are often confined in specific low-field seeking quantum states; inelastic scattering mechanisms can often cause trap loss and in the end a consideration of detection efficiency is key [61].

### 1.2.1 Theoretical descriptions of barrierless processes

In considering barrierless processes theoretically, it is convenient to consider motion on an effective potential surface described by the sum of an appropriate interaction potential and a term that accounts for the conservation of angular momentum in the collision. Given a simple isotropic inverse power law for the intermolecular potential the effective potential would be thus:

$$V_{\text{eff}}(r) = \frac{b^2 E_c}{r^2} - \frac{C_s}{r^s} \tag{1.1}$$

where the impact parameter of the collision $b$ is related to the orbital angular momentum $l$, reduced mass $\mu$ and relative velocity $v_{\text{rel}}$ according to $l = \mu v_{\text{rel}} b$. The impact parameter describes the distance of closest approach for a trajectory

in the absence of intermolecular interactions. This means that, even in the absence of a chemical barrier along the reaction coordinate, there can still be an effective barrier stemming from the orbital angular momentum of the collision. This aspect of barrierless reactions contributes in part to a qualitative understanding of how reaction rates may increase at lower temperature. A reduced relative velocity, and therefore orbital angular momentum, results in a smaller centrifugal barrier contribution to the effective potential (however this may be counterbalanced by the fact that the collision frequency decreases with velocity, and the mean energy available to surmount the barrier is lower). In very low rotational quantum states the rate constant may also be greatly enhanced; this is due to the increased ability of the collision complex to "lock-in" to a more favourable orientation. In other words, the rotational wavefunctions of the lower rotational quantum states have an increased polarisability. Theoretical treatment of this requires an explicit inclusion of anisotropic contributions to the intermolecular potential as we shall see shortly.

Many theoretical approaches — the so-called "capture theories" — of ion-molecule reactions assume that motion along the reaction coordinate proceeds classically, and that if the centrifugal barrier is successfully negotiated, the resultant ion-molecule complex will decompose into the products with unit probability[‖]. For a given collision energy this defines a maximum angular momentum and impact parameter $b_{\max}(E_c)$ for the reaction that allows the Langevin cross-section to be calculated via

$$\sigma_{\mathrm{L}}(E_c) = \pi b_{\max}^2(E_c), \tag{1.2}$$

which, given the isotropic potential in Eq. 1.1, can be calculated to be:

$$\sigma_{\mathrm{L}}(E_c) = \pi \left(\frac{s}{s-2}\right)^{1-2/s} \left(\frac{sC_s}{2E_c}\right)^{2/s}. \tag{1.3}$$

Integration over a thermal distribution of collision energies yields the thermal rate

[‖]These treatments thus ignore the internal states of the reactants.

constant for a reaction involving this isotropic potential, which has the following temperature dependence [62]

$$k(T) \propto T^{(1/2-2/s)}. \tag{1.4}$$

Considering first an ion-molecule reaction involving a non-polar neutral molecule, the dominant force arises from a charge-induced-dipole interaction which varies as $1/r^4$. Thus, for this potential energy function, we can see that this approach yields a rate constant independent of temperature. Such is the case for the Langevin ion-molecule capture theory (the simplest of the capture theories), which assumes an isotropic charge-induced-dipole interaction and ignores molecular rotation. The expression for the Langevin rate constant is given by (in SI units):

$$k_{\mathrm{L}} = \frac{2\pi e}{\sqrt{4\pi\epsilon_0}} \left(\frac{\tilde{\alpha}}{\mu_{\mathrm{r}}}\right)^{1/2} \tag{1.5}$$

where $\mu_{\mathrm{r}}$ is the reduced mass of the collision complex and $\tilde{\alpha} = \alpha/4\pi\epsilon_0$ is the molecular polarisability volume. Typical rate-constants calculated via this method are around $1{\times}10^{-9}$ cm$^3$ s$^{-1}$; for example Langevin theory predicts a rate constant of $8.7{\times}10^{-10}$ cm$^3$ s$^{-1}$ for the reaction of $Ca^+ + CH_3F$.

One extension of the Langevin theory, proposed by Bowers and Su [63, 64], is the Average Dipole Orientation (ADO) theory, which represents an attempt to account for the charge-dipole interaction, which occurs in reactions involving polar neutral molecules. ADO theory augments the Langevin expression with a temperature-dependent term, to provide an approximate description of the charge-permanent-dipole interaction. The more convenient parameterised form of the rate constant is as follows:

$$k_{\mathrm{ADO}} = k_{\mathrm{L}} + 2\pi C(T)\frac{\mu e}{4\pi\epsilon_0}\left(\frac{2}{\mu_{\mathrm{r}}\pi kT}\right)^{1/2}. \tag{1.6}$$

Here the additional term results from an averaging of the ion-dipole interaction over the classical rotation of the molecule, where $\mu$ is the dipole moment and $C(T)$

is a function of $\mu/\tilde{\alpha}$ that describes the tendency of the dipole to assume a particular orientation through interaction with the ion. Typical values are thus slightly larger than those of the Langevin expression; for example in the reaction of $Ca^+ + CH_3F$, $k_{ADO} = 1.79 \times 10^{-9}$ cm$^3$ s$^{-1}$ at a temperature of 300 K.

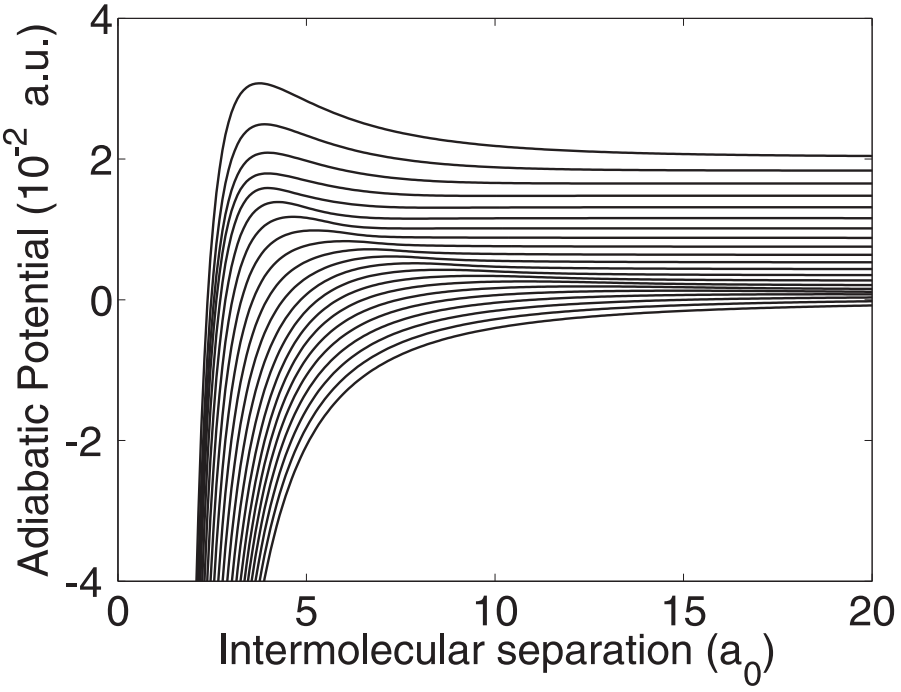


Figure 1.1: Examples of rotationally adiabatic potential curves generated for the reaction of an ion and diatomic molecule, in this case $H^+$ and HCl. The curves shown correspond to diatomic rotational quantum numbers $j = 0$–20 (ascending in energy as $j$ increases). In all cases the projection of the total angular momentum on the internuclear axis, $\Omega = 0$.

More advanced capture theories treat molecular rotation by calculating radial potential curves for all relevant initial rotational quantum states of the molecules involved. This approach forms the basis for the Statistical Adiabatic Channel Model (SACM) of Troe and co-workers [65], and the rotationally adiabatic, capture centrifugal sudden (ACCSA) theory developed by Clary [66, 67]. Both methods take into account the quantisation of the total angular momentum, which is especially important at very low temperatures where only a few angular momentum states may contribute to the rate constant. These two approaches have been shown to be

equivalent when averaged over a thermal distribution of collision energies [68], and for the analysis of the ion-molecule reactions presented later we rely on ACCSA calculations. ACCSA theory explicitly treats the molecular rotation via the formation of an effective Hamiltonian for the ion-molecule system. By invoking the centrifugal sudden approximation (CSA) [67] this Hamiltonian can be diagonalised over a grid of fixed internuclear separations to generate a series of rotationally adiabatic potential energy curves (see Fig. 1.1). Each curve correlates at large internuclear separation with a unique rotational eigenstate of the molecule, and can be used to calculate a rotationally state-selected capture cross-section. As mentioned earlier, this is done by calculating whether there is enough collision energy to surmount the barrier determined by the combination of the rotationally adiabatic potential energy curve, and a centrifugal barrier contribution determined by the total angular momentum of the collision. Thermal state-selected rate constants may be determined by integrating over a Boltzmann distribution of translational energies. Similar averaging of these rotationally state-selected rate constants yields the thermal rate constant.

All of the capture theories discussed so far treat motion along the reaction coordinate classically. Quantisation of this translational motion is not expected to become important until reactions are carried out in the low limit of the cold regime and into the ultracold domain, where collision energies correspond to temperatures less than 1 mK [69]. More complicated and computationally more expensive quantum capture theories are necessary in this regime. In addition, quantum capture calculations require large basis sets for barrierless reactions due to the large number of quantum states supported in the deep potential wells, and the general need to include hyperfine levels which are more important at low temperature [70]; these factors increase the computational expense of these calculations still further. Further detail regarding quantum capture theories is omitted here on account of the

fact that translational quantum effects are not believed to be significant for the temperature ranges of the present work. Classical capture theories have had great success in reproducing the rate constants of barrierless ion-molecule reactions over a wide range of temperatures and down to around 10 K [6]. Their success relies in part upon the centrifugal barrier appearing at large internuclear separations, which is often the case for ion-molecule reactions given the long-range nature of their intermolecular forces.

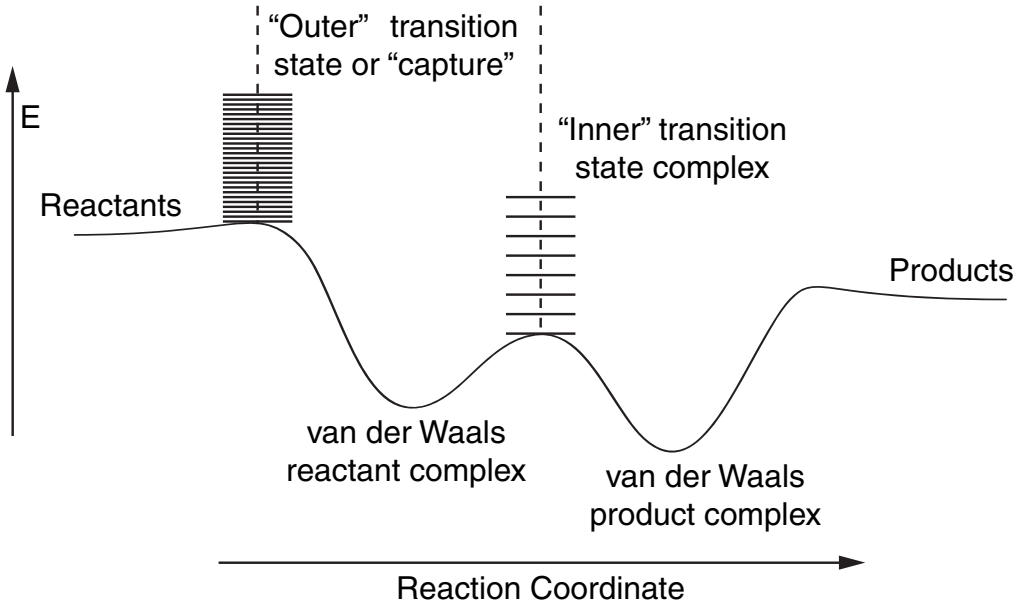


Figure 1.2: Schematic diagram of the reaction profile for a "barrierless" reaction in the context of the two transition state model. Horizontal lines at the transition states represent the energy levels there.

An appreciation of the validity of capture theory rate constant predictions can be gained by considering a "two transition state" model of chemical reactions, as illustrated in Fig. 1.2, which is often invoked in the theoretical analysis of reactions at low temperatures. This theory considers both an outer transition state arising from the capture of the free reactants to form a van der Waals complex, and an inner transition state corresponding to formation of a covalently bound complex at shorter range. These transition states arise due to the fact that forma-

tion of a chemical bond requires a particular orientation of the reactants in order to maximize the overlap of the electronic orbitals involved in the incipient bond. This places a restriction on the range of reactive orientations, and the orientational requirements for bond formation are often different from the lowest energy orientations in the long-range part of the intermolecular potential for either the approaching reactants, or the separating products. This means that, along the reaction coordinate, it is very common for there to be a van der Waals potential minimum either side of the complex associated with bond formation (see Fig. 1.2), and these give rise to the inner and outer transition states as defined above**. Although the importance of the transition state in determining the dynamics is strongly acknowledged, the influence of van der Waals forces in the region of the potential surface far from the transition state can also be decisive in determining the kinetics. For example, in the reaction Cl + HD the product branching ratio is sensitive to van der Waals forces in the entrance channel, especially for lower rotational quantum states [58]. For this reason, and the fact that the properties of the inner transition state arise from a fine balance between long-range interactions, short-range repulsions and chemical bonding, there is a large reliance on *ab initio* calculations in the analysis of these types of reactions. A van der Waals potential minimum in the product channel is generally less important with regard to the kinetics [71], although exceptions do exist. One such special case is the reaction of F + HD, which shows a reactive resonance in the HF + D product channel that gives rise to a pronounced forward-scattering peak in the calculated F+HD ($v = 0$, $j = 0$) HF ($v = 3$) + D differential cross-section [72, 73].

Long-range capture theories can therefore often overestimate the rate constant on

**The existence of the inner transition state can also be rationalised in terms of the free energy: the orientational requirements for bond formation mean that entropy decreases with the reactant separation. At the same time the strength of the newly forming chemical bond increases as the reactants approach. The interplay between these two factors results in the formation of a maximum in the free energy pathway at a separation of roughly 2–4 Å, *i.e.*, a transition state.

the basis that they assume a unit reaction probability if the outer transition state is surpassed. However, should the inner transition state lie close to, or above, the asymptotic energy of the reactants, it can in fact be the dominant kinetic bottleneck [71]. Thus the energy of the inner transition state relative to that of the asymptotic reactant fragments is important in determining the relative importance of short-range interactions. Notable examples can be found in the reactions of $O(^3P)$ with various alkenes, for which the reaction rates tend to correlate with this energy separation [74]. A consideration of the entropy change at the inner transition state is also paramount. In general the larger the number of rotational modes in the fragments, the greater the decrease in the entropy (or number of states) as free rotation becomes heavily restricted at the inner transition state. This, in conjunction with increased steric repulsion effects means that the inner transition state is expected to be more important for two non-linear polyatomic molecules, and less important for atom-diatom reactions. However the type of interaction is also important, for example ion-molecule, radical-molecule or radical-radical. In general, the weaker the intermolecular potential, the higher in energy the inner transition state becomes relative to the reactants. In addition, the position of the outer barrier moves to closer range where chemical bonding effects may become important. The relative importance of the inner and outer transition states in determining the dynamics can be expected to have a certain temperature dependence. One may consider a statistical view in which the number of states at the outer transition state increases faster with rising temperature than the number of states at the inner transition state. Equally, one can think about the dynamics of a single collision in which, given greater thermal energy, the system can explore larger regions of the intermolecular potential, thereby reducing the chance of traversing the inner transition state. Hence, at higher temperatures the tighter inner transition state usually provides the dominant contribution to the rate, especially if the entropy

decrease is large. At low temperatures, given an inner transition state lying below the reactants in energy, the global rate is often determined by the rate for forming the van der Waals complex, and thus the outer transition state can become dominant in this limit [75]. In general both inner and outer transition states should be considered when rationalising kinetic predictions[††], as stressed by Greenwald *et al.* [76] in their study of radical-molecule reactions. These ideas are considered further in the context of the experimental results presented in Chapter 6.

### 1.2.2 Experimental studies of ion-molecule chemistry

We now turn our attention to the experimental methods that have been employed for the study of low temperature ion-molecule chemistry. Beginning in the 1980s, most of the early techniques for studying ion-molecule reactions at temperatures below 80 K relied upon two general cooling methods, often described as cryogenic cooling and expansion techniques respectively.

Cryogenic cooling techniques involve the use of liquid helium (or other cryogens) to maintain the walls of the experimental apparatus at very low temperatures, thus thermalising any admitted gases to similar temperatures. Early measurements involved a selected ion drift flow tube (SIFT) apparatus which could be cooled with liquid helium as well as electrically heated, allowing studies between approximately 45–400 K [77]; soon temperatures as low as 20 K were routinely accessible [78]. Ions produced in the source chamber are mass selected and injected into a drift tube containing a buffer gas with an arbitrary admixture of neutral reactant. The ions are thermalised rapidly via collisions with the buffer or reactant gas, and reactions subsequently occur downstream within the drift tube. This is followed by the measurement of ion currents by a channeltron at the far end. These techniques

[††]The simple expression $1/N^{\dagger}_{\text{eff}} = 1/N^{\dagger}_{\text{inner}} + 1/N^{\dagger}_{\text{outer}}$ is often used to relate the number of states at the inner and outer transition states to the effective transition state number of states $N^{\dagger}_{\text{eff}}$.

are limited by the condensation of neutral reagent on the walls of the vessel. To avoid this the neutral reagent partial pressure must be much lower than its vapour pressure at the wall temperature; unless the vapour pressure is particularly high this requires the use of low concentrations of reagent which negatively influences the kinetics. Ultimately this limits the choice of low temperature neutral reagents to those with very high vapour pressures such as hydrogen and its isotopomers. This limitation does not apply to the ionic reagent as ions can be maintained far from the vessel walls using electric fields, however this means that the ions are not strictly equilibrated to the apparatus temperature. In a similar vein, Dunn and coworkers have developed cryogenically cooled Penning trap experiments, which allow rate measurements of reactions such as $CH_3^+ + H_2 \rightarrow CH_3.H_2^+$ to be performed down to 13 K [79]. However, the use of condensable gases at low temperature still limits the choice of neutral reagent.

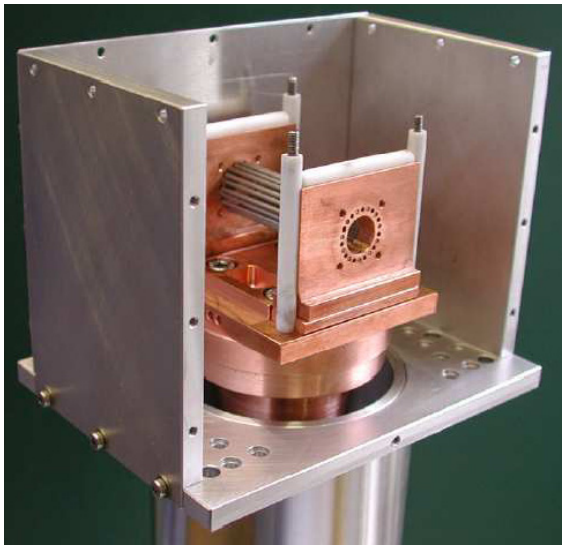

Figure 1.3: Photo of a 22-pole ion trap, mounted onto the two stages of a cold head. Reproduced from reference [80].

Stimulated by the liquid helium-cooled Penning trap of Dunn *et al.*, Gerlich and coworkers have also developed cryogenically cooled multipole ion traps (in particular the 22-pole trap, see Fig. 1.3) for confining molecular ions at low translational

temperatures [81]. Through the use of dense buffer gases, very efficient relaxation of all degrees of freedom of the stored ions is realised. Typical reaction experiments involve filling the trap with ions, and admitting buffer gas and reactants to the trap chamber. After an arbitrary time period the ions are extracted from the trap, mass analyzed and detected. Variation of the extraction pulse delay and reactant pressure allow rate constants and branching ratios to be measured [82–84]. The benefits of higher order multipole traps, which have steeper potentials and larger field-free trapping volumes, include significantly reduced trap-induced ion heating due to the fast oscillating electric fields of radiofrequency (RF) ion traps[‡‡]. The influence of the RF fields on the ion kinetic energies will be an important factor in the work presented later in this thesis. This method can be used to study processes at temperatures down to approximately 10 K which is the present temperature limit of this trapping technology [80]. In general this temperature limit arises due to the condensation of neutral gas on the chamber walls, just as in the case of cryogenically cooled SIFT measurements.

Expansion techniques rely on the supersonic expansion of a high pressure gas (normally a mixture of a given species and a buffer gas) through a small aperture into a vacuum. Multiple collisions between the molecules in the expansion produce an internally cold beam with a narrow velocity distribution travelling at high speed [85, 86]. However, despite their wide ranging use in experimental science, crossed supersonic beams are difficult to apply to very low collision energy studies. Although the mean collision energy can be reduced at shallow crossing angles, the spread of velocities limits the collision energy resolution. Nevertheless, seeding both reagent species into one beam can result in low temperature reactions [87],

[‡‡]RF fields produce a driven oscillation in which the ion's energy is on average conserved because momentum of the ion and the applied force are $\pi/2$ out of phase. Collisions between trapped ions and background species cause random phase shifts that result in energy from the RF field coupling into the motion of the ion; the magnitude of the coupling depends in part on the strength of the RF field.

and the possibility of accelerating an ionised component of the beam into a neutral reagent also present in the beam has been demonstrated successfully in the study of the $H_2^+ + H_2$ reaction [88].

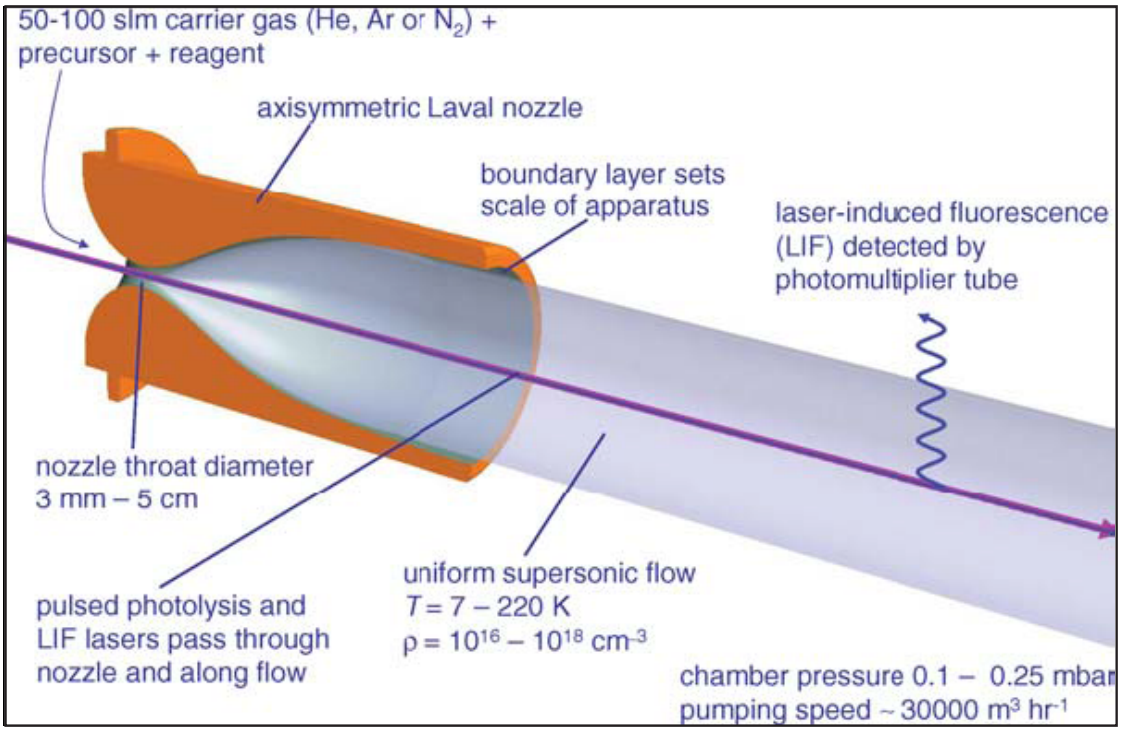


Figure 1.4: Schematic diagram of the CRESU apparatus depicting the Laval nozzle and supersonic flow, combined with pulsed laser photolysis laser induced fluorescence (LIF) detection permitting the study of neutral-neutral reaction kinetics at extremely low temperatures. Reproduced from reference [89].

The isentropic expansion of a buffer gas through a specially designed axisymmetric convergent-divergent "Laval" nozzle creates a collimated supersonic flow that has a genuine thermal equilibrium. The expansion is slow enough to ensure uniformity in temperature, density, and velocity for several tens of centimetres and some hundreds of microseconds downstream of the nozzle exit. However, expansion is rapid enough that condensation is avoided. Each temperature and pressure requires a separate Laval nozzle to be machined, with a carefully calculated internal profile [90]. This methodology, developed by Rowe *et al.* and termed the CRESU

technique [6, 90], has allowed ion-molecule reactions to be studied over a wide range of temperatures, down to as low as 7–8 K, although 15 K is more typical. Also, in the late 1980's I. W. M. Smith adapted this technique to study fast radical-neutral reactions, for example CN + $O_2$ [91]. However, when performed in the manner of a continuous flow, this method is extremely expensive due to the high powered vacuum pumps and large volumes of helium buffer gas, reactant and precursor which are required. In particular, this means that the use of isotopically substituted reagents would be very costly. This method has been developed further by M. A. Smith *et al.* [92, 93], and the most recent incarnation involves a pulsed system wherein buffer gas, neutral reagent and ion precursor are expanded through the Laval nozzle in 10 Hz pulses. Ions are generated by multiphoton ionisation at a distance of 10–30 nozzle diameters downstream of the nozzle where the velocity is almost at the hypersonic limit. The flow continues to expand downstream and the ions eventually react with the neutral molecules. A moveable time-of-flight mass spectrometer perpendicular to the flow monitors reagent and product ion signals as a function of distance from the ionisation beam. Whilst the pulsed design means that lower vacuum pumping rates and smaller volumes of gas are needed, the lowest temperatures yet achieved with this method ($\sim$53 K) are higher than for the continuous flow case. In both cases, the density continuously drops along the flow direction, and earlier in the beam the neutral-neutral collision rate is negligible which creates a non-Maxwell-Boltzmann velocity distribution in the flow. Despite this, it has been shown possible to assign a well defined average kinetic energy [94], however rotational temperatures can diverge considerably from this kinetic temperature.

Both cryogenic cooling and supersonic expansions are used in the merged beam techniques developed by Gerlich *et al.*, which involve the merging of a well characterised beam of slow ions with an internally cold supersonic neutral beam to

produce reactive collisions at low relative velocities [80, 95]. Cryogenically cooled radiofrequency traps assist in the generation of the slow ion beam which is guided in a wire quadrupole through a mass filter. Mass-selected ions are subsequently deflected by a weak magnetic field and injected at the desired velocity into another guide such that they are co-linear with a pulsed supersonic expansion of neutral molecules (the ions may be pulsed in unison). In general this type of apparatus is very challenging to operate however. The results depend critically upon the operating conditions of the supersonic beam, and a quantitative analysis requires measurement of the rotational distribution produced during the expansion. Efforts in this area appear to be ongoing [80].

Reactive and inelastic collisional studies at a tunable collision energy are possible using crossed molecular beams in which one of the beams is passed through a Stark decelerator, either to reduce the beam energy or to produce velocity-selection. At the moment these experiments are focused on the study of inelastic scattering, for example between decelerated OH radicals and velocity-selected Xe atoms [96]. Higher energy resolution is envisaged through the use of two crossed Stark decelerators, whose construction is in progress [97]. One could envisage the use of such an apparatus for cold ion-molecule reactive collision experiments in the future, although this remains speculative.

Although not an ion-molecule system, it is worth noting the achievements of Jin, Ye and coworkers, who have succeeded in studying the reactions of ultracold KRb molecules [98], formed via Feshbach resonance tuning [99] in an optical trap. This is the first study of quantum-state controlled chemical reactions in the ultracold regime. As might be expected in the ultracold regime, the observed reaction rates were seen to be determined by long-range scattering dynamics dictated by quantum statistics, angular momentum barriers, and threshold laws. Reactions between

fully spin-polarised KRb molecules were observed to be 10–100 times slower than reactions observed in a spin-mixed sample, suggesting that even something as seemingly insignificant as the flipping of a single nuclear spin can dramatically influence the reaction dynamics.

## 1.3 Experimental studies involving trapped and laser-cooled ions

### 1.3.1 Experimental developments

Before describing various chemical studies, we now review briefly some of the experimental developments involving trapped laser-cooled atomic ions (however a detailed discussion of many of these points is delayed until Chapter 2). Owing to their charge, ions may be readily confined in specially designed traps that make combined use of static and radiofrequency electric fields to generate an effective three dimensional potential minimum at the centre of the trap. In general, traps are designed such that the ions can be treated as moving within a harmonic effective trapping potential, which simplifies analysis. Suitable trapped atomic ions can then be translationally cooled through the application of Doppler laser-cooling, which exploits the momentum transfer associated with the absorption of photons to reduce the translational temperature of the ions into the millikelvin regime. At low enough energies, typically below 100–150 mK, the laser-cooled ions will condense into ordered lattice structures known as Coulomb crystals. The ions within these structures are strongly localised, with a characteristic spacing of 10-25 $\mu$m, and very low kinetic energies (typically $E_{\mathrm{kin}}/k_{\mathrm{B}} \geqslant 10$ mK near the trap axis[¶]). These properties, and the long lifetimes of these ion crystals within the trap (typ-

[¶]One must be mindful of the dominant contribution to the ion effective kinetic energies which arises away from the trap axis due to the oscillating radiofrequency fields.

ically hours) make Coulomb crystals a very attractive system for the study of cold chemistry [100].

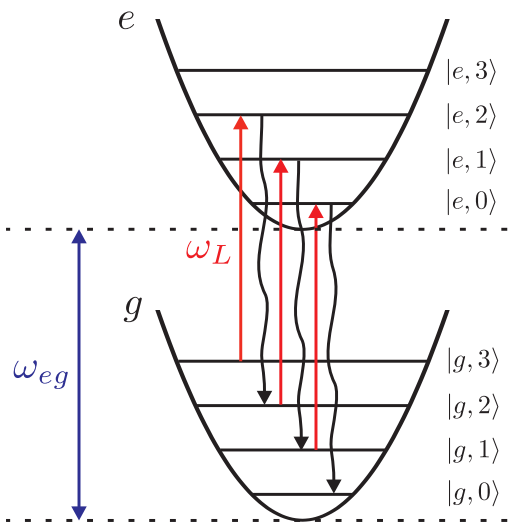


Figure 1.5: Illustration of sideband cooling. A laser resonant with the first red detuned motional sideband promotes a trapped ion to the excited state, but with one less quantum of energy in its vibrational motion within the trap. From here the most probable decay is to the ground state, but without a subsequent change in its motional quantum number. This step is cycled to achieve the population of the zero-point level.

In the regime where the linewidth $\Gamma$ of an internal transition in a trapped ion is much smaller than the trap frequencies (also called the Lamb-Dicke limit), motional sidebands can be resolved in the absorption spectrum of the ion. These sideband frequencies correspond to the transitions between the different motional eigenstates for the ground and excited electronic states of the trapped ions within the effective harmonic potential of the trap — analogous to the transitions between the vibrational levels of a harmonic oscillator. In this regime, and for small numbers of ions, these sidebands can be exploited by employing an additional laser, resonant with the first red detuned motional sideband, in order to reduce the vibrational quantum number (denoted here as $n$) of ions in the harmonic trapping

potential. Each excitation results in $|g, n\rangle \rightarrow |e, n-1\rangle$ followed by a preferred spontaneous decay described by $|e, n-1\rangle \rightarrow |g, n-1\rangle$. The cycle is repeated until the vibrational zero-point energy is reached, whereupon no more absorption occurs (see Fig. 1.5). Sideband cooling, first proposed by Wineland and Dehmelt [101] in 1975, allows the cooling of the ions to translational temperatures in the microkelvin range. However, for dipole transitions, $\Gamma$ is generally of the order of several MHz, and very strongly confining trapping fields and narrow cooling-laser bandwidths are therefore required to resolve these motional sidebands [102]. This technique is limited to small samples of ions (usually arranged along the axis of the trap in string configurations), therefore it is more applicable to areas such as quantum information processing than reaction studies involving large crystals.

A development very much of use in reaction studies is that of sympathetic-cooling, which exploits the fact that trapped molecular ions may be translationally cooled through their Coulomb interaction with the laser-cooled atomic ions. In this way, molecular ions can be cooled to kinetic energies similar to those of the laser-cooled ions ($\gtrsim$10 mK), and this means that a certain degree of generality is afforded through the use of Coulomb crystals. Thus, trapped laser-cooled ions also share many of the potential applications already cited for cold atoms and molecules, for example the high resolution spectroscopy of sympathetically-cooled molecular ions has been demonstrated [103]. At the same time, constituent ion mass/charge ratios are amenable to *in situ* non-destructive identification via techniques such as resonance excitation mass spectrometry [104–106] (which is detailed in Chapter 5). These techniques, along with the monitoring of the fluorescence produced by the laser-cooled ions, can allow the measurement of changes in the composition of ion crystals as a function of time. This allows the investigation of low energy processes occurring within the crystal, such as reactive and inelastic collisions, and makes Coulomb crystal based systems an ideal candidate for the study of various

ion processes.

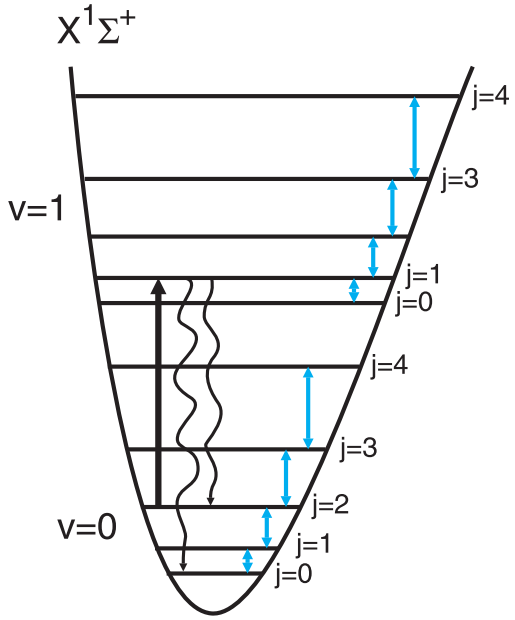


Figure 1.6: Schematic diagram of the optical rotational cooling scheme demonstrated by Drewsen *et al.* [107]. The solid black line represents the driven rovibronic transition, with the wavy lines indicating electric dipole allowed spontaneous decays. Blue lines indicate blackbody radiation induced transitions that redistribute the rotational population.

Sympathetic-cooling is generally only effective in reducing the translational energy of the molecular fraction because of the isotropic $1/r$ nature of the Coulomb interaction between the ions. Additionally, large differences in the energy scales of rovibrational and translational transitions mean that the internal degrees of freedom are not efficiently coupled to the translational motion* [109]. However, proposals exist for methods to optically cool the internal states of large classes of trapped molecular ions. Such proposed schemes generally include the use of additional lasers to drive infra-red vibrational transitions, or Raman transitions between vibrational levels, resulting in rovibronic decays to lower rotational levels, mediated by blackbody radiation or filtered broadband light sources [110–113].

*Although schemes for strengthening this coupling have been proposed [108].

Recently, two such schemes have been experimentally demonstrated. The first, developed by Drewsen and coworkers [107, 113], and illustrated by Fig. 1.6, involves the rotational cooling of sympathetically-cooled $MgH^+$ molecular ions through the coupling of an additional laser to the $|v = 0, j = 2\rangle \rightarrow |v = 1, j = 1\rangle$ transition. Once excited to this upper state, the population will decay to either the rovibronic ground state $|v = 0, j = 0\rangle$ or $|v = 0, j = 2\rangle$; the latter case will simply result in re-excitation. Blackbody radiation (BBR) induced dipole-allowed transitions will redistribute rotational population from higher rotational states towards $|v = 0, j = 2\rangle$ from which it will be efficiently removed (as will population transferred by BBR induced transitions from $|v = 0, j = 0, 1\rangle$). This technique has resulted in the achievement of rotational temperatures corresponding to about 20 K, with 37% of the population detected in the rovibronic ground state. The second method, which has been demonstrated by Schiller *et al.* [114] (see also a similar proposal in Ref. [111]), is essentially similar to the previous case, but with a second additional laser driving the $|v = 0, j = 1\rangle \rightarrow |v = 2, j = 0\rangle$ transition. Using this method, a ground state population fraction of $\geqslant 0.78$ has been achieved for sympathetically-cooled $HD^+$ molecules, corresponding to a rotational temperature of about 26.5 K in this case. At present these effective rotational temperatures could also be achieved through a cryogenic setup, however optical cooling is faster, more convenient and does not compromise the translational temperature of the sample.

Lastly, the use of Fabry-Perot type cavities, in conjunction with single ions or larger ion crystals, promises to be of some importance for advancements in quantum information processing, and more general investigations into light-matter interaction [115–121]. Inside a high-finesse cavity, the electromagnetic field becomes quantised into discrete cavity modes. This has implications for the way in which matter confined inside the cavity interacts with light, including the possibility of coherent

control of quantum states with single photons. Ion crystals offer a number of advantages in these studies relative to trapped neutral atoms. Firstly they may be more tightly confined, and for longer periods of time. Additionally, the spatial structure of the ion lattice means that the decoherence rate due to collisions is low, and there is an inherent ability to study interactions between the ordered ion lattice and a standing wave light-field generated inside the cavity. In the case of neutral atoms, such spatial ordering would require the use of optical lattices. Optical pumping and state preparation are also relatively easily achieved in ion crystals, owing to the low optical density of these systems. Thus, Coulomb crystals in high-finesse cavities represent a promising medium for realising a variety of quantum-information devices, such as a quantum memory for light [116].

### 1.3.2 Chemical studies involving Coulomb crystals

The ion-neutral reactions most easily studied with Coulomb crystals are those involving the direct reaction of the laser-cooled atomic ions themselves, although other reactions may also be studied using sympathetically-cooled molecular ions. A selection of these types of studies are summarised in Table 1.1. Initial experiments involved the formation of cold trapped $CaO^+$ ions by the reaction between laser-cooled $Ca^+$ ions and neutral $O_2$ [122, 123]. The reaction $Mg^+ + H_2 \rightarrow MgH^+ + H$ and its deuterated analogues were also studied, and both the reaction rates and branching ratios were deduced [50]. Charge-exchange reactions such as $Mg^{2+} + O_2 \rightarrow Mg^+ + O_2^+$ and $^{44}Ca^+ + {}^{40}Ca \rightarrow {}^{44}Ca + {}^{40}Ca^+$ have also been studied [124]. Many reactions proceed from the ion ground state, but there are those that require significant photoexcitation of the ions in order to proceed, for example $(Be^+)^* + HD \rightarrow BeH^+(BeD^+) + D(H)$ [125] and $(Mg^+)^* + H_2(D_2) \rightarrow MgH^+(MgD^+) + H(D)$ [50]. Molecular ion-neutral reactions have also been studied using molecular ions embedded in a laser-cooled atomic ion crystal, for example the back reaction

$CaO^+ + CO \rightarrow Ca^+ + CO_2$ [122, 123], and most notably the astrophysically important reaction $H_2^+ + H_2 \rightarrow H_3^+ + H$ [125, 126]. Unimolecular photodissociation studies have been also been performed on sympathetically-cooled molecular ions, most notably in the characterisation of the photodissociation pathway of aniline [105]. This study involved the frequency measurement of the centre-of-mass vibrational modes in pure and bi-component two-ion crystals through the scanning of the frequency of a time-varying force on the ions; these mode frequencies can be related to the mass/charge ratios of the sympathetically-cooled molecular ion. Such "resonance-excitation mass spectrometry" is also used to support the work in this thesis and is described in detail in Chapter 5. In general however, the reaction studies performed thus far cannot really be deemed cold chemistry because, whilst the trapped ions may have low kinetic energies, the neutral reactant is typically introduced as a room-temperature gas. In this instance the kinetic energy of the neutral reactants dominates the ion-neutral collision energy distribution. By way of example, collisions of laser-cooled $Ca^+$ ions with room-temperature $CH_3F$, $CH_2F_2$ and $CH_3Cl$ molecules (see Chapter 6) occur with average kinetic energies between $\langle E_{\mathrm{coll}} \rangle / k_{\mathrm{B}} \approx 200$ and 350 K, depending on the reduced mass of the collision partners.

The use of a translationally cold reactant molecular beam, in conjunction with suitable Coulomb crystals (those with minimal effective ion kinetic energies), is a step towards true cold chemistry. This technique circumvents the limitations imposed by the use of condensable gases at low temperatures. The ion crystals can be reacted directly with an incident beam of cold neutral molecules, generated by recently developed techniques such as velocity-selection or Stark deceleration, with very high sensitivity (a single reactive collision can be observed in the right conditions), and long interaction times (typically hours). Product ions generated in any reaction are sympathetically-cooled by the atomic ions and incorporated into

| Process | Examples | Refs |
|---|---|---|
| Atomic ion-molecule reactions | $Ca^+ + O_2 \rightarrow CaO^+ + CO$ | [122] |
| | $Mg^+ + H_2 \rightarrow MgH^+ + H$ | [50] |
| | $Mg^+ + D_2 \rightarrow MgD^+ + D$ | [50] |
| | $Ba^+ + O_2 \rightarrow BaO^+ + O$ | [127] |
| | $Ba^+ + N_2O \rightarrow BaO^+ + NO$ | [127] |
| | $Ba^+ + CO_2 \rightarrow BaO^+ + CO$ | [127] |
| | $(Be^+)^* + HD \rightarrow BeH^+ + D$ | |
| | $\rightarrow BeD^+ + H$ | [125] |
| | $(Mg^+)^* + HD \rightarrow MgH^+ + D$ | |
| | $\rightarrow MgD^+ + H$ | [128] |
| Molecular ion-molecule reactions | $H_3O^+ + NH_3 \rightarrow H_2O + NH_4^+$ | [129] |
| | $H_2^+ + H_2 \rightarrow H_3^+ + H$ | [125, 126] |
| | $H_3^+ + HD \rightarrow H_2D^+ + H_2$ | [126] |
| | $H_3^+ + O_2 \rightarrow H_2 + HO_2^+$ | [126] |
| | $CaO^+ + CO \rightarrow Ca^+ + CO_2$ | [122] |
| | $BaO^+ + CO \rightarrow Ba^+ + CO_2$ | [127] |
| Charge-exchange reactions | $^{44}Ca^+ + {}^{40}Ca \rightarrow {}^{44}Ca + {}^{40}Ca^+$ | [124] |
| | $Mg^{2+} + O_2 \rightarrow Mg^+ + O_2^+$ | [124] |
| Photodissociation | $MgH^+ + h\nu \rightarrow Mg^+(Mg) + H(H^+)$ | [51] |
| | $C_6H_5NH_2^+ + h\nu \rightarrow C_5H_6^+ + HCN$ | [105] |
| | $C_5H_6^+ + h\nu \rightarrow C_5H_5^+ + H$ | [105] |
| | $C_5H_5^+ + h\nu \rightarrow$ c-$C_3H_3^+ + C_2H_2$ | [105] |
| | $C_{30}H_{46}O_4$ ($GAH^+$) $+ h\nu \rightarrow$ fragments | [130] |

Table 1.1: Selected experimental studies involving laser-cooled atomic ions in radiofrequency traps. Studies presented in this thesis are omitted.

the crystal, assuming that their nascent kinetic energy is less than the trapping depth [50, 131]. The ability to translationally cool molecular ions through their Coulomb interaction with the laser-cooled atomic ions promises a certain degree of generality in the choice of reagents. Work presented herein involves the coupling of a velocity-selected translationally cold neutral molecular beam into an ion crystal in an effort to study reactive collisions at low kinetic energy. As such, Coulomb

crystals and the techniques involved in their application to this study are discussed in greater detail in the ensuing chapters.

## 1.4 Outline of this thesis

This thesis concerns the application of Coulomb crystals, involving laser-cooled $^{40}Ca^{+}$ ions, to the investigation of ion-neutral molecule chemical reactions at low collision energies. Having surveyed the landscape of cold chemistry in Chapter 1, Chapter 2 explores the theory behind trapping and laser-cooling ions, and the formation of Coulomb crystals at low energy. In these Coulomb crystals, the $Ca^{+}$ ions are cooled through their interaction with two sources of continuous laser radiation. Therefore, Chapter 2 also provides a theoretical framework for understanding this interaction, and for simulating the electronic quantum state populations of a laser-cooled $^{40}Ca^{+}$ ion. Chapter 2 also outlines the structural simulation of Coulomb crystals via molecular dynamics computation. These simulations allow the production of simulated analogues of experimental fluorescence images, discussed in Chapter 3, which are key in elucidating ion numbers and temperatures.

In Chapter 3 many of the practical details associated with producing and manipulating both single and multi-component Coulomb crystals are detailed. These methods are employed in reaction studies involving $Ca^{+}$ and $CH_3F$ which are described in Chapter 4. Also detailed here is the coupling of an ion trap apparatus to a quadrupole velocity-selector for the first time. The quadrupole velocity-selector acts as a source of translationally cold neutral molecules and allows the study of ion-molecule reactions at low collision energies. Rate constants obtained from these low-energy experiments are contrasted with those obtained from reactions carried out at collision energies corresponding to room-temperature, and the methods for determining the rate constants for these reactions are outlined. Resonance-

excitation mass spectrometry techniques employed in the non-destructive *in situ* identification of reaction products are presented in Chapter 5, along with results collected in support of the reaction studies presented in this thesis.

In Chapter 6 the focus will turn to the results of more detailed studies concerning a range of reaction systems involving $Ca^+$. These centre on the investigation of the dependence of the overall rate constant on the relative populations of the $Ca^+$ electronic states. Manipulation of the laser-cooling parameters allows us to separate the contributions to the global rate constant from the ground and combined excited states of $Ca^+$. These results are analysed in the context of capture theories and *ab initio* electronic structure calculations. Again these studies involve reactions with neutral molecular samples at room temperature, and with translationally-cold molecules (with $\langle E_{\rm kin}\rangle/k_{\rm B} < 5$ K). Chapter 7 concerns the extension of our investigations to more general cold bimolecular ion-molecule reactions which involve $Ca^+$ only as a spectator; Chapter 8 concludes and suggests extensions and improvements to the experiments considered in this thesis.

# Chapter 2

# Trapping and laser cooling of ions

## 2.1 Introduction

This chapter is primarily concerned with the principles and theory behind the spatial confinement of ions and the removal of their translational energy via laser-cooling. Having covered the basics behind ion trapping, the focus will be on the design and use of the linear Paul trap, and a description the motion of ions confined within it. There will then be an overview of laser-cooling before we concentrate specifically on the Doppler cooling of $Ca^+$ to temperatures in the millikelvin regime. This leads to discussion regarding the formation and nature of ion crystals, and the introduction of the fluid model of a trapped charged plasma. There then follows a brief section which outlines the modification of existing molecular dynamics software and describes it's application to the simulation of Coulomb crystal structures. Finally, there will be a brief derivation of the Optical Bloch Equations (OBE), which underpin the calculation of the steady-state electronic quantum state populations of $Ca^+$ later in this work.

## 2.2 Ion trapping

### 2.2.1 Principles

The first hurdle to be overcome on the path to achieving a sample of translationally cold localised ions is their collective spatial confinement. Given the electrically charged nature of ions, it follows that electric fields may be of use to this end via the generation of some kind of electrostatic potential minimum from which the ions cannot escape.

The partial differential equation which governs electrostatic potentials is the Laplace equation:

$$\nabla^2\phi = 0. \tag{2.1}$$

Re-written in three dimensions,

$$\frac{\partial^2\phi}{\partial x^2} + \frac{\partial^2\phi}{\partial y^2} + \frac{\partial^2\phi}{\partial z^2} = 0 \tag{2.2}$$

it is clear to see that there can be potential minima in no more than two dimensions at any given time, with a potential maximum required in the third dimension in order to balance the equation. This reflects the fact that a true electrostatic potential minimum (or maximum) is not achievable in free space. Earnshaw's theorem which prohibits static electric fields from trapping charged particles follows directly from this [132]. Therefore in the case of charged particles, the best trapping potential achievable with static fields is a 3D saddle point, for which motion in one particular degree of freedom is destabilised by the presence of a potential maximum. This problem is circumvented by the use of dynamic or time-varying electric fields.

If the electric fields are abruptly flipped back and forth in the correct way, the orientation of this saddle-point potential can be repeatedly flipped between two orthogonal orientations. For a charged particle moving in this potential, this means

that the unstable degree of freedom is also being flipped back and forth between two orthogonal axes at a given rate. If the saddle-point is changing orientation fast enough relative to the motion of a charged particle moving in this potential, dynamic confinement becomes achievable*. In practice the rapid re-orientation of these fields can allow multiple charged particles to be confined simultaneously.

The linear Paul trap is one such trap design arising from these ideas, and involves the use of electrodes to which a combination of radiofrequency (RF) and static DC voltages are applied. The linear Paul trap is used exclusively during the work described in this thesis, and detailed description is therefore limited to this design alone. However there are alternative designs such as the hyperbolic Paul trap [133] and the race-track trap [134]. The Penning trap [135] is another alternative design which involves the combination of electrostatic and magnetostatic fields.

Ion trapping is much more robust than the trapping of neutral atoms for the very reason that the electrostatic charge on an ion confers a stronger interaction with external electric fields. Even very hot ions may be successfully confined in a trap via *in situ* ionisation of the corresponding neutral species; this can occur cumulatively as the neutral beam is negligibly affected by the trapping fields. In contrast, neutral atoms must be decelerated to low energies before they can be magnetically and/or optically trapped (for example Zeeman slowing), as the available interactions are weaker in terms of their effect on the motion of neutral atoms.

*An oft-cited mechanical analogue of some value is the idea of a ball confined to the surface of a rotating saddle (or more correctly a saddle flipping between orthogonal orientations). If the saddle rotates too slowly, the ball will roll down one side. If the saddle rotates at just the right speed then as the ball begins to roll down the side, the steeper section will rotate in front of its path just in time to return it towards the centre. If the saddle rotates too quickly the ball can receive a large enough impulse to push it over the saddle edge in any direction.

### 2.2.2 The linear Paul trap

#### Design

The linear Paul trap (LPT) [136] is very similar in design to the quadrupole mass filter, which was developed in part during the 1950's by Wolfgang Paul [137] and for which he shared the 1989 Nobel Prize in physics [138]. The LPT is especially useful for its ability not only to trap and store ions, but also to function as a mass filter and spectrometer. These functions complement each other very well for the purpose of studying reactions involving trapped ions, and offer a non-destructive path to the identification of ions trapped *in situ* (these techniques are detailed in Chapter 5).

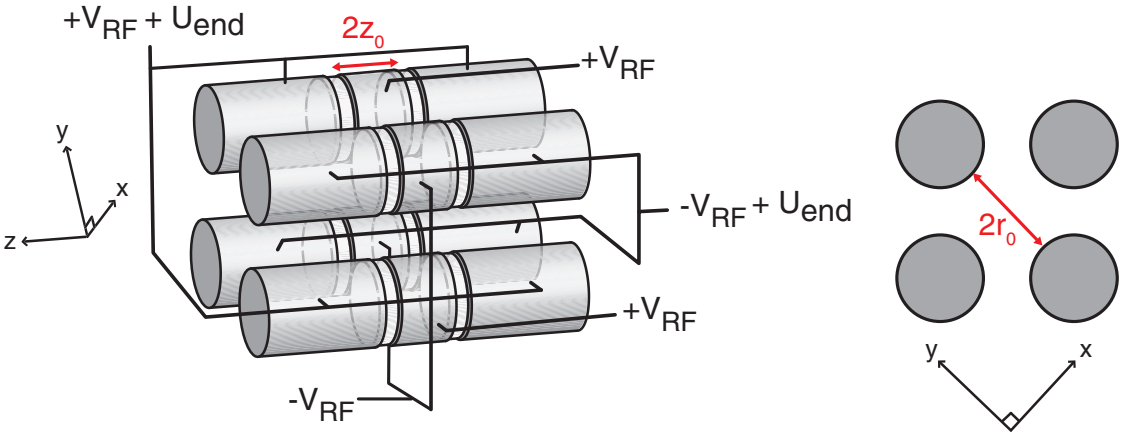


Figure 2.1: The design of the linear Paul trap, including the voltage configuration for ion trapping.

The LPT is based on a quadrupole design, with four cylindrical rods each separated lengthwise into a number of electrode segments. Each of these segments is separated by insulating material (in our case, the machineable glass ceramic MACOR) in order to allow independent voltages to be applied to each electrode. The most basic design employed in the present work involves three separate electrode segments per rod, with each of the four rods being identical in geometric design.

Dynamic trapping in the $x$ and $y$ directions (radial trapping relative to the trap $z$-axis) is achieved by applying oscillating RF voltages, $V_{\mathrm{RF}} = \pm V_{\mathrm{RF},0}\cos(\Omega_{\mathrm{RF}}t)$, equal in magnitude but opposite in polarity, to the two diagonal sets of electrodes comprising the quadrupole trap. These voltages create a saddle-like potential that is orientated along either the $x$ or $y$ axis and flips at the rate of once per RF cycle. As discussed above, when oscillating in the correct frequency range these fields result in a time-averaged pseudopotential minimum at the trap axis, but destabilise charged particle motion along this axis. To introduce axial trapping as well, an additional static DC voltage, $U_{\mathrm{end}}$, is applied to the electrodes at either end of the trap — the so-called end-cap electrodes. These voltages are indicated in Fig. 2.1.

In these types of quadrupolar traps a harmonic trapping potential is desirable, because it means that the equations of motion for a single ion in the trap may be cast in the form of the well-studied Mathieu equations, described in the next section. In actuality, hyperbolic electrode geometries would be required to form a true harmonic potential, and it is purely for convenience and ease of manufacture that cylindrical rods are used instead. However, given the right choice of $r_0$ and rod radius [139] the electric potential near the centre of the trap is, to a close approximation, harmonic or parabolic in form.

The full electric potential in the trap may be generated via multipole expansion (equivalent to Taylor expansion about the trap centre), whereupon the harmonic approximation to the true potential is made by discarding terms of greater than quadratic order. The resulting harmonic potential may be expressed in the following form (NB: $V_{\mathrm{RF}}$ is defined as a peak-to-peak voltage throughout the equations in this thesis, but its quoted values are in terms of zero-to-peak amplitudes unless

stated otherwise):

$$\phi_{\mathrm{RF}}(x,y,t) = \frac{V_{\mathrm{RF}}}{2}\left(\frac{x^2-y^2}{r_0^2}\right)\cos(\Omega_{\mathrm{RF}}t), \tag{2.3}$$

$$\phi_{\mathrm{end}}(x,y,z) = \frac{\kappa U_{\mathrm{end}}}{z_0^2}\left(z^2 - \frac{x^2+y^2}{2}\right), \tag{2.4}$$

$$\phi = \phi_{\mathrm{RF}} + \phi_{\mathrm{end}}. \tag{2.5}$$

The factors $r_0$ and $z_0$ relate to the trap geometry as indicated by Fig. 2.1, and $\kappa$ is also a geometric coefficient uniquely determined for a given trap design. For our trap design this was done by fitting the analytical potential above to a SIMION simulation of the fields resulting from our particular trap geometry; values of these important factors are included within Table 2.1

| | | |
|---|---|---|
| RF frequency | $\Omega_{\mathrm{RF}}$ | $2\pi \times 3.850$ Mhz |
| RF voltage | $V_{\mathrm{RF}}$ | 50–250 V |
| Endcap voltage | $U_{\mathrm{end}}$ | 0.1–40 V |
| Endcap separation | $2z_0$ | 5.5 mm |
| Diagonal electrode surface separation | $2r_0$ | 7 mm |
| Geometric factor | $\kappa$ | 0.244 |
| Electrode radius | R | 4 mm |

Table 2.1: Typical trap parameters used for the stable trapping of $^{40}Ca^{+}$ ions

During the course of the work in developing the experiments described in this thesis, three similar designs of the LPT were used. The first was a five segment design arising from an initial limitation in our ability to apply both a DC and RF voltage to the same electrode simultaneously. The end-cap electrodes were thus separated out and positioned between the longer RF electrodes. With new electronics the simpler symmetric three segment trap was employed, where the axially confining DC voltage could be applied in combination with the RF to all the end-cap electrode segments as described above. In subsequent reaction

studies involving the velocity-selector (detailed in Chapter 4), the asymmetric three segment LPT was used in an effort to offset the geometric trap centre closer to the exit of the velocity-selector. This was done in order to increase the number density of velocity-selected neutral molecules at the position of the trapped ions, and improve sensitivity to low fluxes. Thus, this is the trap used for the majority of the work presented in this thesis, although the principles remain the same for all three designs. The geometric factors, electrode radius, $z_0$, $r_0$, for these traps remain the same and are listed in Table 2.1. For the asymmetric 3-segment trap the electrode lengths are 11 mm, 5.5 mm and 23.5 mm long respectively.

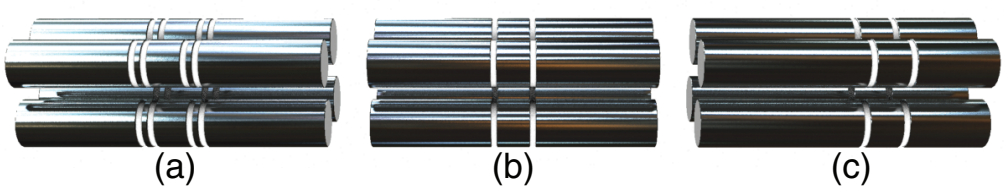


Figure 2.2: The three designs of our linear Paul trap. (a) Early 5-segment design where the end-caps appear as separate electrodes (2nd and 4th segments), due to limitations in our electronics. (b) Symmetric 3-segment design where both RF voltages and static end-cap voltages are applied to the end electrodes. (c) Asymmetric 3-segment design, employed during reaction studies in a bid to increase guided neutral molecule flux at the crystal (see later chapters).

### The motion of ions in the trap

Oscillating quadrupole fields are special for the very reason that the equations of motion for a single ion can be reduced to a set of decoupled one-dimensional differential equations of the Mathieu type. This is advantageous because the solutions of the Mathieu equations are well understood, with the stability of a trajectory dependent on only two dimensionless parameters and not on the initial conditions of the ion [82, 140].

Given the total electric potential in the form of Eq. 2.5, the Newtonian equations of motion for a particle of charge $Q$ and mass $m$ may be written according to

$F = ma = -QE = -Q\nabla\phi$ as:

$$\ddot{x} + \left(\frac{-\kappa Q U_{\text{end}}}{m z_0^2} + \frac{Q V_{\text{RF}}}{m r_0^2}\cos\Omega_{\text{RF}} t\right) x = 0 \tag{2.6}$$

$$\ddot{y} + \left(\frac{-\kappa Q U_{\text{end}}}{m z_0^2} - \frac{Q V_{\text{RF}}}{m r_0^2}\cos\Omega_{\text{RF}} t\right) y = 0 \tag{2.7}$$

$$\ddot{z} + \left(\frac{2\kappa Q U_{\text{end}}}{m z_0^2}\right) z = 0. \tag{2.8}$$

These may then be written in the form of the Mathieu equations,

$$\frac{\mathrm{d}^2 u}{\mathrm{d}\tau^2} + [a_{\text{u}} - 2q_{\text{u}}\cos(2\tau)]u = 0 \ ; \qquad u_{\text{i}} \in \{x, y, z\}, \tag{2.9}$$

by making the substitution $\tau = \Omega_{\text{RF}} t/2$ into equations 2.6, 2.7 and 2.8:

$$\frac{\partial^2 x}{\partial\tau^2} + \left(\frac{-4\kappa Q U_{\text{end}}}{m z_0^2 \Omega_{\text{RF}}^2} + \frac{4 Q V_{\text{RF}}}{m r_0^2 \Omega_{\text{RF}}^2}\cos 2\tau\right) x = 0 \tag{2.10}$$

$$\frac{\partial^2 y}{\partial\tau^2} + \left(\frac{-4\kappa Q U_{\text{end}}}{m z_0^2 \Omega_{\text{RF}}^2} - \frac{4 Q V_{\text{RF}}}{m r_0^2 \Omega_{\text{RF}}^2}\cos 2\tau\right) y = 0 \tag{2.11}$$

$$\frac{\partial^2 z}{\partial\tau^2} + \left(\frac{8\kappa Q U_{\text{end}}}{m z_0^2 \Omega_{\text{RF}}^2}\right) z = 0. \tag{2.12}$$

Finally, direct comparison of these equations with the form of the Mathieu equations yields the dimensionless Mathieu parameters:

$$a_{\text{x}} = a_{\text{y}} = -\frac{a_{\text{z}}}{2} = -\kappa\frac{4 Q U_{\text{end}}}{m z_0^2 \Omega_{\text{RF}}^2} \tag{2.13}$$

$$q_{\text{x}} = -q_{\text{y}} = -\frac{2 Q V_{\text{RF}}}{m r_0^2 \Omega_{\text{RF}}^2} \ ; \qquad q_{\text{z}} = 0. \tag{2.14}$$

The motion of an ion moving in these fields can be adiabatically separated into a higher frequency driven oscillation, termed the micromotion, and a lower frequency drift, known as the secular motion. The micromotion does not occur on the trap axis but increases towards the RF electrodes which drive it. In unstable trajectories the amplitude of this micromotion increases exponentially with time and the ions can either be ejected from the ion trap or crash into one of the electrodes. If

the trajectory is stable — and stability in general is elaborated on in the next section — the ion's secular motion can be interpreted in the context of a time-independent effective potential, $V^*$, which arises from this adiabatic approximation. An abbreviated derivation of this pseudopotential can be found in Appendix A, and a more complete description can be found in [82] and the references therein — we simply quote the main results here. The expression for the time-independent effective potential, $V^*$, experienced by an ion of mass, $m$, and charge, $q$, may be written as:

$$V^*(R_0) = \frac{q^2 E_0^2}{4m\Omega^2} + q\Phi_{\mathrm{s}}, \tag{2.15}$$

and the associated equation of motion for the smooth secular trajectory can therefore be expressed as:

$$m\ddot{R}_0 = -\nabla V^*(R_0). \tag{2.16}$$

Note that the first term in Eq. 2.15 is effectively a time-averaged potential resulting from the oscillating RF fields (which have amplitude $E_0$ and angular frequency $\Omega$); in the second term, $\Phi_{\mathrm{s}}$ represents the potential arising from the static fields.

By analogy to a quantum harmonic oscillator, the harmonic pseudopotential may also be written:

$$V^*(r,z) = \frac{1}{2}mw_r^2 r^2 + \frac{1}{2}mw_z^2 z^2 \tag{2.17}$$

with $r = \sqrt{x^2+y^2}$ the radial distance from the trap axis, and $z$ the axial distance from the trap centre. The corresponding secular motional frequencies $w_z$ and $w_r$ are given by

$$w_i = \sqrt{\frac{q_i^2}{2} + a_i}\frac{\Omega_{\mathrm{RF}}}{2}. \tag{2.18}$$

It is important to note that when $w_i$ is properly substituted for, there is no mass dependence of the axial potential, but there is a $(\frac{1}{m} + constant)$ mass dependence in the radial potential. The radial potential is therefore steeper for lighter ions, leading to a radial separation of ions with differing mass (assuming like charges),

with lighter ions preferentially trapped closer to the trap axis. This is an important point, and will be returned to in due course later in this thesis.

The pseudopotential model is a useful tool as it simplifies the treatment of the ion motion considerably. Its use facilitates calculation of the secular motion and the associated secular temperature of an ion ensemble, and helps establish the criteria for the stable trapping of the ions. In Section 2.5 there is an introduction to the use of molecular dynamics simulations for the purpose of modelling Coulomb crystals, and in this regard in particular a reduction of the full treatment to one involving only the pseudopotential proves very useful. Larger crystal simulations may be carried out faster, and at greater timescales, and without loss of information given situations where the RF oscillation of the fields is not of great importance (calculation of secular temperatures, crystal structure and also ion number determination).

### Stability

A direct result of the decoupling of the equations of motion in the harmonic potential is that the stability of a single ion trajectory within the trap is dependent purely on the values of $a$ and $q$, and not on the initial conditions. This means that a stability "map" can be generated in the $(a, q)$ parameter space. For certain values of $a$ and $q$ there will be stable confined ion trajectories regardless of the initial position of the ion in the trap or the phase of the RF fields. However, outside these zones of stability resonances exist that couple energy from the oscillating RF fields into the ion micromotion such that the ion oscillation amplitude increases exponentially, resulting either in expulsion from the trap or collision with the electrodes.

Another way to consider these stability diagrams is to consider the potentials once again. The harmonic axial potential is effectively a saddle point with a minimum

in the axial direction (ensuring axial trapping), and maxima in all radial directions. As such it provides a defocusing effect in the radial direction. The stable regions are those in which the dynamic radial trapping fields can counteract this defocusing and provide stable dynamic radial trapping as well.

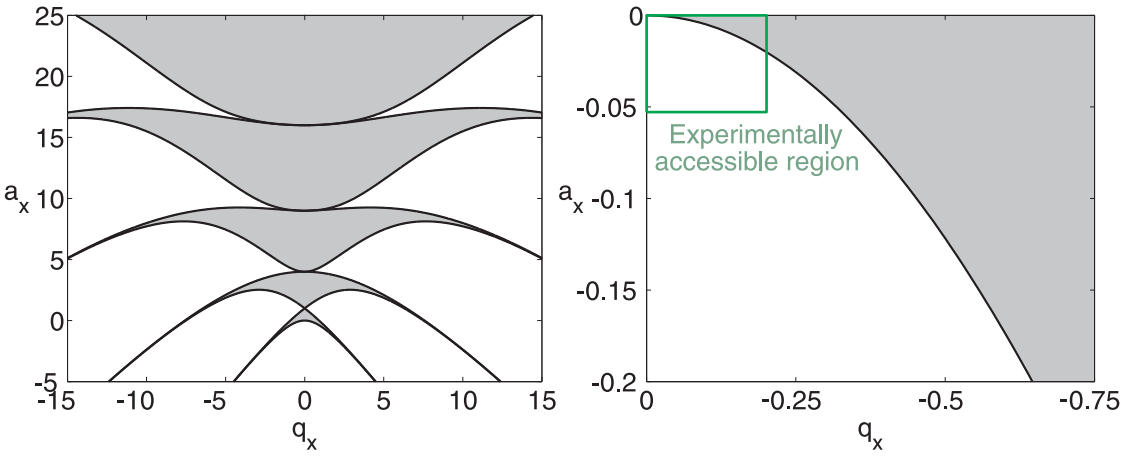


Figure 2.3: Stability regions for a single ion in a linear Paul trap, obtained via analytic solution of the Mathieu equations. Grey shaded areas represent regions of stable trapping.

Stability diagrams may be generated either by analytical solution of the Mathieu differential equations, or via classical trajectory numerical simulations performed over a grid in $(a, q)$ space. As can be seen from the analytical solution in Fig. 2.3, there are a number of separate stability regions within which ion trajectories will be confined indefinitely within the trap. In practice, with reference to the expressions for $(a_i, q_i)$,

$$a_{\mathrm{x}} = a_{\mathrm{y}} = -\frac{a_{\mathrm{z}}}{2} = -\kappa\frac{4QU_{\mathrm{end}}}{mz_0^2\Omega_{\mathrm{RF}}^2} \tag{2.19}$$

$$q_{\mathrm{x}} = -q_{\mathrm{y}} = -\frac{2QV_{\mathrm{RF}}}{mr_0^2\Omega_{\mathrm{RF}}^2}\ ; \qquad q_{\mathrm{z}} = 0, \tag{2.20}$$

it can be seen that only the quadrant negative in both $a_x$ and $q_x$ can be used in the case of a charged particle in a linear Paul trap, as the product of $Q$ and the trapping voltage must be positive. In most cases, only the lowest stability region is used due to the practicality of achieving the necessary parameters experimentally.

The right hand panel of Fig. 2.3 shows the region within which we have practical access, based on $U_{\mathrm{end}} = 0$–100 V and $V_{\mathrm{RF}} = 0$–300 V, with trap parameters listed in Table 2.2.

| | | |
|---|---|---|
| Mathieu $a_x$ parameter | $a_{\mathrm{x}}/U_{\mathrm{end}}$ | $-5.3 \times 10^{-4}\mathrm{V}^{-1}$ |
| Mathieu $q_x$ parameter | $q_{\mathrm{x}}/V_{\mathrm{RF}}$ | $6.7 \times 10^{-4}\mathrm{V}^{-1}$ |
| Radial frequency | $w_r/2\pi$ | 40–360 kHz |
| Radial trap depth | $D_r$ | $<$12.3 eV |
| Longitudinal frequency | $w_z/2\pi$ | 20–280 kHz |
| Longitudinal trap depth | $D_z$ | $\leqslant$1.2 eV |

Table 2.2: Typical Mathieu parameters, secular frequencies and trap depths used in the stable trapping of $^{40}\mathrm{Ca}^{+}$ ions, given where necessary values from Table 2.1, and typical working voltage ranges of $U_{\mathrm{end}} = 1$–20 V, $V_{\mathrm{RF}} = 200$–400 V peak-to-peak.

Numerical generation of the stability regions is achieved by first modelling the trapping fields through the use of SIMION. A 3D grid of electric field gradients derived from a computer model of the electrodes are passed to a FORTRAN program which uses them to repeat multiple single-ion trajectory simulations over a grid in $(a, q)$ space. The trajectories are calculated via 4th-order Runge-Kutta integration of the Newtonian equations of motion, with a fixed time-step much smaller than the length of an RF period. The simulations are propagated up until a user-defined time cap, and the lifetime of the ion in the trap is recorded in each case. A lifetime value less than the simulation time cap indicates that the ion has either been ejected from the trap, or has collided with an electrode, and is therefore in an unstable region of the map. In general a time cap of 1 ms appears adequate for convergence. Experimental generation of the single ion stability zone is performed by repeatedly loading a single ion into the trap and, over a grid of $V_{\mathrm{RF}}$ values, increasing $U_{\mathrm{end}}$ upwards from 0 V until the ion is lost, or the maximum achievable voltage reached.

The numerical simulation of stability diagrams for the $(a, q)$ region practically

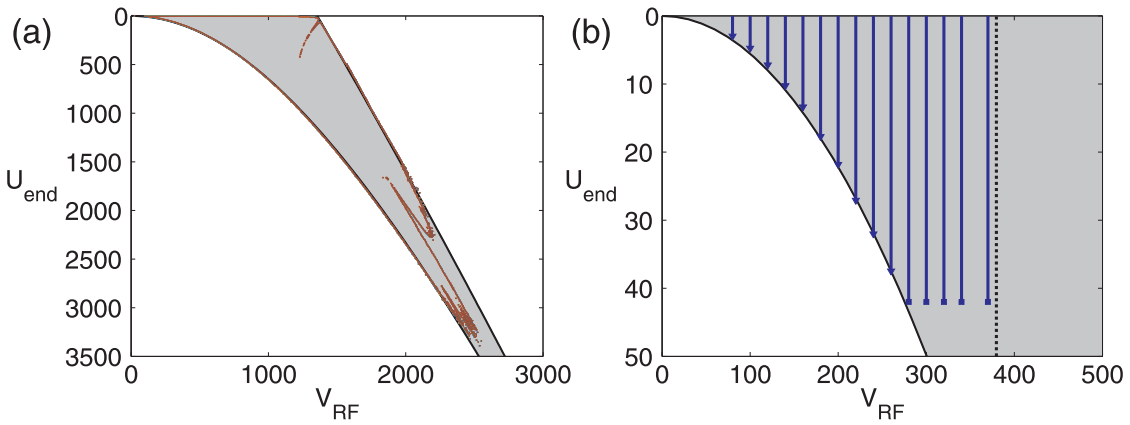


Figure 2.4: (a) Numerically generated stability region (boundary in red) overlaid across the grey shaded stability region obtained via analytical solution of the Mathieu equations. In order to match the two regions, a $\kappa$ value of 0.152 was required to achieve the correct relative scaling of the analytical boundary in voltage space. (b) Measurements of experimental single-ion stability overlaid across the analytical stability zone in grey. Solid lines represent experimentally probed points: triangles indicate the point at which the ion was lost from the trap as $U_{\mathrm{end}}$ was increased, squares denote a practical inability to probe further in $U_{\mathrm{end}}$ due to voltage limitations. The dashed black line indicates practical voltage limitation in $V_{\mathrm{RF}}$. In order to match the two stability regions in voltage space, a $\kappa$ value of 0.186 was required when transforming the analytical stability region from $(a, q)$ space. Both the numerical calculations and the experimental data relate to the earliest trap used: The 5-segment symmetric LPT.

accessible to us was of importance in the early development of the experiment; it provided information regarding the voltages necessary for stable trapping with our particular experimental setup. Fig. 2.4(a) shows a comparison between such a numerically generated stability diagram (whose stable boundary is overlaid in red) and the analytical stability region denoted by the grey shaded area. For this particular calculation, trajectory simulations were performed on a million evenly distributed points in the region $a = -1.50$–$0$, $q = -5$–$0$, with a 1 ms time cap. The starting position of the ion was a point 0.2 mm displaced from the trap centre in all axes, and the starting velocity was 400 m/s corresponding to a $^{40}Ca^{+}$ ion generated from a beam of Ca atoms with a kinetic energy estimated to be $E_{\mathrm{kin}}/k_{\mathrm{B}} =$ 600–900 K. The plot in Fig. 2.4(b) shows a comparison between experimentally-

determined single-ion stability and the analytical stability region, with the latter shaded in grey once again. The overlaid vertical stripes illustrate the directly probed experimental values. For a single trapped $^{40}Ca^{+}$ ion $V_{RF}$ was kept constant whilst $U_{end}$ was increased slowly until the ion was lost from the trap. Ions were lost at the ends of probe lines terminated with a triangle, whilst the square tips indicate an inability to increase $U_{end}$ further due to limitations in the electronics, with the ion remaining trapped at that final probed value.

In both cases the analytic stability zones have been scaled into voltage parameter space with an appropriate choice of the geometric factor $\kappa$, which is unique to a particular field geometry and accounts for the deviation of that field from harmonicity. Discrepancy between the values of $\kappa$ required for the mapping of the analytical stability region onto the numerical and experimental stability regions in Fig. 2.4 ($\kappa = 0.152$ and 0.186 respectively), may be attributed to imperfections in the experimental setup. For example slight electrode misalignment, stray fields/patch potentials, and small fluctuations in applied electrode voltages can all lead to a shift in $\kappa$ away from that of the numerical model. Owing to the fact that some of these contributions do not remain static, $\kappa$ can be seen to vary over a small range over the course of months of experimentation, and in general small corrections in the value of $\kappa$ used in the molecular dynamics simulations described later, are necessary in order to accurately simulate experimentally observed Coulomb crystal structures.

An interesting feature of the numerical stability map, is the presence of islands of instability within the overall envelope of the stable region, as well what appear to be a bifurcations near the tip where the numerical stability region appears to truncate. Both panels of Fig. 2.5 contain magnified regions of Fig. 2.4(a). Panel (a) illustrates a small thread of instability penetrating into the main stability region,

whilst (b) illustrates the bifurcations at the lower tip of the numerical stability region, and its discontinuation towards larger $U_{\text{end}}$ and $V_{\text{RF}}$.

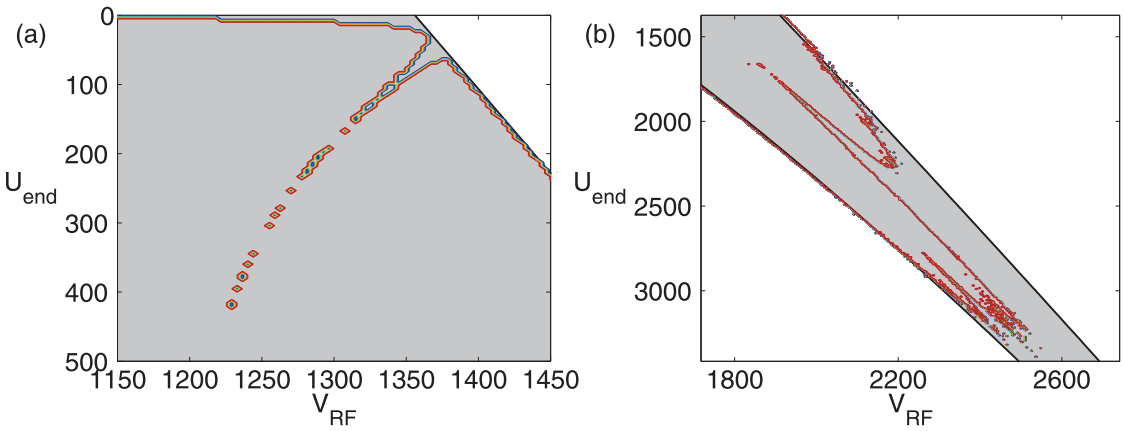


Figure 2.5: Numerically generated stability region overlaid (with boundaries in red) across the grey shaded stability region obtained via analytical solution of the Mathieu equations. Islands of instability exist within the overall envelope of the stable region.

These instabilities are sometimes also called non-linear resonances, and can occur for a number of reasons. In numerical simulations involving only a single ion in the trap, the main contributing factor is the use of non-hyperbolic electrodes. The analytical stability region, based on the eigenvalues of the Mathieu operator, assumes a perfectly harmonic potential which requires a hyperbolic electrode geometry. Higher order terms in the true potential generated by a set of cylindrical electrodes, which are discarded in the harmonic approximation that allows the invocation of the Mathieu equations to describe trapped ion motion, can lead to the appearance of these instabilities. Furthermore, in our SIMION model the cylindrical electrodes of the linear Paul trap are approximated in a cubic grid with a cell diameter of 0.1 mm (the electrode radii are 4 mm), which presumably leads to a further deviation of the numerically-generated fields from harmonicity. Additional factors that can cause non-linear resonances are the Coulomb interactions between multiple trapped ions (with a dependence on the number of ions), misalignment

between the electrodes that comprise the LPT, fabrication errors, field distortion in the edge regions, insulator charging, and noise in applied voltages [141]. To the best of our knowledge these effects have not been observed in our experimental work in the small region of the stability map that we are limited to, and warranted no further investigation with regard to the context of our work.

Stability diagrams also give some insight into the mass-filtering capabilities of the LPT. It is possible to perturb the trapping fields in such a way as to preferentially lose ions with a larger or smaller mass/charge ratio from the trap, providing a way to selectively filter or purify the crystal. This is made possible by the dependence of the $(a, q)$ parameters not only on the voltages but on the ion mass/charge ratios as well. This means that species with differing mass/charge ratios occupy different positions in $(a, q)$ space for a given set of voltages. Therefore mass-filtering involves manipulating the applied voltages such that one species is moved outside of a stable trapping region whilst the others remain inside it and in a confined trajectory. However, there can be complications involving the space-charge interactions of multiple trapped ions, and this can lead to different results based on the crystal composition [142].

The filtering of ions with a larger charge/mass ratio is best achieved by $q_{\mathrm{x}}$-filtering. The voltage $V_{\mathrm{RF}}$ is slowly increased with the ions in a non-crystalline phase, pushing all species towards larger $q$ values. The different species will sequentially reach the edge of the stability region starting with the ions with the largest charge/mass ratio. In contrast the best way to filter out ions with smaller charge/mass ratios is to use $a_{\mathrm{x}}$-filtering, wherein $U_{\mathrm{end}}$ is increased, pushing the various species to more negative $a_{\mathrm{x}}$ values until the desired species are ejected. Alternatively, for ions with small charge/mass ratios, addition of the static voltage configuration $U_{1,4}$, also known as $U_{\mathrm{dc}}$ (see Section 3.3.2 for a description of this configuration), allows preferential

loss from the trap. Geometrically this can be understood as a squeezing of the ion cloud along a radial axis orientated along the trap diagonal. This squeezing pushes heavier ions closer to the electrodes where the vastly increased micromotion causes them to escape from the trap or crash into the electrodes.

## 2.3 Laser cooling of trapped ions

### 2.3.1 Introduction to laser cooling

Given an ensemble of translationally hot confined ions, the next step in the generation of a Coulomb crystal is to reduce the kinetic energy of the ions below the threshold required for phase change into crystalline lattice-like form. The primary method available is that of Doppler laser-cooling.

Laser-cooling of trapped ions, and the trapping and laser-cooling of neutral atoms were together first seriously proposed in 1975 by Hänsch and Schawlow and independently Wineland and Dehmelt [143, 144]. In both cases the cooling mechanism relies on the momentum change associated with absorption of a photon, whose frequency is Doppler shifted into resonance with an atomic transition for atoms or ions travelling towards the source of the counter-propagating laser field. So-called Doppler laser-cooling of trapped ions was first performed in 1978 with $Mg^+$ and $Ba^+$ ions [145]. In 1982 Metcalf and Phillips first showed how a thermal beam of neutral sodium atoms could be laser-cooled using an inhomogeneous magnetic field to tune the resonant frequency of the atoms as they were slowed by the laser (an alternative is to tune the laser frequency itself, known as chirp cooling). In doing so they slowed the beam from 1100 m/s to 40 m/s, corresponding to a translational temperature of $\sim$2 K [143]. In 1985 Chu et al. managed to cool sodium atoms to around 240 $\mu$K [146], which represents the Doppler cooling limit (explained

further in the next section), using 3 orthogonal pairs of counter-propagating laser beams, a configuration termed *optical molasses*. Later in 1985 these techniques for slowing neutral atoms allowed the first confinement of laser-cooled atoms in the earliest magnetic traps, which were followed closely by development of the deeper magneto-optical trap (MOT) in 1987.

In 1988 it was discovered by Phillips *et al.* at NIST that the temperature of atoms in optical molasses were below the Doppler limit predicted by simpler two-level atom cooling theory; they measured temperatures as low as $\sim$43 $\mu$K in samples of sodium atoms [147]. This was explained, in theory extended by Dalibard and Cohen-Tannoudji [148], and Chu [146], via the consideration of multiple atomic energy levels and the spatial variation of laser polarisation in the optical molasses. These techniques were subsequently dubbed sub-Doppler or polarisation gradient cooling.

Further advances in Sisyphus cooling techniques [149] allowed temperatures to approach the smaller recoil limit, where the momentum of an atom is the same as the photon momentum — this represents the lowest temperature achievable for an atom in constant interaction with a light field. Later, methods such as Raman cooling and velocity-selective coherent population trapping allowed cooling below the recoil limit, to temperatures in the nK regime [150, 151]. This latter scheme relies on the stochastic nature of spontaneous emission to enable the atoms to randomly walk into a select region of velocity space where their velocity is less than the recoil velocity. At this point they are decoupled from the laser field via transfer to an optically transparent electronic state. In 1995 three separate groups transferred laser cooled atoms to magnetic traps and used forced evaporation to cool the atomic sample below $1\times10^{-7}$ K. This led to the first observation of Bose-Einstein condensation in a dilute atomic vapour [27], where all the atoms are in the

lowest energy level. In this case temperature, in the usual sense of a distribution amongst energy levels, loses its meaning.

The original reason to cool atoms — which is to say, reduce their translational energy — was to facilitate more precise spectroscopic measurements and later to improve atomic clocks. At the current time there exists a wide variety of research areas which rely on these techniques, such as the fields of quantum information processing where focused lasers interrogate single trapped and laser-cooled ions, high-resolution spectroscopy, and the study of chemical reactions and collisional processes at progressively lower energies.

### 2.3.2 Doppler cooling of $Ca^+$ ions

The principle of laser-cooling is based on the fact that a quantum of light possesses an associated momentum, $p = h/\lambda = \hbar k$, where $k = 2\pi/\lambda$ is the wavenumber. If the frequency of the light is resonant with an atomic transition, it may be absorbed by the atom and in doing so, according to the law of conservation of momentum, transfer its momentum $\hbar k$ to the atom. If the atom was travelling opposite to the direction of photon propagation, it will be slowed or translationally cooled by the photon absorption, and if travelling away its velocity would be increased. In order to tip the balance in favour of a net cooling effect, the frequency of the laser light is detuned, within a certain effective range, to longer wavelength than the target atomic transition (red-shifted). This exploits the Doppler effect to ensure that more photons are absorbed by atoms propagating counter to the photon direction than those travelling in the same direction. Counter-propagating atoms observe a photon frequency which is Doppler-shifted towards the atomic transition, increasing the absorption probability. In contrast, atoms moving away from the photons observe an even greater red-shifted photon wavelength and thus there is a corresponding decrease in absorption probability.

Having absorbed the photon and been excited to a higher electronic state, the slowed atom or ion may then re-emit the photon via spontaneous emission resulting in another atomic momentum change. In general the spatial probability of spontaneous emission is symmetric which means that, over the millions of absorption/emission cycles necessary to cool from thermal temperatures into the mK regime, the momentum change due to emission will effectively average to zero. This means that there will be a net cooling effect given a closed cooling cycle. The shorter the lifetime of the upper state, the faster the photon scattering rate $\Gamma\rho_{22}$, where $\Gamma$ is the decay rate and $\rho_{22}$ is the upper state population, and in principle the more efficient the cooling. The force on the atom in the direction of laser cooling is the rate of change of momentum due to scattering, simply $\hbar k\Gamma\rho_{22}$. An expression for $\rho_{22}$ from the literature for a 2 level atom [132] is

$$\rho_{22} = \frac{s_0/2}{1 + s_0 + (2\Delta/\Gamma)^2} \tag{2.21}$$

where $\Delta$ is the laser detuning and the on-resonance saturation parameter $s_0$ is given by:

$$s_0 = \frac{2|\Omega|^2}{\Gamma^2}. \tag{2.22}$$

The Rabi frequency $\Omega$ corresponds to the strength of the coupling between the laser field and the atomic transition. Substituting these equations into the light force equation gives us

$$F = \hbar k\Gamma \left( \frac{\Omega^2}{\Gamma^2 + 2\Omega^2 + 4\Delta^2} \right). \tag{2.23}$$

A common technique is the use of two counter-propagating lasers in order to provide a restoring force about a central point for an atom moving counter to one beam and in the same direction as the other. If we account for the Doppler shift $kv$ in the observed laser frequencies where $v$ is the atom's velocity (parallel to the two beams), we can write the total force as the sum of the forces of each of the beams.

Force is defined as positive in the direction of the atom motion:

$$F_{\text{total}} = \hbar k \Gamma \left( \frac{\Omega^2}{\Gamma^2 + 2\Omega^2 + 4(\Delta + kv)^2} - \frac{\Omega^2}{\Gamma^2 + 2\Omega^2 + 4(\Delta - kv)^2} \right). \tag{2.24}$$

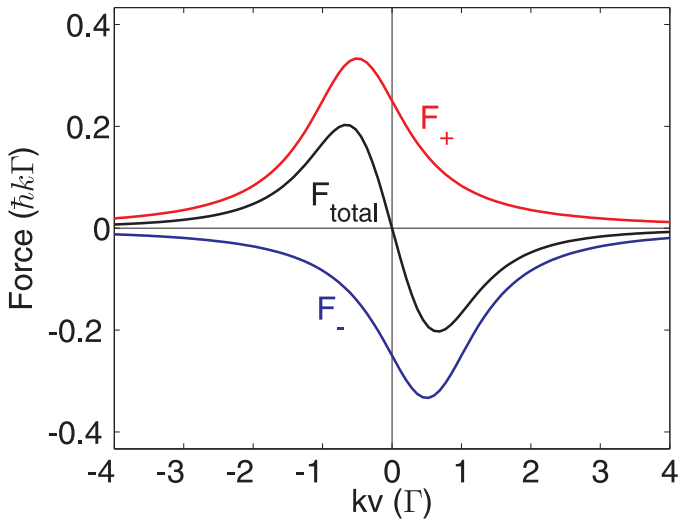


Figure 2.6: Light forces as a function of the ion velocity, with $\Delta = \Gamma/2$, $\Omega = 1$. $F_+$ is the force from the laser whose photons propagate in the same direction as the ion, and $F_-$ the light force of the counter-propagating beam, and the ion's velocity is defined in the positive $x$ direction.

If we treat the force in terms of a friction coefficient $\beta$ via $F = -\beta v$, a Taylor series expansion around $v = 0$ allows us to define

$$\beta = \frac{16\hbar k^2 \Gamma \Delta \Omega^2}{(\Gamma^2 + 2\Omega^2 + 4\Delta^2)^2} = 4\hbar k^2 \frac{s_0 (2\Delta/\Gamma)}{(1 + s_0 + (2\Delta/\Gamma)^2)^2}. \tag{2.25}$$

In order for this friction force to slow the ions, the detuning, $\Delta$, must be positive, and this corresponds to a wavelength red-shifted from the atomic transition as expected from the discussion above. In Fig. 2.7, the friction coefficient $\beta$ is plotted as a function of detuning for various values of the on-resonance saturation parameter $s_0$. It can be seen from the plot in Fig. 2.7 that for optimal cooling the detuning should have a value of $\Delta = \Gamma/2$ with $s_0 = 2$ and therefore, via the relation in Eq. 2.22, the Rabi frequency should have a value of $\Omega = \Gamma$. The plot in Fig. 2.6

illustrates the dependence of the forces (independent and total) on the ion velocity for $\Delta = \Gamma/2$.

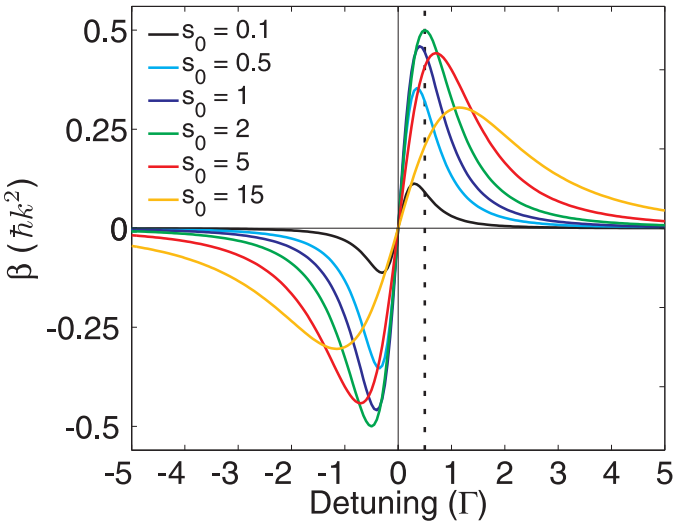


Figure 2.7: Friction coefficient $\beta$ as a function of the laser detuning for different values of the on-resonance saturation parameter $s_0$. It should be noted that this relatively simple model is increasingly limited in accuracy as $s_0$ increases beyond a value of $\sim$1–2 because the transition becomes saturated, limiting the photon scattering rate and therefore the friction coefficient.

In reality the momentum change associated with the spatially symmetric spontaneous emission cannot be completely disregarded as previously suggested. In fact it leads to a limitation on the temperatures that can be reached using Doppler laser-cooling alone — the so-called Doppler cooling limit. Each spontaneous emission results in a momentum change, $\hbar k$, of the atom in a random direction, and over time this corresponds to a random walk in momentum-space with step-size $\hbar k$ and a frequency which is the scattering rate $\Gamma\rho_{22}$. For a random walk such as this the distribution will be centred on the atom's initial momentum, which is to say that the average momentum change will indeed average to zero, $\langle p \rangle = 0$. However the mean square displacement will be finite $\langle p^2 \rangle \neq 0$, which means there will be a spread in the momentum distribution $\langle p^2 \rangle - \langle p \rangle^2$ corresponding to a non-zero temperature. The final steady-state temperature will be a reflection of the bal-

ance between the outward diffusion of this distribution in momentum-space, due to spontaneous emission, and the cooling rate or rate of contraction of the distribution, due to absorption. The rate of diffusion, $R_{\text{diff}}$, can be expressed as twice the diffusion coefficient, $D$, on account of having two lasers coupled to the transition; $D$ may be expressed in terms of the random walk step-size and frequency [132] allowing:

$$\begin{aligned} R_{\text{diff}} &= 2D \\ &= \frac{2(\Delta p)^2}{\Delta t} \\ &= 2(\hbar k)^2 \Gamma \rho_{22} \\ &= (\hbar k)^2 \Gamma \frac{s_0}{1 + s_0 + (\frac{2\Delta}{\Gamma})^2}. \end{aligned} \tag{2.26}$$

The rate of cooling, $R_{\text{cool}}$, depends on the friction coefficient, $\beta$, and the momentum [152] such that substitution of $\beta$ allows:

$$\begin{aligned} R_{\text{cool}} &= \frac{\beta \langle p^2 \rangle}{m} \\ &= \frac{4\hbar k^2 \langle p^2 \rangle}{m} \frac{s_0 (2\Delta/\Gamma)}{(1 + s_0 + (2\Delta/\Gamma)^2)^2}. \end{aligned} \tag{2.27}$$

Assuming the detuning is set for optimal cooling ($\Delta \approx \Gamma/2$) as shown in Fig. 2.7, and assuming a low laser intensity such that $s_0 \ll 1$ we obtain:

$$R_{\text{diff}} = \frac{1}{2}(\hbar k)^2 \Gamma s_0 \tag{2.28}$$

$$R_{\text{cool}} = 2\hbar k^2 s_0 \frac{\langle p^2 \rangle}{2m}. \tag{2.29}$$

In the steady-state these rates must sum to zero, therefore with the help of the relation

$$\frac{1}{2} k_{\text{B}} T_{\text{D}} = \frac{\langle p^2 \rangle}{2m} \tag{2.30}$$

we can write:

$$T_{\text{D}} = \frac{\hbar \Gamma}{2 k_{\text{B}}} \tag{2.31}$$

where $T_D$ is the Doppler temperature limit. Thus the minimal temperature for Doppler laser-cooling (assuming low laser intensities*) is purely dependent on the natural linewidth of the cooling transition. For $^{40}Ca^+$ whose main cooling transition at 397 nm has a decay rate of $\Gamma \approx 130$ MHz, $T_D$ corresponds to $\sim$0.5 mK.

In practice for laser-cooled ions in RF traps, anharmonicities in the trapping fields, along with space-charge interactions between multiple ions, cause a coupling between the translational degrees of freedom such that laser-cooling from a single direction can cool trapped ions efficiently enough for many purposes — quite a contrast with the six lasers required for cooling and trapping a neutral atomic gas in an optical molasses. Additionally there are often more than 2 levels involved within a given atomic cooling cycle, but all the same a closed cooling cycle is eminently achievable for simpler atomic species such as $^{40}Ca^+$ and other group 1 and 2 ions, often with the addition of extra lasers to couple other transitions.

The treatment of Doppler laser-cooling described above is based on a free particle, and of course we are dealing with ions trapped in an effective potential minimum. The motional frequencies of our linear Paul traps are of the order of 100–400 kHz and since the cooling transitions decay at the rate of $10^4$–$10^5$ kHz the ions are well approximated as free particles with respect to the laser-cooling. The motion of the ions in the potential does however introduce sidebands in the absorption spectrum at the motional trap frequencies. Given our trapping frequencies and laser bandwidths, these sidebands are not resolved and have no bearing on the work described here†.

The electronic quantum states involved in the laser-cooling of $^{40}Ca^+$ are illustrated

*If this assumption is not made we ultimately obtain the expression $T_D = \frac{(2+s_0)\hbar\Gamma}{4k_B}$ and therefore higher laser intensities (larger values of $s_0$) result in a higher temperature limit.

†In the regime where sidebands can be resolved, extra lasers tuned to the sideband transitions may be used to cool to the vibrational ground state of the trap [102] — see Section 1.3.1 for further detail.

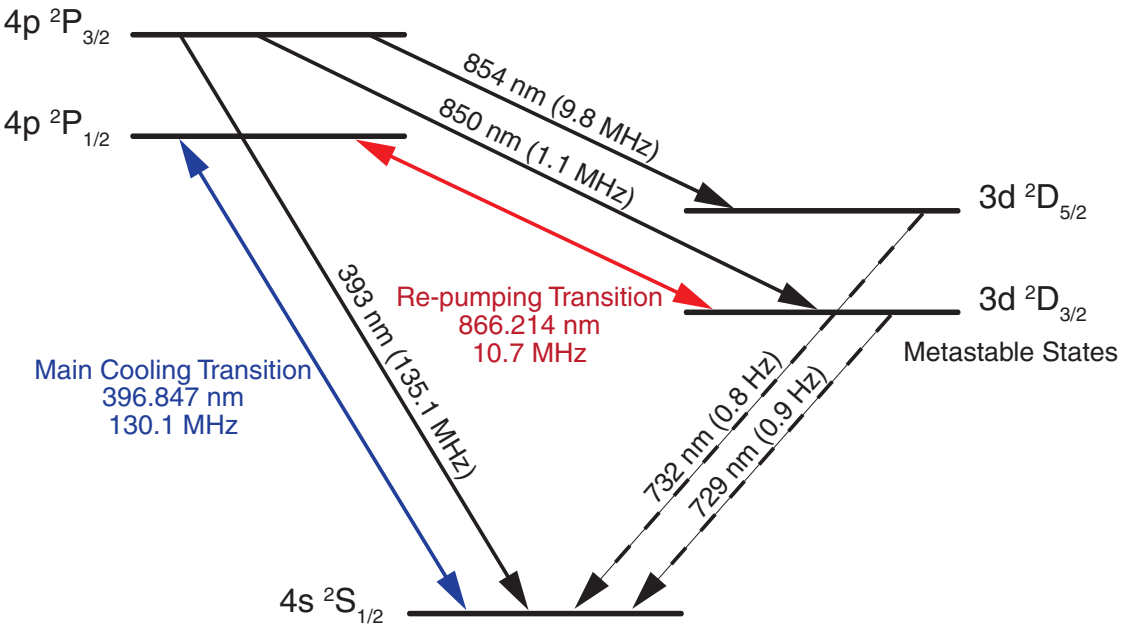


Figure 2.8: Low-lying electronic quantum states of $^{40}Ca^{+}$ illustrating transitions used in the closed laser-cooling cycle. Natural linewidths of the transitions are given in parentheses.

in Fig. 2.8, which also contains the decay rates (the inverse of the natural lifetimes) and wavelengths of the transitions. The main cooling transition occurs between the 4s $^2S_{1/2}$ and 4p $^2P_{1/2}$ levels at 396.847 nm. There is a complication in that the $^2P_{1/2}$ state can decay both to the ground state and to the metastable 3d $^2D_{3/2}$ state, with a branching ratio of about 1:12 in favour of the ground state. The metastable state decays only very slowly back to the ground state, on account of the transition being electric dipole-forbidden. Any attempt to drive the main transition alone would result in optical pumping of the population into the $^2D_{3/2}$ state, and laser-cooling would fail as the scattering rate would become too small. In order to ensure a closed cooling cycle, a second "repumper" laser is employed at 866.214 nm in order to pump the population back up from the metastable state to the $^2P_{1/2}$ state, from which it is most likely to decay rapidly to the ground state via spontaneous emission. The calcium sample used to generate our ions contains the natural relative abundances of the various calcium isotopes. $^{40}Ca$ constitutes

the major fraction at 96.94%, with the other major stable isotopes being: $^{42}$Ca (0.647%), $^{43}$Ca (0.135%), and $^{44}$Ca (2.086%) [153]. Isotopic shifts in the cooling transitions are of the order of GHz and therefore it is only really possible to cool the ions of a single isotope with a single laser system.

In general most of the work presented here only requires laser-cooling to be implemented from a single direction. As explained, the coupling of the translational degrees of freedom (via the Coulomb interaction and anharmonicities in the potential) means that cooling can still be very efficient with crystals of greater than ∼10–20 ions. When working with smaller ion numbers, in particular with just 1–2 ions, cooling from a second direction is generally required to maintain adequate secular temperatures. For work involving ion numbers of this order (see Chapter 5), this is performed by splitting off a component of the main 397 nm beam and introducing it into the chamber on an axis perpendicular with respect to the original cooling axis.

## 2.4 Coulomb crystals

As described so far, an ensemble of trapped ions, or one-component plasma, may be laser-cooled very effectively to temperatures in the millikelvin range. The structure of such an ensemble is governed by the balance of the Coulombic repulsion forces between ions, their kinetic energies or effective translational temperatures, and the effective trapping forces generated by the LPT fields. At translational temperatures of a few hundred millikelvin or more, the ions have enough kinetic energy to overcome the Coulomb repulsion of their surrounding neighbours and move freely. As translational temperatures are reduced below this limit and the ions become more localised in the effective potential minimum, they will be less able to overcome the repulsion of their nearest neighbours and will become more

confined between them. At a certain point there exists a phase transition into a crystalline state where the ions form an ordered 3D lattice-like structure known as a Coulomb crystal (see Fig. 2.9), although they are more correctly described as a gas phase plasma of like-charged Coulomb interacting particles. Within the crystal structure, and for typical trapping parameters, ion spacings are of the order of 10–20 $\mu$m and therefore four orders of magnitude larger than that of a familiar solid-phase crystal. Coulomb crystals are thus not crystals in the conventional sense as they have no true translational symmetry[‡].

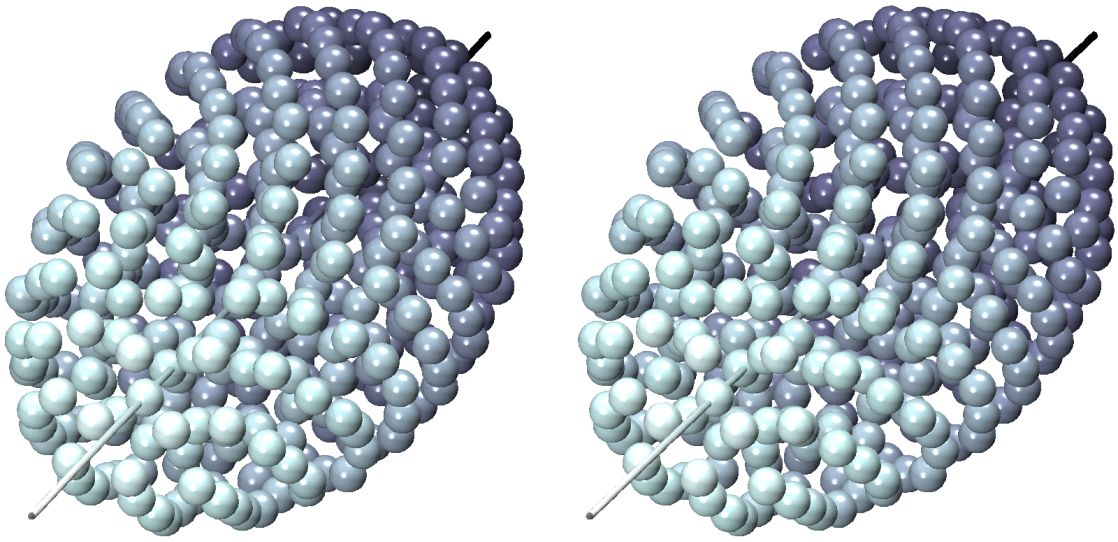

Figure 2.9: Stereoscopic image pair generated from MD simulation of a 400-ion prolate Coulomb crystal, with each ion represented by a shaded sphere. By focusing beyond the page, the left and right images can be merged into a third virtual image giving the impression of depth (viewed best at arm's length). The major axis of the crystal is parallel to the z-axis, which is represented by the cylindrical rod. Shading is depth dependent, graduating from light to dark from $+z \rightarrow -z$.

Matter in this state is believed to exist in the interior of white dwarf stars and the crust of neutron stars [154, 155] and other dense stellar objects [156], and is therefore of interest to astrophysics and indeed astrochemistry. In general most of the plasmas that occur naturally in the universe are believed to be two (or more)

[‡]In very large ion crystals a bcc structure has been observed in the core — see Section 3.3.1.

component plasmas (TCP) [155], where a lattice of heavy like-charged particles are immersed in a sea of lighter oppositely-charged particles such that the plasma as a whole remains neutral, for example a lattice of heavy nuclei immersed in a dense electron gas. Originally proposed theoretically by Wigner [157], and therefore termed "Wigner crystals", the first consideration of this type of crystalline phase involved the formation of a bcc lattice by electrons at low enough densities within a metal. Since the first theoretical treatment, those systems have been realised only in one or two dimensions, for example on the surface of superfluid helium or in carbon nanotubes [158, 159], and the (somewhat) erroneous term of "Coulomb crystal" was carried over to describe these analogous structures involving atomic or molecular ions.

The ratio between average nearest-neighbour Coulomb potential energy, $E_\mathrm{p}$, and kinetic or thermal energy, $E_\mathrm{k}$, is expressed by the plasma coupling parameter:

$$\Gamma = \frac{E_\mathrm{p}}{E_\mathrm{k}} = \frac{Q^2}{4\pi\epsilon_0 a_\mathrm{ws} k_\mathrm{B} T}, \tag{2.32}$$

where $a_\mathrm{ws}$ is the Wigner-Seitz radius defined by $\frac{4}{3}\pi a_\mathrm{ws}^3 = n_0^{-1}$ for the ion density at zero temperature, $n_0$, the particle charge, $Q$, and the ensemble temperature, $T$. The plasma coupling parameter is a measure of the thermodynamical state of the plasma. Spatial correlation between ions (*i.e.*, liquid-like behaviour with short range order) exists for $\Gamma \gtrsim 2$ [160]; below this value the plasma is in the gas phase. Theoretical treatment [161] and molecular dynamics simulations [162, 163] have demonstrated that crystallisation to the solid phase occurs for parameters of $\Gamma \gtrsim$ 150–170 and this is well supported by experiment [164, 165]. Ion densities in a LPT are limited by Coulomb repulsion to approximately $10^8$ ions/cm$^3$ [43]. Given Eq. 2.32 the phase transition to the crystalline state occurs at or below $T \approx$ 100–150 mK.

Even in a crystalline state, ions may still diffuse throughout the lattice structure.

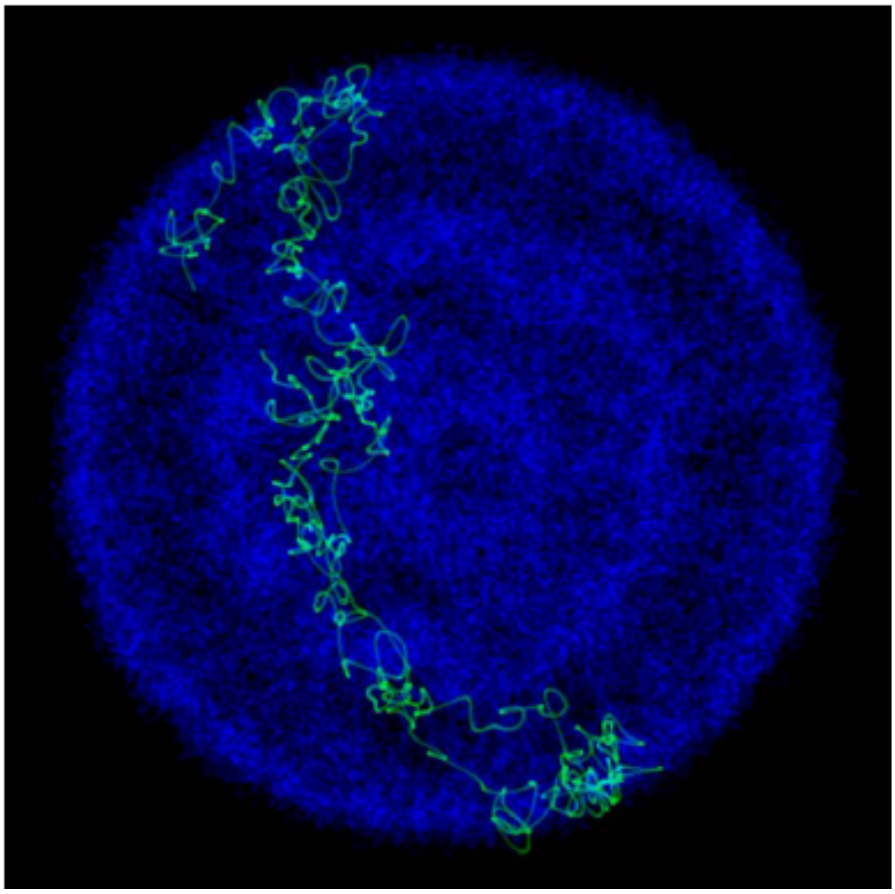

Figure 2.10: Diffusion in an ion crystal. In this axial view of a time-averaged ion crystal at 6 mK the trajectory of a single ion is shown in green. During the exposure time of 5 ms the ion diffuses through the whole ensemble. This simulation did not include micromotion, no heating or cooling were applied. Reproduced from reference [166].

Molecular dynamics simulations involving the harmonic pseudopotential have indicated that on the typical timescale of an experimental image (∼0.5–2 s) a single ion's trajectory may span several metres on account of the non-zero secular kinetic energy [166] (see Fig. 2.10). Along with the ion's micromotion, this results in a contribution to the blurring of experimentally imaged ion fluorescence, which may be considered a plot of ion spatial probability density. Each of the bright spots observed in experimental images of the 397 nm fluorescence therefore represent lattice positions rather than single ions. In a typical 800-ion prolate crystal, the distribution of micromotion amplitudes spans approximately 0–7 $\mu$m depending on

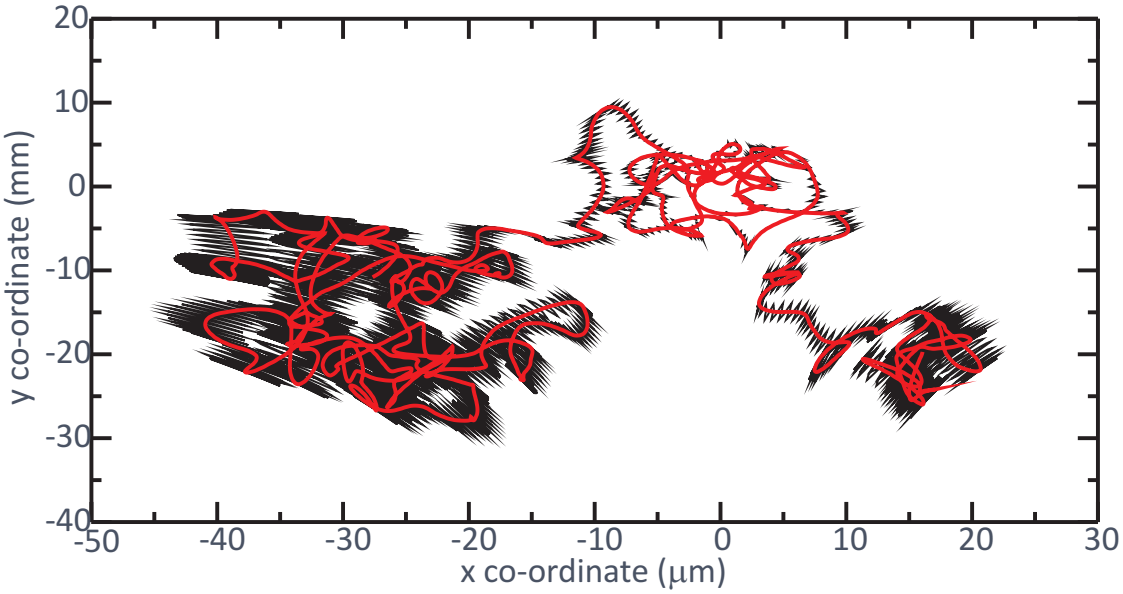


Figure 2.11: Trajectory of a single ion extracted from a molecular dynamics simulation of a Coulomb crystal comprising a few hundred ions, with a secular temperature of approximately 20 mK. This illustrates the diffusion of this particular ion through the crystal at these secular temperatures, with the ion's smooth secular motion superimposed upon its jagged micromotion. The amplitude of the micromotion can be seen to increase as the ion ventures further from the $z$-axis towards the electrodes. Simulation performed by J. M. Oldham.

ion-electrode proximity (See Fig. 3.14). Further consideration of the simulation of experimental images can be found in Section 3.1.2.

### 2.4.1 The fluid model for a trapped charged plasma

A trapped one-component plasma in a liquid phase may be treated theoretically as a macroscopic charged fluid, allowing a number of useful relations to be generated [167, 168]. In particular, as the temperature approaches zero, simple analytical treatment involving the assumption of no net force on any plasma region allows the derivation of the number density. If the force on each ion is assumed to be zero,

$$\mathbf{F}_{\text{ion}} = -Q\nabla\phi_{\text{total}} = 0, \tag{2.33}$$

then the total potential, $\phi_{\text{total}}$, which is the sum of the trapping potential (*i.e.*, the harmonic pseudopotential) and the electric potential of the ions, is constant within the plasma. This implies a balance between the electric field due to the space-charge interactions between ions and the effective trapping forces:

$$\phi_{\text{trap}} + \phi_{\text{ion}} = const. \tag{2.34}$$

Using the Laplace equation, $\nabla^2\phi_{\text{total}} = 0$, in conjunction with Gauss' law within the ion plasma, $\nabla^2\phi_{\text{ion}} = -Qn_0/\epsilon_0$, and using the harmonic pseudopotential to describe the trapping fields in the LPT results in the following expression for the zero-temperature number density [160, 169]:

$$n_0 = \frac{\epsilon_0 V_{\text{RF}}^2}{m\Omega_{\text{RF}}^2 r_0^4} \tag{2.35}$$

where typical parameter values are listed in Tables 2.1 and 2.2. Thus in terms of the trapping fields, the number density is dependent only on $V_{\text{RF}}$ and not on the end-cap voltage $U_{\text{end}}$. This charged fluid treatment is performed in the limit of $T \to 0$, however at low temperatures the plasma does not remain a liquid; instead it crystallises into the aforementioned lattice-like structure comprising concentric ellipsoidal shells. One might assume that the fluid model description becomes erroneous in this regime, however it has been shown to remain applicable given a large enough crystal (ion numbers $\gtrsim 100$) [160, 170]. The fluid model also allows the calculation of the dimensions of the ensemble's ellipsoidal structure in the effective trapping fields [167, 170]. The assumption of constant number density in larger crystals is used in the work described in later chapters where we treat the number of ions in a given crystal as being proportional to the crystal volume. This facilitates the calculation of rate constants for direct reactions of $^{40}Ca^+$ where the product ions are heavier than $^{40}Ca^+$ itself (see Section 4.3.2).

### 2.4.2 A brief discussion regarding "temperature" in the context of Coulomb crystals

The term "temperature" is used a lot in this thesis with regard to the laser-cooled ions confined in the trapping potential of the LPT. It is worth stating a little more carefully what is meant in this case, as it is a somewhat erroneous usage of what is a thermodynamic quantity.

A temperature value implies a characteristic energy distribution, and is often associated with the Maxwell-Boltzmann distribution of velocities in an ideal gas or the Boltzmann distribution of population over rotational, vibrational or electronic states. For example in the latter cases, at a temperature, $T$, the population in a given state, $n_j$, with energy, $E_j$, is given by

$$\frac{n_j}{N} = \frac{g_j e^{-\frac{E_j}{k_{\mathrm{B}}\mathrm{T}}}}{\sum_i g_i e^{-\frac{E_i}{k_{\mathrm{B}}\mathrm{T}}}}, \tag{2.36}$$

where $N$ is the total number of states and $\sum_i g_i e^{-\frac{E_i}{k_{\mathrm{B}}\mathrm{T}}}$ is simply the associated partition function, $Q$, which can be thought of as a measure of the spread of the population over the given states. Temperature in this thermodynamic sense is a parameter of the state of a closed system in thermal equilibrium with its surroundings [132]. The assignment of temperature to a laser-cooled sample of atoms is therefore rather inappropriate, as there is interaction with the surroundings (absorption and emission of light) and no real heat exchange (although there is energy exchange). Furthermore, though there may exist a steady-state it cannot truly be considered thermal equilibrium. Additionally, there is the complication of the RF-induced micromotion, which confers a distinctly non-Maxwell-Boltzmann-like distribution on the effective kinetic energies of ions in the trap (although this vanishes at the central trap axis and, given weak enough coupling between the radial

and axial degrees of freedom, the axial velocity distribution is well approximated by the Maxwell-Boltzmann distribution).

As discussed in Chapter 2.2.2 the motion of ions in the trap is separable into the lower frequency oscillation (secular motion) and the higher frequency micromotion driven by the oscillating radiofrequency fields. The notion of temperature is directly applicable to the secular motion, with the secular velocity distribution of a Coulomb crystal conforming well to a Maxwell-Boltzmann distribution at the associated temperature [171]. Therefore it is somewhat justifiable to consider the secular temperature $T_{\mathrm{sec}}$ in the true thermodynamic sense, although this is a somewhat grey area for a sample of laser-cooled atoms as discussed. However the effective or total kinetic energy distributions do not follow a Maxwell-Boltzmann distribution, due to the dominant contribution of the micromotion, and it is therefore erroneous to consider an effective temperature $T_{\mathrm{eff}}$ in the same manner. Effective kinetic energies are nevertheless often quoted in Kelvin for convenience, and this may be interpreted as $\langle E_{\mathrm{kin,eff}} \rangle / k_{\mathrm{B}}$; we may also use the term "effective translational temperature" to refer to this latter quantity.

Later when we discuss neutral molecular reactants we may also use the term temperature as synonymous with translational temperature where $T_{\mathrm{kin}} = mv^2/2k_{\mathrm{B}}$. However, in the case of the velocity-selector for example, molecules are still rotationally hot in the sense that the distribution of the population over the rotational states is well-approximated by a Boltzmann distribution at $T = 300$ K [43]. Likewise, a discussion of low-temperature reactions may imply a small collision energy or small $T_{\mathrm{kin}}$ value in the centre of mass frame of the approaching reaction partners. This is purely for convenience: It is recognised here that a truly cold or ultra-cold reaction is one in which all degrees of freedom, both internal and external, are minimally excited.

## 2.5 Molecular dynamics simulations of Coulomb crystals

Molecular dynamics (MD) simulations involve the numerical computation of the time-evolution of a bonded and/or non-bonded poly-atomic system. From the folding or solvation of proteins to the behaviour of an ensemble of laser-cooled ions, the basic framework for MD simulation remains much the same. In general the system is first defined through the use of input files to determine the atoms involved and their relationships (*i.e.*, bonded/non-bonded, and the forces acting between them). The evolution of the system can then be calculated based on the integration of the Newtonian equations of motion, with an integrator that can be customised to the regime at hand. Traditionally the most computationally expensive part of these simulations is the force calculation, which is necessarily performed at every time step.

Our usage of MD simulations is primarily aimed at simulating the experimental crystal images generated by projecting the 397 nm spontaneous fluorescence onto a charge-coupled-device (CCD) camera system. As we shall see, closely matching experimental fluorescence images with simulated images allows the accurate determination of ion temperatures as well as the number of different ion species in the trap. This latter use is particularly important in the case of multi-component crystals where non-fluorescing ions are usually only detected via the structural distortions they cause in the fluorescing fraction of the crystal. In the case of some reactions of single component crystals, certain approximations (described in detail in Section 4.3.2) allow rate constants to be obtained from the experimental images alone. However, simulations are extremely useful, or even necessary, for obtaining rate constants for reactions involving multi-component crystals, or direct reactions of pure crystals involving a product species lighter than that of

the reactant ion. Details regarding the production of experimental and simulated images are discussed later in Sections 3.1.1 and 3.1.2 respectively.

For our studies involving Coulomb crystals we searched for pre-existing MD software which would be easily modifiable to our exact specifications. Use of the latest existing software affords us the luxury of well-refined algorithms designed to allow fast simulation of systems of thousands of ions. Early on we identified the MD package ProtoMol [172] as ideally suited to our needs. The source code was freely available and allowed us not only to be sure of what was being calculated, but also to modify the forces involved and more closely mimic our experimental situation.

### 2.5.1 ProtoMol

#### Overview

ProtoMol is an object-oriented, modular C++ framework for molecular dynamics simulations, which started life as the PhD project of Thierry Matthey [173]. It is designed to be easily modifiable and extendable, and incorporates a number of efficient algorithms and techniques (including parallelisation) for high performance demands. The use of fast electrostatic force evaluation algorithms like Ewald, particle Mesh Ewald, and Multigrid summation further enhances performance, which is particularly important given the need to simulate large numbers of Coulomb-interacting ions in large crystals.

ProtoMol already had an integrator optimised for use with a Paul trap type system, however, certain modifications (programmed mainly by J. M. Oldham [171]) were implemented in order to more accurately model our experimental situation.

### Force model modifications

The total force on any given ion in the simulation is calculated at each time-step from the summation of trapping forces, inter-ion Coulomb repulsion, laser-cooling and stochastic heating forces:

$$\mathbf{F}_{\text{total}} = \mathbf{F}_{\text{trap}} + \mathbf{F}_{\text{Coulomb}} + \mathbf{F}_{\text{laser}} + \mathbf{F}_{\text{heat}}. \tag{2.37}$$

In the original code only the trapping and inter-ion repulsion forces were included, along with a general "thermostat" for bringing the temperature of the ensemble towards a pre-designated value. This thermostat was removed on the grounds of being unphysical and replaced with a force to model the laser-cooling, as well as a stochastic heating term to account for random heating due to collisions with background gases.

The trapping term was modified from a time-independent force to a time-dependent one to model the RF trapping fields more accurately; also included was the option to use either the analytic potential (Eq. 2.5) or a grid of field gradients imported from SIMION. The latter option tended to be much slower and was ultimately not used a great deal. The trapping force based on the analytic potential for a given ion is thus

$$\mathbf{F}_{\text{trap},i} = Q_i \mathbf{E}_{\text{trap},i}, \tag{2.38}$$

where

$$\mathbf{E}_{\text{trap},i} = \frac{V_{\text{RF}} \cos(\Omega_{\text{RF}} t)}{r_0^2} (x_i - y_i) + \frac{\kappa U_{\text{end}}}{z_0^2} (2z_i - (x_i + y_i)). \tag{2.39}$$

In order to account for inter-ion Coulomb repulsion, $F_{\text{Coulomb}}$ takes the form of a simple pairwise summation of the Coulomb force between ions. In this case any polarisation of the ions is ignored and they are treated as point charges:

$$\mathbf{F}_{\text{Coulomb},i} = \sum_{j \neq i} \frac{Q_i Q_j}{4\pi\epsilon_0 r_{ij}^2} \hat{\mathbf{r}}_{ij} \tag{2.40}$$

In order to model the laser-cooling, a simple $z$-axis viscous damping term was implemented, on account of the axial laser-cooling setup we employ experimentally. The force on a particular ion is modelled according to

$$\mathbf{F}_{\text{laser},i} = -\beta \dot{\mathbf{z}}_i \tag{2.41}$$

where the viscous damping term $\beta$ is described by Eq. 2.25, repeated here for clarity,

$$\beta = 4\hbar k^2 \frac{s_0(2\Delta/\Gamma)}{(1 + s_0 + (2\Delta/\Gamma)^2)^2}, \tag{2.42}$$

and for which a typical value is $\beta = 870$ m/s [171].

Lastly there is the matter of the stochastic heating term $\mathbf{F}_{\text{heat}}$. This term is there to prevent the simulated ions ultimately cooling to zero temperature (in the absence of any RF micromotion), and is something of a catch-all term to include the various heating contributions that can arise experimentally, the main examples of which are the photon emission recoil and random collisions with background gas molecules. This term involves adding a randomly selected velocity kick to each ion in each degree of freedom at every time-step. Initially these velocities were chosen by multiplying a user-specified magnitude vector by a random number between -0.5–0.5. This was later replaced by selecting velocities at random from a Gaussian distribution whose FWHM is determined by a user-specified vector. In either case this term affords the user control over the final temperature of the simulated crystal, and allows a range of temperatures to be simulated for direct comparison with experimental images.

Additional modifications to the program were mostly for the purpose of outputting raw information about the ions themselves, such as their positions and velocities at designated time-steps. This raw data can be processed further to obtain secular and effective temperatures/kinetic energies, crystal aspect ratios and 3D histograms of

the ion positions over time. In order to obtain secular temperatures, the kinetic energy due to the oscillating micromotion is ignored by considering the average velocity of each ion, $i$, over each RF period:

$$v_{i,\text{average}}^2 = \left( \sum_{\text{step}=1}^{\text{n}} v_{x,i}/n \right)^2 + \left( \sum_{\text{step}=1}^{\text{n}} v_{y,i}/n \right)^2 + \left( \sum_{\text{step}=1}^{\text{n}} v_{z,i}/n \right)^2 , \qquad (2.43)$$

where n is the number of time-steps in an RF cycle. In this way the velocities contributed by the fast oscillatory motion cancel out, leaving only the contribution from the large scale secular motion. The average kinetic energy for each RF period can then be summed and averaged for the ensemble over a large number of RF periods to arrive at the final secular kinetic energy or temperature. In contrast, the effective kinetic energy of the crystal is calculated by considering the average speed of each ion over an RF period. In this case the kinetic energy of the fast micromotion is included with that of the secular motion, resulting in the true average effective kinetic energy, which is usually presented as a temperature through division by $k_\text{B}$ (as discussed in Section 2.4.2).

The aforementioned 3D histograms of ion spatial intensity are used to simulate experimental fluorescence images. A discussion of the CCD imaging system used to image Coulomb crystal fluorescence, and the subsequent simulation of these images through MD simulations, may be found in Sections 3.1.1 and 3.1.2 respectively. The tools provided by molecular dynamics simulation are invaluable to the characterisation of single and multi-component Coulomb crystals, and are invoked often in this work. Deeper examination of the behaviour and properties of ion crystals, especially under a variation of the applied fields, may be found in Section 3.3.1.

## 2.6 Modelling electronic quantum state populations of trapped and laser-cooled ions

In later chapters, a knowledge of the steady-state populations of the low-lying electronic states of $^{40}Ca^{+}$ ions in the presence of two near-resonant laser fields will be required. Determination of the population fractions allows the study of the variation in the rates of reaction of a sample of $^{40}Ca^{+}$ ions at different degrees of total excitation, thereby yielding information on the reaction rates for different electronic quantum states. This section introduces a theoretical basis for determining these populations experimentally.

In order to model the steady-state (and time-evolution) of the electronic quantum state populations of $^{40}Ca^{+}$, in interaction with two near-resonant laser fields, we invoke and solve the Optical Bloch Equations (OBE). Within the OBE framework, the three lowest-lying electronic states of $Ca^{+}$ can be treated as a three-level system in the absence of a magnetic field. However, if the degeneracy of the spin-orbit states is raised by an external magnetic field to a significant degree, an eight-level treatment may become more appropriate [174, 175]. As $^{40}Ca^{+}$ possesses no nuclear spin ($I = 0$) there is no hyperfine splitting to consider.

The rest of this chapter concentrates most heavily on the derivation and solution of the OBE in terms of a three-level treatment. Most of the key points in both the derivation of the OBE and the resultant state dynamics can be illustrated using this treatment, and its relative simplicity facilitates clear presentation. In addition, much of the early experimental analysis was performed using the three-level OBE treatment because it is computationally less expensive than the eight-level version. For example, the three-level treatment was relied upon to investigate the effect of both non-zero ion axial velocities and fluctuations in the laser frequencies on the

state populations of ions in a typical Coulomb crystal (see Section 6.1.2).

Ultimately, as explained further in Chapter 6, an eight-level treatment was relied upon for the calibration of the laser intensities experienced by the Coulomb crystals in later reaction experiments. For this reason, the final part of this chapter introduces an eight-level treatment and, without resorting to a complicated derivation (which may be found in the literature [174, 175]), provides the necessary detail to allow its solution as performed for the work in Chapter 6. A brief comparison of results obtained from the three- and eight-level OBE treatments is made in Appendix G.

The following experimental details are common to both treatments: The two laser fields with which the ions interact are both generated by Toptica DL-100 diode lasers operated at 396.847 nm and 866.214 nm, as indicated within Fig. 2.8. These lasers are both estimated to have linewidths of the order of several MHz, and hereafter shall simply be referred to as the 397 nm (blue) or 866 nm (red) laser, for convenience. Natural linewidth values used for the treatment of $^{40}Ca^{+}$ are also shown in this figure, and have been taken from the literature [176]. Photons arising from stimulated emission occupy the same light mode as the photons that induce their emission, therefore they travel on an axis perpendicular with respect to the imaging direction and are not observed. Experimentally, resonance fluorescence is detected purely due to the spontaneous decay from the 4p $^2P_{1/2}$ excited state to the 4s $^2S_{1/2}$ ground state. The rate of resonance fluorescence, $\Gamma_{397}$, is therefore proportional to the population of the 4p $^2P_{1/2}$ state. Thus, resonance fluorescence intensity provides a useful handle with which to probe the $^2P_{1/2}$ population: In Chapter 6 (and Appendix G) the theoretical treatments outlined here are tested via the comparison of experimental and simulated fluorescence excitation spectra. Within the basis for the three-level OBE treatment, which is shown in Table 2.3,

the population of the 4p $^2\mathrm{P}_{1/2}$ state is denoted $\rho_{22}(t)$.

| State | Label | Population |
|---|---|---|
| 4s $^2S_{1/2}$ | $\|1\rangle$ | $\rho_{11}(t)$ |
| 4p $^2P_{1/2}$ | $\|2\rangle$ | $\rho_{22}(t)$ |
| 3d $^2D_{3/2}$ | $\|3\rangle$ | $\rho_{33}(t)$ |

Table 2.3: State basis and population labels used in the three-level OBE treatment.

### 2.6.1 The Optical Bloch Equations for a three-level system in the absence of a magnetic field

#### Introduction

An ensemble of laser-cooled ions, each of which may either be in the electronic state denoted $|1\rangle$, $|2\rangle$ or $|3\rangle$ at a particular time, represents a *statistical mixture* of pure states. In order to model the dynamical evolution or steady-state fraction of the population of these states, we therefore invoke a treatment based on the use of the density matrix. Density operator techniques are well-established for describing systems such as the one under discussion, and therefore an abbreviated introduction addressing both the need for a density operator and its formalism is presented in Appendix B.

The form of the density matrix operator can be expressed as

$$\hat{\rho} = \sum_{a,b=1,2,3} \rho_{\mathrm{ab}} |a\rangle\langle b|. \tag{2.44}$$

where the diagonal matrix elements $\rho_{11}$, $\rho_{22}$ and $\rho_{33}$ correspond to the expectation values for finding the ion in the corresponding states $|1\rangle$, $|2\rangle$ or $|3\rangle$ and therefore

$$Tr(\hat{\rho}) = \rho_{11} + \rho_{22} + \rho_{33} = 1. \tag{2.45}$$

The off-diagonal matrix elements, or coherences, represent the interference effects that can occur between the states when they comprise a linear superposition. The evolution of the density matrix is governed by the Liouville equation:

$$\dot{\rho}(t) = \frac{1}{i\hbar}[H(t), \rho(t)] \tag{2.46}$$

where $H(t)$ is the Hamiltonian matrix, and whose form we will now consider for the case of the $Ca^+$ three-level system. Subsequently, we will account for decoherence effects such as spontaneous emission and finite laser linewidth, which we have thus far ignored, by including another term in the Liouville equation.

### The Hamiltonian matrix and revised Liouville equation

The Hamiltonian that describes the system comprises three parts, a term describing the atom, a term describing the laser fields, and a final term accounting for their interaction:

$$\hat{H} = \hat{H}_{\text{atom}} + \hat{H}_{\text{field}} + \hat{H}_{\text{int}}. \tag{2.47}$$

Given the prior definitions of the three atomic states under consideration (Table 2.3), we can define $\hat{H}_{\text{atom}}$ in terms of the atomic frequencies $\omega_{\text{a}}$ by

$$\hat{H}_{\text{atom}} = \sum_{\text{a}=1}^{3} \hbar\omega_{\text{a}}|a\rangle\langle a|. \tag{2.48}$$

It is convenient to begin to write these operators in matrix formulation in the basis $|a\rangle$ with $a = 1, 2, 3$ as follows:

$$\begin{aligned} \hat{H}_{\text{atom}} &= \hbar \begin{pmatrix} \omega_1 & 0 & 0 \\ 0 & \omega_2 & 0 \\ 0 & 0 & \omega_3 \end{pmatrix} \\ &= \hbar \begin{pmatrix} \omega_1 - \omega_2 & 0 & 0 \\ 0 & 0 & 0 \\ 0 & 0 & \omega_3 - \omega_2 \end{pmatrix}, \end{aligned} \tag{2.49}$$

where the energy of state $|2\rangle$ has been chosen as the zero point.

Single-mode laser light fields with high photon numbers can be treated to a very close approximation as classical monochromatic electromagnetic waves. The two lasers are thus described by $\mathbf{E} = \mathbf{E}_\mathrm{b}\cos(\omega_\mathrm{b}t) + \mathbf{E}_\mathrm{r}\cos(\omega_\mathrm{r}t)$, with laser linewidths denoted $\Gamma_\mathrm{b}$ and $\Gamma_\mathrm{r}$, where the subscripts b and r denote the 397 nm and 866 nm lasers respectively. Typical laser powers are in the region of 0.5 mW and 5 mW at 397 nm and 866 nm respectively. This corresponds to $\sim 10^{15}$ or $10^{16}$ photons/s respectively, values much greater than the typical scattering rates of $\sim 10^8$ or $10^7$ photons/s in either case. Any absorption of photons from the beam by the ions will have a negligible effect on the energy of the beam. Therefore we disregard $\hat{H}_\mathrm{field}$ and additionally the effect of the atom-laser interaction on the light field. The atom-laser interaction is then restricted to the electric dipole interaction (ignoring electric and magnetic moments of higher order).

The interaction Hamiltonian can therefore be written according to

$$\hat{\mathbf{H}}_\mathrm{int} = -\hat{\mathbf{D}}\cdot\hat{\mathbf{E}}, \tag{2.50}$$

where $\hat{\mathbf{D}}$ is the atomic dipole operator

$$\hat{\mathbf{D}} = e\begin{pmatrix} x \\ y \\ z \end{pmatrix}, \tag{2.51}$$

which may also be expressed using the atomic eigenvectors as

$$\hat{\mathbf{D}} = \sum_{\mathrm{a,b}=1,2,3} \mathbf{D}_\mathrm{ab}|a\rangle\langle b| \tag{2.52}$$

with dipole matrix elements

$$\mathbf{D}_\mathrm{ab} = \langle a|\hat{\mathbf{D}}|b\rangle. \tag{2.53}$$

For a transition between states $|a\rangle$ and $|b\rangle$ the atomic dipole is thus given in terms of what are effectively raising and lowering operators:

$$\hat{\mathbf{D}} = \mathbf{D}_{\mathrm{ab}}\big(|a\rangle\langle b| + |b\rangle\langle a|\big). \tag{2.54}$$

A number of assumptions are made at this stage. Firstly, given that the 3d $^2\mathrm{D}_{3/2}$ to 4s $^2\mathrm{S}_{1/2}$ transition is electric dipole-forbidden, the $^2\mathrm{D}_{3/2}$ state is treated as stable, which is a good approximation given that its decay occurs on a timescale $\sim 10^9$ times larger than the other transitions under consideration. This means that we can ignore this transition entirely, and consider only the transitions $|1\rangle \leftrightarrow |2\rangle$ and $|2\rangle \leftrightarrow |3\rangle$. We can also assume that there is no interaction between the 397 nm beam and the 866 nm transition and vice-versa, because in each case they are so far from resonance. For simplicity let us consider the contribution to $\hat{\mathbf{H}}_{\mathrm{int}}$ from the $|1\rangle \leftrightarrow |2\rangle$ transition, $\hat{\mathbf{H}}_{12}$, according to

$$\hat{\mathbf{H}}_{\mathrm{int}} = \hat{\mathbf{H}}_{12} + \hat{\mathbf{H}}_{32}, \tag{2.55}$$

as the result is analogous for $\hat{\mathbf{H}}_{32}$. Given Eqs. 2.50, 2.54, and the classical wave description we can write

$$\begin{aligned} \hat{\mathbf{H}}_{12} &= -\hat{\mathbf{D}_{12}}\cdot\hat{\mathbf{E}}_{12} \\ &= -\mathbf{D}_{12}\mathbf{E}_{\mathrm{b}}\cos(\omega_{\mathrm{b}}t)\big(|1\rangle\langle 2| + |2\rangle\langle 1|\big). \end{aligned} \tag{2.56}$$

Using the relation $\cos\theta = 1/2(e^{\mathrm{i}\theta} + e^{-\mathrm{i}\theta})$,

$$\begin{aligned} \hat{\mathbf{H}}_{12} &= -\frac{\mathbf{D}_{12}\mathbf{E}_{\mathrm{b}}}{2}\Big(|1\rangle\langle 2|(e^{\mathrm{i}\omega_{\mathrm{b}}t} + e^{-\mathrm{i}\omega_{\mathrm{b}}t}) + |2\rangle\langle 1|(e^{\mathrm{i}\omega_{\mathrm{b}}t} + e^{-\mathrm{i}\omega_{\mathrm{b}}t})\Big) \\ &= \frac{\hbar\Omega_{\mathrm{b}}}{2}\Big(|1\rangle\langle 2|(e^{\mathrm{i}\omega_{\mathrm{b}}t} + e^{-\mathrm{i}\omega_{\mathrm{b}}t}) + |2\rangle\langle 1|(e^{\mathrm{i}\omega_{\mathrm{b}}t} + e^{-\mathrm{i}\omega_{\mathrm{b}}t})\Big), \end{aligned} \tag{2.57}$$

where $\Omega_{\mathrm{b}} = (-\mathbf{D}_{12}\mathbf{E}_{\mathrm{b}})/\hbar$ is the characteristic Rabi frequency that defines the strength of the coupling between the laser and the atomic dipole (for information on how the Rabi frequencies are calculated experimentally see Section 6.1.3). By

transforming into a reference frame rotating at the atomic transition frequency, via a unitary transformation $\hat{\overline{\mathbf{H}}}_{12} = U\hat{\mathbf{H}}_{12}U^{\dagger}$ with $U = e^{\mathrm{i}\omega_{12}t}|2\rangle\langle 2|$ (see Appendix C for further explanation), we may factorise Eq. 2.57 into

$$\hat{\overline{\mathbf{H}}}_{12} = \frac{\hbar\Omega_{\mathrm{b}}}{2}\left(|1\rangle\langle 2|\left(e^{\mathrm{i}\Delta_{\mathrm{b}}t} + e^{-\mathrm{i}(\omega_{12}+\omega_{\mathrm{b}})t}\right) + |2\rangle\langle 1|\left(e^{-\mathrm{i}\Delta_{\mathrm{b}}t} + e^{\mathrm{i}(\omega_{12}+\omega_{\mathrm{b}})t}\right)\right), \tag{2.58}$$

where $\Delta_{\mathrm{b}}$ is the detuning of the 397 nm laser away from resonance $(\omega_{\mathrm{b}} - \omega_{12})$. As we have invoked the dipole approximation, via Eq. 2.50, we have assumed the laser field is near resonance with the atomic transition. Therefore $\Delta_{\mathrm{b}} \ll (\omega_{12} + \omega_{\mathrm{b}})$ and $e^{\pm\mathrm{i}(\omega_{12}+\omega_{\mathrm{b}})t}$ will oscillate much more rapidly than $e^{\pm\mathrm{i}\Delta_{\mathrm{b}}t}$. These faster oscillations are assumed to average to zero on any appreciable timescale and therefore we make the rotating wave approximation (RWA) and set any $e^{\pm\mathrm{i}(\omega_{12}+\omega_{\mathrm{b}})t}$ terms to zero, before transforming back to the original frame via the reverse operation $\hat{\mathbf{H}}_{12} = U^{\dagger}\hat{\overline{\mathbf{H}}}_{12}U$ which yields:

$$\hat{\mathbf{H}}_{12} = \frac{\hbar\Omega_{\mathrm{b}}}{2}\left(|1\rangle\langle 2|e^{\mathrm{i}\omega_{\mathrm{b}}t} + |2\rangle\langle 1|e^{-\mathrm{i}\omega_{\mathrm{b}}t}\right), \tag{2.59}$$

and by analogy,

$$\hat{\mathbf{H}}_{32} = \frac{\hbar\Omega_{\mathrm{r}}}{2}\left(|3\rangle\langle 2|e^{\mathrm{i}\omega_{\mathrm{r}}t} + |2\rangle\langle 3|e^{-\mathrm{i}\omega_{\mathrm{r}}t}\right). \tag{2.60}$$

The interaction Hamiltonian may therefore be written according to Eq. 2.55 as:

$$\hat{\mathbf{H}}_{\mathrm{int}} = \hbar\begin{pmatrix} 0 & \frac{\Omega_{\mathrm{b}}}{2}e^{\mathrm{i}\omega_{\mathrm{b}}t} & 0 \\ \frac{\Omega_{\mathrm{b}}}{2}e^{-\mathrm{i}\omega_{\mathrm{b}}t} & 0 & \frac{\Omega_{\mathrm{r}}}{2}e^{-\mathrm{i}\omega_{\mathrm{r}}t} \\ 0 & \frac{\Omega_{\mathrm{r}}}{2}e^{\mathrm{i}\omega_{\mathrm{r}}t} & 0 \end{pmatrix}, \tag{2.61}$$

and the full Hamiltonian, according to Eqs. 2.47, 2.49 and 2.61, may then be written as:

$$\hat{\mathbf{H}} = \hbar\begin{pmatrix} \omega_1 - \omega_2 & \frac{\Omega_{\mathrm{b}}}{2}e^{\mathrm{i}\omega_{\mathrm{b}}t} & 0 \\ \frac{\Omega_{\mathrm{b}}}{2}e^{-\mathrm{i}\omega_{\mathrm{b}}t} & 0 & \frac{\Omega_{\mathrm{r}}}{2}e^{-\mathrm{i}\omega_{\mathrm{r}}t} \\ 0 & \frac{\Omega_{\mathrm{r}}}{2}e^{\mathrm{i}\omega_{\mathrm{r}}t} & \omega_3 - \omega_2 \end{pmatrix}. \tag{2.62}$$

We may further simplify the full Hamiltonian, by transforming into a reference frame rotating at the laser frequencies. The operator that performs this can be

represented in terms of the atomic eigenvectors as:

$$\hat{U} = e^{-i\omega_{\rm b}t}|1\rangle\langle 1| + |2\rangle\langle 2| + e^{-i\omega_{\rm r}t}|3\rangle\langle 3|, \tag{2.63}$$

and also in matrix notation as:

$$U = \begin{pmatrix} e^{-i\omega_{\rm b}t} & 0 & 0 \\ 0 & 1 & 0 \\ 0 & 0 & e^{-i\omega_{\rm r}t} \end{pmatrix} \quad , \quad UU^{\dagger} = U^{\dagger}U = 1. \tag{2.64}$$

In matrix form the transformed Hamiltonian and density operators may be written as (see Appendix C):

$$\rho' = U\rho U^{\dagger} \qquad , \qquad H' = UHU^{\dagger} - i\hbar U\dot{U}^{\dagger}, \tag{2.65}$$

and the resulting transformed Hamiltonian matrix is:

$$H' = \hbar \begin{pmatrix} \Delta_{\rm b} & \frac{\Omega_{\rm b}}{2} & 0 \\ \frac{\Omega_{\rm b}}{2} & 0 & \frac{\Omega_{\rm r}}{2} \\ 0 & \frac{\Omega_{\rm r}}{2} & \Delta_{\rm r} \end{pmatrix}, \tag{2.66}$$

where the laser detunings are defined as:

$$\Delta_{\rm b} = \omega_{\rm b} - (\omega_2 - \omega_1), \tag{2.67}$$

$$\Delta_{\rm r} = \omega_{\rm r} - (\omega_2 - \omega_3). \tag{2.68}$$

For convenience we now assume the use of the transformed Hamiltonian and density matrices without including the associated notation.

We now have our full Hamiltonian, and in conjunction with a density matrix containing the initial state populations, we can now use the Liouville equation (as specified by Eq. 2.46) to calculate the time evolution of the populations. However before doing so we must account for the as-yet unconsidered decoherence effects that exist in this system. Decoherence effects arise from the spontaneous emission from the upper excited state to both the ground state and metastable state,

and also in the two independent laser phase fluctuations. These decoherence effects are accounted for in this treatment by the addition of the Lindblad operator, $L(\rho)$, to the Liouville equation (this operator is unaffected by any of the frame transformations done so far) which gives us:

$$\dot{\hat{\rho}} = -\frac{i}{\hbar}[\hat{H}, \hat{\rho}] + \hat{L}(\rho), \tag{2.69}$$

where

$$\hat{L}(\rho) = -\frac{1}{2}\sum_{\mathrm{m}} \left( \hat{C}_{\mathrm{m}}^{\dagger}\hat{C}_{\mathrm{m}}\hat{\rho} + \hat{\rho}\hat{C}_{\mathrm{m}}^{\dagger}\hat{C}_{\mathrm{m}} - 2\hat{C}_{\mathrm{m}}\hat{\rho}\hat{C}_{\mathrm{m}}^{\dagger} \right). \tag{2.70}$$

The sum over $m$ represents a sum over all the relevant operators $\hat{C}_{\mathrm{m}}$ which describe the various dissipative processes, and these are as follows:

$$\hat{C}_{21} = \sqrt{\Gamma_{21}}|1\rangle\langle 2| \tag{2.71}$$

$$\hat{C}_{23} = \sqrt{\Gamma_{23}}|3\rangle\langle 2| \tag{2.72}$$

$$\hat{C}_{\mathrm{b}} = \sqrt{2\Gamma_{\mathrm{b}}}|1\rangle\langle 1| \tag{2.73}$$

$$\hat{C}_{\mathrm{r}} = \sqrt{2\Gamma_{\mathrm{r}}}|3\rangle\langle 3|. \tag{2.74}$$

The operators $\hat{C}_{21}$ and $\hat{C}_{23}$ represent the spontaneous decay from the excited state to the ground and metastable states respectively. The operators $\hat{C}_{\mathrm{b}}$ and $\hat{C}_{\mathrm{r}}$ account for the finite laser bandwidths of the diode lasers, with the 397 nm and 866 nm laser bandwidths denoted $\Gamma_{\mathrm{b}}$ and $\Gamma_{\mathrm{r}}$ respectively. The first two terms in the Lindblad operator describe the removal of population from the excited state and evolution of the coherences, whereas the last term introduces the decaying population into the lower states, and is often called the "feeding term". The first two terms may be incorporated into an effective Hamiltonian as follows using Eqs. 2.69 and 2.94:

$$\begin{aligned}
\dot{\rho} &= -\frac{i}{\hbar}\left(H\rho - \rho H\right) - \frac{1}{2}\sum_{\mathrm{m}} \left( \hat{C}_{\mathrm{m}}^{\dagger}\hat{C}_{\mathrm{m}}\rho + \rho\hat{C}_{\mathrm{m}}^{\dagger}\hat{C}_{\mathrm{m}} - 2\hat{C}_{\mathrm{m}}\rho\hat{C}_{\mathrm{m}}^{\dagger} \right) \\
&= -\frac{i}{\hbar}\left( \left( H - \frac{i\hbar}{2}\sum_{\mathrm{m}} \hat{C}_{\mathrm{m}}^{\dagger}\hat{C}_{\mathrm{m}} \right)\rho - \rho\left( H + \frac{i\hbar}{2}\sum_{\mathrm{m}} \hat{C}_{\mathrm{m}}^{\dagger}\hat{C}_{\mathrm{m}} \right) \right) + \sum_{\mathrm{m}} \hat{C}_{\mathrm{m}}\rho\hat{C}_{\mathrm{m}}^{\dagger} \\
&= -\frac{i}{\hbar}\left( \widetilde{H}\rho - \rho\widetilde{H}^{*} \right) + \sum_{\mathrm{m}} \hat{C}_{\mathrm{m}}\rho\hat{C}_{\mathrm{m}}^{\dagger}
\end{aligned} \tag{2.75}$$

where the effective Hamiltonian

$$\widetilde{H} = \left( H - \frac{i\hbar}{2} \sum_{\mathrm{m}} \hat{C}_{\mathrm{m}}^{\dagger} \hat{C}_{\mathrm{m}} \right) \tag{2.76}$$

is no longer Hermitian.

### Solution of the Optical Bloch Equations for a three-level atom in the absence of a magnetic field

With the revised Liouville equation (Eq. 2.75), we arrive at an expression that governs how the $N \times N$ density matrix, and therefore the electronic state populations, evolve with time. Taking advantage of the linearity of this equation in the components of the density matrix, $\rho$, we are able to transform it into a system of linear equations — the so-called Optical Bloch Equations:

$$\dot{\rho}_{\mathrm{i}} = \sum_{\mathrm{j}} \mathbf{M}_{\mathrm{ij}} \rho_{\mathrm{j}}. \tag{2.77}$$

Here, $\rho$ is a column vector that holds that holds the $N^2$ elements of the density matrix

$$\rho^{\mathrm{T}} = [\rho_{11}, \rho_{12}, \rho_{13}, ..., \rho_{32}, \rho_{33}], \tag{2.78}$$

and $\mathbf{M}$ is the $N^2 \times N^2$ Liouvillian matrix. $\mathbf{M}$ retains all the information necessary for the evolution of the system and is formed from effective Hamiltonian and feeding terms according to Eq. 2.75 (see Appendix D for further discussion, along with MATLAB code for solution of the OBE). Therefore all the experimental parameters such as the laser detunings, Rabi frequencies, natural and laser linewidths are contained in this matrix.

Given the matrix equation

$$\dot{\rho} = \mathbf{M}\rho \tag{2.79}$$

and assuming that $\mathbf{M}$ is time-independent, we are able to integrate Eq. 2.79 and arrive at an expression for the populations at time $t$ using the matrix exponential:

$$\rho(t) = e^{(\mathbf{M}t)}\rho(0), \tag{2.80}$$

where $\rho(0)$ are the normalised initial populations such that

$$\sum_{\mathrm{i}} \rho_{\mathrm{ii}}(t) = 1 \qquad \forall t. \tag{2.81}$$

The steady-state solution can be obtained via Eq. 2.79 by first setting $\dot{\rho} = 0$ such that

$$0 = \mathbf{M}\rho_{\mathrm{ss}} \tag{2.82}$$

where $\rho_{\mathrm{ss}}$ is the steady-state density matrix. Before solving this equation for $\rho_{\mathrm{ss}}$, the normalisation condition must be enforced by replacing one of the linear equations contained therein with

$$\sum_{\mathrm{i}} \rho_{\mathrm{ii}} = 1. \tag{2.83}$$

resulting in (assuming the top/first linear equation is replaced):

$$\mathbf{x} = \overline{\mathbf{M}}\rho_{\mathrm{ss}} \tag{2.84}$$

where for the three-level system

$$\mathbf{x}^{\mathrm{T}} = [1\ 0\ 0\ 0\ 0\ 0\ 0\ 0\ 0] \tag{2.85}$$

and where $\overline{\mathbf{M}}$ is identical to $\mathbf{M}$ except that the top row has been replaced such that (in MATLAB notation)

$$\overline{\mathbf{M}}(1,:) = [1\ 0\ 0\ 0\ 1\ 0\ 0\ 0\ 1] \tag{2.86}$$

$$\overline{\mathbf{M}}(2:9,:) = \mathbf{M}(2:9,:). \tag{2.87}$$

Solution of the resulting equation can then be carried out very easily numerically. In MATLAB this is achieved using the backslash operator: $\rho_{\mathrm{ss}} = \overline{\mathbf{M}}\backslash\mathbf{x}$.

### Solutions for some general cases

The evolution of the three state populations under certain conditions is now briefly examined to illustrate some important features of the dynamics. In these calculations the initial density matrix is prepared to correspond to a fully populated ground state.

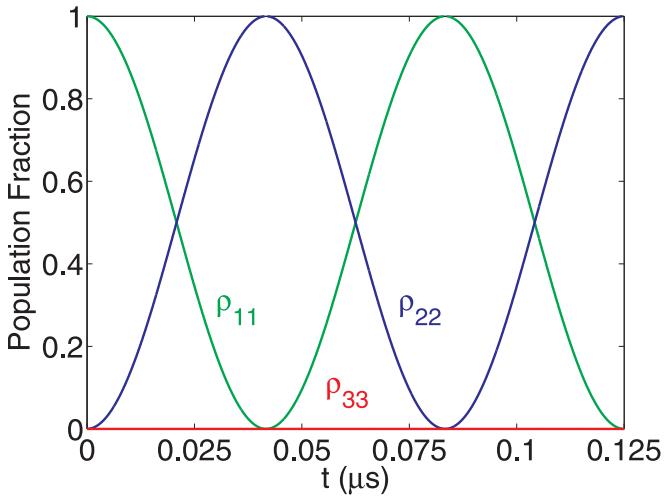


Figure 2.12: The evolution of state populations with parameters: $\Omega_{12}/2\pi = 12$ MHz, $\Omega_{32}/2\pi = 0$ MHz, $\Delta_b/2\pi = \Delta_r/2\pi = 0$ MHz, $\Gamma_b/2\pi = \Gamma_r/2\pi = 0$ MHz, and the spontaneous decay rates have been set to zero to illustrate the undamped Rabi oscillations.

The simulation shown in Fig. 2.12, which is calculated in the absence of the 866 nm laser ($\Omega_{32}/2\pi = 0$ MHz), and without any spontaneous decay contributions ($\Gamma_{12} = \Gamma_{32} = 0$ MHz), clealy shows the expected Rabi oscillation between the states coupled by the 397 nm laser. If the spontaneous decay is accounted for, the states for $^{40}Ca^{+}$ evolve according to Fig. 2.13. The Rabi oscillations are damped by the spontaneous decay, and the lack of repumping results in all the population being optically pumped into the 3d $^2D_{3/2}$ metastable state.

If the repumper laser is coupled in by setting a non-zero Rabi frequency, the initial Rabi oscillations are quickly damped as the populations tend towards their

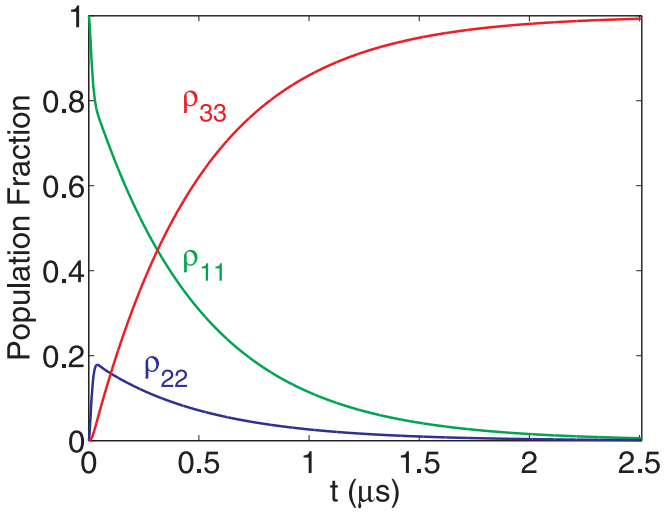


Figure 2.13: The evolution of state populations with parameters: $\Omega_{12}/2\pi$ = 12 MHz, $\Omega_{32}/2\pi = 0$ MHz, $\Delta_b/2\pi = \Delta_r/2\pi = 0$ MHz, $\Gamma_b/2\pi = \Gamma_r/2\pi = 0$ MHz, and the spontaneous decay rates have been set to those of $^{40}Ca^+$. This demonstrates optical pumping into the 3d $^2D_{\frac{3}{2}}$ metastable state, which occurs without the presence of a repumping laser.

steady-state values. The simulation shown in Fig. 2.14 illustrates this, and includes non-zero laser linewidths along with non-zero detunings for either laser. The steady-state population fractions in each of the three electronic states exhibit a dependence on the Rabi frequencies and laser detunings, and are therefore readily manipulated experimentally. Work in Chapter 6 capitalises on this situation, and investigates the influence of different steady-state population distributions on the rate of reaction of $Ca^+$ with a number of molecular species, in two different collision energy regimes.

An important feature of this system is the ability to pump population into states which do not interact with the light fields; these states can be described by a superposition of the pure electronic states and therefore by the off-diagonal elements or coherences in the density matrix. This behaviour is analogous to a Raman transition between the ground and metastable states, and occurs when both 397 nm and 866 nm laser detunings are equal. Population of these coherent states can give

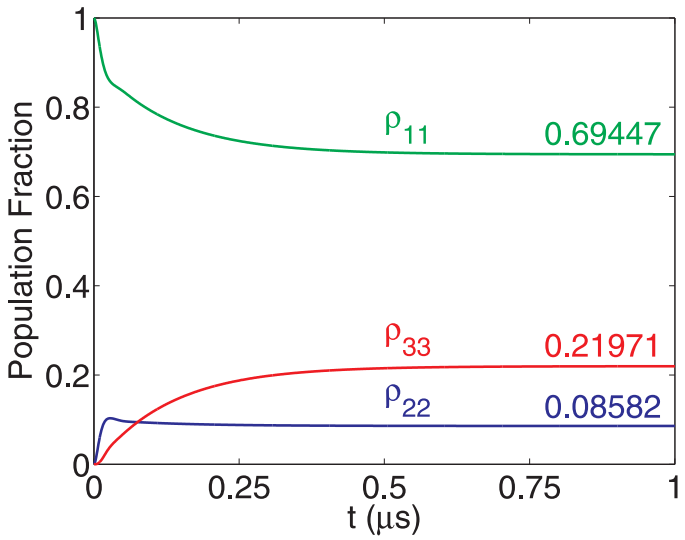


Figure 2.14: The evolution of state populations with parameters: $\Omega_{12}/2\pi$ = 125 MHz, $\Omega_{32}/2\pi$ = 12 MHz, $\Delta_b/2\pi$ = 10 MHz, $\Delta_r/2\pi$ = 30 MHz, $\Gamma_b/2\pi$ = 5 MHz, $\Gamma_r/2\pi$ = 5 MHz, spontaneous decay rates are those of $^{40}Ca^+$. The presence of a repumper laser closes the optical cycle and results in a finite steady-state population fraction in each of the three electronic states.

rise to "dark resonances" in resonance fluorescence excitation spectra, where the population of the 4p $^2P_{1/2}$ state ($\rho_{22}$) drops to zero (see Fig. 2.15). In this limit no fluorescence can be observed because the rate of fluorescence is proportional to $\rho_{22}$, hence the term "dark resonance". The population of an optically decoupled superposition state such as this is a purely quantum mechanical phenomenon, and is known as coherent population trapping (CPT) or electronically induced transparency (EIT). In contrast, optical pumping describes the population of a single uncoupled pure state (usually via spontaneous emission) and not a coherent superposition; optical pumping can therefore be described classically.

In general $\rho_{22}$ becomes fully depopulated when the detuning of both lasers are equal and their linewidths are equal to zero (in the absence of other sources of decoherence such as $m_J$-mixing due to Larmor precession in a magnetic field). Non-zero laser linewidths are a reflection of phase noise and introduce decoherence into the system. In terms of the OBE treatment this dephasing results in a decay

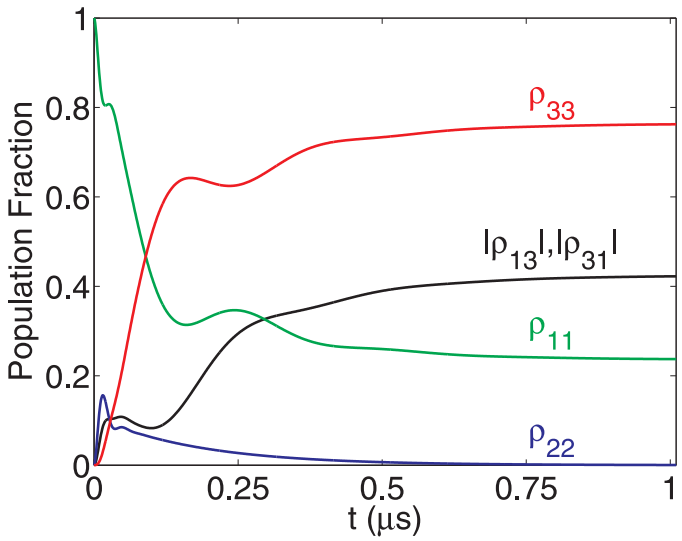


Figure 2.15: The evolution of state populations with parameters: $\Omega_{12}/2\pi$ = 18 MHz, $\Omega_{32}/2\pi$ = 10 MHz, $\Delta_b/2\pi$ = 20 MHz, $\Delta_r/2\pi$ = 20 MHz, $\Gamma_b/2\pi$ = $\Gamma_r/2\pi$ = 0 MHz, and spontaneous decay rates are those of $^{40}Ca^+$. This demonstrates the population of the coherences between the ground and metastable states and the depopulation of the 4p $^2P_{1/2}$ state, resulting in the loss of observable fluorescence and the occurrence of a so-called dark resonance. Non-zero laser linewidths will mitigate this effect slightly as shown in Fig. 2.16.

in the population of the coherences in the density matrix, partially destroying the coherent superposition between the ground and metastable states. This means that the population of the $^2P_{1/2}$ excited state no longer drops all the way to zero and fluorescence will still be observed even when the laser detunings are equal. The simulation in Fig. 2.16 illustrates the resultant "washing-out" of these dark resonances as a consequence of increasing laser linewidths. Further discussion regarding fluorescence excitation spectra and related phenomena can be found in Chapter 6, and in particular Section 6.1.3 where simulated excitation spectra are compared with experimental scans in order to calibrate effective laser intensities.

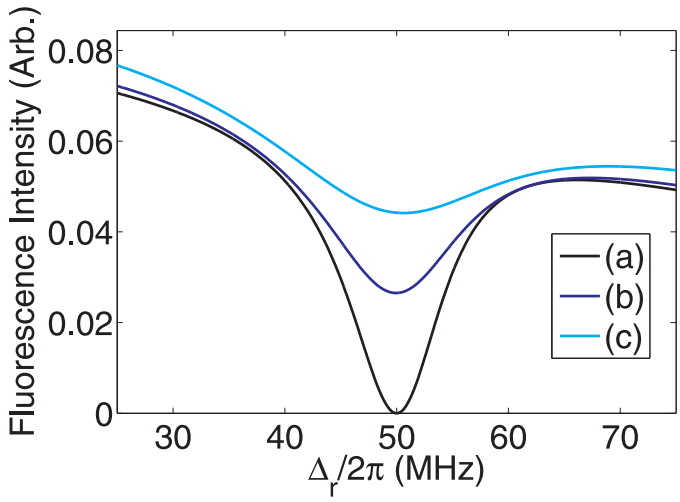


Figure 2.16: Resonance fluorescence excitation spectra with parameters: $\Omega_{12}/2\pi = 30$ MHz, $\Omega_{32}/2\pi = 15$ MHz, $\Delta_b/2\pi = 50$ MHz, spontaneous decay rates are those of $^{40}Ca^+$. (a) $\Gamma_b/2\pi = \Gamma_r/2\pi = 0$ MHz, (b) $\Gamma_b/2\pi = \Gamma_r/2\pi = 0.5$ MHz, (c) $\Gamma_b/2\pi = \Gamma_r/2\pi = 2$ MHz. Dark resonances occur where the laser detunings are equal, although non-zero laser linewidths introduce decoherence into the system, reduce the extent of $\rho_{22}$ depopulation, and broaden observed dark resonances.

### 2.6.2 The Optical Bloch Equations for an eight-level system in a magnetic field

#### Introduction

The three-level treatment of $Ca^+$ effectively ignores the fact that each of the three states previously considered consists of $(2J+1)$ spin-orbit sub-levels (labelled with the $m_J$ quantum number), with each set of $m_J$ states degenerate in the absence of a magnetic field. The excitation of population between these various sub-levels is dependent on the polarisation of the laser coupling them according to the following selection rules: $\sigma^{\pm} \rightarrow \Delta m_J = \pm 1$, $\pi \rightarrow \Delta m_J = 0$. Given that both the 397 nm and 866 nm diode lasers are linearly polarised they can excite only $\Delta m_J = 0$ transitions, whilst spontaneous decay couples transitions according to $\Delta m_J = 0, \pm 1$. According to Fig. 2.17 this would result in optical pumping (via spontaneous decay) into the $m_J = \pm 3/2$ sub-levels of the $^2D_{3/2}$ state [174, 175, 177] and therefore complete loss

of fluorescence.

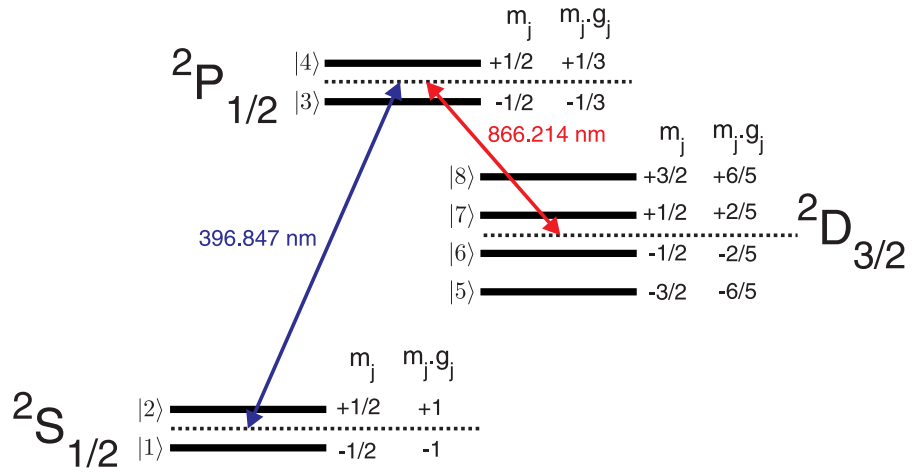


Figure 2.17: Fine structure level scheme of $^{40}Ca^{+}$, adapted from Ref. [174].

The presence of a magnetic field causes the Zeeman splitting of the $m_J$ states by an energy equal to

$$\Delta E = m_J g_j \mu_B |\mathbf{B}|, \tag{2.88}$$

where $g_j$ is the Landé g-factor, $\mu_B$ is the Bohr magneton and $|\mathbf{B}|$ is the magnetic field strength. If the magnetic field vector is not parallel to the quantisation axis then mixing will occur between the populations of these $m_J$ states as they undergo Larmor precession. This is another source of decoherence in the system: according to the expression for the classical Larmor precession frequency,

$$\hbar\omega = g_j \mu_B |\mathbf{B}|, \tag{2.89}$$

and using the Landé g-factors given in Fig. 2.17, a field of B = 1 G would result in a precession frequency of approximately 1 MHz for the $^2D_{3/2}$ state. This provides strong enough $m_J$-mixing to prevent the shelving of the population into the $^2D_{3/2}$ $m_J = \pm 3/2$ sub-levels. In our experiments, fluorescence is observed despite the use of linearly-polarised lasers, and without the application of additional magnetic fields. These observations alone suggest that an appreciable magnetic field component exists perpendicular to the quantisation axis within our trap, and therefore

that the full eight-level treatment may be necessary in accurately determining the state populations for work in Chapter 6. To this end there now follows a brief description of the eight-level OBE treatment and methods for its solution. A fully detailed derivation is omitted, but may be found in the literature [174].

### Abbreviated derivation and solution of the Optical Bloch Equations for an eight-level atom in a magnetic field

In the basis defined in Fig. 2.17, the atomic Hamiltonian may be expressed as

$$\begin{aligned}\hat{H}_{\text{atom}} &= \sum_{\text{a}=1}^{8} \hbar\omega_{\text{a}}|a\rangle\langle a| \\ &= \hbar(\omega_S - u)|1\rangle\langle 1| + \hbar(\omega_S + u)|2\rangle\langle 2| \\ &\quad + \hbar(\omega_P - u/3)|3\rangle\langle 3| + \hbar(\omega_P + u/3)|4\rangle\langle 4| \\ &\quad + \hbar(\omega_D - 6u/5)|5\rangle\langle 5| + \hbar(\omega_D - 2u/5)|6\rangle\langle 6| \\ &\quad + \hbar(\omega_D + 2u/5)|7\rangle\langle 7| + \hbar(\omega_D + 6u/5)|8\rangle\langle 8| \end{aligned} \tag{2.90}$$

where the Zeeman frequency shifts of each sub-level are incorporated using $\Delta\omega = m_{\text{j}} g_{\text{j}} u$ with $u = \mu_{\text{B}}|\mathbf{B}|/\hbar$.

In our experiment, the co-linear 397 nm and 866 nm lasers are both p-polarised (in the plane of the laser table and parallel to the trap $z$-axis). Within the eight-level OBE treatment, their polarisation vectors are therefore considered to be equal and at an angle, $\alpha$, to the magnetic field vector.

$$\epsilon_b = \epsilon_r = \epsilon = \begin{pmatrix} \sin\alpha \\ 0 \\ \cos\alpha \end{pmatrix}. \tag{2.91}$$

This simplifies the derivation of the atom-laser interaction Hamiltonian, which is omitted here but may be found in Ref. [174]. The presence of a magnetic field component perpendicular to the laser polarisations causes mixing of the $m_J$ sub-levels;

as discussed, the absence of this field component would result in optical pumping of the population into the $m_J = \pm 3/2$ levels of the $^2\mathrm{D}_{3/2}$ state [174, 177]. No additional magnetic field is applied experimentally; we assume that the magnetic field component oriented at $\alpha = \pi/2$ to the laser polarisations, and centred within the ion trap, arises from the (dominant) vertical component ($\sim$0.48 G) of the Earth's magnetic field.

As in the three-level case, the Hamiltonian for the laser field is ignored such that the full Hamiltonian for the system is the sum of the atomic and interaction Hamiltonians. Using a similar sequence of transformations to those described in Section 2.6.1, the full eight-level Hamiltonian can be expressed within the rotating wave approximation as:

$$\mathbf{H} = \hbar \times$$

$$\begin{pmatrix}
\Delta_\mathrm{b} + u & 0 & \frac{\cos\alpha}{\sqrt{3}}\Omega_\mathrm{b} & -\frac{\sin\alpha}{\sqrt{3}}\Omega_\mathrm{b} & 0 & 0 & 0 & 0 \\
0 & \Delta_\mathrm{b} - u & -\frac{\sin\alpha}{\sqrt{3}}\Omega_\mathrm{b} & -\frac{\cos\alpha}{\sqrt{3}}\Omega_\mathrm{b} & 0 & 0 & 0 & 0 \\
\frac{\cos\alpha}{\sqrt{3}}\Omega_\mathrm{b} & -\frac{\sin\alpha}{\sqrt{3}}\Omega_\mathrm{b} & -\frac{1}{3}u & 0 & -\frac{\sin\alpha}{2}\Omega_\mathrm{r} & -\frac{\cos\alpha}{\sqrt{3}}\Omega_\mathrm{r} & \frac{\sin\alpha}{2\sqrt{3}}\Omega_\mathrm{r} & 0 \\
-\frac{\sin\alpha}{\sqrt{3}}\Omega_\mathrm{b} & -\frac{\cos\alpha}{\sqrt{3}}\Omega_\mathrm{b} & 0 & +\frac{1}{3}u & 0 & -\frac{\sin\alpha}{2\sqrt{3}}\Omega_\mathrm{r} & -\frac{\cos\alpha}{\sqrt{3}}\Omega_\mathrm{r} & \frac{\sin\alpha}{2}\Omega_\mathrm{r} \\
0 & 0 & -\frac{\sin\alpha}{2}\Omega_\mathrm{r} & 0 & \Delta_\mathrm{r} - \frac{6}{5}u & 0 & 0 & 0 \\
0 & 0 & -\frac{\cos\alpha}{\sqrt{3}}\Omega_\mathrm{r} & -\frac{\sin\alpha}{2\sqrt{3}}\Omega_\mathrm{r} & 0 & \Delta_\mathrm{r} - \frac{2}{5}u & 0 & 0 \\
0 & 0 & \frac{\sin\alpha}{2\sqrt{3}}\Omega_\mathrm{r} & -\frac{\cos\alpha}{\sqrt{3}}\Omega_\mathrm{r} & 0 & 0 & \Delta_\mathrm{r} + \frac{2}{5}u & 0 \\
0 & 0 & 0 & \frac{\sin\alpha}{2}\Omega_\mathrm{r} & 0 & 0 & 0 & \Delta_\mathrm{r} + \frac{6}{5}u
\end{pmatrix} \tag{2.92}$$

where $\Delta_i$ are the laser detunings, $\Omega_i$ are the Rabi frequencies [§] and the subscripts $b$ and $r$ refer to the 397 nm and 866 nm transitions respectively.

The $Ca^+$ state populations are described by the diagonal elements of the 8 $\times$ 8 density matrix, $\rho$, with the off-diagonal elements representing coherences between

[§]Note that in the derivation of Eq. 2.92 the Rabi frequency, $\Omega$, is defined as $\hbar\Omega = \mathbf{E}.\mathbf{d}/2$, whereas in the three-level OBE derivation it is defined as $\hbar\Omega = -\mathbf{E}.\mathbf{d}$ (see Eq. 2.57).

the eight Zeeman sub-levels of the three electronic states. As in the case of the three-level treatment, the evolution of the density matrix is governed by the quantum mechanical Liouville equation:

$$\dot{\rho} = -\frac{i}{\hbar}[\hat{H}, \rho] + \hat{L}(\rho), \tag{2.93}$$

where $\hat{L}(\rho)$ is the Lindblad operator [178],

$$\hat{L}(\rho) = -\frac{1}{2}\sum_{\mathrm{m}} \left( \hat{C}_{\mathrm{m}}^{\dagger}\hat{C}_{\mathrm{m}}\rho + \rho\hat{C}_{\mathrm{m}}^{\dagger}\hat{C}_{\mathrm{m}} - 2\hat{C}_{\mathrm{m}}\rho\hat{C}_{\mathrm{m}}^{\dagger} \right), \tag{2.94}$$

which, for the eight-level system, accounts for decoherences phenomenologically using the operators:

$$\begin{aligned}
\hat{C}_1 &= \sqrt{\frac{2}{3}\Gamma_{\mathrm{PS}}}|1\rangle\langle 4|, \\
\hat{C}_2 &= \sqrt{\frac{2}{3}\Gamma_{\mathrm{PS}}}|2\rangle\langle 3|, \\
\hat{C}_3 &= \sqrt{\frac{1}{3}\Gamma_{\mathrm{PS}}}(|1\rangle\langle 3| - |2\rangle\langle 4|), \\
\hat{C}_4 &= \sqrt{\frac{1}{2}\Gamma_{\mathrm{PD}}}|5\rangle\langle 3| + \sqrt{\frac{1}{6}\Gamma_{\mathrm{PD}}}|6\rangle\langle 4|, \\
\hat{C}_5 &= \sqrt{\frac{1}{6}\Gamma_{\mathrm{PD}}}|7\rangle\langle 3| + \sqrt{\frac{1}{2}\Gamma_{\mathrm{PD}}}|8\rangle\langle 4|, \\
\hat{C}_6 &= \sqrt{\frac{1}{3}\Gamma_{\mathrm{PD}}}(|6\rangle\langle 3| - |7\rangle\langle 4|), \\
\hat{C}_7 &= \sqrt{2\Gamma_{\mathrm{b}}}(|1\rangle\langle 1| + |2\rangle\langle 2|), \\
\hat{C}_8 &= \sqrt{2\Gamma_{\mathrm{r}}}(|5\rangle\langle 5| + |6\rangle\langle 6| + |7\rangle\langle 7| + |8\rangle\langle 8|).
\end{aligned}$$

Here, $\hat{C}_1$ through $\hat{C}_6$ describe the spontaneous emission from the $^2\mathrm{P}_{1/2}$ excited state to the $^2\mathrm{S}_{1/2}$ ground and $^2\mathrm{D}_{3/2}$ metastable states, which occurs with angular frequencies of $\Gamma_{\mathrm{P}S}$ and $\Gamma_{\mathrm{P}D}$ respectively, while $\hat{C}_7$ and $\hat{C}_8$ account for the finite bandwidths of the 397 nm and 866 nm diode lasers respectively.

Once again, the Liouville equantion (Eq. 2.93) may be transformed into a system of linear equations to give the Optical Bloch Equations:

$$\dot{\rho}_{\mathrm{i}} = \sum_{\mathrm{j}} M_{\mathrm{ij}}\rho_{\mathrm{j}}, \tag{2.95}$$

in which $\rho$ is a column vector that contains the $N^2$ elements of the density matrix,

$$\rho^{\mathrm{T}} = [\rho_{11}, \rho_{12}, \rho_{13}, ..., \rho_{86}, \rho_{87}, \rho_{88}],$$

and $\mathbf{M}$ is the $N^2 \times N^2$ Liouvillian matrix, which can be formed efficiently using Kronecker products of the Hamiltonian and the Lindblad operator matrix representations,

$$\mathbf{M} = -\frac{i}{\hbar}\left(\widetilde{\mathbf{H}} \otimes \mathbf{I} - \mathbf{I} \otimes \widetilde{\mathbf{H}}^{\dagger}\right) + \sum_{m} \mathbf{C}_m \otimes \mathbf{C}_m. \tag{2.96}$$

In this equation, $\mathbf{I}$ is the $N \times N$ identity matrix and the non-hermitian effective Hamiltonian $\widetilde{\mathbf{H}}$ is given by

$$\widetilde{\mathbf{H}} = \mathbf{H} - \frac{i\hbar}{2} \sum_{m} \mathbf{C}_m^{\dagger} \mathbf{C}_m. \tag{2.97}$$

As for the three-level system, we find the steady-state populations by setting $\dot{\rho} = \mathbf{0}$ and replacing one of the linear equations with the normalisation condition:

$$\sum_{\mathrm{i}} \rho_{\mathrm{ii}} = 1.$$

The total population of the $^2\mathrm{P}_{1/2}$ state is proportional to the observed rate of spontaneous fluorescence. This means that experimental measurements of the spontaneous fluorescence intensity as a function of the cooling-laser intensities or detunings (resonance-fluorescence excitation spectra) provide a convenient means to probe the sum $\rho_{33} + \rho_{44}$. Of the twelve dark resonances possible when the detunings with respect to certain Zeeman sub-levels are equal, four are degenerate. Therefore in eight-level fluorescence spectra up to eight dark resonances can occur simultaneously depending on the angle $\alpha$ (see Ref. [174]). The energy or frequency separation of these dark resonances increases with the magnetic field strength. As shown later in Chapter 6, the resultant magnetic field present in our experiments does not produce a very large splitting, and the decoherences present due to finite laser linewidths and $m_J$-mixing are sufficient to prevent any resolution of separate dark resonances — typically only a single broad dip in fluorescence intensity is observed.

# Chapter 3

# Production and manipulation of Coulomb crystals

## 3.1 Experimental Apparatus

The apparatus used to generate Coulomb crystals is constructed in and around an ultra-high vacuum chamber with an internal breadboard for mounting equipment — a schematic of the apparatus is shown in Fig. 3.1. Typical working pressures are ideally $< 5\times10^{-10}$ mbar or lower, in order to minimise the ion-heating which arises from collisions with background gas molecules. To achieve this a turbo-molecular pump (Leybold Turbovac 361) is mounted to the underside of the chamber, backed by a rotary pump. A titanium sublimation pump (filament type, Varian) is also attached to the chamber for use in the initial evacuation; a stainless steel shield is fixed in the main chamber to protect the trap apparatus. The chamber pressure is monitored with a hot-cathode ionisation pressure gauge (Leybold Ionivac ITR90).

The ion trap sits centrally in the chamber beneath a recessed window in the chamber lid. The recess allows the objective lens of the CCD-camera system, which is

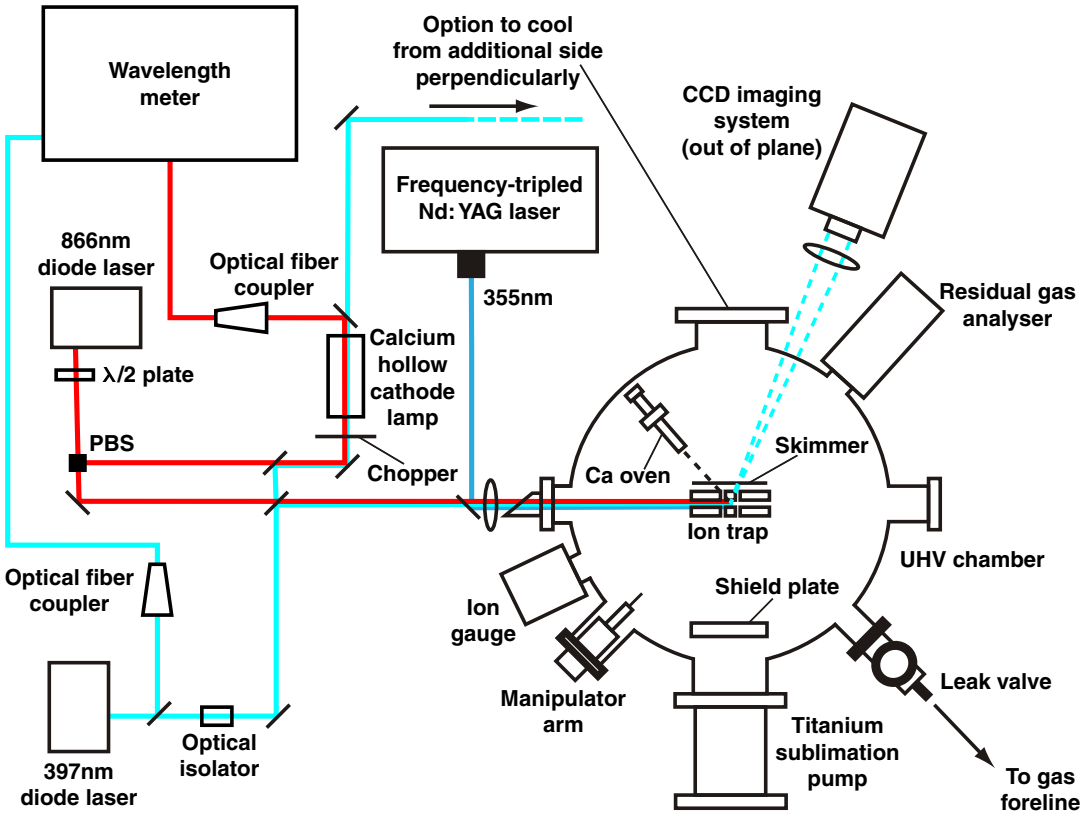


Figure 3.1: Schematic of the experimental apparatus for generating Coulomb crystals.

mounted onto the lid above the chamber on an $xyz$ translation stage, to come to within approximately 25 mm of the geometric trap centre. The trap voltages are carried by copper wires directed through a feed-through to the external electronics. A slit skimmer is mounted to the trap holder in order to skim the incoming beam of calcium atoms from the calcium oven, which is mounted nearby and aimed at the trap centre. The oven itself consists of a hollow stainless steel tube half-filled with calcium filings, and capped on the end facing away from the trap. The oven is resistively heated via two wires attached either end, which exit the chamber through a feed-through and operate in the region of 10–15 A. When heated to somewhere in the region of 600–900 K the oven sprays forth a beam of calcium atoms towards the trap centre. The skimmer minimises any calcium deposition on the inner surfaces of the electrodes or the insulators. This is necessary to minimise

the production of additional stray fields which can perturb the crystal — so called "patch potentials".

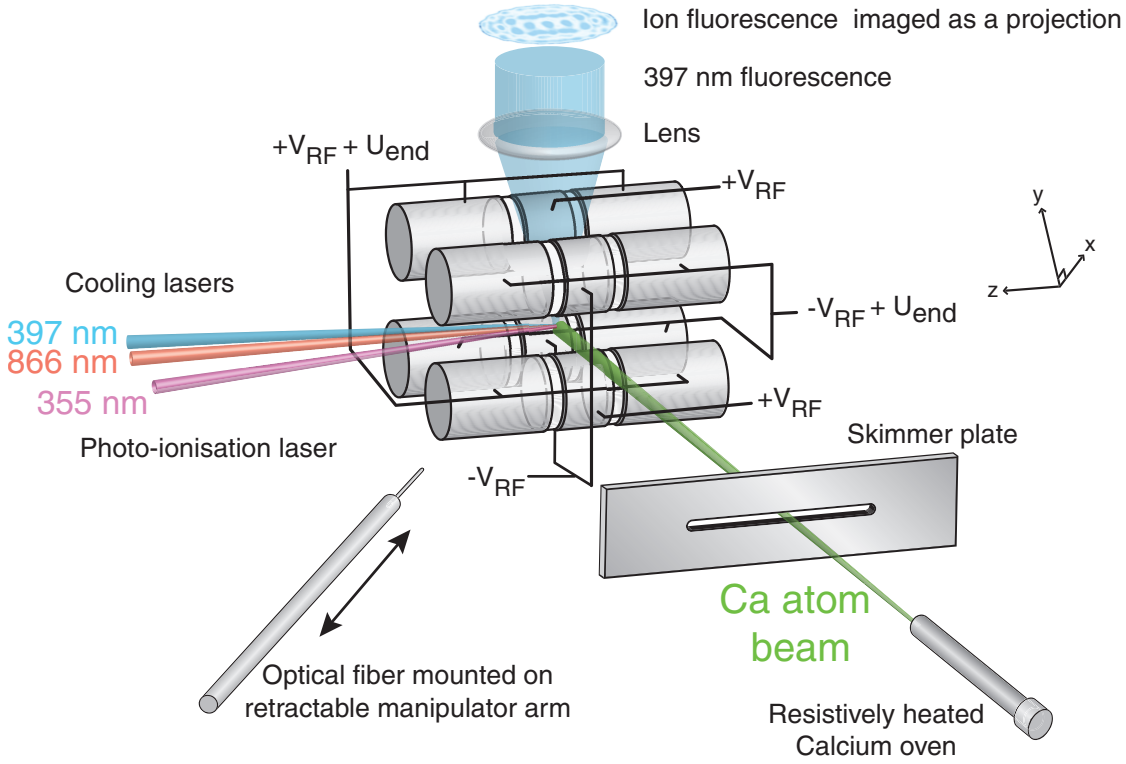


Figure 3.2: The ion trap and associated apparatus.

An optical fiber is mounted on a manipulator arm which allows it to be positioned in the geometric trap centre for ease of laser alignment and camera positioning and focusing. Lenses of 25 cm and 60 cm focal length are positioned on flip-mounts in front of the Brewster window leading into the chamber, approximately 30 cm from the center of the ion trap. In general the 25 cm focal length lens is used for ionisation with the 355 nm frequency tripled Nd:YAG laser, and the 60 cm focal length lens is preferred during experimentation to ensure the cooling laser beam waists are wide enough to fully encompass the crystal. The 397 nm and 866 nm cooling beams are generated by two Toptica DL-100 diode lasers, both with associated linewidths estimated to be of the order of several MHz.

A High Finesse WS-U wavemeter simultaneously monitors both diode laser frequencies by virtue of a fiber-switcher (Leoni M1x2 SI50/125). Also, a portion of each cooling laser beam is directed through a calcium hollow cathode lamp (connected to a lock-in amplifier) in order to ensure that the laser frequencies are matched to the appropriate atomic transitions for the laser-cooling of the $Ca^+$ ions. In general, the hollow cathode lamp is only used when locating fluorescence for the first time since having adjusted apparatus within the vacuum chamber. A high precision leak valve is also connected to the UHV chamber to allow the controlled leaking of reactant gases into the chamber. A residual gas analyser (RGA) is mounted onto the main chamber (Pfeiffer Prisma QMS-200). The RGA affords a number of useful functions, in particular helium leak testing, measurement of the mass spectrum of the chamber background gas and the monitoring of the partial pressures of selected mass peaks.

### 3.1.1 Imaging ion fluorescence

In order to monitor the ions in real time, we image the 397 nm fluorescence emitted during the normal cooling cycle of the calcium ions. We employ a CCD camera mounted above the chamber on an $xyz$ translation stage, with a 10× magnification Nikon lens mounted approximately 36 cm away from the camera inside a telescopic tube. The top flange is recessed to the objective lens to sit approximately 25 mm from the trap centre. This lens focuses the fluorescence from the trapped ions and transmits it onto the CCD sensor where it forms a 2D projection (see Fig. 3.2). The depth of field of the system is approximately 50 $\mu$m — enough for 2–3 ion layers to be in reasonable focus in the image. The output from the CCD camera is sent through an image intensifier and then through a video capture card into a PC.

Additionally the image intensifier may be gated so that the camera can be made to

intensify light only at discrete intervals. This is particularly important for single ion mass spectrometry as described further in Chapter 5.

### 3.1.2 Simulating an experimental image

Simulations of the experimentally acquired fluorescence images may be generated through the use of Molecular Dynamics simulations (*i.e.* ProtoMol - see Section 2.5), followed by post-processing of the simulation data. To begin, the desired number of ions, whose positions and general properties are defined in text files input to the simulation, are initially structured into a bcc lattice with a spacing of 10–25 $\mu$m. From this starting point the simulation is run for a period of time (usually the order of $1\times10^5$ steps or 880 $\mu$s) in order for the ions to cool to the steady state, as determined by a stable temperature. At this point the ion positions are output to a file at each step over approximately $5\times10^4$ steps or 440 $\mu$s, which corresponds to about 1700 radiofrequency periods. From these position data a 3D histogram of time-averaged ion spatial intensity can be generated in a user defined grid, and from a particular camera angle.

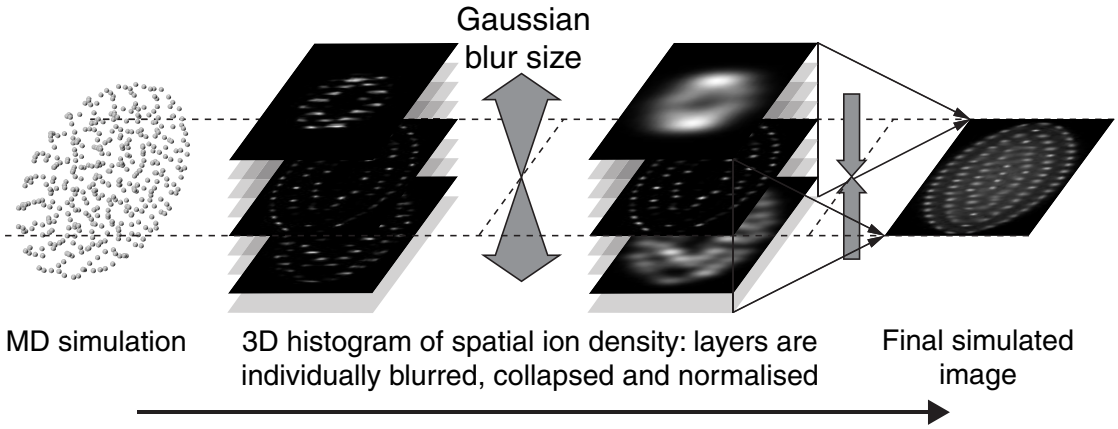


Figure 3.3: The method used to generate a simulated fluorescence image.

As illustrated in Fig. 3.3, the resulting histogram is processed using a Matlab script in order to correctly blur the individual slices in the histogram depending on their

distance along the viewing direction of the camera system. The focal point is set at the central plane of the histogram along the viewing direction, corresponding to a crystal which is properly in focus. A Gaussian blur is applied to each individual slice or layer with a magnitude determined by the product of a constant calibration factor and the layer's distance from the central/focal plane. These processed spatial intensity slices are then summed and normalised to produce the final image.

The blur calibration factor is determined for our particular camera setup in the following manner: a translation stage, which allows the entire camera system to be shifted along the view direction, enables the focal point of the imaging system to be offset with micron precision. Using a well-centred (radially and axially) string of ions (necessarily located in a single plane, perpendicular to the view direction), multiple images are taken at micron intervals in the camera offset. A simulation is generated, comprising a string of the same number of ions. As the distance of the focal plane offset is known in the experimental case, we are then able to find the constant calibration factor which gives us the best reproduction of our experimental images at all focal plane offsets — over a range which matches the typical width of large crystal.

Even in the case of multi-component crystals, where there are non-fluorescing ions present, the number of dark ions may be inferred by the distortions present in the $^{40}Ca^{+}$ ion structure. This is illustrated in Fig. 3.4, which shows a simulated image calibrated to match an experimental image. The non-fluorescing ions have been made visible in the simulated images and one can see how the distortions to the $Ca^{+}$ structure arise through the Coulomb repulsions between the ions. These distortions are surprisingly sensitive to the relative number of ions and therefore constituent ion numbers can generally be determined with reasonable accuracy. This is quantified and discussed further with regard to multi-component simulations in Chapter

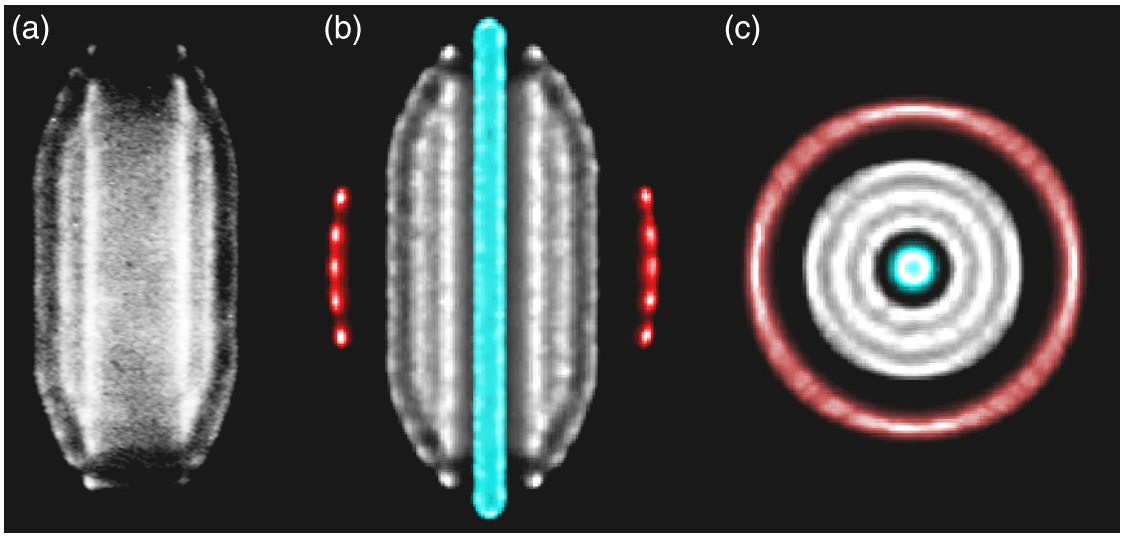


Figure 3.4: (a) Experimental image of a tricomponent crystal involving $Ca^+$, $OCS^+$ and $ND_3^+$. (b) Simulated image of a tricomponent crystal with 480 $Ca^+$ ions (white), 114 $OCS^+$ ions (red) and 56 $ND_3^+$ ions (blue). (c) Simulated image of the crystal in (b), but viewed as a projection along the $z$-axis. Note that the mass/charge ratio of the ions in each segregated group decreases towards the $z$-axis.

7, which deals with the reaction of sympathetically-cooled molecular ions. Additionally, the increased effective kinetic energy of the ions further from the $z$-axis is visible in Fig. 3.4(c) as an increased radial blurring of the fluorescence.

The images shown in Fig. 3.5 demonstrate the accuracy with which simulated images can allow the determination of both secular temperatures and ion numbers purely from visual comparison with an experimental image. For each simulated image on the left hand side, the number of ions in the associated simulation was varied, whilst the trapping parameters were matched to the experiment. Careful matching of the crystal extents suggests that ion numbers can generally be reproduced to within ∼5 ions for a ∼500-ion crystal (*i.e.* 1 %). In a similar way, the stochastic heating term can be systematically changed to vary the kinetic energies of the ions, as shown in simulated images on the right hand side. Extracting these values from the simulations allows us to estimate the secular temperature of a

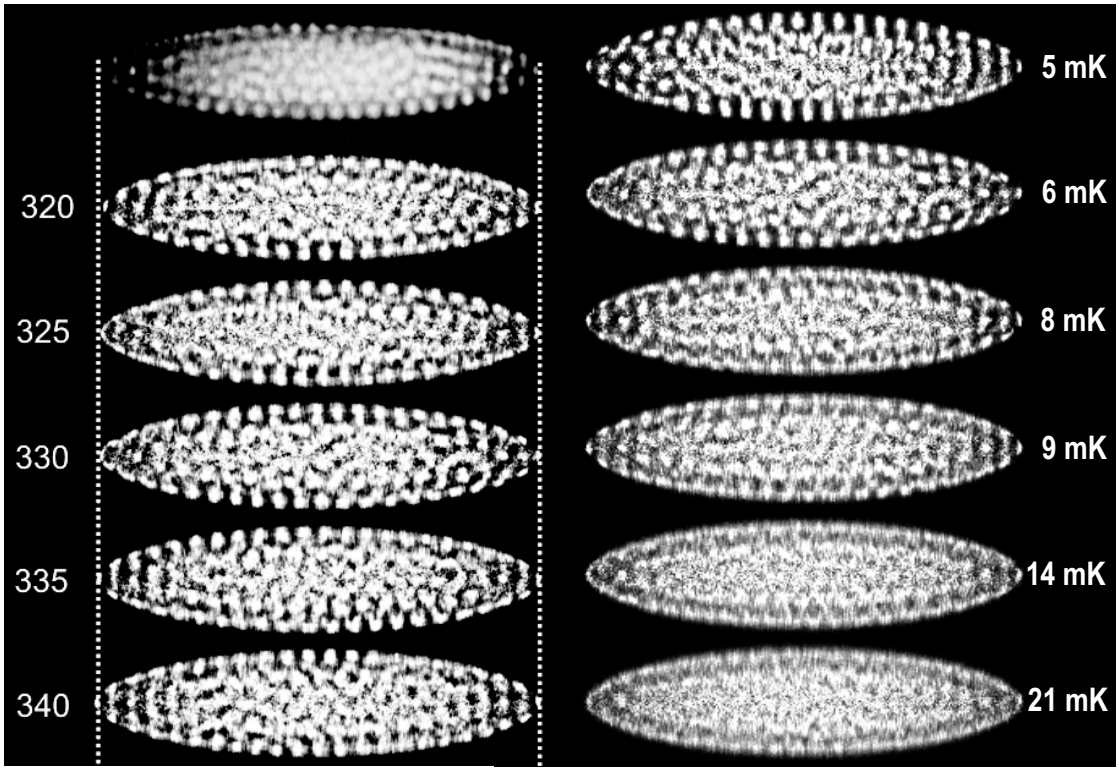


Figure 3.5: Comparison of an experimental image (top left) with various simulations with different ion numbers (left) and at different secular temperatures (right). From these simulations we can determine that there are 325(5) ions at a secular temperature of 6–8 mK.

crystal simply by matching the blurring of the fluorescence between simulated and experimental images — an increased secular temperature results in an increase in the blurring of the time-averaged spatial fluorescence intensity.

## 3.2 Procedure for loading the ion trap

### 3.2.1 Locating ion fluorescence for the first time

Locating ion fluorescence in the first instance can prove to be difficult on account of the large number of experimental parameters that must be finely tuned simultaneously, and imperfections in the effective trapping fields that may lead to displacement of the ions from the geometric centre of the trap. Achieving success at

this stage relies on narrowing down the parameters that need to be varied, carefully monitoring all parameters, and systematically searching the region closest to the geometric trap centre. In general the search is best conducted by sweeping certain trap offsets in an attempt to bring the ions into the confluence of the cooling lasers, rather than by changing the beam alignments.

As described in the previous section an optical fiber (of diameter 400 $\mu$m) may be positioned at the geometric trap centre by virtue of a manipulator arm. In order to achieve the correct laser alignments the fiber tip is moved into the right position (as determined visually whilst the chamber was prepared) and both cooling lasers and the ionisation beam are all aligned to the fiber tip. The camera system is moved into place such that the fiber tip is central on the screen and in focus when scattering the 397 nm laser.

A calcium hollow cathode lamp is critically important at this stage for ensuring that both cooling lasers are at the correct frequencies (thereby removing uncertainty from these two experimental parameters). Subsequently the cooling lasers are detuned by 20–60 MHz in order to ensure adequate laser-cooling for the hot trapped ions. The 866 nm and 397 nm diode laser powers are attenuated to approximately 5 mW and 500–800 $\mu$W respectively. The radiofrequency and end-cap voltage are typically set to a value lower than might be used for clear observation of a crystal to ensure that any ion cloud is relatively large in size so that the probability of at least clipping it with the cooling lasers is greater. Values of 130–150 V and 0.5–4 V for $V_{\mathrm{RF}}$ and $U_{\mathrm{end}}$ are typical for our system in this regard.

The calcium oven is turned up to around 11–13 A and given 2–3 minutes to achieve a stable working temperature in the region of 600–900 K. The 355 nm ionisation laser is then focused down into the trap centre via a 25 cm focal length lens at a power of 2–3 mW. The ionisation beam is admitted for a period of around 1–3

minutes to ensure a large number of ions are generated. The ions formed at this point are then confined by the fields within the trap as discussed in Chapter 2. After this time the ionising beam is blocked and the 25 cm lens is rotated out of the beam path and replaced with a 60 cm focal length lens. This longer focal length means that the cooling lasers are not as tightly focused at the trap centre and we achieve elliptical spot sizes with minor and major diameters of $\sim$0.125 mm $\times$ 0.25 mm and $\sim$1 mm $\times$ 2 mm for the 397 nm and 866 nm beams respectively. The oven is typically then turned off.

At this stage we expect that we have successfully loaded ions into the trap, but they may not be visible due to the effective trap centre being displaced from the position of our fiber tip (to which the camera was aligned). To proceed, we wish to apply additional static voltage offsets to the trap electrodes in a bid to move the ions into the cooling beams so that they emit fluorescence and become visible on the imaging setup. The notation describing these static voltage offsets and their effect on the crystal position within the trap is elaborated upon in Section 3.3.2; for this section it suffices to say that their combined manipulation allows the crystal to be offset both radially and axially. Having ensured that the image intensification is at the maximum setting possible (allowing for saturation due to any stray light present), variation of these static voltage offsets permits a systematic search for the ion fluorescence.

Once the slightest hint of fluorescence is suspected, one must determine that it is indeed due to ion fluorescence by changing one of the cooling laser wavelengths in an effort to modulate the fluorescence. It is possible to image a reflection of the crystal, and this too may be identified by observing an unexpected response to movement generated by altering the static voltage offsets. In the event of a reflection it is often a simple case of using the camera system's translation stage

to search in the horizontal plane – the crystal usually being close-by in such an instance.

Having found the ion cloud, one must now optimise the trapping and cooling parameters in an effort to increase the observed fluorescence intensity. In general this is achieved by first using the static offsets to bring the ions into the cooling lasers more fully, with a slight adjustment in relative beam alignment if necessary. Next one would adjust the laser detunings and attenuation. The ion cloud's axial size may be adjusted using $U_{end}$ at this stage. Now $V_{\mathrm{RF}}$ may be adjusted to try and increase fluorescence and promote crystallisation. This is normally attempted by dropping $V_{\mathrm{RF}}$ to around 100–120 V and carefully observing the fluorescence.

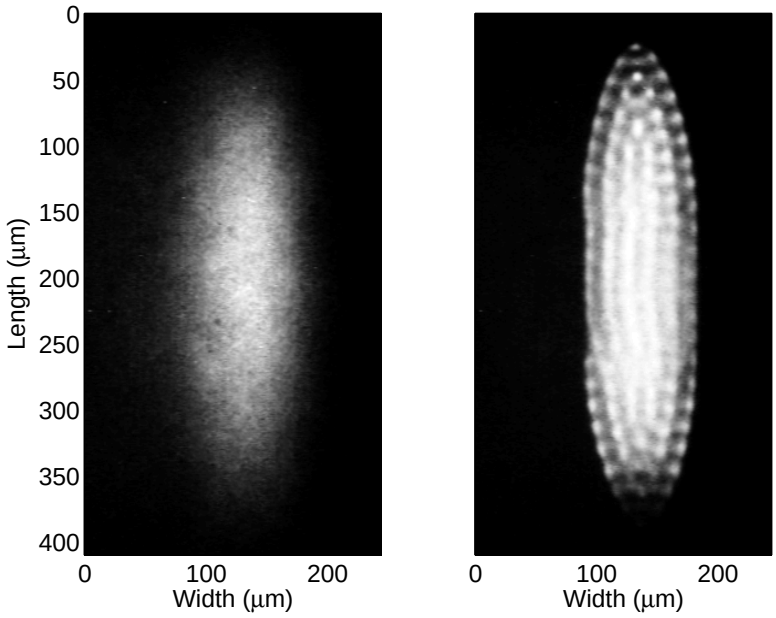


Figure 3.6: Comparison between experimental fluorescence images before and after crystallisation. Parameters have been well optimised beforehand.

As mentioned in the previous chapters, micromotion arising from the oscillating RF potential is the dominant contribution to the ion's kinetic energy. If the RF voltage is dropped, there is a significant decrease in the amplitude of their oscillation (the frequency remains constant) and therefore in their kinetic energy. Thus,

in conjunction with laser-cooling, lowering $V_{\mathrm{RF}}$ is an effective method for bringing the energy of the ion ensemble below the critical energy limit described in Chapter 2, promoting their crystallisation. This event is observable as a practically instantaneous transition from a diffuse cloud of fluorescence into a more intensely fluorescent ellipse with better defined edges (see Fig. 3.6). Single ions within the structure may or may not be resolved at this stage, depending on the other parameters involved. The finer tuning of these parameters is generally repeated each time a new crystal is loaded, as discussed in the next section.

If the crystal is displaced radially during a change in $V_{\mathrm{RF}}$, then static voltage offsets have displaced the ions from the true trap axis, which is determined by the oscillating radio-frequency fields. One should attempt to change $V_{\mathrm{RF}}$ incrementally, each time correcting for horizontal ion displacement with the available static voltage offsets, until such time as $V_{\mathrm{RF}}$ may be changed with no observed translation of the ion fluorescence as a whole. This will be observed as a contraction or expansion of the radial extent of the ion cloud or crystal, which remains well centred. If the cloud has not undergone crystallisation at this stage, $V_{\mathrm{RF}}$ should again be reduced until this occurs. Optimisation should be good enough at this stage to reload the ions in the trap if the number of ions is not ideal. Too many ions (more than a few thousand) can prove difficult to crystallise as there is usually not enough cooling power to counteract the large amount of RF heating occurring. Conversely, too few ions may provide too few structural indications regarding the relative displacement from the true radial trap centre.

Having located and then maximised ion fluorescence intensity, and possibly also having achieved crystallisation, the camera position, static voltage offsets and laser parameters will all be optimised well enough to allow the standard trap loading and optimisation procedures to be used. Further optimisation of all these parameters

may occur in an iterative fashion as described in the next section, until good resolution of single ions within the crystal is achieved.

Typically, the daily drift in all of these parameters is not great enough to require a new search for ion fluorescence on a daily basis. A new search may be required if there is a longer period of time without use (*e.g.*, more than a month), although it is likely to be trivial in comparison to the very first search attempt. In general the most difficult and time-consuming part is ascertaining the position of the true trap centre relative to the optical fiber tip in the first instance.

### 3.2.2 Standard ion loading and parameter optimisation procedures

The general procedure for loading a crystal comprising hundreds of ions or more is as described below, and this is followed by the procedure for loading only a few ions or less. For the majority of the reaction studies in this thesis crystals comprising around 400–1000 ions are used.

The cooling laser frequencies are set to the effective atomic transition frequencies according to the last working values. In general these are slightly offset from the true atomic transition frequencies on account of a small drift in the wavemeter measurement, and these drifts are monitored from day to day and recorded. Then the laser frequencies may both be detuned by 20–60 MHz and the laser powers attenuated to approximately 5 mW and 600–800 $\mu$W for the 866 nm and 397 nm diode lasers respectively, much the same as when searching for fluorescence for the first time. The trapping voltages $V_{\mathrm{RF}}$ and $U_{end}$ are set to values of around 150 V and 4 V respectively. Loading of the ions into the trap proceeds as described in the previous section, although typically the calcium oven current is kept at 11 A. The number of ions in a crystal is controlled simply by the length of time the ionising

laser is admitted (see Fig. 3.7).

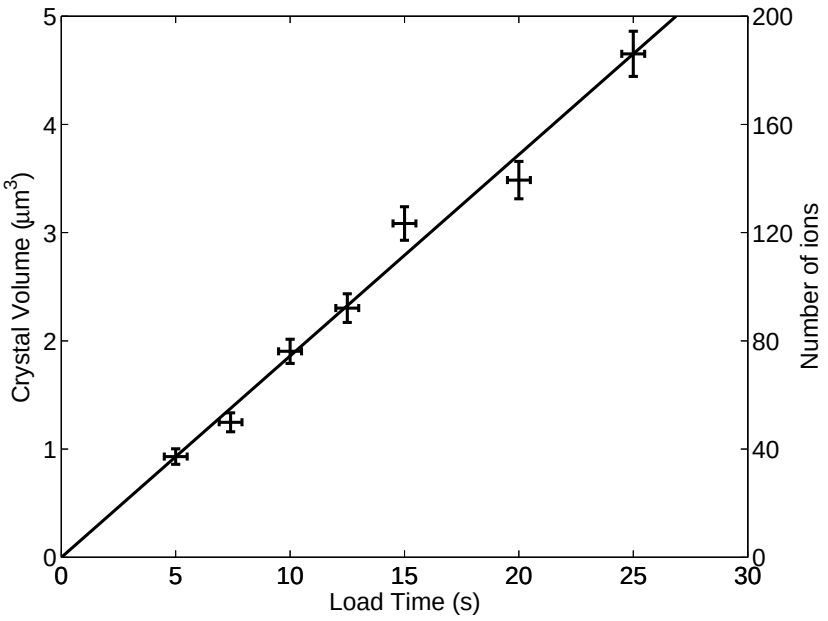


Figure 3.7: Coulomb crystal volume vs. loading time at an oven current of 11 Amps.

With experimental parameters optimised to the state described in the previous section, the ions should become visible at once, and usually the crystal growth can be observed in real time if the cooling lasers are well-aligned during ionisation. Having ionised with a 25 cm focal length lens, a 60 cm focal length lens is then used for a slightly broader beam profile (the lens being approximately 30 cm from the crystal). Ideally the beam width at the trap centre is broad enough to completely encompass the crystal. In most cases small changes in patch potentials, relaxation of any optics mountings, or fluctuations in the trapping fields can lead to the crystal being slightly offset relative to the laser beams or geometric trap centre. In this case the laser alignments and/or crystal offsets (again, see Section 3.3.2) may be adjusted to compensate.

The first step in fine tuning the optimisation is to use the optics to perform a fine adjustment of the laser alignment such that the fluorescence of the ions is

maximised and there is a good overlap of the beams. Often, if the 397 nm beam power is high enough, at optimal alignment we observe a dimming in the very tip of the crystal as illustrated in Fig. 3.8(c) and 3.11(c–e). This is believed to be a consequence of radiation pressure axially separating those $Ca^+$ ions which are currently absorbing 397 nm photons from those $Ca^+$ ions which have been "shelved" into the metastable $^2D_{5/2}$ state* and are therefore temporarily decoupled from the 397 nm beam until spontaneous decay (similar in rate to that of the $^2D_{3/2}$ state) can return them to the ground state. Such an effect is only observed if cooling from a single axial direction.

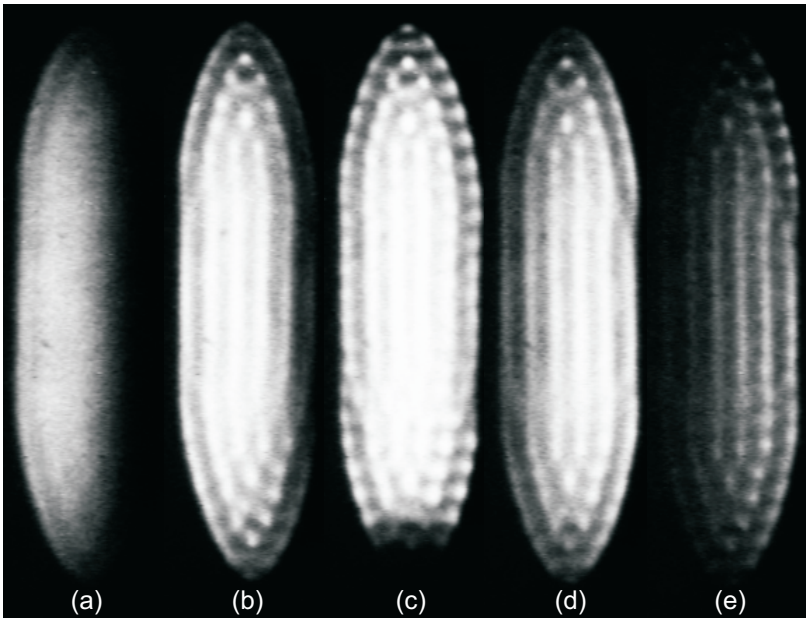


Figure 3.8: Horizontal alignment sweep of 397 nm diode laser beam (a)-(e).

If the ions have not already undergone a phase change to the crystalline lattice form, $V_{RF}$ is dropped to around 110–120 V or until crystallisation occurs. The next step is to ensure the crystal is perfectly centred in the trap. If it remains

*Shelving into the $^2D_{5/2}$ state can occur via spontaneous emission from the $^2P_{3/2}$ state (should the lasers used produce a non-zero probability of populating the $^2P_{3/2}$ state), or from background collisions which occur at an energy appropriate to the transfer of population from the $^2D_{3/2}$ to the $^2D_{5/2}$ state.

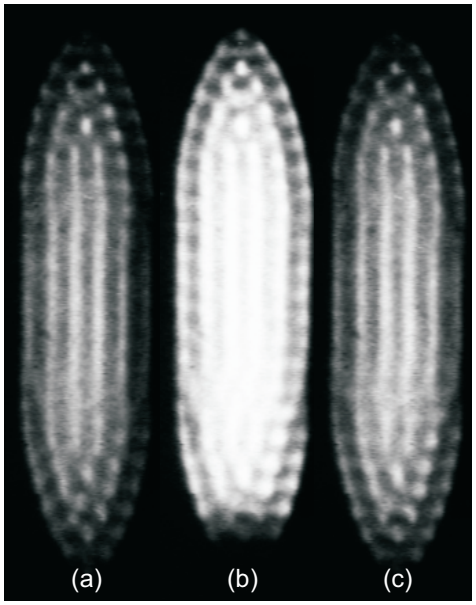


Figure 3.9: Vertical alignment sweep of 397 nm diode laser beam (a)-(c).

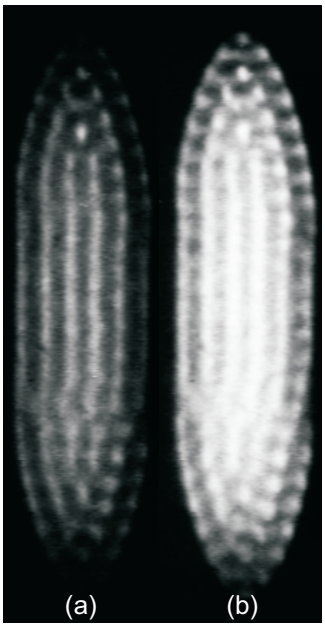


Figure 3.10: Alignment of 866 nm diode laser beam: (a) Poor alignment, (b) Well aligned with fluorescence maximised.

radially offset, due to patch potentials or poorly optimised manual static voltage offsets, any change in the composition of the crystal will lead to asymmetries in the observed fluorescence and hinder accurate calculation of ion numbers. In general,

these asymmetries are most likely already present and detectable in the nascent crystal due to the production of impurity ions (especially when ionising $Ca^+$ non-resonantly). They typically appear as a distortion at the outer edge of the crystal on account of the presence of ions heavier than $^{40}Ca^+$ — such as the heavier isotopes of calcium — or contaminants in the oven or chamber background gas also ionisable at 355 nm. A small amount of heavier impurity is not completely undesirable, as it provides the best practical marker for the centring of a crystal prior to any reaction experiments (mainly due to the difficulty in observing symmetrical crystal contraction/expansion in the direction parallel to the camera axis). Prior centring is important because reaction experiments can occur on a timescale which is fast compared to that of manual adjustment of the crystal offsets. The crystal is thus re-centred radially using the static voltage offsets, and this process (along with axial-centring) is described in Section 3.3.2. Axial centring can also be performed, although the crystal structure and stability are less dependent on the axial offset and as such this step is typically omitted.

Following an adjustment of the voltage offsets it may be necessary to re-optimise the alignment of the cooling laser beams. The attenuation of the 397 nm laser is increased until the power admitted to the chamber is approximately 150 $\mu$W, and the image intensification is increased to counter the drop in fluorescence. At this stage a re-focusing of the camera can occur and a clear image of the crystal should be obtained, including a good resolution of each single lattice site near the focal plane of the imaging system. Fluorescence collected from ions that are not in the focal plane results in a distribution of diffuse fluorescence, particularly at the centre of the crystal where the depth of the crystal parallel to the view direction is greatest. This can wash out detail in the centre of the crystal, but, in general, reduction of the laser intensities and boosting of the image intensification mitigates this somewhat, as shown in the power sweep presented in Fig. 3.11. More

difficulty may be had in this regard with extremely large crystals comprising several thousand ions or more.

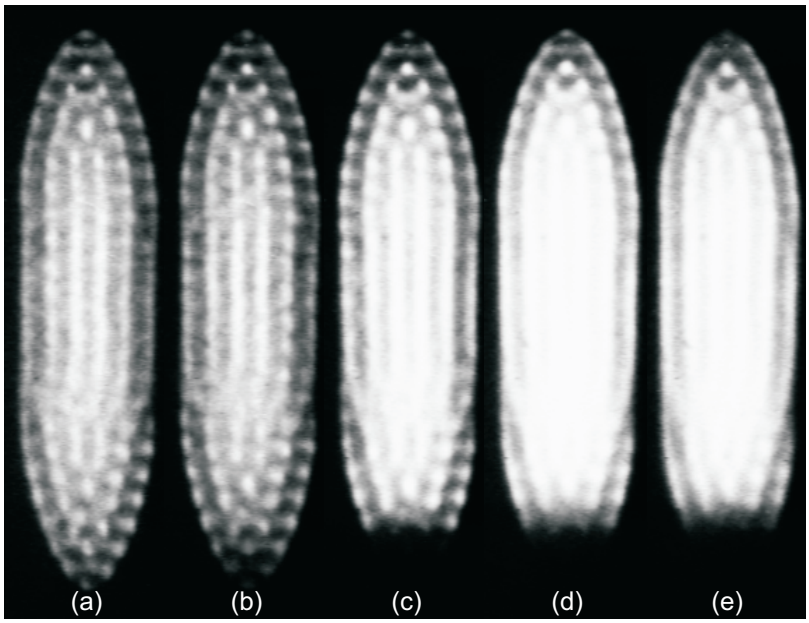


Figure 3.11: Fluorescence images obtained at laser powers of $P_{866} = 5.26$ mW and $P_{397}$ equal to: (a) 162 $\mu$W, (b) 294 $\mu$W, (c) 581 $\mu$W, (d) 818 $\mu$W, (e) 883 $\mu$W.

If stray background light causes problems in resolving the crystal structure it is sometimes possible to avoid the incidence of the background light by tracking the camera system axially whilst simultaneously displacing the crystal a short distance (less than $\sim$0.5 mm) by using a constant axial offset generated by an additional static voltage applied to one set of end cap electrodes. This method has been used with some success for experiments with one or two ions only, when ion fluorescence is much less intense and may be of the order of the background light intensity at the desired image intensification. Subsequently, the inclusion of irises inside the chamber has been found to be very effective in minimising stray reflected light, in conjunction with the use of Brewster windows.

In order to load single ions into the trap, the technique remains generally the same. It is usually best to first load a larger crystal in order to ensure the fields are already

optimised to centre the ions; this is not possible with only a few ions loaded. Once this is achieved the crystal may be removed from the trap by turning off the radial trapping field momentarily. The oven is then turned to a slightly lower current, around 9–10 A, to produce fewer calcium atoms per unit time. The ionising beam is usually admitted for only a few seconds (or less) through the 25 cm lens. Upon switching back to the 60 cm lens, some time is allowed for the ions to cool and appear stable at the trap centre. It is possible for extra $Ca^+$ ions (or even impurity ions) to suddenly crystallise after a period of a few minutes, presumably these ions have been travelling in larger trajectories and have not interacted efficiently with the few ions that are being laser-cooled. With practise it becomes consistently achievable to load 1–2 ions within a couple of attempts in this manner.

## 3.3 Manipulation of Coulomb crystals with applied electric fields

### 3.3.1 General morphology and temperature distributions

The morphology of a Coulomb crystal is dependent both on the number of ions and the relative and absolute magnitudes of the axial and radial trapping forces. In general, as the number of ions in a crystal increases, the most stable configuration progresses from single ion to string, through a fluxional helical arrangement and into a three dimensional spheroidal lattice. These shapes reflect the balance between the repulsive Coulomb interaction between ions and the effective potential generated by the trapping fields. In the spheroidal lattice structure the ions are arranged in concentric shells and, within each shell, there is a near-2D hexagonal ordered structure over short distances. Whilst there is generally no true translational symmetry in Coulomb crystals as a whole, body centred cubic structures

have been observed in the core of near-spherically symmetric crystals with ion numbers above approximately 1000 ions [179], and in Penning traps in systems of around $1\times10^5$ ions or more [180–182].

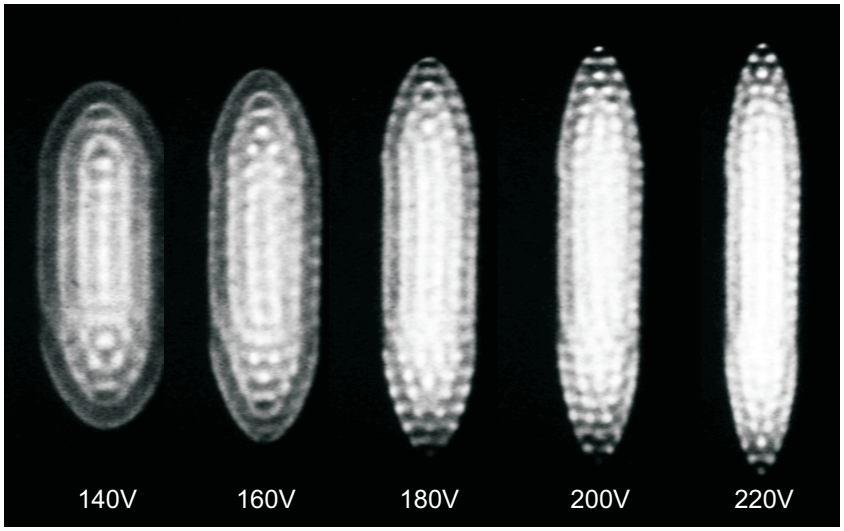


Figure 3.12: Crystal morphology: Variation of $V_{\mathrm{RF}}$, $U_{\mathrm{end}} = 4$ V. The radial trapping force increases with $V_{\mathrm{RF}}$ and squeezes the crystal radially. Notice that the ions become more spatially defined as they move closer to the trap axis, due to the decrease in micromotion and therefore their effective kinetic energy.

The shape of a spheroidal crystal with cylindrical symmetry about the trap $z$-axis may be characterised by its aspect ratio, $\alpha$, which is simply the ratio of its diameter along the trap $z$-axis to its radial diameter. The aspect ratio of a Coulomb crystal in such a spheroidal configuration may be adjusted by changing the relative amplitude of the radial and axial trapping fields. Increasing $V_{\mathrm{RF}}$ results in stronger radial trapping forces and a more prolate crystal (see Fig. 3.12). In contrast, an increase in $U_{\mathrm{end}}$ results in stronger axial trapping forces, squeezing the crystal axially and resulting in an increasingly oblate crystal shape (see Fig. 3.13). According to the fluid model discussed in Chapter 2, the ion density is only dependent on $V_{\mathrm{RF}}$. For our particular trap design, true strings are only achievable for ion numbers of around 30–40 or less, and at $U_{\mathrm{end}}$ values of 0.05–2 V.

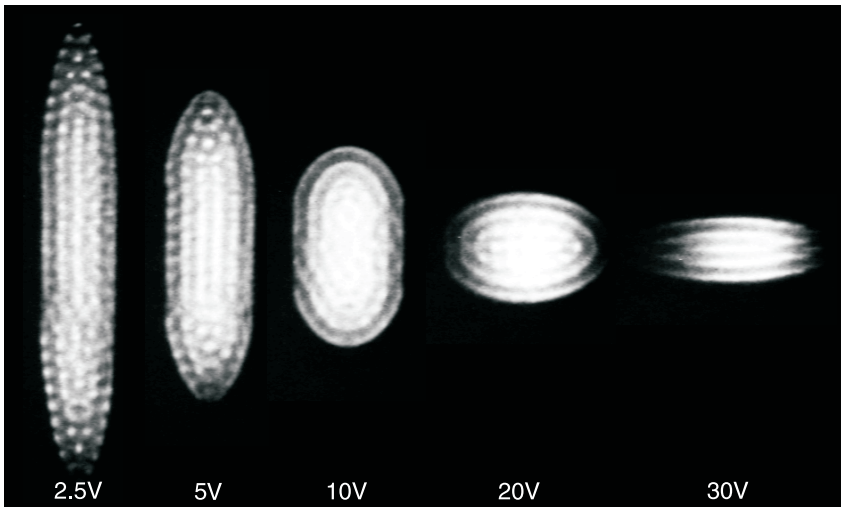


Figure 3.13: Crystal morphology: Variation of $U_{\text{end}}$, $V_{\text{rf}} = 180$ V. The axial trapping force increases with $U_{\text{end}}$ and compresses the crystal along the trap axis. The darkened edges of the most oblate crystals reflect the fact that they are now partially outside of the cooling lasers. More spatial smearing of the fluorescence intensity is observed when moving from the prolate to the oblate case (left to right). This due to the ions being on average closer to the electrodes and therefore having a higher average effective kinetic energy due to the RF micromotion.

The ion micromotion is the dominant contribution to the total kinetic energy of the trapped ions and increases the closer the ions are to the electrodes (see Fig. 3.14). This micromotion vanishes when the ions lie on the $z$-axis and therefore strings are the lowest energy configuration. Typical ion temperatures in a string are ∼5–10 mK and, as such, are near to the Doppler cooling limit (derived in Section 2.3.2), which is defined for an atomic transition as

$$T_{\text{D}} = \frac{\hbar\Gamma}{2k_{\text{B}}}. \tag{3.1}$$

This formula gives a temperature limit of ∼0.5 mK using the natural linewidth of ∼130 MHz for the main 397 nm atomic transition involved with the laser-cooling of $Ca^+$.

Secular temperatures for spheroidal crystals are also typically around ∼5–10 mK and are the lesser contribution to the total effective temperatures for these crystals

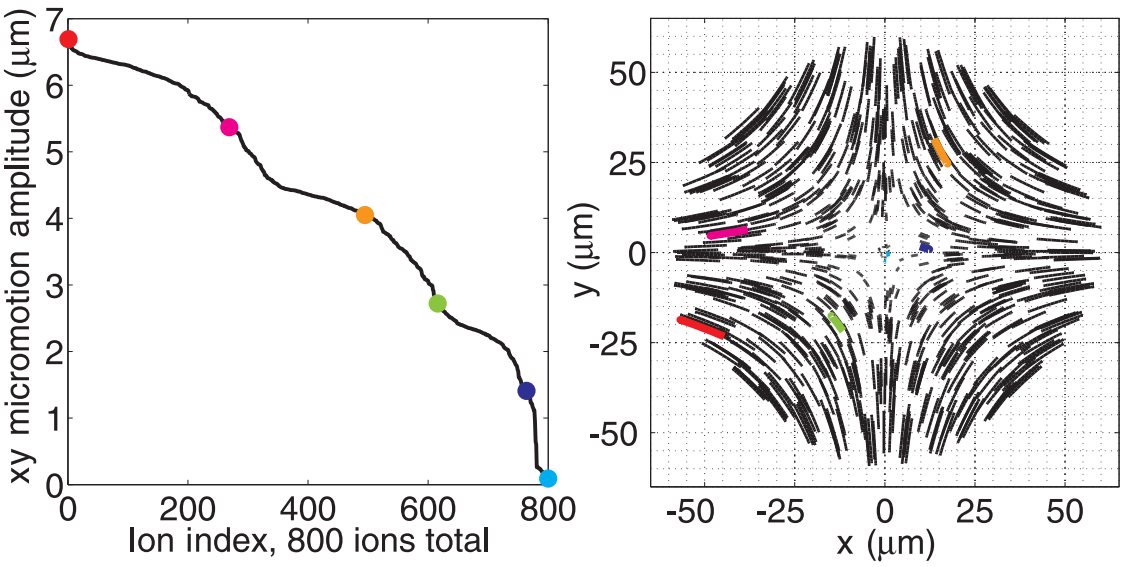


Figure 3.14: Illustration of the increase of micromotion amplitude away from the $z$-axis and towards the electrodes. In the right hand panel, the four quadrupole rods are situated above, below and to the left and right of the image. This results in a characteristic pattern in the $xy$ projection of the ion motion. Selected ions are highlighted in both panels, and the spheroidal shell structure is the source of the undulation observed in the micromotion amplitude distribution. This 800-ion crystal was simulated at $V_{\mathrm{RF}} = 180$ V, $U_{\mathrm{end}} = 4$ V.

which are generally of the order of ∼1 K. As more ions are added to the crystal and successive concentric shells are built up, each new shell lies on average closer than the last to the trap electrodes, and therefore each successive ion shell's average kinetic energy increases. Simulated kinetic energy distributions of larger crystals (particularly the more oblate crystals) show clear, well-separated, peaks corresponding to contributions from the individual shells. Additionally, for a given ion number, a more oblate configuration will place more ions on average closer to the electrodes than a prolate one, resulting in a larger average ion kinetic energy, as illustrated in Fig. 3.15. This means that the average kinetic energy of the ions may be manually controlled to some degree by a change in the trapping forces, or more specifically, the amplitudes $V_{\mathrm{RF}}$ and $U_{\mathrm{end}}$.

Kinetic energy distributions can be determined from experimental images through

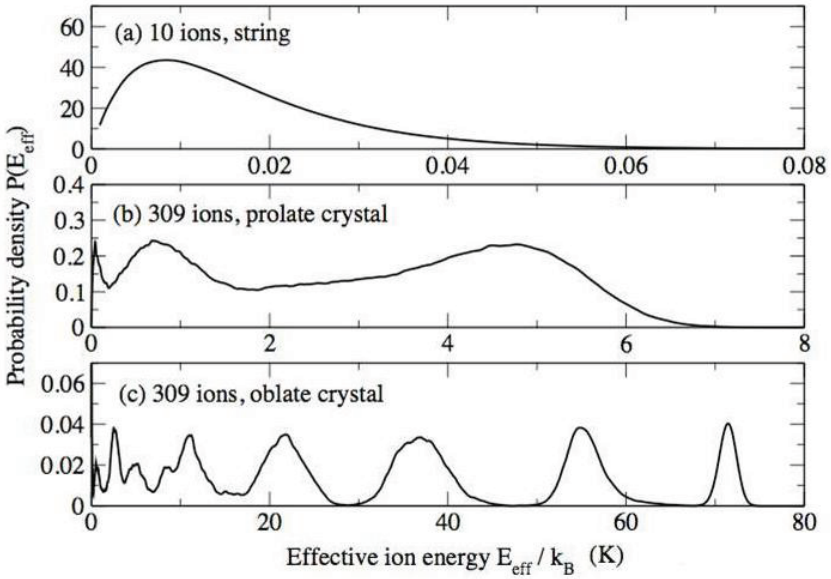


Figure 3.15: Kinetic energy distributions for simulated crystals: (a) Strings represent the lowest energy configurations, on account the lack of micromotion at the central trap axis, whilst in (b),(c), average ion kinetic energy increases as the crystals move from prolate to oblate due to increasing micromotion nearer the trap electrodes. Note the peak separation on account of the discrete concentric shell structure of the spheroidal crystal.

simulations (see also Section 2.5). Figure 3.16 shows simulated energy distributions corresponding to experimental images of a string comprising 15 ions, and for a prolate and oblate crystal of 900 and 500 ions respectively. This figure again illustrates the dominance of the micromotion with regard to the kinetic energy distributions, as the effective ion energies increase rapidly with the radial displacement of the ion from the trap axis. In Fig. 3.16(a) time-averaged simulations of the ion fluorescence, projected along the $z$-axis, clearly show the blurring associated with the micromotion of the spheroidal crystal fluorescence. This is most obvious in the oblate case (iii) where, in the $z$-axis projections, the electrodes are situated at the corners of the image.

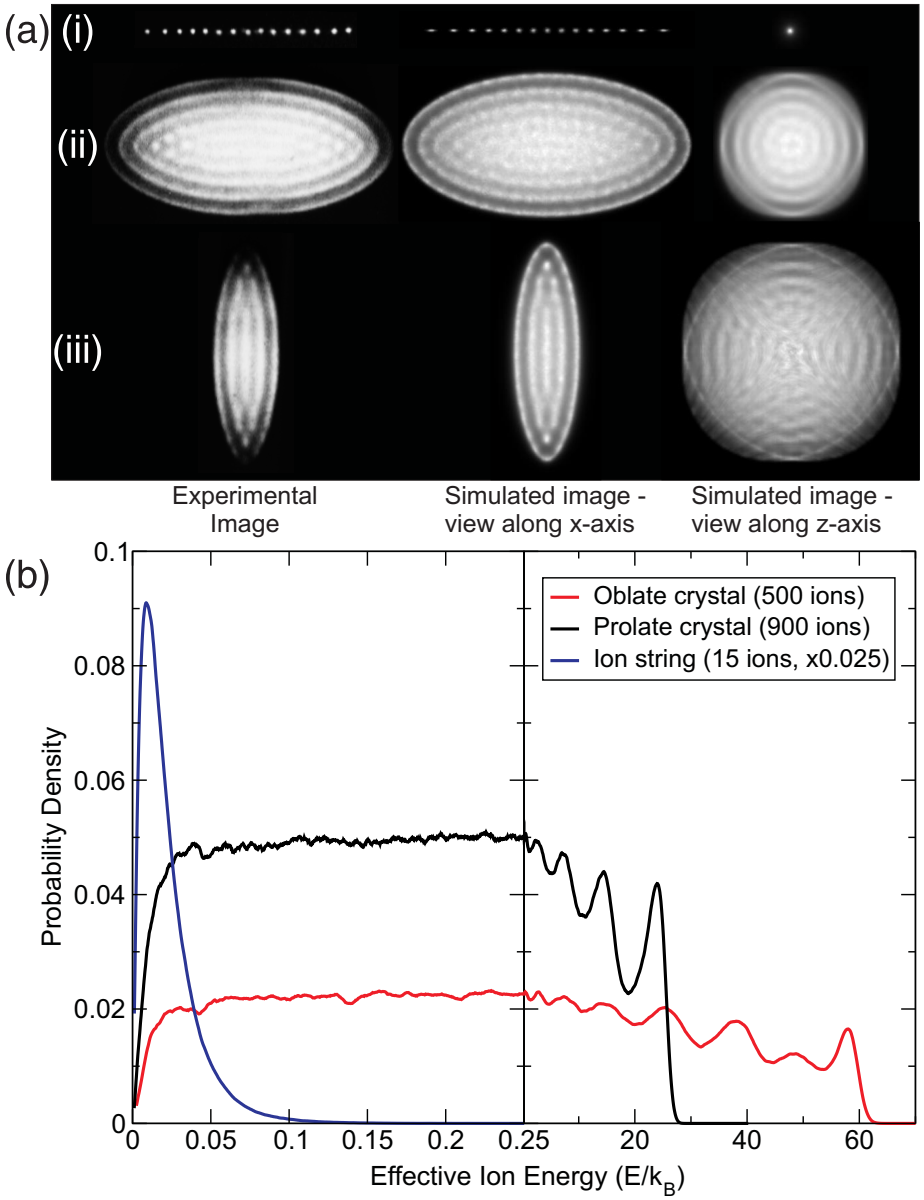


Figure 3.16: (a) Experimental and simulated Coulomb crystal images for (i) a string of 15 ions, (ii) a prolate crystal of 900 ions (long axis of spheroid along the trap axis), and (iii) an oblate crystal of 500 ions (short axis parallel to the trap axis). In the projection along the $z$-axis, strong directional blurring due to the micromotion is clearly observable in the simulated image. (b) Calculated ion kinetic energy distributions for the crystals in (a), including both secular and micromotion. Note the change in the horizontal scale at $E_{\mathrm{K,eff}}/k_{\mathrm{B}} = 0.25$ K.

### 3.3.2 Static voltage offsets

Static voltages may be applied to specific electrodes in certain configurations for extra control over the orientation and shape of Coulomb crystals held in the linear Paul trap. The electrode configurations used in the current design are illustrated in Fig. 3.17, along with the voltage ranges that are available.

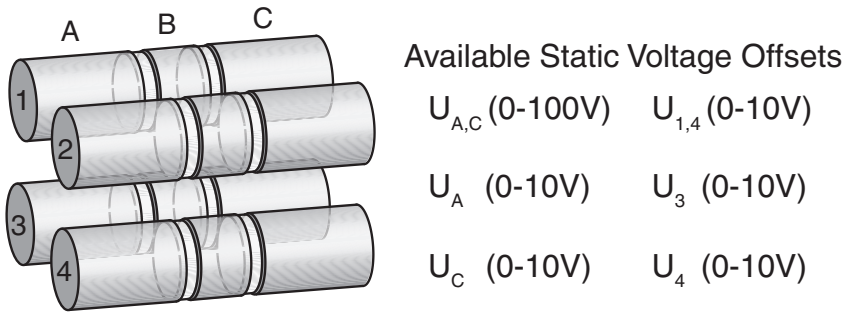


Figure 3.17: Electrode configuration of the available static voltage offsets. The numeric labels refer collectively to all electrode segments along the associated rod, whereas the alphabetical labels refer to the associated electrode segment across all quadrupole rods.

$U_{\mathrm{A,C}}$ is otherwise known throughout this thesis as $U_{\mathrm{end}}$; it is the static end cap voltage that provides axial trapping. $U_{\mathrm{A}}$ and $U_{\mathrm{C}}$ control additional static voltages applied to either set of end caps independently and allow an axial displacement of the trapped ions as illustrated in Fig. 3.18. Adjustment of $U_{\mathrm{end}}$ should result in a symmetrical contraction/expansion of the crystal along the $z$-axis. If the crystal is axially displaced instead this is an indication that it is not axially centred in the trap, and $U_{\mathrm{A}}/U_{\mathrm{C}}$ may be used to adjust the axial crystal offset until it is centred. The further the crystal is from the trap centre, the greater the anharmonicity and the coupling of the micromotion to the axial motion. For small axial offsets ($\leqslant$0.5 mm) this is not observable in our case, and perfect axial centring does not appear to be a prerequisite for our reaction experiments. However, harmonicity is more important when performing single-ion mass spectrometry experiments, as discussed further in Chapter 5.

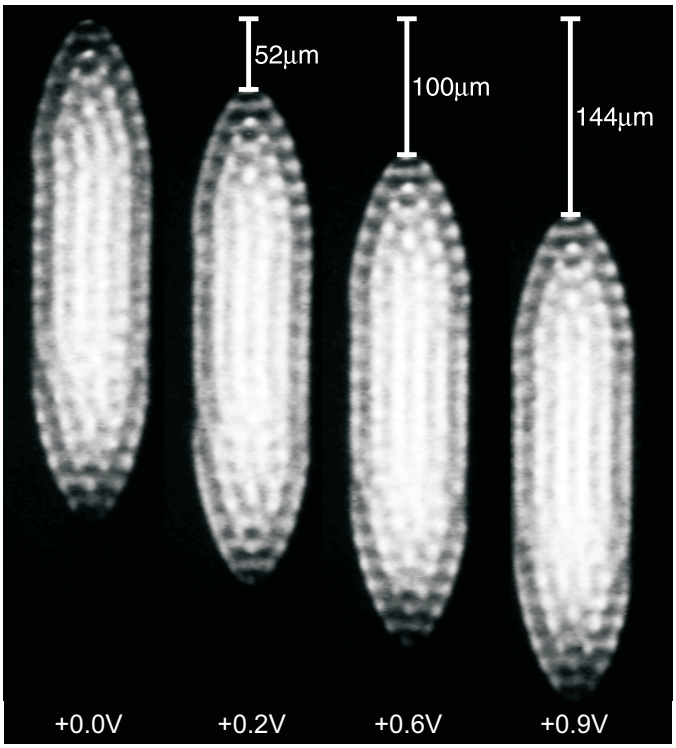


Figure 3.18: Axial displacement of Coulomb crystal by variation of $U_{\mathrm{A}}$.

$U_3$ and $U_4$ provide between them a capability to displace ions or crystals radially. As illustrated later in Figs. 3.19 and 3.20, a simultaneous positive or negative change in both offsets together will results in a vertical displacement in the lab frame (along the camera observation vector), whilst a simultaneous opposite change in both will provide the means to displace ions horizontally, or perpendicular to the view direction of the camera system.

$U_{1,4}$ is a static offset applied to two diagonally opposite sets of electrodes. Its action is to squeeze the ion cloud between these two sets of electrodes such that the ions are spread further out radially in the plane between the remaining two sets of electrodes. Heavier ions are preferentially pushed closer and closer to these remaining electrodes and consequently heat up due to increased micromotion, eventually being lost from the trap. It is possible to begin to selectively lose heavier ions from a multi-component crystal in this manner and, for this reason, this configuration

is generally known as the mass filter configuration of a quadrupole type trap, often denoted $U_{\mathrm{dc}}$.

Having described the available static offsets it may prove useful to elaborate on the usage of $U_3$ and $U_4$ to provide a fuller description of how they are used to centre crystals radially. This is a process of optimisation that is repeated frequently in order to ensure cylindrical symmetry of a single or multi-component crystal. This symmetry is particularly important because it greatly simplifies the process of determining ion numbers within these crystals, whether by volume estimation or by direct simulation.

As discussed in Chapter 2, two species with differing mass numbers are radially separated within the trap on account of the fact that the dynamic fields produce an effective radial trapping potential that is mass dependent. Heavier ions experience a shallower radial potential than lighter ions and consequently, in a multicomponent crystal, sit further away from the trap $z$-axis. Deformation of the typical spheroidal structure of a pure $Ca^+$ crystal is observed when heavier ions are present in the crystal. These heavier ions, which are typically not being laser-cooled and are therefore invisible, sit around the central $Ca^+$ core in a cylindrical sheath and through the Coulomb interaction squeeze the $Ca^+$ core into what is effectively a capped cylindrical conformation. This is readily observable experimentally, and well supported by simulation. Possible reasons for the (typically minor) presence of heavier impurities in the crystal include: Contamination of the calcium oven, the presence of a small fraction of heavier isotopes of calcium and ionisation of any relevant species in the chamber background gas.

In general the presence of a small number of ions heavier than $^{40}Ca^+$ is useful in ensuring radial centring of a crystal. Manipulation of the radial static offsets has enabled a good understanding of how we might infer the relative position of a

crystal relative to the true radial trap centre. If a bi-component crystal is perfectly centred on the $z$-axis, the heavier ions will symmetrically surround the lighter ion core radially. Therefore, inward deformation of the core will be symmetrical also, resulting in a capped cylindrical conformation. When the fluorescence of the laser-cooled ion core is viewed as a 2D projection it appears as an ellipse with symmetrically flattened sides. If the ions are offset radially perpendicular to the image projection vector, the radial distribution of the heavier ions around the lighter core becomes increasingly asymmetric. The heavier ions experience a weaker effective radial potential than the lighter ion core and sit further away in the radial direction. Therefore if the lighter ions are increasingly offset from the $z$-axis the heavier ions will eventually move entirely to one side of the lighter ions, at greater radial extent.

Viewing the 2D projection of the ion core fluorescence in this limit, we can see that the deformation of the fluorescence also becomes asymmetric. If the radial offset is perpendicular to the view vector as in Fig. 3.19 then heavier ions move to the left or right of the crystal and the flattening of the ion core occurs increasingly on one side only. If the radial offset occurs parallel to the view vector as in Fig. 3.20 then heavier ions are now above or below the crystal and the flattening is no longer visible, as it occurs in the plane of the image.

This means that we can centre the crystal (with a precision of less than 5 $\mu$m) via manipulation of $U_3$ and $U_4$ in the following manner. Both offsets are usually always altered in tandem: An increase or decrease in both together will change the effective vertical offset, whilst an opposite change will effect a purely horizontal offset. The goal is simply to maximise the apparent deformation or flattening of the core fluorescence (vertically centred), whilst ensuring that it is horizontally symmetric (horizontally centred). Typically the ion starts both vertically and

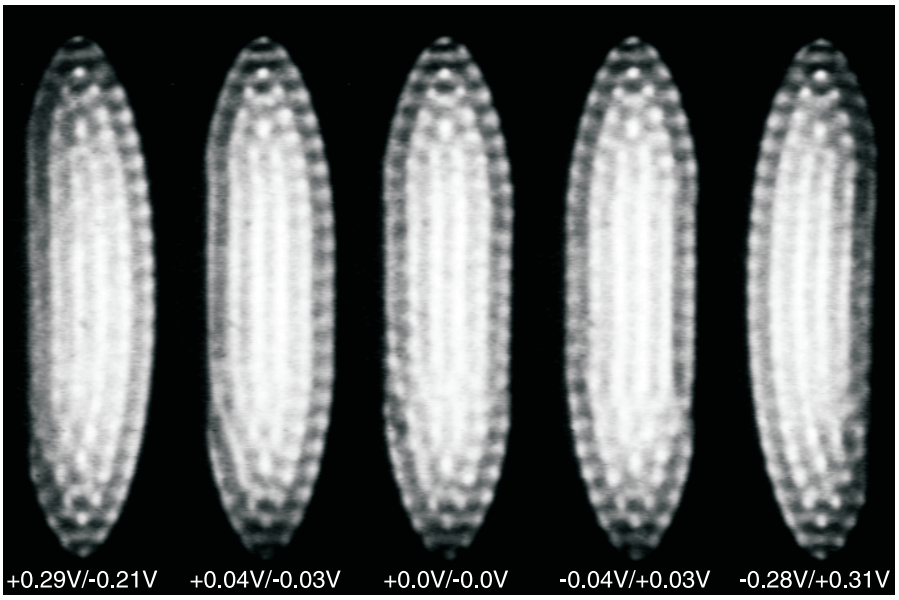


Figure 3.19: Radial displacement of Coulomb crystal perpendicular to view vector by variation of $U_3/U_4$.

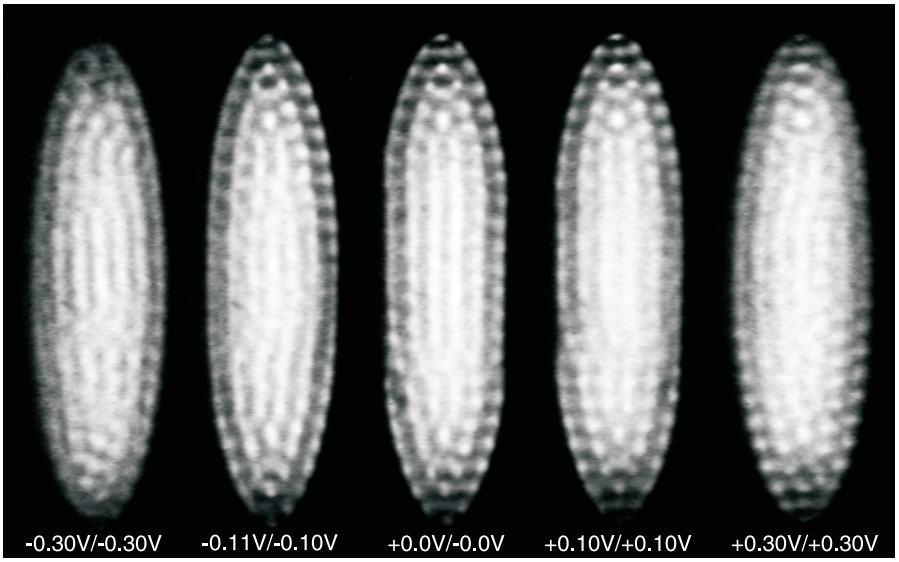


Figure 3.20: Radial displacement of Coulomb crystal parallel to view vector by variation of $U_3/U_4$.

horizontally offset, and is first vertically centred, and then horizontally offset until the deformation is symmetric. In situations where there are few heavier impurity ions it can be useful to manually offset further away from the $z$-axis horizontally to amplify the deformation by putting all of the heavier ions on one side of the $Ca^+$

core. Vertical centring is thus facilitated, and then careful horizontal centring will finish the job. Once again it may be necessary to use a larger crystal to perform this optimisation if the goal of the experiment to be performed involves the use of much smaller crystals comprising fewer than 30–50 ions.

It is possible to horizontally centre a crystal without any impurities by simply offsetting it until a modulation of $V_{\mathrm{RF}}$ results in a symmetric radial squeezing or expansion, and no additional horizontal offset. However it is a little more difficult to centre the crystal parallel to the view direction in this manner as small vertical offsets cannot be observed as easily.

## 3.4 Sympathetic-cooling of atomic and molecular ions

### 3.4.1 Principle

Multi-component crystals have been mentioned numerous times earlier in this thesis, and the process of so-called "sympathetic-cooling" of non-laser-cooled ions alluded to also in Sections 1.3.1 and 1.3.2. This section serves to explain this idea in more depth as well as to clarify how this is achieved experimentally.

Laser-cooled ions in an electromagnetic trap can be used as a heat sink to channel kinetic energy away from other ions that are also contained within the trap. The faster, hotter non-laser-cooled ions interact with the laser-cooled ions via the Coulomb interaction and transfer some of their kinetic energy. The laser-cooled atomic ions are constantly losing the kinetic energy transferred to them due to the repeated absorption/emission of laser photons and the net loss of momentum associated with this cycle.

In this manner these non-laser-cooled atomic or molecular ions are nevertheless brought down in energy until they become incorporated into the cold lattice of

ions that comprises the Coulomb crystal [50, 52, 170] (early attempts involved sympathetic-cooling with non-crystallised ions [49, 183]). Sympathetic-cooling is a very useful technique in the field of cold atoms and molecules and in the study of cold chemistry [126]. This is especially true in the case of molecular ions given that, in general, they cannot be laser-cooled directly because their complex energy level structure causes difficulty in implementing a closed optical cycle. Early experiments involving the reaction of sympathetically-cooled molecular ions were performed by Baba and Waki using non-crystallised ions [129], and since then additional refinement and extension involving the use of ion crystals has been achieved by the groups of Drewsen and Schiller [50, 52, 53, 124] (see also Section 1.3.2).

Not only is it possible to add additional atomic and even molecular ions into the structure of a Coulomb crystal, but any product ions generated from a reaction in the region of the crystal, with an energy less than the depth of the effective trap potential, will also be sympathetically-cooled into the crystal [50, 131]. Thus there are two main routes to introducing non-laser-cooled ions into the crystal: reaction of the existing ions in the crystal and capture of the ion product, or production of entirely new ions.

Reaction of trapped ions and subsequent capture of the ionic product provides a route to a very sensitive method for monitoring the progress of many ion-molecule reactions (single reactive collisions can be observed), and for measuring reaction rate constants. This technique forms the basis for much of the work in this thesis and is discussed in more detail in Chapters 4,6 and 7. Additional ions may be introduced to an existing pure crystal of laser-cooled atomic ions via ionisation of the corresponding neutral species inside the trap itself. This is typically performed by leaking a room temperature gas into the chamber at a partial pressure typically around $1\times10^{-9}$–$1\times10^{-8}$ mbar and ionising it with the relevant laser system. More

information on the experimental side of this technique, can be found in Chapter 7.

Only ions which are being actively laser-cooled in the trap, and are therefore fluorescing, can be imaged directly. Studies have been performed where both constituent atomic species of a bi-component crystal underwent Doppler laser-cooling [170]. In this case both species are visible and the structure is clearly resolved (see Fig. 3.21). However, in a multi-component crystal where only one species is laser-cooled, the presence of the remaining dark ions must be inferred from their Coulomb interaction with the visible ions. To this end Molecular Dynamics simulations are an invaluable tool in understanding the structure and constitution of multi-component Coulomb crystals, this is particularly important for the reaction of sympathetically-cooled ions (see Chapter 7).

### 3.4.2 Properties of multi-component crystals

In terms of their structure, multi-component Coulomb crystals tend towards the spheroidal geometry typical of pure crystals. However, if the constituent ions have different mass/charge ratios, they will be separated in the radial direction on account of the mass/charge dependence of the effective radial potential (see also section 2.2.2). Heavier or less highly charged ions respond more slowly to the changing radial trapping fields and consequently have a shallower potential than lighter or more highly charged ions. Therefore there is complete radial spatial separation of species with different mass/charge ratios; species with smaller mass/charge ratios lie closer to the $z$-axis.

This is well illustrated by the structure of an $Mg^+/Ca^+$ bi-component crystal (see Fig. 3.21, from work by the Drewsen group [170]) in which both atomic ions are being laser-cooled. The fluorescence emitted by each species can be imaged separately and the resulting images combined to give a complete 2D projection. As

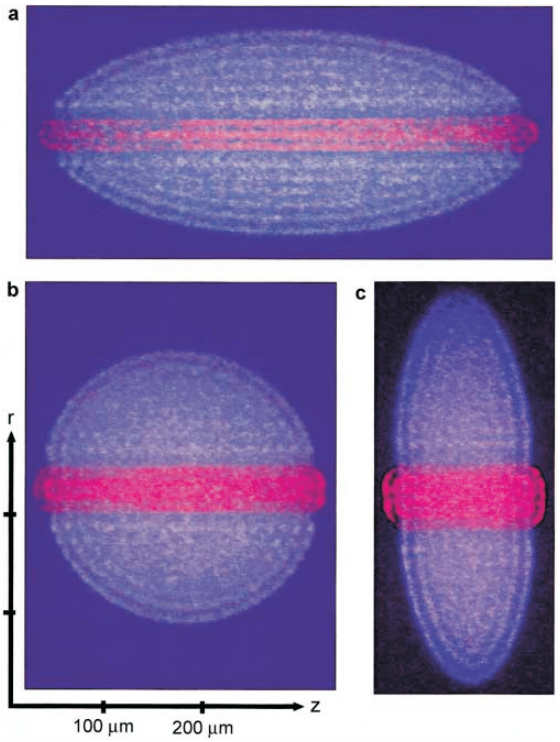


Figure 3.21: A $^{40}Ca^{+}$ $^{24}Mg^{+}$ bicrystal at three different end cap voltages. The crystal is symmetric under rotations around the trap axis, $z$, and contains approximately 300 $^{24}Mg^{+}$ ions (red) and 3000 $^{40}Ca^{+}$ ions (blue). The ratios of the axial and effective radial trapping frequencies for $^{40}Ca^{+}$ and $^{24}Mg^{+}$ ions in the three cases shown are (a) $\omega_z$,$Mg^{+}/\omega_r$,$Mg^{+} = 0.4$ and $\omega_z$,$Ca^{+}/\omega_r$,$Ca^{+} = 0.6$; (b) $\omega_z$,$Mg^{+}/\omega_r$,$Mg^{+} = 0.7$ and $\omega_z$,$Ca^{+}/\omega_r$,$Ca^{+} = 1.0$; (c) $\omega_z$,$Mg^{+}/\omega_r$,$Mg^{+} = 1.1$ and $\omega_z$,$Ca^{+}/\omega_r$,$Ca^{+} = 1.8$. Reproduced from reference [170].

well as causing the mass separation, the mass/charge dependence of the effective radial potential results in a small radial gap at the interface between the separate species. This discontinuity is a reflection of the fact that the heavier $Ca^{+}$ ions experience a shallower radial potential, yet the Coulomb repulsion force between all singly charged ions remains the same. This gap increases with the radius of the core and the square root of the mass ratios and this is discussed further in [170] and the article cited therein.

Studies on the photodissociation of sympathetically-cooled molecular ions illustrate the presence of dark non-laser-cooled ions very clearly. In work performed

by the Drewsen group in Aarhus [51], $H_2$ was leaked into a chamber containing a $Mg^+$ Coulomb crystal. The $H_2$ reacted with $Mg^+$ to form $MgH^+$ which was sympathetically-cooled into the crystal. The spheroidal shape of the pure crystal was distorted as the heavier dark $MgH^+$ ions sit further out in the radial direction, surrounding the lighter $Mg^+$ core. Had the $MgH^+$ ions simply been lost from the trap, the $Mg^+$ crystal would have shrunk whilst maintaining its spheroidal shape and aspect ratio. As the $MgH^+$ ions remain trapped they distort the inner $Mg^+$ core into a capped near-cylindrical arrangement. The $MgH^+$ ions were then photo-dissociated. The $H^+$ ions produced were not stable in the trap and were lost, leading to a rearrangement of the remaining $Mg^+$ into the expected smaller spheroidal arrangement (see Fig. 3.22).

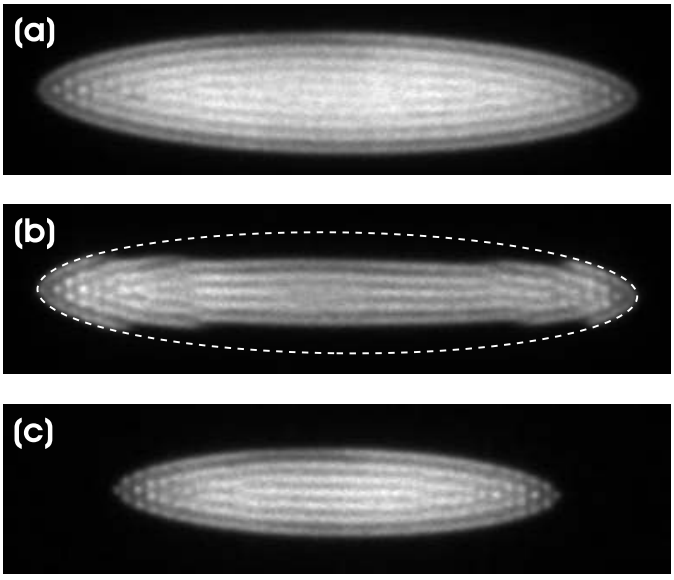


Figure 3.22: (a) CCD-image of a Coulomb crystal with a total of a few thousand $Mg^+$ ions. (b) CCD-image after the ions in the Coulomb crystal in (a) have been reacting with $H_2$ molecules. Roughly half of the initial fluorescing $Mg^+$ ions have been converted into non-fluorescing $MgH^+$. The dashed lined ellipse illustrates the outer boundary of the $Mg^+$-$MgH^+$ Coulomb crystal. (c) CCD-image after the photo-dissociation laser beams have been present long enough that all $MgH^+$ ions have been dissociated. Nearly no non-fluorescing ions are left, proving that almost all $MgH^+$+ molecules have been dissociated. The length of the CCD-images corresponds to 950 $\mu$m. Reproduced from reference [51].

Sympathetic crystallisation can be achieved for effectively any molecular mass, given an appropriate molecular charge, and mass of the laser-cooled atoms [184]. Cooling is most effective if the sympathetically-cooled ions are in close contact with the laser-cooled ions, and this occurs for equally-charged ions with similar masses. This results in the common choice of light ions such as $Be^+$ for the sympathetic-cooling of lighter species such as $H_2$. The use of heavier laser-cooled ions such as $Ba^+$ allows the sympathetic-cooling of very large molecules, with molecular weights of up to ∼500 u for singly charged species, *e.g.*, Rhodamine 6G ions: $R6G^+$, with a mass of 479 u [126]. A larger charge can facilitate the cooling of heavier molecules still, because an increased charge results in a steeper effective radial potential. This means that more highly charged molecules lie closer to the laser-cooled ions radially and thus interact more strongly with them allowing more efficient cooling. This means that even proteins such as cytochrome-c with a mass of ∼12390 u can be sympathetically-cooled, as long as they have a high enough charge, *e.g.*, cytochrome-$c^{17+}$ has been sympathetically-cooled successfully below 1 K [185]. Simulations suggest that molecular masses of up to 16000 u can be supported given a charge of 10–20 [126]. The temperature of dark ions may be inferred experimentally through their interaction with, and subsequent heating of, the visible laser-cooled ions. The increased fluorescence spot-size can be interpreted using Molecular Dynamics simulations: The temperature of the ions in the simulation is varied until the best match of simulated to experimental fluorescence images is achieved.

It is possible to support many dark ions in a crystal with relatively few laser-cooled atomic ions without the heating rate overcoming the rate of cooling and causing the crystal to melt. Simulations show that we regularly observe stable crystals with a ratio of $N_{Ca^+}$:$N_{dark}$ of at least 1:8 (see Fig. 3.23) involving non-fluorescing molecular ions heavier than $Ca^+$ (generally $CaF^+$ or $CaCl^+$). A review

of the literature suggests that work has been done with stable crystals containing a molecular ion fraction of up to ∼95% [50].

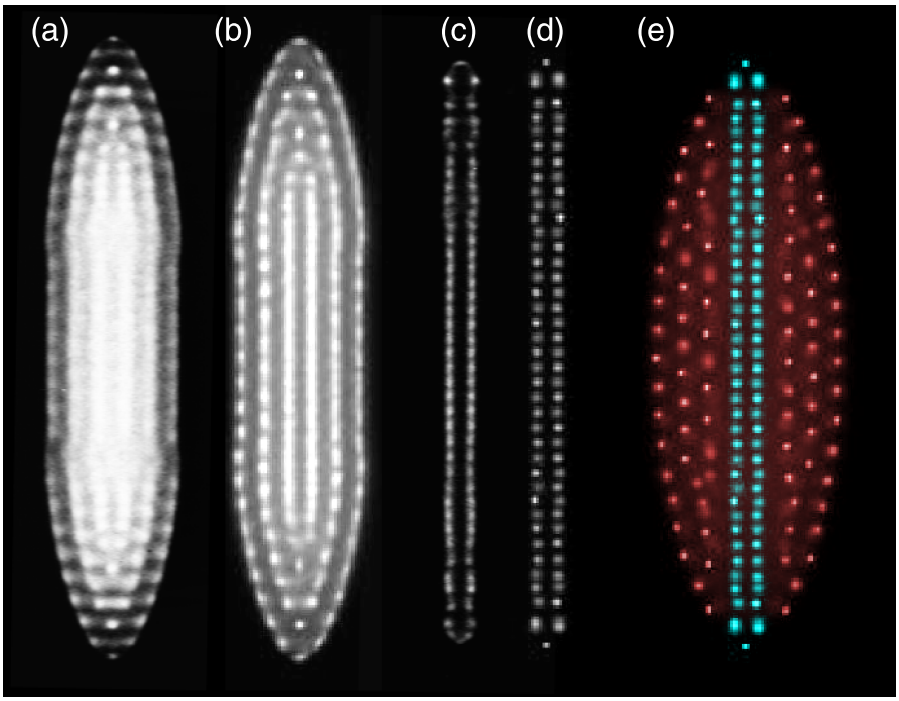


Figure 3.23: Comparison of experimental and simulated images illustrating that a large fraction of sympathetically-cooled molecular ions may be supported by relatively few laser-cooled ions. (b) shows a simulation of experimental image (a) with 550 $Ca^+$ ions and 75 sympathetically-cooled $CaF^+$ ions generated through reaction of $Ca^+$ with $CH_3F$. Admission of $CH_3F$ is continued until almost all $Ca^+$ ions have reacted. (d) shows a simulation of experimental image (c) with 80 $Ca^+$ and 545 sympathetically-cooled $CaF^+$ ions. (e) shows the same simulation as (d), but the non-fluorescing $CaF^+$ ions have been made visible and colourised red, with $Ca^+$ in blue.

Simulations have indicated that the sympathetic-cooling of dark ions results in only a very slight increase in the overall secular temperature of the crystal, with a relatively small sensitivity to the actual composition. Simulations of $Ca^+/CaF^+$ bi-component crystals show an increase of ∼5 mK in $T_{sec}$ as the fraction of $Ca^+$ ions is the crystal is decreased from around 1 to 0.3 [171]. Simulations by the Schiller group place an upper limit on the secular temperature of lighter or heavier dark molecular ions (relative to the laser-cooled species) of ∼+20 mK. Lighter

sympathetically-cooled ions will of course radially displace heavier laser-cooled ions from the trap axis, thereby causing their effective kinetic energy to increase due to the micromotion induced by the changing RF fields. Though the trap micromotion is perpendicular to the direction of the cooling lasers, small asymmetries in the trap potentials as well as the Coulomb interactions between multiple ions couple the radial and axial degrees of freedom, and could result in a reduced laser-cooling efficiency which in turn may be expected to contribute to an increased secular temperature. This appears to be practically negligible however, and for our purposes it is the total or effective kinetic energy that we are concerned with. It is also worth noting that the presence of a high enough fraction of lighter sympathetically-cooled ions will eventually push the $Ca^+$ ions outside of the cooling-laser beam waist!

The total kinetic energy of a multi-component crystal, much like that of a pure crystal, is again dominated by the RF-induced micromotion of its constituent ions. Thus in general, ion kinetic energy increases with radial displacement from the trap axis; however the magnitude of this increase is dependent on the mass/charge ratio, which governs the magnitude of the radial potential (see Fig. 3.24). Lighter or more highly charged species will experience larger accelerations on approach towards the RF electrodes and thus, at a given radial displacement, their effective kinetic energies will be greater than those for ions with a larger mass/charge ratio. Also, as ions are pushed further out radially they occupy larger concentric shells sizes and the number of ions supported in a crystal shell at a given radial displacement increases. This means that the average crystal effective energy increases more slowly with increasing numbers of ions, as further out in radius more and more ions will be required to move out to the next successive ion shell.

The value of a crystal's average effective kinetic energy can therefore be seen to reflect the balance of several contributing factors. Of importance are the total

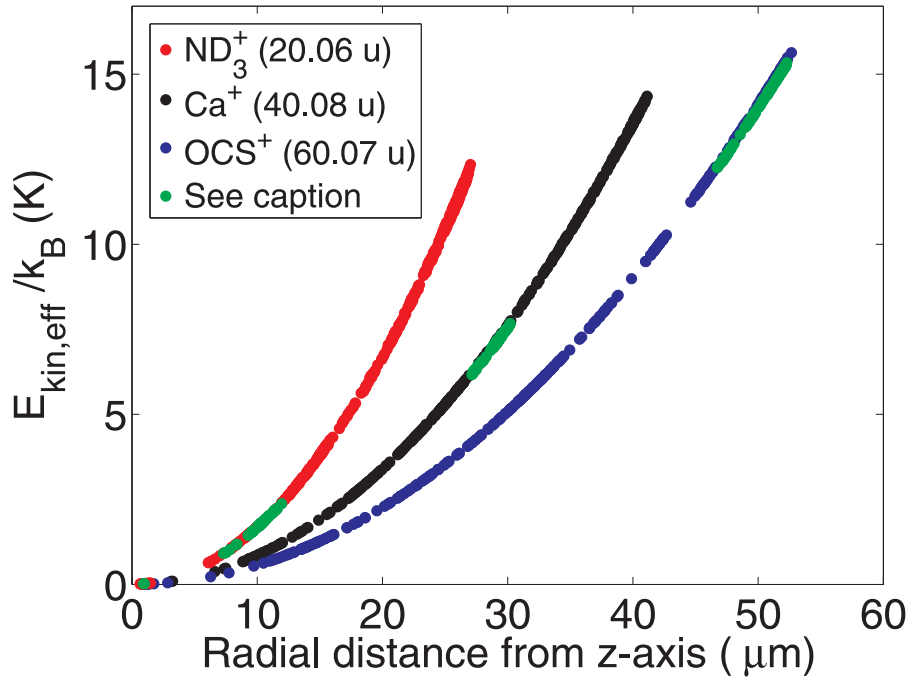


Figure 3.24: Illustration of the ion effective kinetic energy as a function of radial displacement from the $z$-axis, for different ion masses. This figure was generated from MD simulations of three 400-ion, singly charged ion, single component crystals, with masses as indicated (shown in red, black and blue). An additional multi-component simulation, shown in green, involves 133 $Ca^+$, 133 $OCS^+$ and 133 $ND_3^+$ ions respectively. The plot shows that each species within the multi-component crystal is separated radially, conforming to the radial positions and effective energies expected from the single species simulations (which are analogous to the effective trapping potential). At a given radius, heavier ions have a lower effective kinetic energy relative to lighter ions. Trapping voltages for all simulations were $V_{RF} = 180$ V, $U_{end} = 4$ V.

number of lighter or heavier (relative to the laser-cooled ions) sympathetically-cooled ions, the number of laser-cooled ions, the relative/absolute trapping voltages/frequencies (and also therefore shape and shell structure of the crystal) and the absolute mass/charge ratios of the constituent ions. For the 400–1000-ion prolate multi-component crystals (containing laser-cooled $Ca^+$ and sympathetically-cooled $ND_3^+$ and $OCS^+$ ions) used in the reaction studies presented in Chapter 7, typical ion effective kinetic energies were $E_{kin}/k_B \approx 10$ mK–25 K. Due to the radial separation and mass dependence illustrated by Fig. 3.24, the heavier

sympathetically-cooled ions ($OCS^+$) generally have the highest kinetic energies with $E_{kin}/k_B$ between 10 and 25 K, the lighter sympathetically-cooled ions ($ND_3^+$) have the lowest with $E_{kin}/k_B$ between 10 mK and 1 K, and the laser-cooled $Ca^+$ ions occupy the range of $E_{kin}/k_B \approx$ 10 mK–15 K. Simulations suggest that the variation of the composition of the crystal during a reaction (for example the loss of $OCS^+$ and formation of $ND_3^+$) would not be expected to cause a change in the average effective energy of the crystal or any fraction therein of more than 1–2 K in either case. Collision energy calculations are described in more detail in Chapter 4 and in particular Section 4.4.3.

# Chapter 4

# Reaction of Coulomb crystals with neutral molecules

In many ways the experimental work presented in this thesis represents a further step towards the goal of a fully controlled chemical reaction. From a research perspective, the ultimate idealised bimolecular chemical reaction would involve both reactants occupying well-defined quantum states before being brought together at a tunable (and preferably very low) collision energy. This would bypass the huge amount of averaging over thermal and quantum states that must be accounted for in the study of room temperature reactions, and provide a greater test of our understanding of the fundamental dynamics of chemical reactions. When the collision energy is low enough ($\lesssim$ mK) the size of the de Broglie wavelength can reach and exceed the range of the forces governing the interaction between the atoms or molecules, and quantum mechanical effects such as tunnelling and reactive resonances [73] are expected to dominate the reaction dynamics. This is one motivating factor for lowering the collision energies in reactive collision studies towards the $\mu$K regime.

This chapter describes how Coulomb crystals may be used as the source of reac-

tant ions in an ion-neutral reaction, at collision energies equivalent to both room temperature and as low as ∼1 K. The validity of this approach is discussed, as well as some of the benefits, especially in the low temperature regime. A brief outline of three systems for introducing a neutral molecular reaction partner to the crystal is given: the first involves neutral molecules at translational energies corresponding to room-temperature, whilst the latter two involve cold molecular sources. We characterise in detail the quadrupole guide velocity-selector, which was the source of translationally-cold molecules used in the studies presented in this thesis.

Using these different sources, new experimental methods for studying low collision energy ion-molecule reactions are detailed (as well as an existing method involving collision energies of around 300 K). The methods outlined here have allowed reactions such as that between $^{40}Ca^{+}$ and $CH_3F$, used as the example system throughout this chapter, to be studied for the first time at collision energies down to almost 1 K. These techniques form the foundation for further studies described in Chapters 6 and 7.

## 4.1 Coulomb crystals in the context of ion-molecule reactions

The characteristic spacing of the ions in a Coulomb crystal (10–25 $\mu$m) is large in comparison with the distance over which ion-molecule interactions become important (typically nanometer scale). This means that when a molecule approaches any given ion in a Coulomb crystal close enough to react with it, to a good approximation the presence of the other ions may be disregarded, and one can consider the encounter an isolated ion-molecule collision in the purest sense.

Coulomb crystals represent a source of translationally-cold and well-localised ions

that may be trapped for hours at a time, and imaged to single-particle resolution. As such they are ideally situated to provide the ions for low-temperature ion-molecule reactive collision studies, where long interaction times and high sensitivity are staunch requirements on account of the fact that most commonly available sources for translationally cold molecules generate very low number densities. For example, molecular densities downstream of the quadrupole guide velocity-selector are typically $10^5$–$10^6$ molecules cm$^{-3}$ (although the densities are higher within the guide), and for alternative sources rarely exceed $10^9$ molecules cm$^{-3}$. At these densities, reactive collisions may occur at rates as low as a few reactions per minute, and it can take anywhere from a minute to several hours total interaction time to react the majority of the ions in a crystal.

The depth of the trapping potential (see Table 2.2) is generally large relative to typical reaction exoergicities, leading to the retention of product ions in the trap and their sympathetic-cooling into the Coulomb crystal. The large sensitivity involved with the imaging of Coulomb crystals, confers a similar sensitivity to the study of ion-molecule reactions. For example, some of the work described in this thesis involves detection of a single reactive collision.

By way of contrast, an alternative source of cold ions for reaction studies would be buffer-gas cooled ions confined in an RF trap (see also Section 1.2.2). The application of RF quadrupole confinement to ions using a background of cold buffer gas was first demonstrated by Teloy and Gerlich [186]. Since then, the majority of work in this area has been performed at collisional temperatures between 10 and 300 K, a regime that is most relevant to processes naturally occurring in the high-atmosphere and space. In these experiments ion temperatures are limited by that of the buffer gas — use of a 22-pole trap and helium buffer gas allows molecular ions to be cooled to just a few Kelvin [55]. There is some confidence that this

method can be extended, with the use of a very slow beam of neutrals to study reactions at temperatures below 1 K [81].

Buffer gas cooling of molecular ions brings with it the benefit of thermalising the internal degrees of freedom as well, something which does not necessarily occur when molecular ions are sympathetically-cooled. However, the generation of internally cold or state-selected sympathetically-cooled molecular ions remains a possibility. For example, the use of appropriate photoionisation schemes such as REMPI should allow the generation of rovibrationally quantum-state-selected molecular ions. Once generated however, these state-selected molecular ions can undergo a re-thermalisation, for example blackbody radiation can drive the redistribution of rotational population in molecules that are polar or have IR active modes. These effects are likely to be mitigated through cryogenic cooling of the trap environment, and by use of non-polar molecular ions. In addition, as discussed in more detail in Section 1.3.1, schemes for optically-cooling the internal states of sympathetically-cooled molecular ions have been proposed [111, 112, 187], and are beginning to be demonstrated experimentally [107, 114]. These active cooling methods constantly drive the rotational population towards the ground rovibronic level, and are likely to be important in future state-selected reaction studies.

## 4.2 Molecular sources: Reaction partners for cold localised ion ensembles

### 4.2.1 Room-temperature background gas

The most general method for supplying a neutral molecular reactant for reaction with a Coulomb crystal is simply to admit a room-temperature sample of neutral gas at a controlled rate into the vacuum chamber containing the ion trap. Given

a constant pumping rate on the chamber by the rotary-backed turbomolecular pumps, a constant flow rate will result in a stable partial pressure of the gas in the chamber. Typically this is achieved through the use of an ultra-high vacuum leak valve, backed by a gas foreline which has been evacuated and then filled to approximately atmospheric pressure with the target gas.

Given a normal working pressure of $\leqslant 5\times10^{-10}$ mbar, the amount of gas leaked in must be carefully controlled in order not to raise the partial pressure of reactant gas too high. If this occurs, reaction of the ions will either proceed too quickly to be monitored successfully, or the increased collision rate will cause the crystal to melt. The leak valve used in our experiments (LVM940, Vacuum Generators) allows partial pressures as low as $1\times10^{-10}$ mbar to be achieved.

Although this method is completely general, it involves a room-temperature gas for which the kinetic energy and internal state distributions are characteristic of 300 K.

### 4.2.2 The quadrupole guide velocity-selector

The quadrupole guide velocity-selector, originally developed by Rempe and coworkers [46, 188], represents a continuous source of translationally cold (but often rotationally hot) polar molecules. Based on a bent electrostatic quadrupole, the bend in the guide accepts a constant flow of a room-temperature gas and selectively removes molecules travelling at a velocity above a certain threshold, while the slower moving molecules remain confined by the electrodes. Its effectiveness depends on the neutral molecule having an appreciable Stark effect, and it is therefore not completely general, although it is applicable to a fairly wide range of polar molecules. The guided molecules can have velocities as low as 20 m $s^{-1}$ corresponding to translational temperatures of around 1–5 K. Combining this neutral molecular source

with the Coulomb crystal apparatus provides the basis for our work on cold collisions. As such, we shall briefly review the principle of operation and construction of the guide in a little more detail, before the methods for determining the guided molecular flux, and characterising the velocity distribution of the guided molecules are described. The guide was developed by M. T. Bell within our group and more detail may be found in his D.Phil thesis [43].

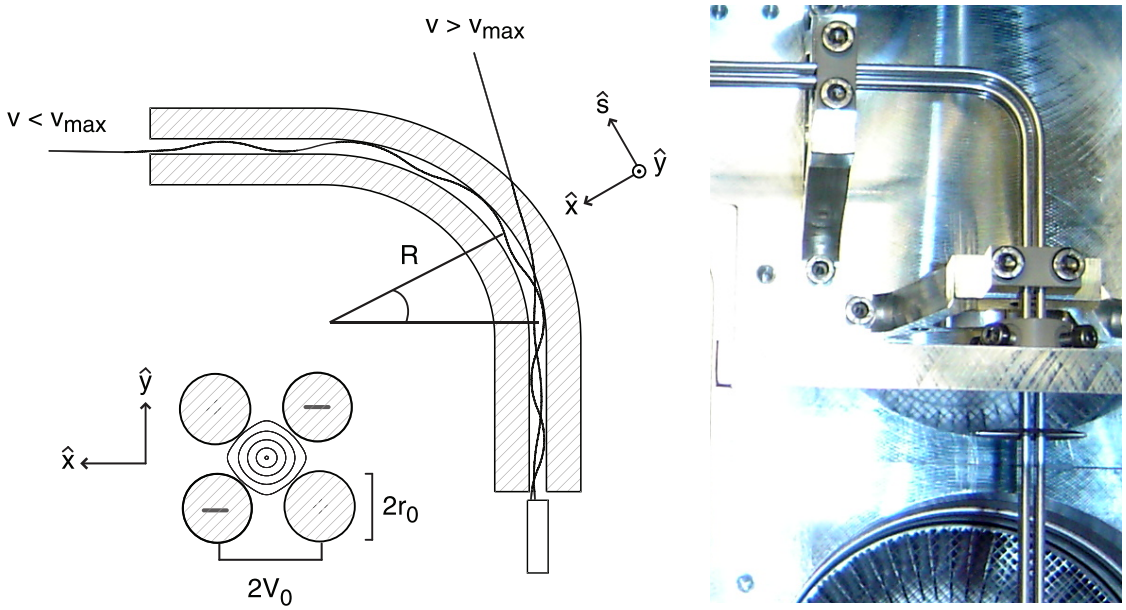


Figure 4.1: Left: an illustration of simulated neutral molecule trajectories within the guide for molecules above and below the kinetic energy threshold. Right: A photograph of the bend in the quadrupole guide, which is situated in the vacuum chamber. Adapted from [43].

The guide consists of a bent quadrupole design, with electrodes comprising polished circular stainless steel rods of 2 mm diameter, with a 1 mm separation between rods. The bend in the guide has a curvature of radius 12.5 mm, and the rods are mounted using MACOR spacers similar to those used in the linear Paul trap. Molecules are admitted to the guide through a capillary of internal diameter 1.2 mm which is mounted 1 mm in front of the quadrupole. The capillary is typically backed with a pressure of around $8\times10^{-2}$ mbar, provided via a needle valve connected to a room-

temperature reservoir of gas. The quadrupole guide electrodes are usually operated at static voltages of ±3–5 kV, resulting in electric fields at the electrode surfaces of up to 115 kV/cm, and initial conditioning is required to achieve these voltages [43]. The high-voltage power supplies that generate these electrode voltages are placed in series with ammeters and several large resistors. The ammeters allow any current flowing between electrodes to be monitored, whilst the resistors protect the electrodes/ammeters from any large currents that may flow in the event of insulator failure. Smaller "pre-breakdown" currents are sometimes observed and can be an indication of impending malfunction should they persist.

The guide spans three differential pumping stages each of which have their own turbomolecular pump; the first stage contains the effusive source and an initial straight section of the guide, and operates at a typical pressure of around $1\times10^{-6}$ mbar. The quadrupole bend is enclosed within a second stage which is maintained at around $2\times10^{-7}$ mbar; molecules exiting the guide at the bend fly directly into the turbomolecular pump mounted to this stage. The third stage contains the final straight guide section and typically operates at a pressure of approximately $1\times10^{-9}$ mbar.

The static voltages applied to the guide generate a large inhomogeneous electrostatic field, which is zero along the central axis of the guide and rises linearly towards the electrodes. Molecules leaving the capillary with sufficiently low transverse velocities, in low-field seeking states, will be confined inside the guide in this 2D trapping potential, and continue along the initial straight guide section. Given the nature of the room-temperature source, there will be a Maxwell-Boltzmann distribution of velocities in the sample, with a fraction of molecules already travelling at low velocities. These molecules are extracted by the bent section of the guide, which acts as a low-pass kinetic energy filter. Rather than cooling the molecules

directly, the bend simply transmits only the slower moving portion of this Maxwell-Boltzmann distribution. At the bend the guide turns ninety degrees, and in this section the effective confining potential is dependent on the tangential velocity of a given molecule. Fast moving molecules are not confined strongly enough and fly out of the side of the quadrupole, where they are pumped away. The slower moving molecules are successfully guided around the bend and down the final straight section of the guide before exiting. As the Stark shift is dependent on the rotational state of the molecule, there is a non-equilibrium distribution of rotational states in the sample of gas exiting the guide. However the rotational state distribution is still expected to broadly resemble that of room-temperature gas (this is supported by Monte-Carlo trajectory simulations [43, 189]) and the molecules are therefore still rotationally excited. Furthermore there is not a sharp cut-off of filtered velocities, and this reflects the quantum state dependence of the effective Stark potential depth in the bend section. As the guide voltages are increased in magnitude, theory predicts a quadratic increase in guided flux assuming a linear Stark shift over the relevant electric field strengths [43]. This is because a larger proportion of the Maxwell-Boltzmann distribution can be guided around the bend by applying higher guide voltages. Therefore, higher guide voltages mean not only an increase in flux, but a slightly hotter velocity distribution of the guided flux. For example, measurement of the molecular flux at guide voltages between 3 and 5 kV show that there is an increase of $\sim$0.6 K in the translational temperature of guided $CH_3F$.

For molecules in a single low-field seeking Stark state with a linear Stark shift, the following expression can be derived as an approximate upper bound for the guided

flux [43, 188]:

$$\begin{aligned} \phi_{\text{guide}} &\approx \phi_0 \tilde{v}_{\text{max}}^2 \tilde{v}_{\text{z,max}}^2 \\ &\approx \phi_0 \left(\frac{R}{2r_0}\right) \left(\frac{W_{\text{max}}}{k_{\text{B}}T}\right)^2, \end{aligned} \tag{4.1}$$

where $\tilde{v}_{\text{max}}$ and $\tilde{v}_{\text{z,max}}$ are the maximum transverse and longitudinal velocities that can be confined by the guide. The reduced velocity $\tilde{v} = v/v_w$, where $v_w = \sqrt{2k_{\text{B}}T/m}$ is the most probable velocity in the Maxwell-Boltzmann distribution. The guided flux thus depends on: $\phi_0$, the flux of molecules entering the guide from the source at temperature $T$; $R$, the radius of the bend; $r_0$, the radius of the quadrupole electrodes; and $W_{\text{max}}$, the depth of the confining potential in the straight sections. The fraction of molecules contained in the bend region is kinetic energy dependent and therefore mass independent for thermal samples, hence there is no explicit mass dependence in Eq. 4.1. However, in practice there is an inverse mass dependence associated with the flux entering the guide from the effusive source, $\phi_0$, and, to complicate matters, the atomic masses within the molecule also influence the rotational energy level spacings and the Stark energies. One can say that the total flux of molecules exiting the guide increases with the squared dipole moment, and that the highest transmitted flux is generally observed for light, strongly polar molecules.

### Determination of guided molecule number densities

In order to characterise the performance of the guide, a quadrupole mass spectrometer (Prisma QMS200, Pfeiffer) can be mounted at the exit of the guide. A grounded mesh (85% transmission) mounted at the end of the guide shields the QMS from the large electric fields generated by the quadrupole electrodes. Given the ultimate goal of guiding into the ion trap, the QMS is positioned such that its ionisation cage, or detection region, is coincident with the position that the centre

of the ion trap would occupy (for example see Section 4.4.1). The total length of the guide from entrance to this detection region is 811 mm.

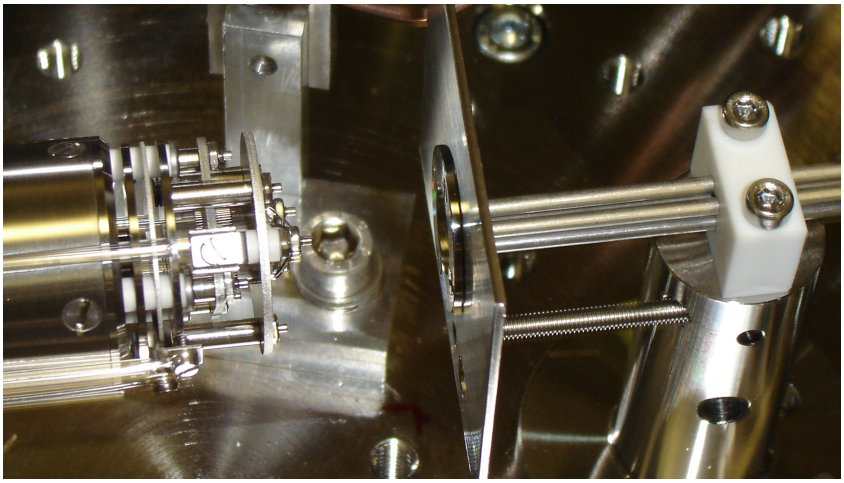

Figure 4.2: The ionisation cage of the residual gas analyser was placed in the position of the ion trap centre relative to the quadrupole guide, in order to measure guided flux and characterise velocity distributions.

This setup allows the QMS, once properly set for the desired mass peak, to register a current proportional to the molecular flux exiting the guide. These currents may be converted into a number density in the following way: The target gas is admitted into the chamber through the leak valve and the current response of the QMS is systematically measured against the gas partial pressure in the chamber. In conjunction with the use of appropriate gas-specific calibration factors for the hot cathode ionisation pressure gauge, this current response may be extrapolated to the low pressure regime (assuming a linear QMS response in this limit) in order to convert the channeltron-amplified current detected when using the quadrupole guide into a partial pressure. This pressure is converted to the number density of the guided molecules at the position of the detector.

This calibration procedure is performed for every reactant gas over a range of guiding voltages — typically in 0.5 kV steps from 0–5 kV. Previous experiments

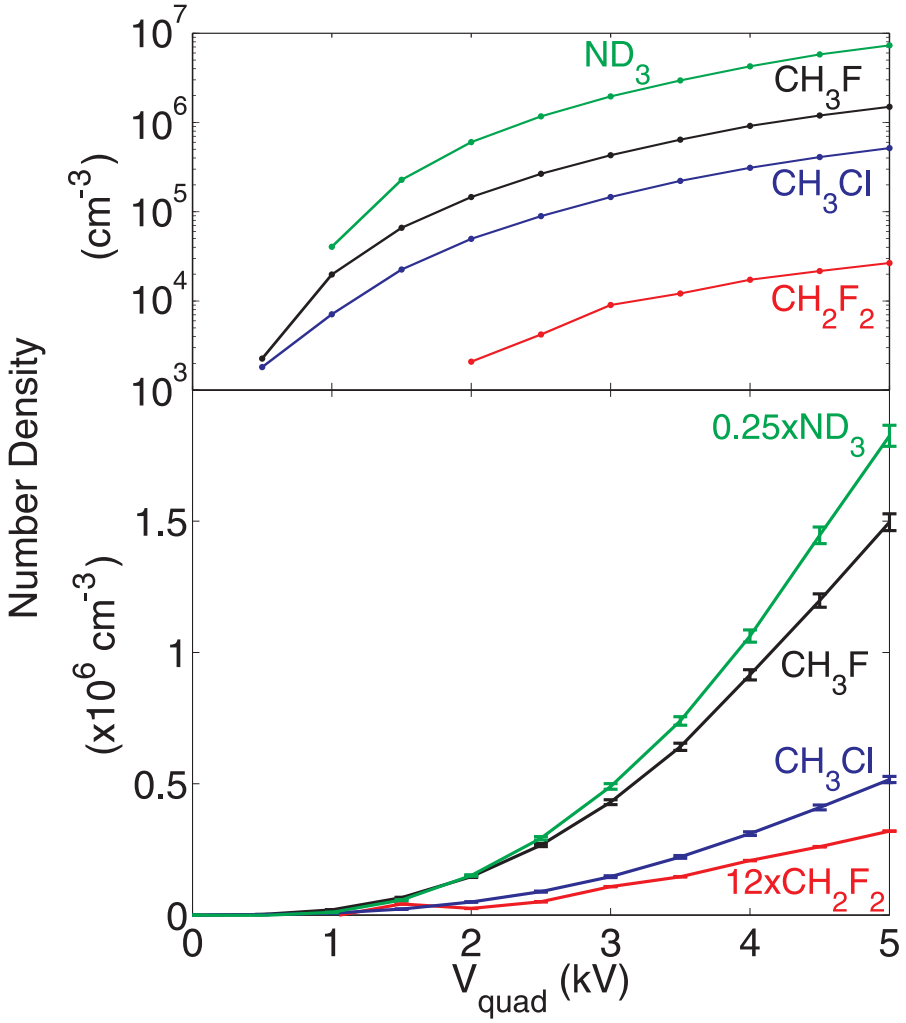


Figure 4.3: Calibration of number density against quadrupole guide voltage for the gases used in the reaction studies in Chapters 4, 6 and 7. All gases were admitted to the guide capillary at $P = 8 \times 10^{-2}$ mbar, except for $CH_2F_2$ for which $P = 0.1$ mbar. The upper panel shows the same data as the lower panel, but using a logarithmic scale.

[43] have determined that the optimal backing pressure for the guide capillary is approximately 0.08–0.1 mbar. Initially, as the source pressure rises, the capillary emits more gas into the guide and flux increases. Once the pressure becomes large enough however, collisions of the faster moving molecules with the slower moving molecules "boosts" the gas velocity distribution to higher energies, depleting the beam of molecules with low kinetic energies [43]. Number densities for the gases studied in this thesis are presented in Fig. 4.3. Note that, despite the very low flux

associated with $CH_2F_2$, reaction with $Ca^+$ could be clearly observed, reflecting the high sensitivity of this technique.

### Determination of velocity distributions

In order to determine the velocity or kinetic energy distribution of molecules exiting the quadrupole guide, the static voltage normally applied is changed to a pulsed voltage. This allows the distribution of arrival times for molecules travelling from the quadrupole entrance to the detector region to be measured. These distributions can then be processed to obtain the velocity or kinetic energy distributions.

The voltages applied to the guide are pulsed at high-frequency using fast high-voltage switches driven by a square-wave function at a frequency of 5–10 Hz. Initially, when the guide is off, no molecules are detected. When the guide is pulsed to high voltage, molecules begin to be guided, and the fastest moving molecules are incident in the QMS detection region first, followed by those moving more slowly. This results in a characteristic time-of-flight (TOF) profile which rises as the slower moving molecules arrive at the detector and levels out to a constant signal when the slowest moving molecules in the distribution have begun to arrive at the detector. The pulse frequency is set such that when the guide pulses off, there is enough time for the signal to drop to baseline again (as molecules are no longer guided around the bend) before the guide cycles on again. A typical TOF profile comprises an average of ∼2000–3000 such measurement cycles. Characteristic arrival times are around 20–50 ms; direct readout of the channeltron-amplified signal from the QMS is necessary for measurement at these timescales.

The velocity or kinetic energy distributions of the guided molecules may then be obtained by first fitting a smooth function* to the QMS signal data, $S(t)$.

*The data were found to be well modelled using a Gompertz function, $f(t) = e^{-e^{-k(t-t_c)}}$, where $k$ and $t_c$ are parameters determined by a non-linear least-squares fitting procedure.

The resulting function may then be processed in the following way [43]. The longitudinal velocity distributions are calculated from the time derivative of the fitted function, $S(t)$, using the transformation:

$$f(v)\mathrm{d}v \propto \frac{L}{v^2}\dot{S}(L/v)\mathrm{d}v, \tag{4.2}$$

where $L = 811$ mm is the path length, and $v = L/t$. The kinetic energy can be obtained from the velocity distribution via the additional transformation:

$$f(E)\mathrm{d}E \propto \frac{1}{\sqrt{2Em}}g(\sqrt{2E/m})\mathrm{d}v. \tag{4.3}$$

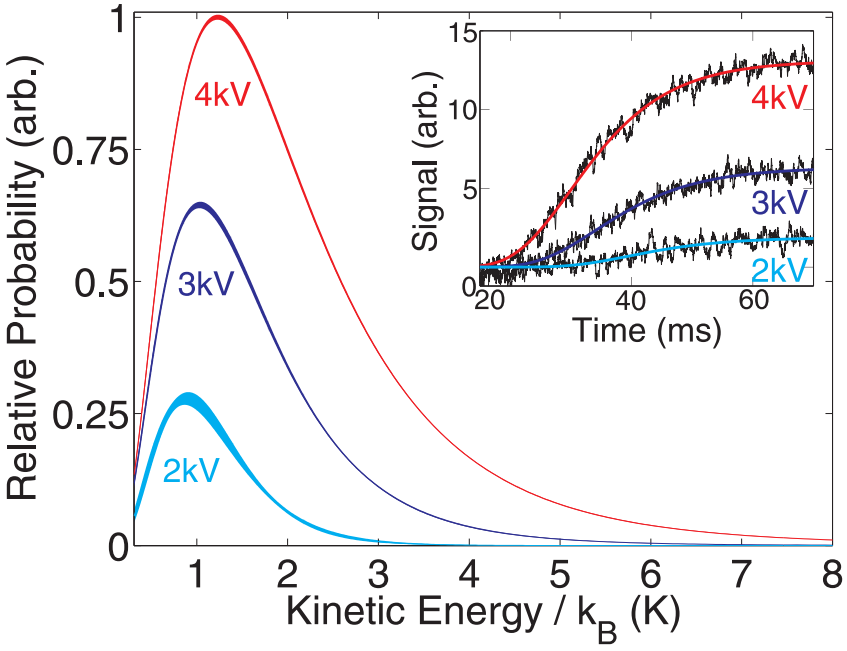


Figure 4.4: Translational energy distributions of guided $CH_3Cl$ at different values of guide voltage $V_{\mathrm{quad}}$. Uncertainty in the fitted parameters is reflected by the filled region defined by $\pm 2\sigma$ from the calculated values. Inset, typical time of flight profiles recorded directly from the channeltron on the residual gas analyser. These are fit with a Gompertz function which is transformed to obtain both velocity and energy distributions. The final uncertainty stems from the uncertainty in the fitting of the Gompertz function.

Kinetic energy distributions were generated for all of the species guided for the purpose of the reactions detailed in this thesis, and for a number of guide voltages.

TOF profiles are necessarily measured in the absence of the aforementioned ammeters/resistors and therefore were generally only measured up to a guide voltage of ±4 kV in order to avoid potential damage to the guide electrodes/insulators. Translational energy distributions measured for $CH_3F$ are shown in Fig. 4.5, whilst Fig. 4.4 shows those measured for $CH_3Cl$. Kinetic energy distributions for guided $ND_3$ may be found in publications resulting from the work herein [189], and are very similar in profile. In the case of $CH_2F_2$ the low signal levels precluded the extraction of the velocity distribution from the TOF profile. Given the similarity in translational energy between the other halomethane species, it is expected that $CH_2F_2$ is transmitted from the guide with similar kinetic energies. Heavier molecules still, such as $CH_3NO_2$ and $CH_3CHO$, have been shown to be guided with peak translational energies less than 5 K [43].

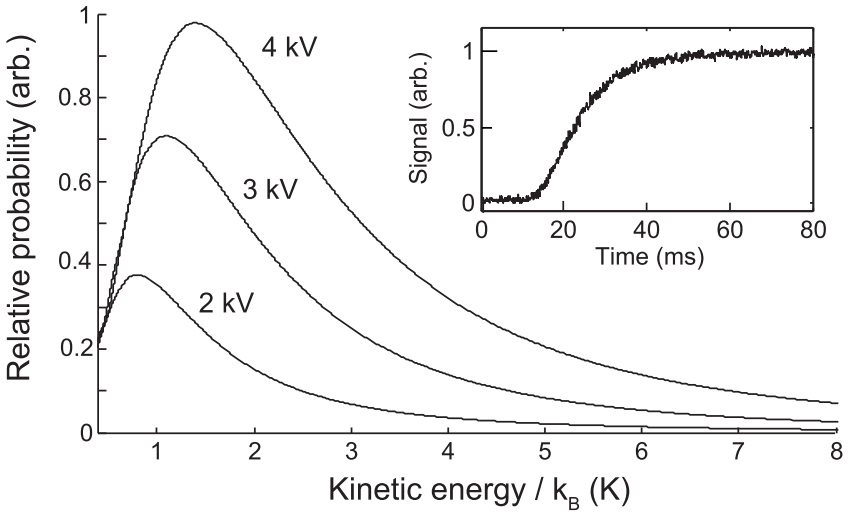


Figure 4.5: Velocity distributions of guided $CH_3F$ at different values of guide voltage $V_{\mathrm{quad}}$. Inset, a typical time of flight profile recorded with the residual gas analyser which can be processed to obtain the velocity distributions. Reproduced from Ref. [43].

Measured velocity distributions show that only very small numbers of molecules exit the guide with velocities lower than 20 m/s (for example in the case of $ND_3$). This is possibly attributable to fringe fields at the end of the electrodes accelerating

the outgoing molecules, as supported by trajectory simulations [43]. In theory this limits the production of molecules at translational temperatures much below 1 K. Lowest energy beams are obtained for light molecules, see for example $ND_3$ and $CH_3F$, which have peak kinetic energies[†] of 1.6 K and 1.8 K respectively when guided at ±4 kV. For heavier molecules the kinetic energies are larger, for example the peak energy for $CH_3NO_2$ is 3.8 K when guided at the same voltage [189].

### 4.2.3 The Stark decelerator

The Stark decelerator, which has been developed and first used successfully by the Meijer group [42], is another apparatus that exploits the Stark effect to produce cold neutral molecules. In contrast to the velocity-selector, the Stark decelerator actively slows a fraction of the target gas. Loaded via a supersonic expansion from a pulsed valve, the Stark decelerator relies on a number of consecutive electrode pair stages, to which high voltages are pulsed on and off in a complex computer-controlled sequence. Molecules in a particular low-field seeking state[‡] travelling towards an electrode stage at high voltage approach a region of high electric field and therefore experience a retarding force, losing translational energy as they climb the potential hill. Just before passing the region of highest field (and being accelerated) the voltages on the electrodes are switched such that the molecules are now in a region of low electric field, and heading towards the next electrode stage which is now at high voltage. This process repeats anew, with the switch timing compensated to account for the reduction in velocity of the molecules. In this way a packet of molecules can be decelerated to an arbitrary final velocity [190], or stopped completely [191].

[†]Here and elsewhere in this thesis, for convenience we often express kinetic energies in Kelvin, and this stems from equating the energy to $k_B T$ such that $T = E/k_B$.

[‡]High-field seeking states may be decelerated also, by turning a given stage to high-voltage once the molecules have just passed through, thereby pulling them backward and slowing them in this manner. However this is generally a more problematic approach (see Ref. [55]).

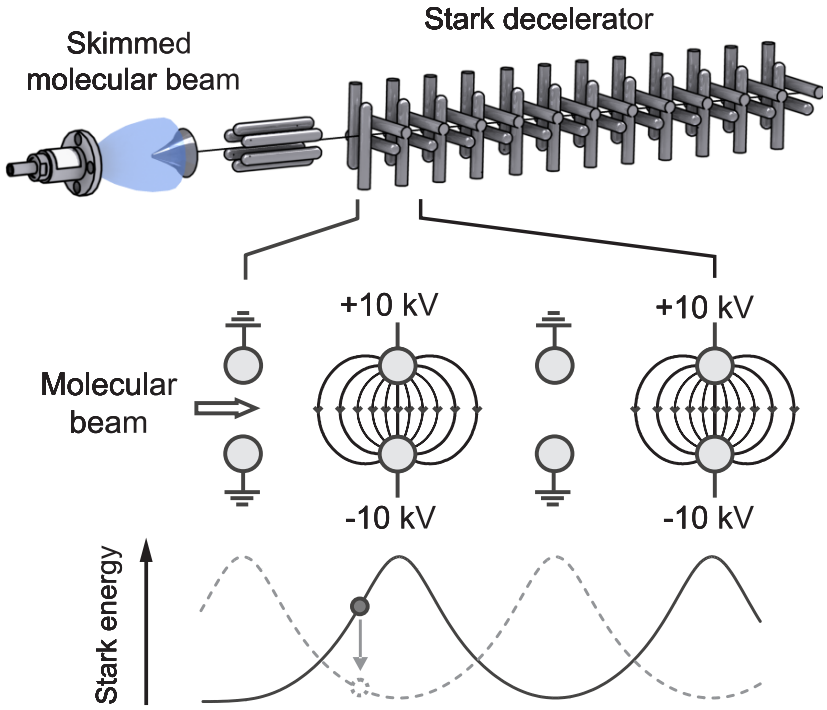


Figure 4.6: Illustration of the Stark decelerator, reproduced from Ref. [43].

Number densities of molecules leaving the decelerator, focused at the position of a Coulomb crystal near the end of the decelerator, could in theory reach $10^8$–$10^9$ molecules cm$^{-3}$. However, the decelerator is operated at 10 Hz, and reactive collision frequencies are expected to be similar to the case of the continuous velocity-selector as the average flux is comparable. Also, the final laboratory frame kinetic energies achievable through the use of the decelerator are comparable to those of the velocity-selector given that we must transmit the molecules to the ion trap[§]. The Stark decelerator offers considerable advantages over the velocity-selector for the study of chemical reactions: The final velocities of the molecules are more easily tunable, and the energy resolution is much improved over that of the velocity-selector owing to the narrower velocity distribution of the decelerated

[§]Meijer and coworkers have demonstrated that a decelerated sample can subsequently be electrostatically trapped at mK temperatures, for example OH radicals have been trapped at 50–500 mK [191]. The combination of methods for trapping neutral molecules with those for trapping ions may allow smaller collision energies to be studied, but this is expected to be challenging.

molecules. Collision energy resolution of the order of 100 mK has been predicted for the reaction of $Ca^+$ with $CH_3F$ molecules decelerated in the $|J, MK\rangle = |1, -1\rangle$ state [43], whereas collision energy resolution in a velocity-selector based experiment is typically of the order of ∼5–20 K. Also, due to the initial supersonic expansion, the molecules loaded into the decelerator are rotationally cold, and furthermore the Stark deceleration process itself is quantum state-selective. Therefore the Stark decelerator, in conjunction with a quantum state-selected Coulomb crystal could provide full control over a chemical reaction.

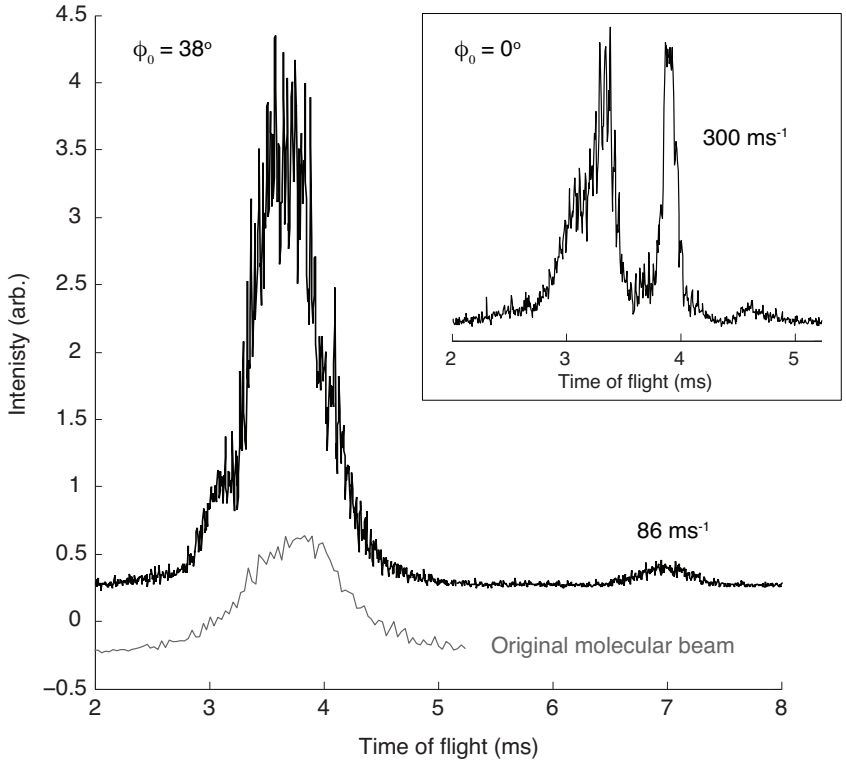


Figure 4.7: A time of flight spectrum illustrating the Stark deceleration of $ND_3$ from 300 m/s to 86 m/s [192], given a phase angle of 38°. The phase angle $\Phi$ parameterises the extent to which molecules are decelerated. Inset, a zero phase angle does not result in deceleration, but bunches the molecules into packets.

Recent results from the Stark decelerator developed in our group, shown in Fig. 4.7, demonstrate the deceleration of $ND_3$ molecules which have been seeded in xenon and cryogenically-cooled in the pulsed valve. This reduces the average velocity of

the molecular beam entering the decelerator to 300 m/s. Work on combining the Stark decelerator with our Coulomb crystal apparatus is under way at the time of writing. The current goal is to use a solenoid based shutter to block the carrier gas and admit only the decelerated molecular packets to the ion crystal. As the Stark decelerator was not used for any of the experimental work described in this thesis, further elaboration is omitted. More information can be found regarding the Stark decelerator in Refs [43, 55].

## 4.3 Performing a room-temperature ion-molecule reaction: $Ca^+ + CH_3F$

### 4.3.1 Experimental Procedure

The experimental apparatus for performing these reactions does not differ from that for generating Coulomb crystals, and is therefore the same as illustrated in Fig. 3.1.

For room-temperature reactions, the reactant gas is admitted to the chamber through a leak valve. In working with our particular leak valve (LVM940, Vacuum Generators) it was discovered that some of the gas passing through the valve may become trapped, or possibly condensed on the inner faces of the valve. In practice this means that even if the foreline gas is purged and swapped, a certain proportion of the previous gas leaked through the valve will remain, and purging of the valve must be performed to ensure that the newly admitted gas is pure and not an ill-defined mixture. In practice this is achieved by using the QMS to measure a mass spectrum of the chamber background during the leaking of the target gas. In the event that the mass spectrum contains mass peaks corresponding to the previous gas, the target gas is leaked at partial pressures of up to $1\times10^{-6}$ mbar

until the undesired mass peaks have disappeared and the admitted gas is pure. This typically takes 5–10 minutes when changing reactant gases, and a return to baseline chamber pressures of $\leqslant 5\times10^{-10}$ mbar can take a couple of hours in this instance (though use of the titanium sublimation pump can help).

Having ensured that a pure gas can be admitted, a crystal is loaded and centred in the trap as described in Section 3.3.2. Laser detunings may be measured/set according to the method outlined in Section 6.2.1 (these steps will in future be assumed implicit when it is stated that a crystal is loaded). MATLAB scripts are used to process the intensified video signal from the camera system in real time. In this manner the video signal may be averaged over a number of frames (typically 100–200 frames) in order to compile an experimental image of the crystal fluorescence at a given time. To conduct the reaction experiment, the leak valve is opened carefully until the ionisation pressure gauge reads a specified constant pressure above the baseline. In general, room-temperature reactions are carried out at partial pressures of $5\times10^{-10}$–$1\times10^{-9}$ mbar. At these pressures, total reaction of a crystal (assuming the gas is reactive) is usually complete within 1–5 minutes.

The progress of the reaction is monitored by recording experimental images of the ion fluorescence at a sequence of times during the reaction. Reactions with an ion product heavier than $^{40}Ca^{+}$ result in a flattening of the radial edges of the crystal as outer $^{40}Ca^{+}$ ions are replaced by the heavier dark product ions, which are sympathetically-cooled around the central $^{40}Ca^{+}$ core (see Sections 2.2.2 and 3.4.2 and also Fig. 4.11). Given that the crystal has been centred prior to reaction, the 2D projection of the ion fluorescence which constitutes the experimental image should be symmetrical. In practice, small manual tweaks to the static voltage offsets (see Section 3.3.2) may be required to maintain this cylindrical symmetry, which is desirable for more accurate measurements of the $^{40}Ca^{+}$ core volume.

Under ideal vacuum chamber conditions the background loss rate of $^{40}Ca^+$ ions from the crystal is negligible. However a small loss rate is sometimes observable, owing to reaction with low concentrations of background gases[¶]. In general, during any set of reaction rate measurements frequent measurements of the background loss rate are required. These loss rate measurements are performed in an identical manner to those described above, except that no gas is admitted through the leak valve. Owing to the low loss rate it can sometimes take an hour or more to observe a clear change in the crystal, nevertheless these background loss rates are factored out of the final reaction rates in all cases (as described in the following section).

### 4.3.2 Determination of rate constant

The rate of the reaction $Ca^+ + CH_3F \rightarrow CaF^+ + CH_3$ can be expressed in the context of this experiment as

$$-\frac{\mathrm{d}n_{\mathrm{Ca}^+}}{\mathrm{d}t} = k_2\ n_{\mathrm{Ca}^+}\ n_{\mathrm{CH_3F}}, \tag{4.4}$$

where the bi-molecular rate constant $k_2$ is sometimes referred to as $k_{\mathrm{bi}}$, $n_{\mathrm{Ca}^+}$ is the number density of $Ca^+$ ions in the crystal and $n_{\mathrm{CH_3F}}$ is the number density of $CH_3F$ molecules. Given the assumption of constant ion density (see Section 2.4.1), we may treat the volume of the $^{40}Ca^+$ portion of the crystal as proportional to the average number density of $^{40}Ca^+$ ions (averaged over the whole crystal), allowing us to write

$$\frac{\mathrm{d}V_{\mathrm{Ca}^+}(t)}{\mathrm{d}t} = -k_2\ V_{\mathrm{Ca}^+}(t)\ n_{\mathrm{CH_3F}}. \tag{4.5}$$

Furthermore, the number density of the guided molecular flux at the crystal remains constant on account of the continuous nature of the flux passing through the crystal from the guide. Therefore the rate law can be expressed in terms of the

[¶]Single ion mass spectrometry measurements, as described in Chapter 5, have shown that background reaction product ions include $CaOH^+$, suggesting a reaction of $Ca^+$ with $H_2O$.

pseudo-first-order rate constant, $k_1 = k_2 n_{CH_3F}$, and integrated to obtain:

$$V_{Ca^+}(t) = V_{Ca^+}(0)\ e^{-k_1 t}. \tag{4.6}$$

Values for the volume of the $^{40}Ca^+$ fraction of the crystal are obtained for each image in a reaction sequence by analysis with a custom MATLAB script (outlined separately in Appendix E). A plot of $\ln[V_{Ca^+}(t)/V_{Ca^+}(0)]$ as a function of $t$ will have a gradient equal to $-k_1 = -k_2 n_{CH_3F}$. This pseudo-first-order rate constant $k_1$ represents the total ion loss rate, and should have any background loss rate subtracted from it to obtain the pseudo-first-order rate constant for the reaction itself. The bimolecular rate constant can then be recovered, given knowledge of the fluoromethane number density, $n_{CH_3F}$.

The number density of the molecular reactant is obtained during the experiment by carefully monitoring the pressure reading of the hot-cathode ionisation gauge whilst the gas is admitted through the leak valve. This pressure is baseline subtracted and processed with gas-specific ionisation gauge calibration factors (see Table 4.5) in order to obtain the final value of $n_{CH_3F}$ for the given reaction.

### 4.3.3 Collision energy distribution

The collision energy distribution in reactions of trapped cold ions with room-temperature neutral gases is dominated by the kinetic energy distribution of the neutral gas. Given an ionic reactant, A, and room-temperature neutral reactant, B, we assume that the ion is at rest such that the average collision energy

$$\langle E_{coll} \rangle = \frac{1}{2}\mu \langle v_{coll}^2 \rangle = \frac{1}{2}\mu \langle v_B^2 \rangle, \tag{4.7}$$

where $\mu$ is the reduced mass of the collision complex, $\langle v_{coll}^2 \rangle$ is the average relative collision velocity and $\langle v_B^2 \rangle$ is the average velocity of reactant B. Given that

$$\left\langle \frac{1}{2} m v^2 \right\rangle = \frac{3}{2} k_B T, \tag{4.8}$$

we substitute for $\langle v_{\mathrm{B}}^2 \rangle$ and obtain:

$$\langle E_{\mathrm{coll}} \rangle = \frac{3m_{\mathrm{A}}}{2m_{\mathrm{A}}m_{\mathrm{B}}} k_{\mathrm{B}} T. \tag{4.9}$$

Table 4.1 lists average collision energies, calculated using this treatment and assuming $T = 300$ K, for the room-temperature reactions presented in this work.

| Reaction | $\langle E_{\mathrm{coll}} \rangle / k_{\mathrm{B}}$ (K) |
|---|---|
| $^{40}Ca^+ + CH_3F$ | 243 |
| $^{40}Ca^+ + CH_2F_2$ | 196 |
| $^{40}Ca^+ + CH_3Cl$ | 199 |
| $OCS^+ + ND_3$ | 337 |

Table 4.1: Average collision energies for the reaction of selected laser- or sympathetically-cooled ions with selected room-temperature neutral reactants.

## 4.4 Performing a low-temperature velocity-selected ion-molecule reaction: $Ca^+ + CH_3F$

### 4.4.1 Experimental Procedure

In order to study this reaction at low collision energies we have, for the first time, joined together an apparatus for generating Coulomb crystals with the quadrupole guide velocity-selector detailed in Section 4.2.2. The experimental setup is illustrated in Fig. 4.8.

When using the velocity-selector in conjunction with the ion trap, a fourth differential pumping stage separation is fitted between the ion trap chamber and the adjoining guide section. The guide extends through into the main UHV chamber, and the tip rests 19–20 mm from the centre of the trap (the experiments reported

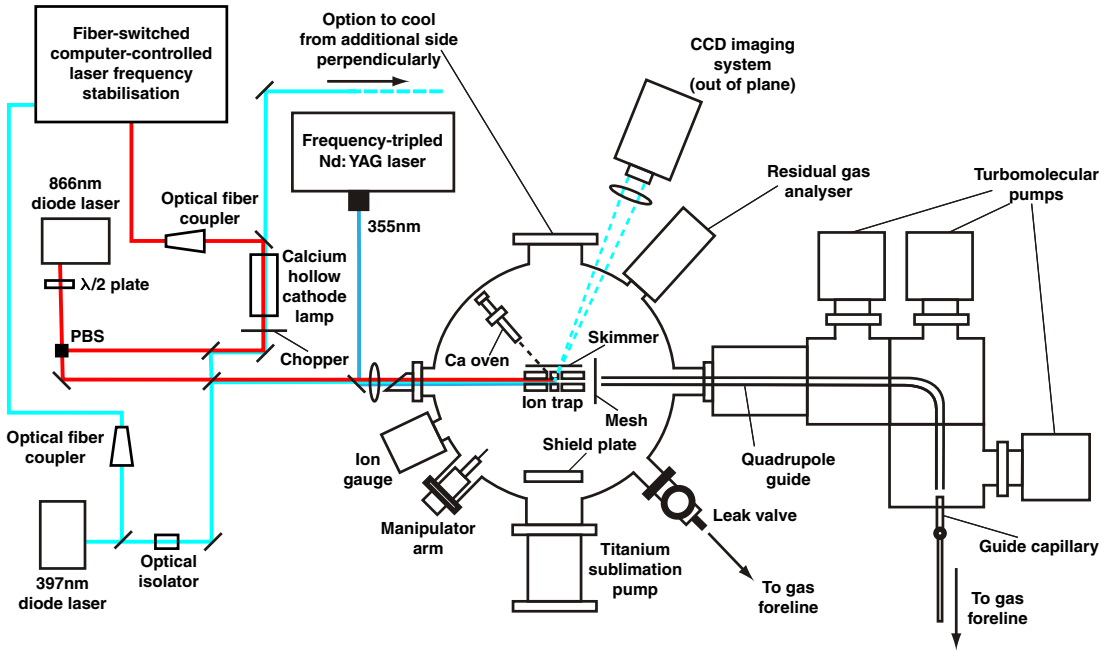


Figure 4.8: Schematic of the experimental apparatus for performing low-temperature ion-molecule reactions with the quadrupole guide velocity-selector.

here used the three-segment asymmetric trap in a bid to maximise guided flux at the centre of the ion trap). In order to shield the ion trap from the large electric fields associated with the guide, a grounded mesh (85% transmission) is mounted on a steel plate between the end of the guide and the ion trap.

Reactions are performed by first loading and preparing a suitable Coulomb crystal in the normal manner. The gas reservoir which feeds the guide capillary is purged and filled with the desired gas, and the needle valve is opened such that the pressure in the foreline behind the capillary is stable at $\sim 8 \times 10^{-2}$ mbar, which is generally optimal for guiding efficiency [43]. At this point, the guide voltages are turned on to the desired setting, and molecules begin to be guided towards the crystal. A timer is started and, as for the room-temperature reactions, a regular sequence of fluorescence images are collected to record the extent of reaction with time. During the reaction, the ammeters which measure current between the guide electrodes are monitored closely for any large current spikes. These can indicate discharges

across the high voltage electrodes, which may produce decreased guide performance temporarily[‖].

In general, the guiding of molecules results in smaller number densities at the position of the ion trap than leaking gases at low pressure, and reactive collisions occur less frequently as a result. The full extent of reaction (*i.e.*, from a pure crystal to the crystal melting on account of almost complete reaction of the laser-cooled ions) for the reactions considered here can be achieved in anywhere between 5 and 95 minutes. The reaction time depends on the reactivity of the gas and the quadrupole guide voltage (with 3–5 kV being the commonly used range, and higher voltages producing larger number densities of neutral reactant).

### 4.4.2 Determination of rate constant

Determination of the rate constant of a low temperature guided reaction occurs as for the room-temperature case (Section 4.3.2), with the exception of the determination of the molecular reactant number density at the crystal. Number densities of the guided molecules are determined from the QMS measurements with a calibration performed separately for given guide voltage/gas combinations (as detailed in Section 4.2.2). It should be noted that background loss rates are more important in the case of low-temperature reactions, where the timescales for collisions are much longer, particularly with less reactive gases.

### 4.4.3 Collision energy distribution

The distribution of collision energies in the combined ion trap, quadrupole guide apparatus is a convolution of the translational energy distribution of the guided

[‖]Large constant currents usually indicate a more permanent breakdown of the insulators, and in this case guide performance is degraded or interrupted completely (necessitating a replacement of the insulators).

molecules and that of the ions comprising the crystal. As such, this distribution can be controlled to a certain degree by adjusting the mean kinetic energies of the molecules being guided, or by changing the effective kinetic energy distribution of the ions in the crystal.

The translational energy distribution of the guided molecules, and therefore the mean kinetic energy may be tuned via the quadrupole guide electrode voltages. As mentioned in Section 4.2.2, a larger voltage implies that a larger fraction of the room-temperature Maxwell-Boltzmann distribution of initial velocities can be successfully guided around the quadrupole bend. This means an increase in mean velocity (and guided flux) for larger guide voltages, as observed in the velocity distributions shown in Section 4.2.2. Additionally, the average kinetic energy of the ions comprising the Coulomb crystal is dependent on the trapping voltages, crystal size, and cooling parameters (see Sections 3.3.1, 2.3.1, and particularly Fig. 3.16), and may be determined via a comparison of the experimental fluorescence with detailed MD simulations (see Section 3.1.2, [166]). The mean effective kinetic energy of the ions generally used in these experiments ranges from $\langle E_{\mathrm{kin,eff}}\rangle/k_{\mathrm{B}} \approx$ 400 mK to 3.5 K.

The collision energy is dependent on the relative velocity of the reactants according to $E_{\mathrm{coll}} = \frac{1}{2}\mu_r v_{\mathrm{rel}}^2$ where $\mu_r$ is the reduced mass and $v_{\mathrm{rel}}$ is defined according to

$$v_{\mathrm{rel}}^2 = v_{\mathrm{Ca^+}}^2 + v_{\mathrm{CH_3F}}^2 - 2\mathbf{v}_{\mathrm{CH_3F}}.\,\mathbf{v}_{\mathrm{Ca^+}} \approx v_{\mathrm{Ca^+}}^2 + v_{\mathrm{CH_3F}}^2. \tag{4.10}$$

The above approximation is due to the fact that the dominant contribution to the ion energy is the micromotion which occurs radially and therefore perpendicular to the guided molecule approach vector, which is oriented axially in the experimental geometry. Figure 4.9 contains collision energy distributions obtained by convolution of the guided-molecule kinetic energy distributions with those for $^{40}Ca^+$ ions obtained from MD simulations. Collision energy distributions are coldest ($\sim$1 K)

for reactions involving linear strings of ions, and increase in energy as the number of ion shells grows or the crystals become more oblate. Oscillations in the distribution simply reflect the shell structure of larger crystals.

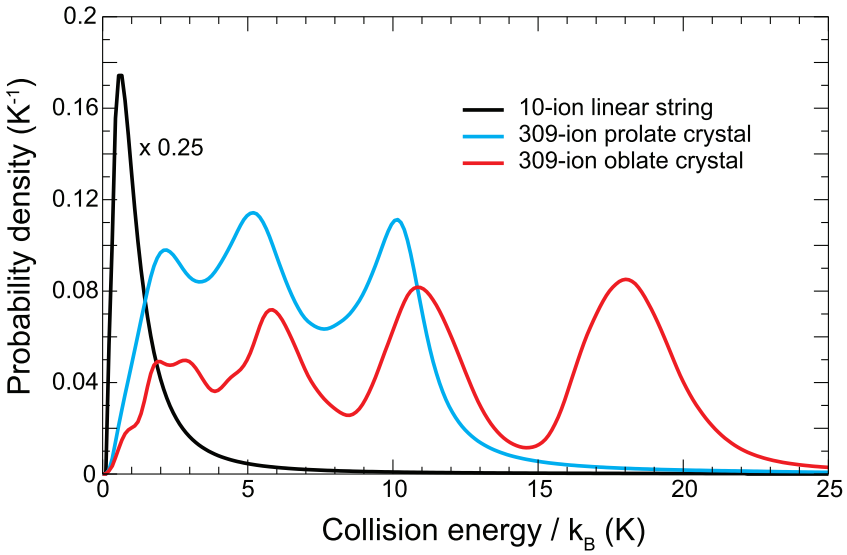


Figure 4.9: Collision energy distributions for guided $CH_3F$ reactions involving a $Ca^+$ string, and 309-ion prolate and oblate crystals. These distributions are calculated via convolution of the guided molecule and ion energy distributions, obtained by experimental measurement and MD simulations respectively. The oscillations in the crystal distributions reflect the concentric shell structures of the spheroidal crystals.

For guide voltages of between 3 and 5 kV, the average collision energy has been calculated to increase by approximately 0.6 K for a typical reaction system, *e.g.*, $Ca^+ + CH_3F$ [131], however this change is somewhat insignificant given the width of the collision energy distribution (see Fig. 4.9). Larger variations in collision energy are accessible by performing reactions with crystals ranging in aspect ratio from strongly prolate to strongly oblate. For a 900-ion crystal undergoing such a transformation, the ion average kinetic energy can increase by the order of 10–20 K [189], leading to similar changes in the average collision energy. However, for $Ca^+ + CH_3F$, collision energy changes of this magnitude do not appear to produce large differences in the reaction rate: In either case, as described in the following section,

only a very slight inverse dependence on the average collision energy is suggested by experiment, with experimental uncertainty preventing the resolution of any clear trend over these collision energy ranges. Note also the clearly non-Maxwell-Boltzmann distributions in Fig. 4.9 — one must remain mindful that when we talk of a collisional or an effective kinetic temperature, we are simply referring to $E/k_{\mathrm{B}}$ for convenience.

## 4.5 Experimental results

A number of initial experiments were carried out using the reaction:

$$\mathrm{Ca}^{+} + \mathrm{CH_3F} \rightarrow \mathrm{CaF}^{+} + \mathrm{CH_3} \tag{4.11}$$

as the test system for this new technique. This reaction is strongly exothermic with a total energy release (for $\mathrm{Ca}^{+}$ in the ground state) of approximately 1.05 eV, which is lower than the minimum trap depth of ∼1.2 eV. In fact, the mass ratio of the products is such that, by conservation of momentum, only 20% of this energy can be partitioned to the kinetic energy of the $\mathrm{CaF}^{+}$ product ions. These ions are thus trapped and sympathetically-cooled post-reaction.

The stochastic nature of a single reaction event is illustrated by Fig. 4.10, which shows the reaction of a small 17-ion crystal. The reaction can be followed by eye, as each single reactive collision results in the disappearance of one of the fluorescence spots corresponding to a single $\mathrm{Ca}^{+}$ atom. With small numbers of ions, such as this, many repetitions of the experiment would be necessary to calculate the rate constant for the reaction. Smaller crystals are nevertheless good candidates for resonant-excitation mass spectrometry, which yields additional proof of sympathetically-cooled product ions, and ultimately information regarding product mass. We have used this technique to support all of our reaction studies and this is detailed separately in Chapter 5.

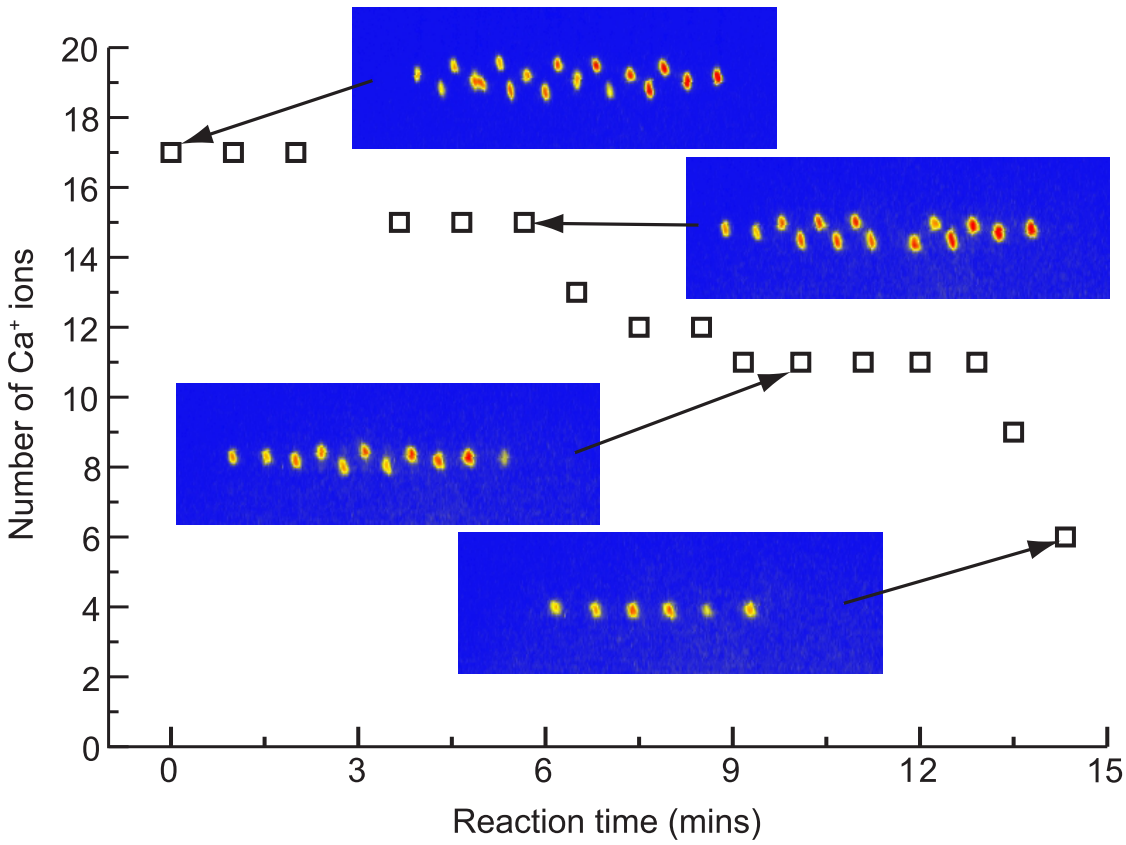


Figure 4.10: Reaction of a 17-ion $Ca^+$ Coulomb crystal with $CH_3F$. The progress of reaction for smaller crystals can be followed with single-particle sensitivity by monitoring the stochastic disappearance of single $Ca^+$ ions from the crystal.

Reaction of a larger prolate $Ca^+$ crystal with $CH_3F$ is illustrated by Fig. 4.11 which shows a log plot of the decreasing core volume over the course of the reaction. The gradient of this plot is equal in magnitude to the pseudo-first order rate constant, and a knowledge of the $CH_3F$ number density at the crystal allows recovery of $k_2$ for both room-temperature and guided low-temperature reactions. Although the reaction of a single ion is a stochastic event, in the case of the larger crystals a continuous loss rate can be assumed and the rate constant is therefore obtainable from a single experiment. Early values for the bimolecular rate constants were determined to be $k_2 = 4.2(4) \times 10^{-10}$ cm$^3$s$^{-1}$ for reactions at $\langle E_{\rm coll}\rangle/k_{\rm B} = 243$ K (room-temperature gas admitted through the leak valve), and $k_2 = 1.3(6) \times 10^{-9}$ cm$^3$s$^{-1}$ for guided reactions at $V_{\rm quad} = \pm 3.0$ kV where the average collision energy corre-

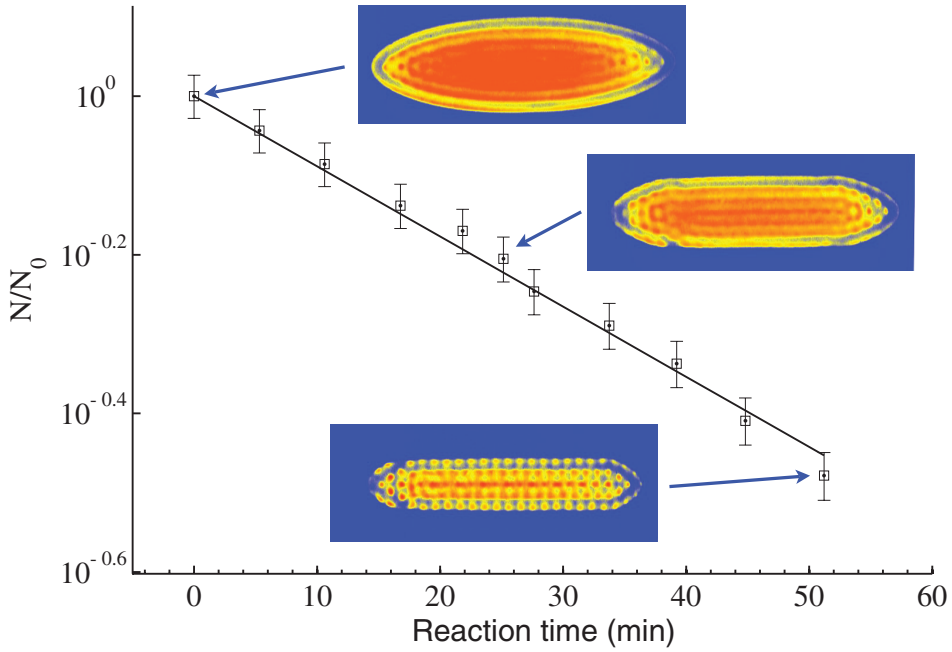


Figure 4.11: Log plot of the $Ca^+$ core volume, $V/V_0 \approx N/N_0$, against reaction time, using data obtained from the reaction of $Ca^+$ with $CH_3F$. Note the flattening of the outside of the core due to Coulomb repulsion with the surrounding sympathetically-cooled product ions.

sponds to a temperature of approximately 2.6 K, and the rotational temperature of the neutral molecules was still effectively 300 K [43].

Variation of the rate constant with collision energy (at low energies) was probed initially via a systematic change in the guide voltages, and subsequently by varying the aspect ratio of the crystal to access a larger temperature range. Variation of $V_{\text{quad}}$ was performed between ±3–5 kV, corresponding to a change in average collision energy, $\langle E_{\text{coll}} \rangle / k_{\text{B}}$, from 2.6 to 3.2 K. The resulting relative values of for $k_2$ show a slight inverse dependence on collision energy, which is expected in the context of ion-molecule adiabatic capture theories. A wider temperature range was probed by varying the aspect ratio of larger Coulomb crystals from prolate to

oblate, thereby increasing the ion average effective kinetic energy. This resulted in average collision energies of $\langle E_{\rm coll}\rangle/k_{\rm B} = 14$ K and 29 K for the prolate and oblate crystals respectively. Again there appears to be an inverse dependence of the rate on collision energy, as shown in the lower panel of Fig. 4.12; however for both of these studies the dependence is weak, and therefore somewhat contentious as the rate constants mostly agree within the bounds of experimental error.

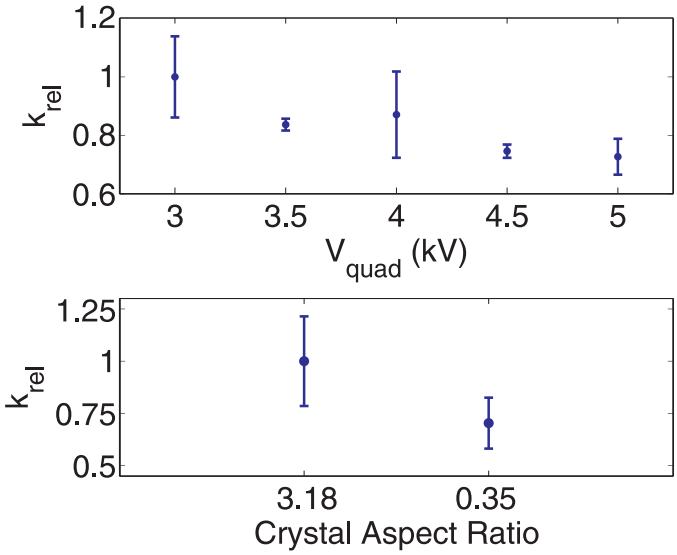


Figure 4.12: Normalised rate constants as a function of both $V_{\rm quad}$ where $k_{\rm rel} = k_2/k_2(V_{\rm quad} = \pm 3.0$ kV), and the crystal aspect ratio, $\alpha$, where $k_{\rm rel} = k_2/k_2(\alpha = 3.18)$. Error bars in both plots reflect the $1\sigma$ uncertainty in the 3–4 measurements performed for each data point. In these reactions, the 866 nm and 397 nm laser detunings were as follows: $\Delta_{866} \approx 0$ MHz in all measurements, and $\Delta_{397} = 20$ MHz and 28.5 Mhz for measurements in the top and bottom plots respectively.

The experimental error in the calculation of these rate constants predominantly reflects the uncertainty in determining the number density of $CH_3F$ molecules at the crystal, particularly in the case of the low-temperature reactions. For some gases, gas sensitivity factors for use with the hot-cathode ionisation pressure gauge were unavailable, and a close match was assumed with a similar species. The gas calibration factors, $C_{\rm gas}$, used for all reactants referenced within this thesis are listed in Table 4.5. These factors, obtained from the literature (see [193, 194]

and references therein), are defined according to $P_{\text{eff}} = P_{\text{meas}}/C_{\text{gas}}$ where $P_{\text{meas}}$ is the partial pressure recorded using our particular pressure gauge (Leybold Ionivac ITR90). These factors are known to vary significantly between different seemingly identical gauges. A variation of up to 20% is entirely possible [193], and therefore uncertainty in the true partial pressures of these gases represents a considerable portion of the error in an absolute rate constant value.

| Reactant gas | $C_{\text{gas}}$ used | Substituted gas (if any) |
|---|---|---|
| $CH_3F$ | 1.8 | $CH_3OH$ |
| $CH_2F_2$ | 2.0 | $CH_3OH$* |
| $CH_3Cl$ | 3.1 | |
| $ND_3$ | 1.23 | $NH_3$ |

Table 4.2: Gas calibration factors used in number density calculations.
*The value for $CH_2F_2$ was arrived at by modification of the value for $CH_3OH$ to account for the addition of another heteroatom. This was performed through comparison to similar transformations between compounds whose factors are available in the literature.

To summarise, this chapter has demonstrated the feasibility of using the combined ion trap/velocity-selector apparatus for the study of low collision energy ion-molecule reactions. Single-ion sensitivity has been demonstrated in the example reaction of a 17-ion crystal**. Reactions have been demonstrated with larger crystals, from which we have obtained rate constants at both room-temperature and low-temperature collision energies. We have investigated the collision energy dependence of the rate constant by varying both the guide voltage, and the average kinetic energy of the ions (via a change in crystal aspect ratio), finding a suggestion of a weak dependence in both cases. Rate constants determined for the $Ca^+ + CH_3F$ reaction were later found to depend on both the laser detunings and

**A similar 15-ion reaction appears in Chapter 5, where the sympathetic-cooling of heavier product ions is confirmed using *in situ* mass spectrometry techniques. An extension of these techniques, described in the same chapter, has also allowed the identification of the product ion mass using just a pair of $Ca^+$ ions and a single reaction event.

powers, and therefore on the fraction of excited state population in the $^{40}Ca^{+}$ ions. Further investigation of these effects in this system, and in the reactions of $^{40}Ca^{+}$ with other molecules, is detailed separately in Chapter 6. Therefore, discussion of the absolute or relative values of these measured rate constants in the context of theoretical models is delayed until the latter part of that chapter.

# Chapter 5

# Identification of product ions via in situ resonance-excitation mass spectrometry

A necessary tool in the study of any reaction is the ability to detect the reaction products. To this end, detection techniques such as laser-induced fluorescence (LIF) are commonly used when large enough product densities are generated. However, fluorescence detection on specific molecular lines is not sufficiently sensitive to detect just a few molecular ions. Other detection methods such as resonantly-enhanced multi-photon ionisation (REMPI) and time-of-flight mass spectrometry are more sensitive and more generally applicable, but destroy the sample being measured. The charged nature of the product ions generated in ion-molecule reactions proves to be a useful property however, as it can be exploited to both detect these ions with high sensitivity, and to determine their mass/charge ratios.

This chapter deals with techniques for using the linear Paul trap itself to perform mass spectrometry on ions trapped *in situ* in a non-destructive manner. These methods can be used to identify the mass/charge ratio of product ions that are gen-

erated in ion-molecule reactions carried out within the trap, and sympathetically-cooled into the Coulomb crystal. After a brief discussion of the general theory, there is a description of the experimental procedure, followed by a discussion of results from work done primarily in support of the reaction studies presented in this thesis.

## 5.1 Principle

The general principle of using the LPT to perform *in situ* mass spectrometry is that a time-varying force may be applied to the ions in order to excite a collective oscillatory motional mode within the trapping potential [106, 195] (usually the axial centre-of-mass vibration). The resonant frequencies of these modes are dependent on the mass/charge ratios of the constituent ions, and measurements of the former may be exploited to obtain the latter. A time-varying force may be provided either by the use of additional RF electric fields [196], or by modulation of the laser-cooling forces [104] (this can be achieved by chopping the cooling lasers themselves). Of the many advantages inherent to this technique, not least is the fact that it is non-destructive. Thus, it can be used to identify the constituents of a crystal as a function of time, making it a useful technique for reaction studies such as those of sympathetically-cooled $H_2^+ + H_2$ [126], or for the characterisation of each step in a sequence of chemical changes, *e.g.*, pathways for consecutive photodissociations [105].

In our work we have chosen to apply an additional RF voltage to one set of end-caps of the LPT as detailed in Fig. 5.1. Here, the time-varying drive voltage may be expressed as $V_{\text{drive}} = V_{\text{drive},0}\cos(\Omega_{\text{drive}}t)$, and we are able to scan the frequency, $\Omega_{\text{drive}}/2\pi$, over the range 30–400 kHz. When the drive frequency approaches a vibrational mode of the crystal the ions will begin to oscillate axially. The am-

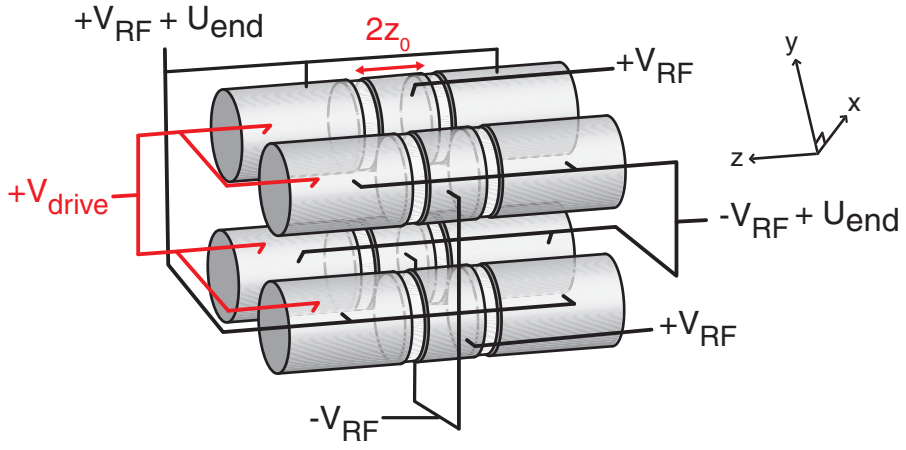


Figure 5.1: The voltage configuration used in our experiments for exciting axial vibrational modes via additional RF electric fields. The oscillating RF drive voltage $V_{\text{drive}}$ is applied to one set of end-caps.

plitude of this oscillation increases to a maximum as the drive frequency reaches the centre of the resonance, before falling as the frequency moves away. This is observed experimentally as an axial "smearing out" of the ion fluorescence, often accompanied by a change in fluorescence intensity. This former observation occurs as a consequence of the ion oscillation period being small relative to the exposure time associated with the time-averaged imaging of the fluorescence. The oscillatory ion motion leads to an associated Doppler shift of the cooling-laser frequencies which increases towards the resonance, and this can result in an increase or decrease in fluorescence intensity depending on the laser detunings and the amplitude of the drive voltage. If $V_{\text{drive},0}$ is large enough, this Doppler shift can cause a complete loss of fluorescence and melt the crystal. When oscillatory modes of dark sympathetically-cooled ions are excited, the Coulomb interaction ensures the simultaneous oscillation of the laser-cooled ions and a change in fluorescence is still observed. The change in fluorescence is strongest during direct motional excitation of the laser-cooled ions, but modes due to darker non-fluorescing ions are nevertheless clearly visible given the strong Coulomb interaction between the two sets of ions. In general, heavier or less highly charged ions are slower to respond to

the changing fields and their motional modes tend towards lower frequencies, and vice-versa.

## 5.2 Early experimental results

Initial experiments in our laboratory involving *in situ* mass spectrometry focused on providing additional evidence for the presence of sympathetically-cooled product ions in larger crystals, and attempts to measure the masses of these product ions [131]. In larger crystals accurate mass determination is made very difficult by the space-charge interactions between the many ions in the ensemble. This space-charge drag can shift and broaden vibrational resonances and hamper any kind of simple quantitative treatment. The best results were therefore seen for smaller crystals.

Figure 5.2 illustrates results obtained from the reaction of a 15-ion $Ca^+$ crystal with translationally-cold $CH_3F$ (see Chapter 4). In this figure, panel (a) corresponds to the fluorescence image produced by the initially pure $Ca^+$ crystal, and panel (b) is the result after 80 minutes of exposure to velocity-selected $CH_3F$. The quadrupole guide voltage was $V_{\mathrm{quad}} = \pm 2.0$ kV which corresponds to guided molecule translational energies of $\langle E_{\mathrm{kin}} \rangle / k_{\mathrm{B}} = 2.0$ K. The average effective kinetic energy of the 15-ion crystal was determined by simulation to be $\langle E_{\mathrm{kin,eff}} \rangle / k_{\mathrm{B}} \approx 450$ mK. Convolution of the reactant kinetic energy distributions allows us to determine an average collision energy of $\langle E_{\mathrm{coll}} \rangle / k_{\mathrm{B}} = 1.3$ K for the reaction. Over time, a decrease in the number of fluorescence spots was observed, and this was attributed to reactive collisions with the velocity-selected $CH_3F$ molecules*. As discussed in Section 4.5, the

*A control experiment, in which the flow of cold neutrals was switched off, showed a loss of only two ions from a similarly sized crystal over the same period of time. This was attributed to reactive collisions with background gas molecules. The importance of trap-loss processes stemming from elastic collisions was studied by exposing the crystal to $5{\times}10^{-9}$ mbar of non-reactive $ND_3$. The loss rates were found to be negligible in this case.

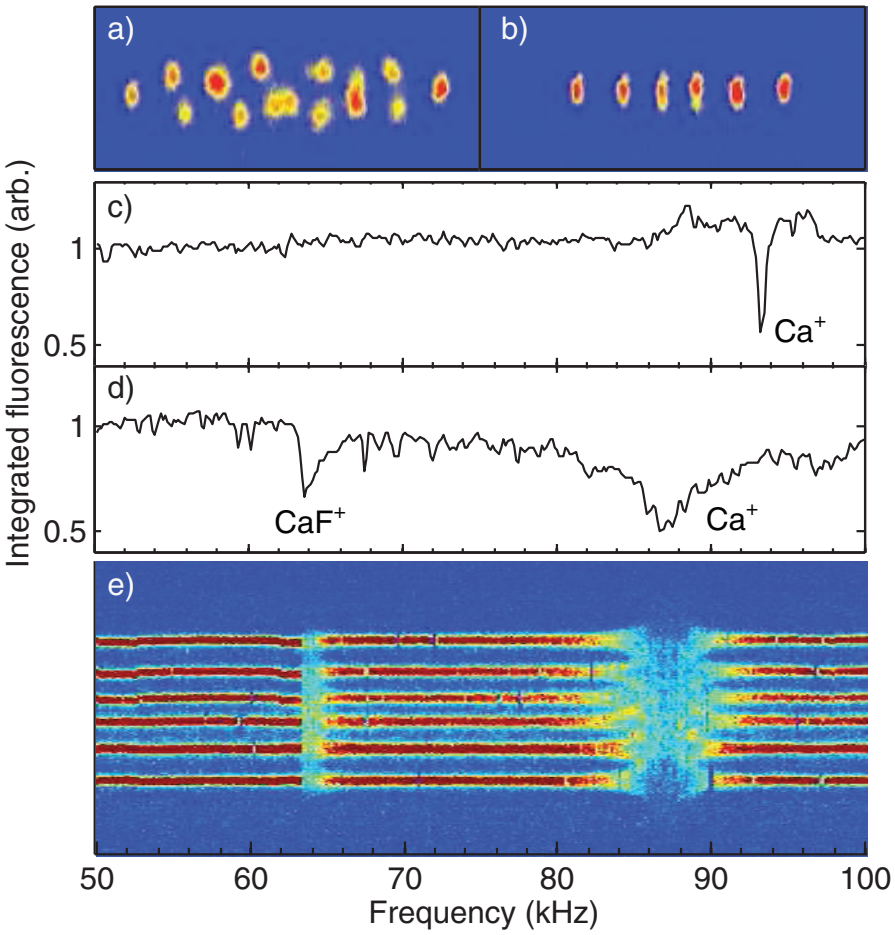


Figure 5.2: False-colour fluorescence images of a small 15-ion $Ca^+$ Coulomb crystal (a) before and (b) after the chemical reaction with velocity-selected $CH_3F$ molecules. (c),(d) Resonant-excitation mass spectra of the Coulomb crystals in (a) and (b), measured by monitoring the integrated fluorescence of the $Ca^+$ ions as a function of the RF drive frequency. The decrease of the $Ca^+$ fluorescence at the position of the resonances in (d) is caused by a reversible melting of the crystal as can be seen in (e), which shows the sequence of fluorescence images of the crystal in (b) (rotated by 90°) recorded during the mass scan.

non-fluorescing product ions are retained in the trap and sympathetically-cooled into the crystal. This means that, post-reaction, we assume that nine dark $CaF^+$ ions surround the six visible $Ca^+$ ions in Fig. 5.2(b). Resonant-excitation mass spectra were recorded before and after the reaction, as illustrated by Fig. 5.2(c) and (d) respectively. These spectra were performed at $V_{\text{drive}} = 3$ mV, and involved monitoring the total integrated fluorescence signal as a function of drive frequency.

Before the reaction, a single sharp peak is observed at 93.5 kHz corresponding to the excitation of the motional resonance (centre of mass vibrational mode with all $Ca^+$ moving in phase[†]) of the $Ca^+$ ions in the pure crystal. Post-reaction however, two features are observed; these are attributed to the excitation of $CaF^+$ and $Ca^+$. The higher-frequency peak associated with the lighter $Ca^+$ ions is broadened and shifted to lower frequency (with respect to the single-species spectrum) as a consequence of the space-charge drag of the different ion species — this is indicative of the close packing of the ions in a bi-component crystal [195].

These results offer conclusive proof that reactive collisions between cold ions and neutral molecules occur inside the trap, and that at least some of the product ions are retained in the crystal via sympathetic-cooling. It also indicates that the product ions are heavier than $Ca^+$, as a consequence of their lower vibrational mode frequency (along with the observation that the lighter $Ca^+$ ions remain on axis). We have described how the best results are seen in spectra involving smaller crystals, where the spectral broadening due to space-charge interactions between multiple ions is reduced. Taking this idea to its logical conclusion, it has been shown that in a two-ion bi-component system these contributions are minimised, and more quantitative determination of product ion masses may be achieved [104].

## 5.3 Single ion mass spectrometry

Drewsen and coworkers were the first to develop the mass spectrometry of a single sympathetically-cooled ion [104]. They have demonstrated the effectiveness of the technique by characterising the photodissociation/isomerization pathway of a

[†]The centre of mass mode of a pure crystal is effectively $\omega_z$, the axial trap frequency — see Eqs. 2.17 and 2.18.

single complex molecular ion (aniline) [105]

$$C_6H_5NH_2^+ \xrightarrow{h\nu} C_5H_6^+ \xrightarrow{h\nu} C_5H_5^+ \xrightarrow{h\nu} c\text{-}C_3H_3^+ \tag{5.1}$$

with a mass resolution of $\Delta m/m \approx 10^{-4}$. Whilst this mass resolution is far from that of the best mass spectrometry methods, which can reach relative mass resolutions of $\leqslant 10^{-11}$ [197, 198], it is perfectly adequate for the purposes of reaction studies, allowing the clear differentiation between isotopic species with a high degree of convenience in the current context. With optimisation the technique is expected to be able to achieve a mass resolution of $\Delta m/m \approx 10^{-5}$–$10^{-6}$ [199].

For the harmonic potential at the centre of the LPT, it can be shown that [104, 200], close to their equilibrium positions, the two eigenfrequencies for the axial motion of two equally-charged ions are given by:

$$\nu_\pm^2 = \left((1+\xi) \pm \sqrt{1-\xi+\xi^2}\right)\nu_1^2. \tag{5.2}$$

In this expression, $\xi = m_1/m_2$ where $m_1$ and $m_2$ are the masses of the two ions and $\nu_1$ is the oscillation frequency of a single ion with mass $m_1$. The centre-of-mass mode frequency is labelled $\nu_-$ and the frequency of the breathing mode $\nu_+$. If $\nu_1$ is determined using an ion of known mass $m_1$, the mass of a second sympathetically-cooled ion $m_2$ can be deduced from measurement of $\nu_-$ or $\nu_+$. Importantly, the centre-of-mass mode frequency for a pure crystal (of two ions for example) is identical to that of a single ion. Given that two equally-charged ions have equilibrium positions that are independent of their masses, it is therefore possible to measure $\nu_1$ (with two laser-cooled ions) and $\nu_\pm$ (with one laser-cooled and one sympathetically-cooled ion) with both sets of ions in the same trap positions. This minimises systematic error stemming from slight anharmonicities or spatial variations in the effective trap potential, and furthermore speeds up the overall process of calibrating $\nu_1$, performing a reaction and then measuring $\nu_\pm$. This has

been found to be invaluable, as any fluctuation in the damping from laser-cooling, or the trapping fields (either from a variation in electrode voltages or due to patch potentials) can cause a shift in the mode frequencies, and result in increased error in the calculated product mass.

Less ambiguous assignment of the resonant frequency is possible through use of in-phase detection of the ion fluorescence in conjunction with modulation of the axial radiation pressure forces [104]. In this scheme, the imaging system is set to only record data at the turning point of the ion oscillations, and this is achieved by gating the camera intensifier with an RF voltage synchronous with the modulation of the laser. The modulation of the axial radiation pressure is achievable either by computer-controlled oscillation of the detuning, or more commonly by directing one beam through an electro-optical chopper [104]; in either case this reduces the optical damping of the ion motion, which serves to narrow the vibrational resonances. When an ion is only imaged at the turning point of its oscillation it can be seen to become progressively more offset (axially) as it approaches the resonance and its oscillation amplitude is increasing. When it passes the resonance it undergoes a $\pi$ phase shift and appears on the other side of its equilibrium position before slowly returning there as the amplitude of the oscillation decreases. This can often afford greater precision in the measurement of the resonance position in comparison to the non-gated case. Typically for these experiments, the cooling lasers are directed from more than one side (usually three sides) due to the reduced efficiency of single-sided cooling with very small ion numbers (where there is reduced coupling of the translational degrees of freedom due to a decrease in the number of space-charge interactions). The higher resolution afforded by this technique can be used to differentiate between equally charged atomic or molecular ions with the same total nucleon number [104]. It should be noted that the use of oscillating RF fields to provide the time-varying force on the ions limits any possible motional

excitation to that of the centre-of-mass mode $\nu_-$, necessitating calibration of $\nu_1$ for the determination of $m_2$. In contrast, electro-optical modulation can excite both the centre of mass mode, $\nu_-$, and the breathing mode, $\nu_+$, and in this case calibration of $\nu_1$ is not necessary for the determination of $m_2$.

## 5.4 Experimental procedures

In general, we have attempted two distinct types of experiment relating to this technique, and in both cases we induce an excitation of the centre of mass mode $\nu_-$ with an additional RF voltage $V_{\text{drive}}$ as outlined earlier. We rely mainly on an in-phase detection scheme and therefore gate our imaging system with an RF voltage synchronous with the oscillation of $V_{\text{drive}}$, phase matched in order that the ions are imaged at the turning point of their oscillation (as described above). The first reaction types studied involved direct reaction of $Ca^+$ and were done mostly in support of the reactions under study in Chapter 6. The second type was the reaction of a single sympathetically-cooled molecular ion in the presence of a single laser-cooled $Ca^+$ ion. This was attempted in support of work in Chapter 7.

In order to perform direct reactions, we first load two $Ca^+$ ions into the trap according to the procedure outlined in Section 3.2.2. Once the ions have been loaded, the trapping voltages remain unchanged in order to prevent a shift in the vibrational mode frequencies. In order to determine $\nu_1$ we then perform a mass scan, and this measurement is typically repeated 3–4 times. In general the applied drive voltage amplitude for our single ion studies is of the order of 0.1 mV, and we can scan over a range of 30–400 kHz. Once the approximate location of the resonance has been determined, a higher resolution scan is performed. This higher resolution scan usually spans 4 kHz and is roughly centred on the resonance, with 5–15 frames averaged per frequency step at a resolution of 0.05–0.1 kHz; such

a scan usually takes of the order of 1 minute to complete. Typically the video sequences recorded during these scans are used in the analysis (described below), via compilation into plots of axial intensity slices as a function of drive frequency, similar to Fig. 5.2(e). The drive amplitude is normally varied somewhat in order to yield the clearest scan in this regard.

The reaction of one of the two $Ca^+$ ions is then attempted, either via introduction of a neutral room temperature gas through the leak valve (at partial pressures of $10^{-9}$–$10^{-8}$ mbar depending on reactivity), or via the guiding of neutral molecules with the velocity-selector. Reaction of a single ion is signified by the disappearance of one of the observed fluorescence spots, whilst the other remains in position at the same lattice site. From this we infer that the second lattice site remains occupied, but with a dark ion. On occasion, one of the ions is lost from the trap and, in this case, the single remaining ion occupies an equilibrium position in the middle of the original two, at the trap centre. The presence of a dark ion is further verified by the frequent interchange of the ions between the two lattice sites, which can be observed as the bright ion jumping back and forth on the screen. This process tends to occur once every few seconds or so, and is often driven in the approach to an axial vibrational resonance. This can make a clean in-phase scan profile difficult to achieve, as often the ion will flip position near the resonance (see Fig. 5.4). As long as this does not happen too often, a clear fit can still be achieved and the resonant frequency clearly identified. However if the amplitude is too large a loss of efficient cooling can melt the crystal and cause difficulties therein. Once the reaction of a single $Ca^+$ ion has been observed, a second set of mass scans is initiated immediately in order to determine $\nu_-$, and these are performed as before.

Analysis of the axial intensity versus drive frequency plots then involves overlaying and fitting an analytic expression for the resonance profile to the pre- and post-

reaction scans. The dispersion profile resulting from the in-phase detection is modelled according to the following expression for the ion's axial offset $z_{\text{ion}}$ [104]:

$$z_{\text{ion}} = -\frac{a_z(\nu_{\text{drive}} - \nu_-)}{(\nu_{\text{drive}} - \nu_-)^2 + \gamma_z^2} + z_{\text{ion,0}}. \tag{5.3}$$

Here, $a_z$ is the amplitude of the dispersion, $\nu_{\text{drive}}$ is the drive frequency, $z_{\text{ion,0}}$ is the ion's $z$ offset in the absence of $V_{\text{drive}}$ and $\gamma_z$ relates to the width of the dispersion. At this stage, measurements of $\nu_1$ and $\nu_-$ have been achieved and, armed with a knowledge of $m_1$, the mass of the bright $Ca^+$ ion, we can use equation 5.2 to calculate $m_2$.

In contrast to direct reactions of laser-cooled ions, the attempt to monitor the reaction of a sympathetically-cooled molecular ion (*e.g.*, $OCS^+$) begins by loading a single $Ca^+$ ion, again in accordance with Section 3.2.2. Ideally, scans of the vibrational mode frequency are then performed in order to calibrate $\nu_1$[‡]. The next step is to load a single sympathetically-cooled molecular ion. In general this is performed via the introduction of a low partial pressure of the target gas (*e.g.*, OCS) to the chamber, and the controlled application of a suitable ionisation laser to generate the molecular ion inside the trap. It can take up to ∼10 seconds [105] or more for any sympathetically-cooled ions to be incorporated into the crystal lattice itself. Often a short application of the ionisation beam (even a single laser shot) is succeeded by a minute or so of waiting to ensure that the right number of ions has been loaded. In the event that a single ion is loaded, a small axial offset will occur to the lone $Ca^+$ ion, and it will be observed to exchange positions with a single dark ion periodically. At this stage the leaking of the target gas is stopped and more excitation scans can be performed to determine the mass of the loaded

[‡]Due to difficulties in the next step, this step was often omitted with the knowledge that new $Ca^+$ ions could be reloaded after any subsequent successes. This would not be ideal however as often small perturbations in mode frequency were observed on timescales associated with reloading the trap, possibly due to small patch potentials associated with calcium deposits from the oven, or introduction of the ionisation lasers.

dark ion.

Once a clean scan has been achieved, the introduction of reactant molecules can begin (either by leaking into the ion trap chamber or guiding with the velocity-selector), usually at low number densities to ensure adequate time to perform scans and monitor any changes (for example further reactions, possibly with background gases). There will be no indication of a successful reaction of the sympathetically-cooled ion, save for a change in vibrational mode frequency. Therefore excitation scans gated around the frequency corresponding to the initially loaded sympathetically-cooled ion should be performed periodically. When this resonance disappears or shifts, the frequency scan can be widened and the product resonance located in the usual manner.

## 5.5 Experimental results

Direct reactions of $Ca^+$ with a range of neutral reactant molecules were studied, including $CH_3F$, $CH_2F_2$, $CH_3Cl$, and $H_2$. In all cases the reaction product ions were identified by their mass, and in one case ($CaH^+$) further reaction was observed.

Both normal and in-phase detection axial intensity profiles are illustrated in Fig. 5.3, which shows profiles before and after the reaction of a single $Ca^+$ ion with $CH_2F_2$, which was admitted to the chamber via the leak valve. The dashed line indicates the equilibrium position of the dark ion in the second lattice site. In the ungated scans the fluorescence can be seen to smear axially as a result of the centre of mass vibration of the crystal, and the resonant frequency of the ion pair has shifted by $\sim$10 kHz (from about 94 to 84 kHz) post-reaction. As discussed earlier, when the camera intensifier is gated in-phase with the oscillation of the drive voltage, the ion fluorescence is only detected at the turning point of the ion's oscillation. Therefore, as the drive frequency approaches the vibrational resonance, the ion fluorescence

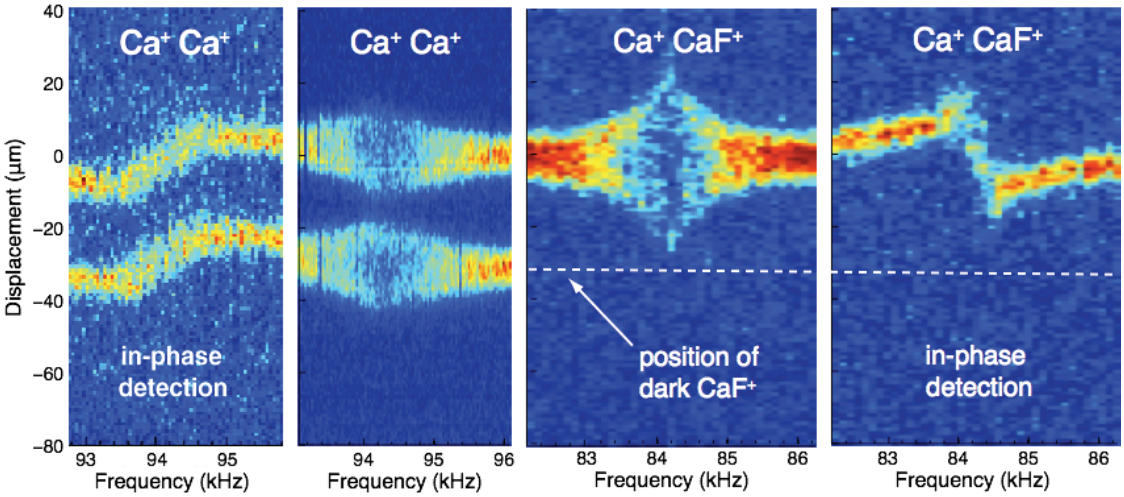


Figure 5.3: Pre- and post-reaction axial intensity profiles as a function of the driving radiofrequency, measured in the reaction of $Ca^+$ and $CH_2F_2$ using both normal and in-phase detection methods.

can be seen to be increasingly offset in one axial direction as the amplitude of the oscillation increases. As the drive frequency moves through the resonance frequency, the ion fluorescence abruptly flips to an equally large offset in the opposite axial direction due to the $\pi$ phase change when a driven harmonic oscillator moves through resonance. The ion fluorescence then gradually returns to the equilibrium position as the drive frequency moves away from the resonant frequency. It is in most cases easier to make an accurate assignment of the resonant frequency using this detection scheme. In these particular reactions the product ion average mass was determined to be 59.06(14) u, consistent with the expected product of $CaF^+$ at a mass of 59.08 u.

Figure 5.4 shows the in-phase detection scans for a reaction sequence that begins with the reaction of $Ca^+$ with $H_2$ (admitted through the leak valve). The average mass of the initial product ion was identified as 40.96(25) u corresponding to $CaH^+$ at 41.09 u. After a short period of time (∼10 minutes), the detection of a shift in the resonant frequency indicated that a subsequent reaction had occurred. The mass of the new product ion was identified as 57.02(23) u. This is consistent with

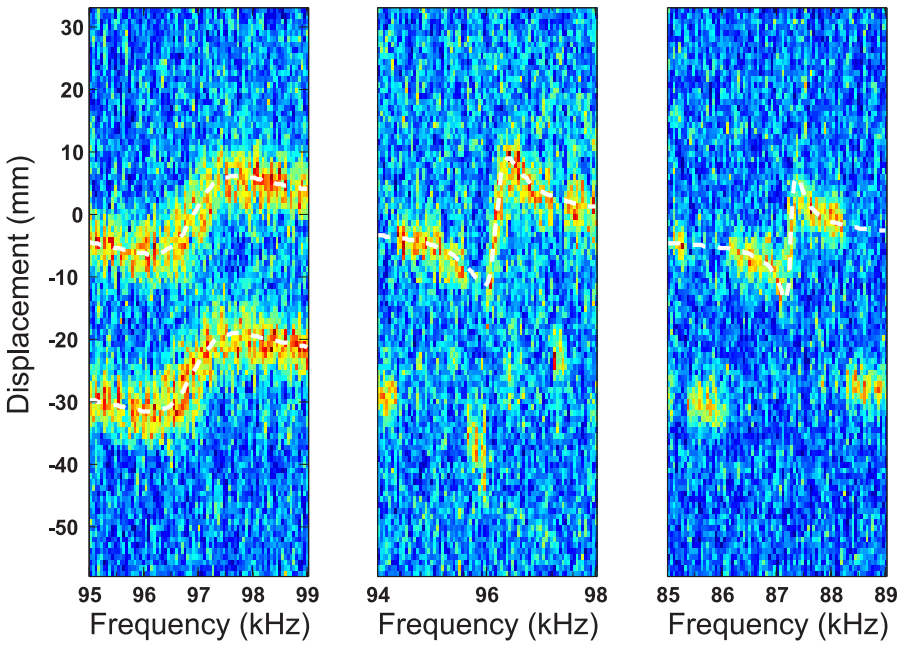


Figure 5.4: Pre- and post-reaction axial intensity profiles measured in the reaction sequence beginning with $Ca^+$ and $H_2$ using in-phase detection methods. Note that the $Ca^+$ ion swaps lattice sites with the dark ion a number of times during these scans, however the fitting of an overall dispersion profile is still possible, allowing the resonant frequency to be obtained.

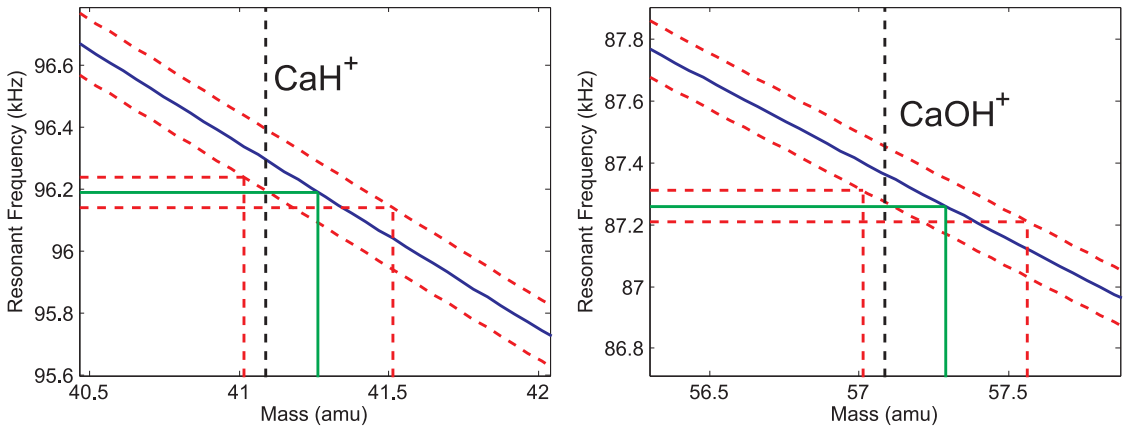


Figure 5.5: Illustration of the determination of the product ion mass, $m_2$, in each stage of the reaction sequence beginning with $Ca^+ + H_2$. The blue calibration curve is calculated from a knowledge of $\nu_1$ and $m_1 = 40.08$ u.

the formation of $CaOH^+$ at a mass of 57.08 u. Presumably this occurs as a result of the reaction of $CaH^+$ with $H_2O$ molecules present at very low concentrations in the chamber as a background gas. The determination of product masses is

performed using a calibration curve generated from a knowledge of $m_1$ and $\nu_1$; this is illustrated in Fig. 5.4 for the first (left) and second (right) reactions in this sequence. Dashed red lines reflect the uncertainty in the resonant frequencies $\nu_1$, and $\nu_-$, and therefore govern the uncertainty in $m_2$ for a given measurement. The dashed black lines show the masses of $CaH^+$ and $CaOH^+$ respectively.

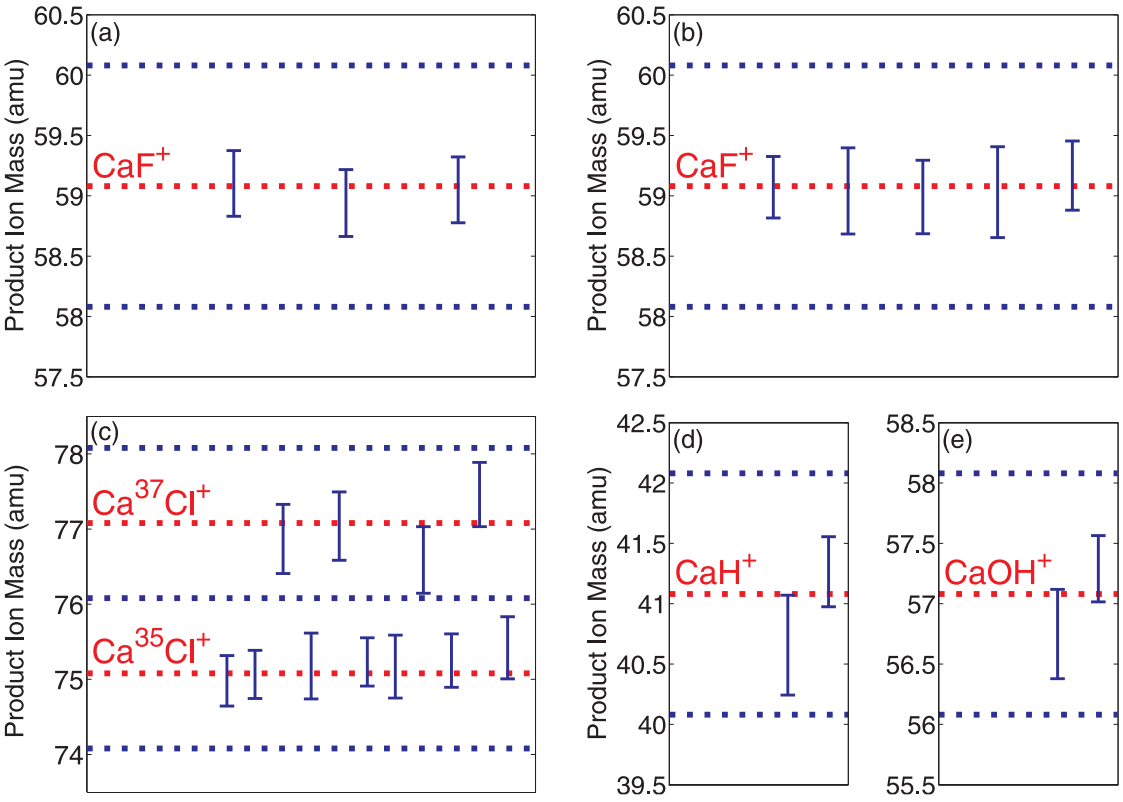


Figure 5.6: Measurements of product ion masses for the following reactions:
(a) $Ca^+ + CH_3F \rightarrow CaF^+ + CH_3$,
(b) $Ca^+ + CH_2F_2 \rightarrow CaF^+ + CH_2F$,
(c) $Ca^+ + CH_3Cl \rightarrow CaCl^+ + CH_3$,
(d) $Ca^+ + H_2 \rightarrow CaH^+ + H$, followed by:
(e) $CaH^+ + H_2O \rightarrow CaOH^+ + H_2$ (suggested).

The results for all of the direct reactions that were studied are summarised in Fig. 5.6, which shows a single point for each individual measurement performed. These values are also averaged and summarised in Table 5.5. In general, resonant frequencies were found to drift over a fairly short timescale, and measurements of

product mass were most accurate (relative to assumed product mass) when the measurements of $\nu_1$ and $\nu_-$ were performed as close together in time as possible. The resonant frequencies are dependent on trapping voltages and sensitive to stray fields; short-term fluctuations in these parameters were assumed to be the cause of this drift.

| Reactants | Product ion mass (u) | True mass (u) | Identity |
|---|---|---|---|
| $Ca^+ + CH_3F$ | 59.03(16) | 59.08 | $CaF^+$ |
| $Ca^+ + CH_2F_2$ | 59.06(14) | 59.08 | $CaF^+$ |
| $Ca^+ + CH_3Cl$ | 75.18(14) | 75.08 | $Ca^{35}Cl^+$ |
| | 76.99(22) | 77.08 | $Ca^{37}Cl^+$ |
| $Ca^+ + H_2$ | 40.96(25) | 41.09 | $CaH^+$ |
| $CaH^+ + H_2O$ | 57.02(23) | 57.09 | $CaOH^+$ |

Table 5.1: Product ion masses calculated via single sympathetically-cooled ion resonant-excitation mass spectrometry. Note that $H_2O$ is assumed to be the reactant in the final reaction.

Attempts were also made to verify the loading and sympathetic-cooling of $OCS^+$ and its subsequent charge-transfer reaction with $ND_3$ (see Chapter 7). A single $Ca^+$ ion was loaded into the trap, and then, using single pulses of a Nd:YAG pumped dye laser operating at 10 Hz, 280 nm, the loading of a single $OCS^+$ ion was attempted. In order to facilitate this, the partial pressure of OCS was varied over a wide range, as were the ionisation laser power density and alignment. However, the addition of a single sympathetically-cooled $OCS^+$ ion was not originally achieved. The main problem was the frequent sympathetic-cooling of unwanted additional dark ions. Often extra ions would take of the order of 5 minutes to cool into the crystal, despite other dark ions crystallising in the order of 5–15 seconds. In addition, application of the 280 nm ionising beam would often introduce extra $Ca^+$ ions, even though the calcium oven had been turned off for some time. However, the experimental setup was not refined for the purpose of this particular experiment,

and a number of improvements could be made in order to facilitate more work in the area of single ion reactions of sympathetically-cooled molecules, as suggested below.

## 5.6 Further work

In the first instance, a mechanical shutter should be installed to allow the Ca oven to stay on at a lower current, and allow more control over the loading of single ions. This would greatly increase the speed of subsequent attempts and provide more consistency in the loading of a single ion. The 280 nm laser beam used for ionisation of OCS was incident on a stainless steel plate shielding the chamber from the titanium sublimation pump. It was felt that this could result in the unwanted ejection of particles (possibly from deposited calcium) into the vacuum and disruption of trapping. A proper beam dump should be implemented in this regard. Since the attempts detailed here, irises have been introduced inside the chamber in an effort to reduce the stray light from the cooling lasers. This has proved to be effective in increasing our signal-to-noise ratio in the detection of single ion fluorescence. This will improve the quality of the resonance-excitation scans and provide a clearer picture during attempts to load single ions. Current ongoing work centres on introducing single $ND_3^+$ or $Kr^+$ ions into a two-ion crystal, along with $Ca^+$. Their ionisation schemes are somewhat simpler and occur at energies that may introduce fewer impurities due to ionisation of background material.

There are many possible applications of this technique, especially as a tool in the support of reaction studies such as those described in this thesis. Other possible applications include the study of isotopic branching ratios. For example, through over 300 repetitions of a single ion reaction, Staanum *et al.* [128] succeeded in

measuring the isotopic branching ratio of the reaction

$$\begin{aligned} \mathrm{Mg^+ + HD} &\rightarrow \mathrm{MgH^+ + D} \quad [1] \\ &\rightarrow \mathrm{MgD^+ + H} \quad [2] \end{aligned}$$

as 1:5 between channels [1]:[2]. Another possibility using our current experimental setup would be study of the isotopic branching ratio in the reaction:

$$\begin{aligned} \mathrm{Ca^+ + HDO} &\rightarrow \mathrm{CaOH^+ + D} \\ &\rightarrow \mathrm{CaOD^+ + H,} \end{aligned}$$

which could be performed at different steady-state electronic quantum state populations of calcium (as in Chapter 6), and allow the investigation of any variation of the branching ratio in this regard. This technique allows the detection of a single reaction event, or the monitoring of a sequence of chemical changes such as the consecutive photodissociation of a complex molecule [105]. In addition, the use of heavier laser-cooled ions such as $Ba^+$ allows the sympathetic-cooling of very large molecules ($\sim$500 u). A larger molecular charge can facilitate the cooling of heavier molecules still, even proteins, thus further broadening the potential scope of this technique. In summary, resonance-excitation mass spectrometry serves as an invaluable and general diagnostic tool in support of the study of chemical reactions, and provides wide scope for further investigations.

# Chapter 6

# Reactions of electronically-excited $^{40}Ca^{+}$ ions with translationally-cold neutral molecules

As discussed in Chapter 2, the continuous irradiation of the ions in the laser-cooling process results in a steady-state population of the $Ca^{+}$ electronic states involved with the cooling cycle. These populations, which are sensitive to the laser parameters, must be quantified in any reaction studies as the rate of reaction for the ground and excited states will likely be different. This chapter describes an investigation into the variation of the rate constants in the reaction of $^{40}Ca^{+}$ with $CH_3F$, $CH_2F_2$ and $CH_3Cl$ with different steady-state populations of the electronic states of $^{40}Ca^{+}$. The determination of the populations, using the Optical Bloch Equation (OBE) theory outlined in Section 2.6, allows us to obtain the contributions to the global rate constant from the ground and excited states of $^{40}Ca^{+}$ — from such data we can infer information about the potential energy surfaces of these reactions and of the reaction dynamics.

Initially we consider the necessary experimental measurements required to obtain

the parameters used in the OBE, along with methods of checking the results of the OBE calculations experimentally. The key to this latter step is the fitting of simulated lineshapes to laser-induced fluorescence spectra. There then follows an outline of how the OBE were applied for our experimental geometry. Specifically, we consider how to obtain the average steady-state quantum state populations within a particular ion crystal, and the importance of factors such as fluctuations in laser detuning and non-zero axial secular temperatures. This leads naturally to a brief investigation of fluorescence excitation spectra, which ultimately validates the OBE treatment for $^{40}Ca^{+}$ and allows the calibration of the effective laser intensities and linewidths. Modifications to the experimental apparatus and procedure are detailed and there is then a discussion of the rate constants measured for the aforementioned systems at both high ($\sim$196–243 K) and low (5 K) collision energies. Finally these measured rate constants are compared with theoretical calculations.

## 6.1 Application of the OBE given our experimental parameters

### 6.1.1 Experimental considerations

The theory for formulating and solving the three- and eight-level optical Bloch equations in order to obtain the electronic state populations of a $^{40}Ca^{+}$ ion under continuous laser irradiation is described in Section 2.6. The state populations depend on the intensity and detuning of the two lasers interacting with the ion, as well as the spontaneous emission rates and the laser linewidths. In the eight-level theory, which treats the magnetic sub-levels explicitly, extra parameters include the magnetic field strength and the angle between the magnetic field vector and the laser polarisations. These models have been used very successfully in the past

to model the populations of single ions [152, 174, 175]. When performing similar calculations for ion crystals we must be mindful of the fact that a spatial inhomogeneity of the cooling lasers on the scale of the crystal would lead to a distribution of laser intensities experienced by the ions in the crystal, and therefore to a corresponding distribution in Rabi frequencies. Additionally, a range of effective ion velocities parallel to the cooling lasers leads to a distribution of Doppler shifts, and therefore effective detunings, throughout the crystal at any given time. These factors will result in a distribution of ion quantum state populations in the crystal at a particular time. We therefore wish to find a sensible way to apply the OBE theory to our particular experimental situation, in order to calculate the average crystal quantum state populations for the set of measured laser powers and detunings associated with a particular reaction experiment.

A key factor in the following discussion will be the fact that the rate of resonance fluorescence emitted by the laser-cooled ions is proportional to the population of the upper excited states. As described in Section 2.6, for the three-level treatment this corresponds to $\rho_{22}$ and for the eight-level treatment $\rho_{33} + \rho_{44}$. By scanning either the 397 nm or 866 nm laser detuning, and collecting the fluorescence with a photomultiplier tube (PMT) in place of the CCD camera, we can generate experimental fluorescence excitation spectra. Comparison of these experimental spectra with simulations provides a means to calibrate experimental parameters such as the Rabi frequencies and laser linewidths. It allows us to gauge the importance of factors such as non-zero axial ion velocities and laser detuning fluctuations. Ultimately, these comparisons serve to validate our theoretical treatment of the experiment.

Spontaneous emission rates are taken from the literature [176] as detailed in Chapter 2. Laser linewidths for our particular diode lasers have been estimated by Toptica using a self-heterodyne technique over 5 $\mu$s at around 1–2 MHz. However,

they acknowledge that larger linewidths are feasible given measurements performed at timescales of minutes or more [201]. Ultimately this appears to be a parameter we must calibrate experimentally, and this may be achieved by the examination and fitting of experimentally-observed dark resonances (discussed initially in Chapter 2).

Though we have taken steps to stabilise the wavelength of both cooling lasers against the wavemeter reading itself (detailed later in Section 6.2.2), one must be aware of drifts in the wavemeter's absolute wavelength calibration. These drifts can be caused by variations in the environmental temperature and humidity, and depending on the circumstances can be in the 10–100 MHz/day range unless the laser is actively stabilised against a reference [201]. Unfortunately, this remains to be implemented in our setup. Thus, variation in the detunings represents one of the largest contributions to the error in the determination of the state populations.

### 6.1.2 Laser detunings and linewidths

In this section we consider the effect of the axial motion of the ions on the effective laser detunings, along with independent short-timescale fluctuations in the laser wavelengths themselves. To investigate the relative importance of these factors we employ the three-level OBE theory, which is computationally less expensive than the eight-level version and therefore facilitates the analysis.

It is useful to think about the effect of ion axial motion or fluctuating laser frequencies in the context of the steady-state population of the upper excited state $^2P_{1/2}$, which describes a surface in the two dimensional space parameterised by the 397 nm and 866 nm laser detunings. Figure 6.1(a) shows a contour plot generated by iterating the steady-state solution of the three-level OBE over a grid of 397 nm and 866 nm laser detunings with the laser linewidths set to zero, whilst

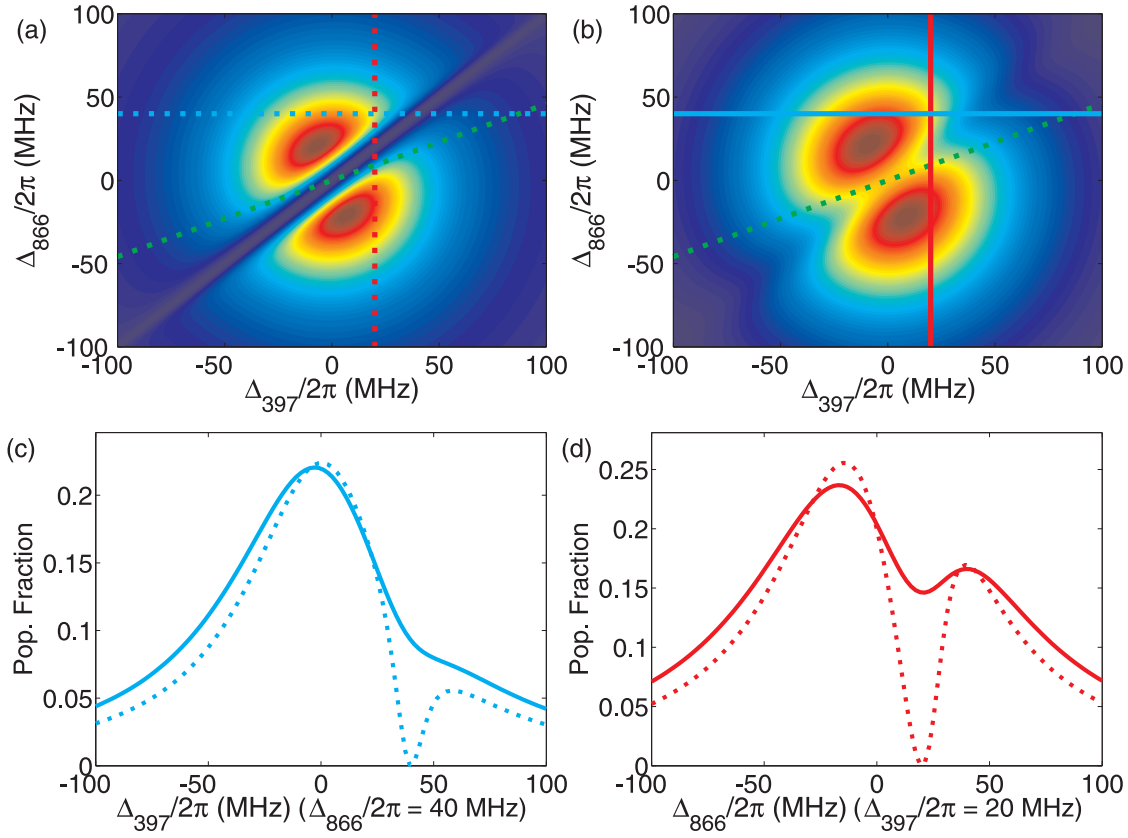


Figure 6.1: Contour plots of $\rho_{22}$ or the fractional population of the upper excited state ($^2P_{1/2}$) in detuning space. (a) is calculated with linewidths $\Gamma_{397}/2\pi = \Gamma_{866}/2\pi = 0$ MHz, (b) is calculated with $\Gamma_{397}/2\pi = \Gamma_{866}/2\pi = 5.5$ MHz. (c) and (d) illustrate 1D slices through these two surfaces which are proportional to fluorescence excitation spectra. Each spectrum corresponds to the matching line on the contour plots, the green dashed line is referenced later when considering finite axial crystal temperatures.

6.1(b) shows the same surface but calculated with finite laser linewidths. These surfaces simply denote the fractional population in the upper excited state, and are therefore proportional to the rate of fluorescence. When the laser linewidths have been set to zero, we observe strong coherent population trapping when the two detunings approach the same value. This results in the complete disappearance of population from the upper excited state and the surface drops to zero along an axis at 45° with respect to the blue detuning axis. When the laser linewidths are finite, a decoherence is introduced that partially destroys the coherent superposi-

tion between the ground and metastable state, and we see that population is then partially restored in the dark resonance region.

The bottom two panels in Fig. 6.1 illustrate 1D slices through these surfaces, which are proportional to the fluorescence excitation spectra along the same detuning coordinates. Note however that in all final simulated fluorescence spectra, the fluorescence intensity is arbitrarily set to zero if $\Delta_{397} < 0$ to reflect the fact that the crystal melts under these conditions and the observed fluorescence disappears. Experimentally we maintain one laser at constant detuning whilst scanning the other, and for this reason only typical slices with $\Delta_{397}$ scanned ($x$-axis, see Fig. 6.1(c)), and $\Delta_{866}$ scanned ($y$-axis, see Fig. 6.1(d)) are illustrated.

Let us consider a short-term oscillatory fluctuation of the 397 nm laser detuning arising from both temperature and humidity fluctuations in the laboratory. Given a long enough timescale relative to the frequency of the fluctuation, we can model the time-averaged distribution of detunings as a Gaussian distribution centred on the user-set and stabilised value of the detuning:

$$f_{\mathrm{G},397} = Ae^{-(\Delta_{397}-\Delta_{397,0})^2/(2\sigma_{397}^2)} \tag{6.1}$$

where $\Delta_{397,0}$ is the set value of the blue laser detuning and the Gaussian function is normalised by setting $A = 1/(\sigma_{397}\sqrt{2\pi})$. The full-width half-maximum (FWHM) of this Gaussian function is scaled according to the size of the fluctuations, and determines $\sigma_{397}$ according to FWHM$= 2\sqrt{2\ln 2}\sigma_{397}$. The resultant populations can then be considered as the convolution of the original 2D population surface with this Gaussian function along the 397 nm detuning axis. Each point in the resulting surface is the weighted average of the corresponding point from the original surface with its nearest neighbours along the 397 nm detuning axis. By analogy we can consider the independent 866 nm detuning fluctuations as a convolution with another independent Gaussian function, but this time along the y-axis corresponding

to the 866 nm laser detuning. Thus, the relative change at any point in any given spectrum is dependent on the topology of the excited state surface in its vicinity. Fluctuations in the 397 nm and 866 nm wavelengths are constantly monitored and rarely exceed ±4–8 MHz and ±1–4 MHz in total magnitude respectively (see Fig. 6.5). Gaussian functional fits to these $\Delta\lambda$ distributions therefore have FWHM that are of the order of approximately 4-8 MHz and 1–4 MHz for the 397 nm and 866 nm lasers respectively. Where possible these fluctuations are measured for each and every reaction experiment but, in cases where this was not performed, the upper bounds have been assumed when considering population uncertainties. Figure 6.2(a) illustrates the inclusion of laser fluctuations to a basic simulated fluorescence spectrum for the upper and lower bounds of the range of fluctuations discussed here. In these simulated spectra the laser linewidths are set to zero in order to examine these averaging effects in isolation, and the plot is centred on a dark resonance in an experimental 866 nm detuning scan, with parameters as detailed in the caption. Even at the upper bound of the frequency fluctuations that we observe in the laboratory, there is only a very slight change in any simulated spectra within our measured fluctuation range.

Let us now consider the case of non-zero axial ion motion. In the reaction studies described in this chapter, both the 397 nm and 866 nm laser beams are directed along the trap axis from a single side only. This axial cooling geometry is important because the distribution of axial ion velocities is only weakly affected by the RF-driven micromotion, which occurs radially in the trap and can be disregarded for our treatment of the state populations. Further to the discussion in Section 2.4.2, this means that within the harmonic approximation it is also correct to consider a Maxwell-Boltzmann distribution of effective (not just secular) axial kinetic energies. This means that we can consider a Gaussian distribution of axial ion velocities, with a FWHM obtained from Molecular Dynamics simulations. These

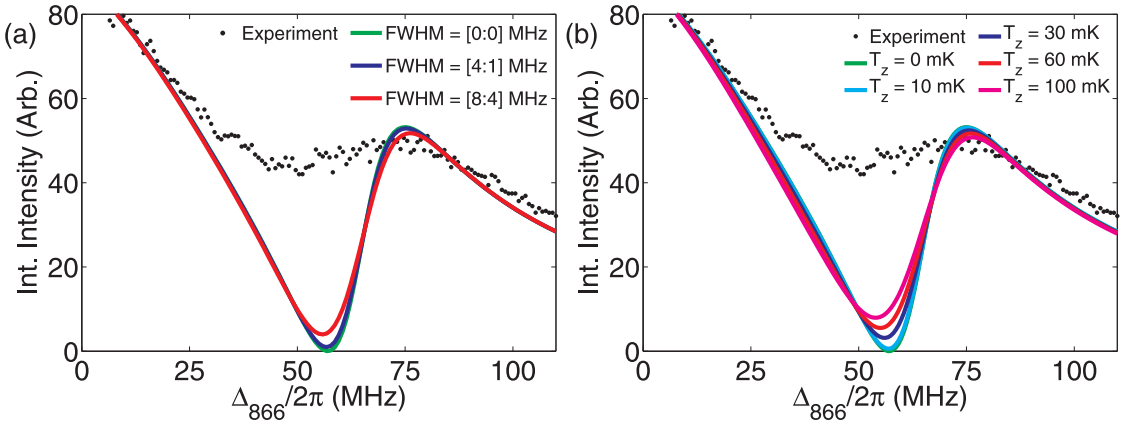


Figure 6.2: Simulated fluorescence spectra incorporating: (a) Frequency fluctuations in both lasers, with legend format [FWHM(397):FWHM(866)], (b) Non-zero axial effective crystal temperatures. In each plot these simulated scans are parameter matched to an experimental fluorescence scan, with the exception that the laser linewidths are set to zero, *i.e.*, $\Gamma_{397}/2\pi = \Gamma_{866}/2\pi = 0$ MHz. Experimental parameters: $P_{397} = 673$ $\mu$W, $P_{866} = 5.310$ mW, $\Delta_{397}/2\pi = 57.06$ MHz or 30 fm. Additional fit parameters (explained later): $A_{\text{eff;397}} = 0.11(2)$ mm$^2$, $A_{\text{eff;866}} = 11.4(11)$ mm$^2$.

simulations suggest that typical axial crystal temperatures are between 10–60 mK for large crystals. We recall from Section 2.32 that above 100–150 mK the crystal will typically melt as the ion kinetic energies overcome their local confining potential.

Given an ion velocity vector that is not orthogonal to either laser, there will be a simultaneous Doppler shift of both laser frequencies, and therefore both laser detunings. The magnitude of the shift in detuning for each laser, $kv$, is clearly dependent on both the photon wavenumber $k = 2\pi/\lambda$ and therefore frequency, as well as the ion velocity $v$ in the axis of the beam. As ion axial velocity increases we would be restricted to traversing a straight line path in our 2D detuning space, at an angle $\theta$ with respect to the x-axis with $0 < \theta < \pi/2$. The angle $\theta$ is dependent on the ratio of detuning shifts of the two lasers and therefore on the ratio between

the two laser wavelengths:

$$\arctan\theta = \frac{k_{866}v_{866}}{k_{397}v_{397}} = \frac{\lambda_{397}}{\lambda_{866}}. \tag{6.2}$$

It should be noted that the components of ion velocity in each beam propagation direction are equal because the lasers are co-linear and therefore $v_{866}/v_{397} = 1$. If both lasers are at the same frequency the resultant detuning shifts in each laser are always equal and the line would be oriented at 45° (assuming laser co-linearity). In our particular case $\theta \approx \arctan(396.847\,\text{nm}/866.214\,\text{nm}) = 0.43$ rad or 24.61°, which is delineated by the green dashed line in Fig. 6.1(a,b) for a detuning coordinate centred at the origin. We assume that any change in detuning of the lasers from the atomic transition frequencies has a negligible effect on this angle (which is reasonable given the small range of detunings used). A Gaussian distribution of axial ion velocities will result in a 1D Gaussian distribution of detunings, restricted along a line in detuning space oriented at an angle $\theta$ with respect to the $x$-axis. Therefore we must now perform additional convolution of the surface at $\theta \approx 24.61°$ with respect to the 397 nm detuning axis. We employ the normalised Gaussian function, $f_{\mathrm{G},T_z}$, defined by

$$f_{\mathrm{G},T_z} = ae^{-\Delta_{\mathrm{L}}^2/(2\sigma_{T_z}^2)} \tag{6.3}$$

where $\Delta_{\mathrm{L}}$ is the detuning coordinate along the restricted line in detuning space with

$$\sigma_{T_z} = \frac{\delta\omega_{(\mathrm{D,\ Tot})}}{2\sqrt{2\ln(2)}}; \tag{6.4}$$

and normalised such that $a = 1/(\sigma_{T_z}\sqrt{2\pi})$. The total Doppler width $\delta\omega_{(\mathrm{D,\ Tot})}$, is defined by

$$\delta\omega_{(\mathrm{D,\ Tot})} = \sqrt{\left(\delta\omega_{(\mathrm{D,\ 397})}^2 + \delta\omega_{(\mathrm{D,\ 866})}^2\right)} \tag{6.5}$$

where the individual Doppler widths for each laser-cooled transition, $i$, are given in Hz by [202]:

$$\delta\omega_{(\mathrm{D,\ i})} = 7.16 \times 10^{-7}\nu_{i,0}\sqrt{T/m}. \tag{6.6}$$

In these equations $T = T_{\mathrm{z,eff}}$ is the effective translational temperature associated with the axial ion motion (determined by MD simulations), $m$ is the ion mass and $\nu_{i,0}$ is the atomic transition frequency.

Figure 6.2(b) illustrates the effect of non-zero effective axial crystal temperatures, $T_z$, in isolation from either frequency fluctuations or non-zero laser linewidths. In general, axial ion motion contributes an averaging effect of about the same order as the frequency fluctuations previously discussed; this means that it represents a very minor perturbation on a simulated spectrum. Thus, neither of these effects, either in isolation or combination, come close to accounting for the strong washing out of the dark resonances observed in the experimental spectra. Furthermore, it appears as though they can be effectively disregarded from our OBE model and therefore our simulated fluorescence lineshapes — any small contribution present in the experimental scans would easily be matched by assuming slightly larger laser linewidths.

The major sources of decoherence are assumed to result from the finite laser linewidths and any $m_J$-mixing due to the presence of a magnetic field. As with the factors discussed above, we assume that any decoherence resulting from $m_J$-mixing is incorporated phenomenologically into the laser linewidth parameters used in the OBE model. These laser linewidths, which are assumed equal for the two DL-100 diode lasers, are estimated by performing fits of simulated spectra to experimental spectra (see Fig. 6.3 for an example). Through the examination of multiple spectra (taken at different 397 nm laser powers with each laser's detuning scanned in turn), and using simulated lineshapes based on the eight-level OBE treatment, the value of both linewidths, $\Gamma_{397}$ and $\Gamma_{866}$, was determined to be 5(1) MHz. Optimization of the fitting required a vertical magnetic field of B = 1.1 G, suggesting the presence of stray magnetic field contributions of a similar order to Earth's magnetic

field; these stray fields are assumed to arise from the apparatus. As explained in Section 2.6.2, a magnetic field of this magnitude perpendicular to the laser polarisations would be expected to cause $m_J$-mixing of the $^2D_{3/2}$ sub-levels with a frequency of the order of ∼1.1 MHz. Therefore it would appear that the laser linewidths represent the major source of decoherence in the system. Note that, as shown in Fig. 6.3, lineshape splitting due to multiple dark resonances is visible in the zero linewidth simulation, however, as the laser linewidths increase, this fine detail is washed out in agreement with the experimental data. Note also that whilst our experimental spectra can be matched well with either the three- or eight-level treatment (and in fact both yield similar linewidth values — see Appendix G), the eight-level treatment is used in the analysis of the final results in this Chapter because it is believed to be a more accurate model of the experimental conditions (see also Section 2.6.2).

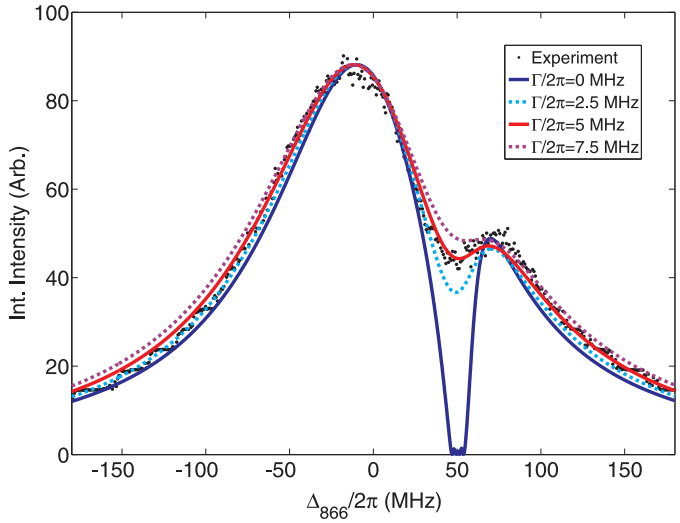


Figure 6.3: Fluorescence spectra simulated with the 8-level OBE treatment superimposed on an experimental scan. We determine our laser linewidths by matching the spectra around the dark resonance. Here we can see that $\Gamma_{397}/2\pi = \Gamma_{866}/2\pi \approx 5$ MHz is the most accurate fit, with both 397 nm and 866 nm laser linewidths are assumed equal. Experimental parameters: $P_{397} = 673$ $\mu$W, $P_{866} = 5.310$ mW, $\Delta_{397}/2\pi = 57.06$ MHz or 30 fm. Additional fitting parameters: $B = 1.1$ G, $\alpha = \pi/2$, $A_{\text{eff};397} = 0.055(3)$ mm$^2$, and $A_{\text{eff};866} = 1.90(3)$ mm$^2$.

### 6.1.3 Rabi frequencies and laser intensities

The Rabi frequencies which appear in the OBE are calculated from experimental measurements of the laser intensity, along with a knowledge of the properties of the atomic transitions involved. We recall that the Rabi frequency, $\Omega$, is a measure of the strength of the coupling between the laser field and atomic transition. In the eight-level OBE treatment* (see Section 2.6.2) it is defined according to:

$$\Omega_i = (\mathbf{D}_i . \mathbf{E}_i)/2\hbar, \tag{6.7}$$

where the index $i$ refers to a particular atomic transition and the laser coupled to it. The electric dipole moment of the transition $i$ is related to $\gamma_i$, the spontaneous decay rate of the upper state to the lower state, and $\lambda_i$, the transition wavelength, by [203]:

$$\mathbf{D}_i^2 = \frac{3\hbar\epsilon_0\lambda_i^3}{8\pi^2}\gamma_i. \tag{6.8}$$

The electric field strength of a laser is related to its intensity by

$$I = \frac{1}{2}c\epsilon_0 E_0^2. \tag{6.9}$$

Therefore, with a knowledge of the decay rate $\gamma_i$, $\Omega_i$ may be measured experimentally with the use of the relation [175]:

$$\Omega_i = (1 \times 10^{-6}) \times \sqrt{\left(\frac{3I_i\lambda_i^3\gamma_i}{16\pi^2\hbar c}\right)} \tag{6.10}$$

which produces the Rabi angular frequency in units of MHz.

In practice however, there is a certain amount of difficulty associated with the measurement of the laser intensities at the position of the crystal. Though it is possible to measure the total beam power, there is some difficulty in obtaining accurate beam cross-sectional areas at the crystal. The total beam power, $P_{\text{meas}}$,

*NB: In the three-level OBE derivation (see Section 2.6.1) the Rabi frequency is defined in Eq. 2.57 according to $\Omega_i = -(\mathbf{D}_i . \mathbf{E}_i)/\hbar$. This means that an additional factor of 2 should be included on the right hand side of Eq. 6.10 when it is applied in the three-level case.

is measured with an electronic power meter just prior to entering the vacuum chamber. It is recognised that there may be small subsequent power losses due to scattering at the viewport, and the power at the crystal has been estimated at around 90% of our externally measured reading. The transverse dimensions of each laser beam must be measured in order to obtain the cross-sectional area at the crystal, $A_{\text{meas}}$, however the bulky ion trap/UHV chamber apparatus make an *in situ* measurement problematic. Both cooling lasers are weakly focused through a 60 cm focal length lens, positioned approximately 30 cm from ion trap centre. Estimates of the beam areas at the crystal can be made by measuring the transverse beam dimensions at the position of the lens, by observing the laser-induced fluorescence on laser cards, and assuming that these dimensions are halved at a distance of half the focal length. It is recognised that both the measured power and area ($P_{\text{meas}}$ and $A_{\text{meas}}$ respectively) can only be considered estimates of the true values, and therefore further calibration is necessary to accurately obtain the Rabi frequencies for each laser. One possible treatment is to introduce an "effective" area, $A_{\text{eff}}$, for each laser that relates the externally-measured laser power to the effective laser intensity at the crystal, $I_{\text{eff}}$, according to:

$$I_{\text{eff}} = P_{\text{meas}}/A_{\text{eff}}. \tag{6.11}$$

The effective areas of each laser, $A_{\text{eff;397}}$ and $A_{\text{eff;866}}$, are independent of laser power and can be determined via the fitting of simulated lineshapes to experimental fluorescence spectra. Once these effective areas have been calibrated, the effective Rabi frequencies can be calculated given a measurement of the total external power for each cooling laser. This treatment ignores any spatial inhomogeneity of the laser intensities on the scale of the crystal, or at least makes the assumption that a fluorescence spectrum stemming from a group of ions in an intensity gradient is well-modelled by ions experiencing a constant mean intensity. This assumption is reasonable as long as the intensity gradient across the crystal is not too large.

Calculations have confirmed the validity of this assumption for our experiment, and these are detailed in Appendix F.

Fluorescence excitation spectra were recorded at combinations of laser powers and detunings reflecting the range of parameters used in the reaction experiments detailed later in this chapter. Effective areas for the 397 nm and 866 nm diode lasers were found to be $A_{\text{eff;397}} = 0.055(3)$ mm$^2$ and $A_{\text{eff;866}} = 1.90(3)$ mm$^2$ respectively. Figure 6.4 shows a selection of final eight-level OBE simulations which have been fit to experimental fluorescence spectra measured at both high and low $P_{397}$, and with either the 397 nm or 866 nm laser detuning scanned.

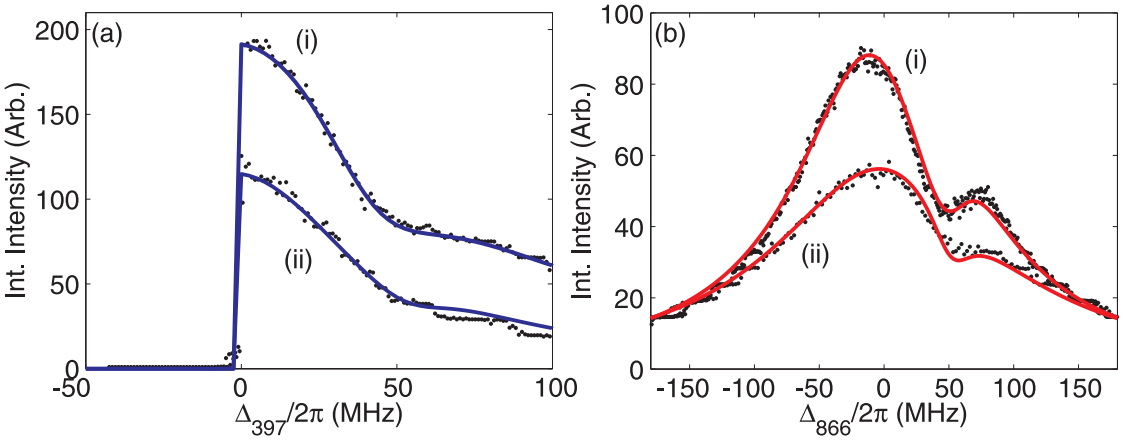


Figure 6.4: Eight-level OBE simulations overlaid across experimental fluorescence excitation spectra at the upper and lower bounds of the 397 nm laser powers used in the reaction experiments. Panel (a) shows 397 nm detuning scans with $\Delta_{866}/2\pi =$ 40 MHz, whilst panel (b) shows 866 nm detuning scans with $\Delta_{397}/2\pi = 57$ MHz. Laser powers are as follows:
(a): (i) $P_{397} = 600$ $\mu$W, $P_{866} = 5.2$ mW, (ii) $P_{397} = 220$ $\mu$W, $P_{866} = 5.3$ mW,
(b): (i) $P_{397} = 670$ $\mu$W, $P_{866} = 5.3$ mW, (ii) $P_{397} = 220$ $\mu$W, $P_{866} = 5.3$ mW.
Fitting parameters are as follows:
$A_{\text{eff;397}} = 0.055(3)$ mm$^2$, $A_{\text{eff;866}} = 1.90(3)$ mm$^2$,
$\Gamma_{397} = \Gamma_{866} = 5(1)$ MHz, $B = 1.1$ G, $\alpha = \pi/2$.

In summary, we have related the externally-measured laser powers to the effective laser intensities experienced by a Coulomb crystal via the calibration of effective cross-sectional areas, $A_{\text{eff}}$, for each laser. The good agreement between simulations

involving constant calibrated values for these effective areas and experimental fluorescence spectra measured at both high and low 397 nm laser power provides a confirmation of the validity of this treatment. We have determined that even at the upper bounds of the crystal axial temperature and the laser detuning fluctuations associated with our experimental setup, the impact of these factors on fluorescence spectra, and therefore steady-state populations, is minor. We assume that the experimental deviations from lineshape predictions involving zero laser linewidths, such as in Fig. 6.2, arise solely from a combination of finite laser linewidths (thought to be the dominant contribution) and $m_J$-mixing. The latter effect occurs due to the presence of a magnetic field whose component perpendicular to the laser polarisations was determined through lineshape fitting to be $B = 1.1$ G. The 397 nm and 866 nm laser linewidths were assumed equal and determined to be 5(1) MHz also through lineshape fitting. With these various parameters calibrated, the experimental Rabi frequencies may be calculated from measurement of the total beam powers.

## 6.2 Experimental detail and procedure

### 6.2.1 Experimental determination of laser detuning

The procedure for determining and setting the detuning of the 397 nm and 866 nm lasers from their atomic transition involves first measuring the position of the atomic resonances according to the WS-U wavemeter. Having done this, the desired detuning is manually set using the computer-controlled wavelength stabilisation system outlined in the next section.

In order to measure the atomic resonances practically, a crystal is loaded into the trap, and the detunings of both lasers are manually set such that the crystal

fluoresces moderately, indicating that both detunings are not close to being zero. The 397 nm laser is attenuated to approximately 100 $\mu$W in order to reduce power-broadening and provide a narrow fluorescence spectrum. The computer controlled 397 nm wavelength is then scanned towards smaller wavelength until the crystal melts and the fluorescence disappears as shown in Fig. 6.4(a). This is taken to be the approximate position of the 397 nm atomic resonance, and the blue detuning is then set at approximately 50 fm or $\Delta_{397} = 95$ MHz by simply stabilising the laser at the corresponding wavelength. This moves the position of the dark resonance to 95 MHz and prevents a dip in fluorescence from occurring at $\Delta_{866} = 0$ MHz which would otherwise correspond to the brightest observed fluorescence in a scan of the red laser detuning. Using both Labview and MATLAB scripts, $\Delta_{866}$ is then scanned through approximately 400–450 fm (or 180 MHz) around the peak, and the integrated fluorescence intensity is plotted. The peak fluorescence corresponds to the wavelength associated with the 866 nm atomic resonance, and at this point $\Delta_{866} = 0$ MHz.

Once the red detuning is known (usually within 5–10 fm (2–4 MHz)), it is then set to $\Delta_{866} = 100$ fm (40 MHz) to once again prevent a dark resonance from occuring near zero detuning. A more accurate 397 nm detuning is then acquired by scanning the wavelength towards the atomic resonance until the crystal melts, with multiple readings taken until a consistent reading is achieved. Early crystal loss can occur due to wavelength fluctuations, which at their smallest can be of the order of 1–2 fm (around 2–4 MHz at 397 nm); this represents the uncertainty in the measurement of the blue detuning although wavemeter drifts can occur subsequently as outlined below.

Once obtained, each laser detuning is set to the value selected for the experiment, which for the 866 nm laser is 0 MHz for all the reactions described in this thesis.

Labview scripts are used to stabilise the lasers at the corresponding wavelengths as described further in the next section.

### 6.2.2 Laser wavelength stabilisation

During the development of the experiment, two separate stabilisation schemes have been employed for maintaining our diode laser frequencies. Initially we were only capable of stabilising a single diode laser, and we opted to stabilise at 397 nm. The crystal fluorescence is less sensitive to a small change in the wavelength of the 866 nm re-pumping laser (*e.g.*, a 15 fm change in the wavelength is a smaller relative detuning at 866 nm than at 397 nm). Therefore we had a finer manual control on the 866 nm detuning and additionally this diode appeared more stable over the long term. Therefore a portion of the 397 nm beam was coupled via an optical fiber into our High Finesse WS-U wavemeter which offers a voltage feedback into the DL-100 control system via the DCB110 interface.

In early experiments, during a reaction we would manually attempt to keep fluorescence maximised via the voltage offset control on the 866 nm DL-100 controls, whilst the 397 nm detuning was more accurately maintained via the WS-U wavemeter. The WS-U voltage feedback loop maintained the wavelength to ±2–4 fm or ∼8 Mhz at 397 nm, with a data collection rate of 400 Hz, and therefore a minimum feedback period of a few milliseconds. In subsequent experiments (including all those described in the current chapter) both diode lasers were stabilised automatically. Manual detuning adjustments are more likely to introduce error due to the fact that the absolute crystal fluorescence naturally declines as the $Ca^{+}$ ions react. Thus the user has to continually make judgements about whether a perceived loss in fluorescence has arisen due to a drift in the 866 nm detuning or naturally in the course of a reaction, and this can lead to unnecessary fluctuations in the 866nm detuning during reaction. These concerns are largely irrelevant in the

consideration of a room temperature reaction as they typically last no more than 2–3 minutes when leaking a reactive gas at $1\times10^{-9}$ mbar. However over the course of a slower velocity-selected reaction (with timescales ranging from 10 minutes to 1.5 hours) automatic dual stabilisation is advantageous.

To achieve automatic dual stabilisation without the costly purchase of a second High Finesse WS-U wavemeter, we opted instead to couple a portion of both the 397 nm and 866 nm diode laser beams into the single WS-U wavemeter, using multi-mode optical fibers and a fiber optical switch (Leoni M1x2 SI50/125). A custom Labview program, in conjunction with the wavemeter's own software, and an external USB Labjack allowed us to provide a voltage feedback loop to the DCB110 interface of both lasers simultaneously. In this manner[†] we were able to stabilise the 397 nm laser wavelength to ±2–4 fm or 4–8 MHz at 397 nm, and the 866 nm laser wavelength to ±2–4 fm or 1–2 MHz at 866 nm, as shown in Fig. 6.5. The Labview feedback loop alternates between either laser once every 400–500 ms. This means that the described setup results in a much less frequent feedback loop than when using the WS-U to stabilise the 397 nm alone, but it does allow dual stabilisation. Short term wavelength fluctuations are therefore possible, but on the timescale of the reactions we would expect any corresponding fluctuations in the populations (and therefore measured rate constants) to average to zero.

Once again, it bears repeating that unless the WS-U wavemeter is locked to a reference, it is susceptible to drifts in wavelength calibration stemming from variation in laboratory temperature and humidity. Whilst attempts have been made to mitigate these drifts by partitioning the wavemeter away from laboratory air currents, we nevertheless experience oscillatory drifts in the region of approximately 0–10 fm

[†]Large (10–100 MHz) frequency fluctuations can be caused by the presence of optical feedback into the lasers, but this can be mitigated by careful re-alignment of the optics on the bench (and/or via the use of optical isolators).

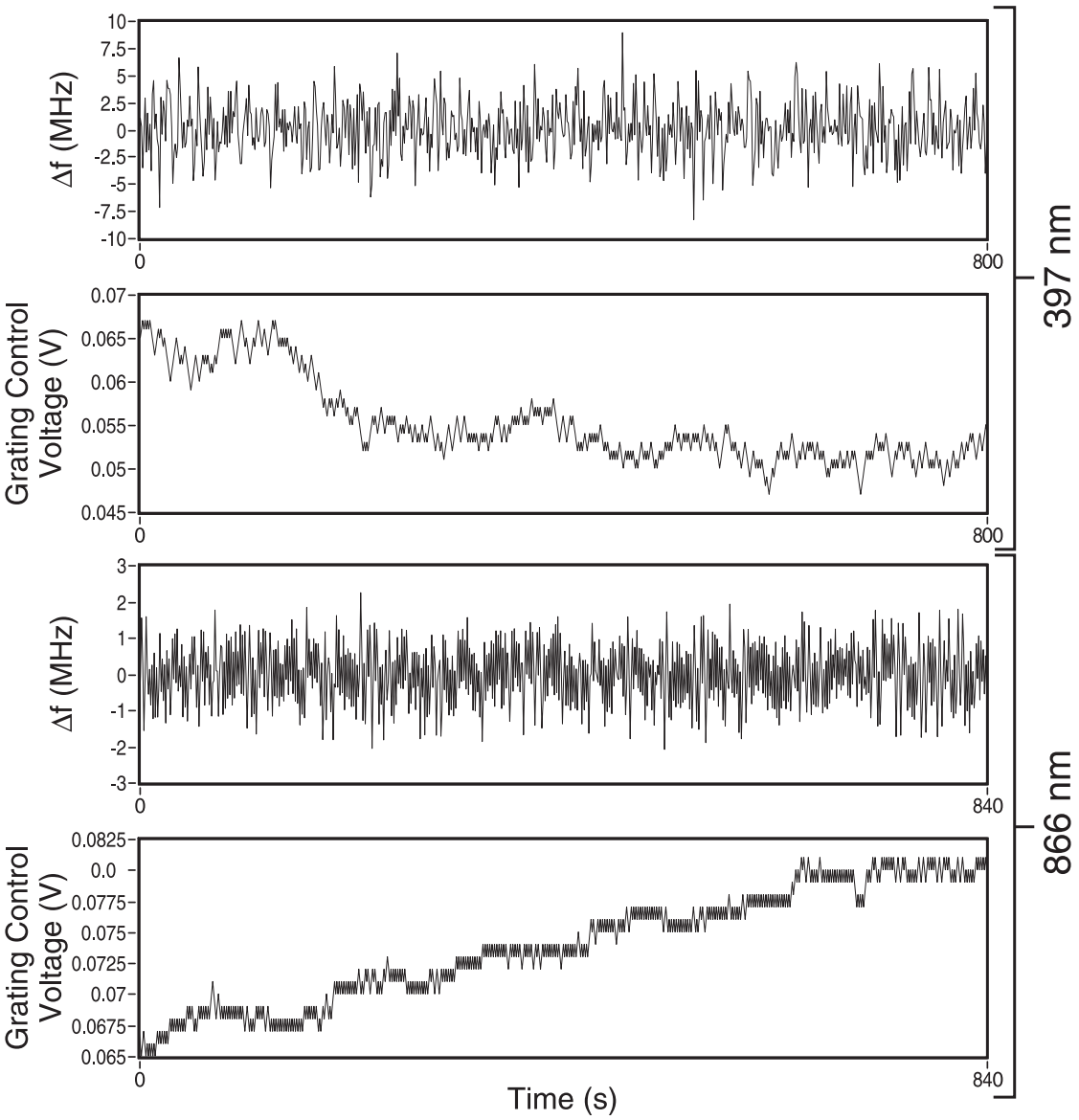


Figure 6.5: Typical frequency fluctuations over a period of 10–15 minutes, along with the variation in feedback control voltage. The minimum voltage increment applicable by the labjack was 0.01 V; up to 20 Db attenuation was subsequently applied before feedback of the voltage into the DCB110 analogue input board on the Toptica DL-100 laser control units.

per hour depending on conditions. This corresponds to 0–20 MHz at 397 nm or 0–4 MHz at 866 nm. These are recognised as a change in the measured wavelength of the atomic resonances, and therefore regular reference measurements are necessary in order to obtain accurate detunings for any reaction currently being performed.

### 6.2.3 Experimental procedure

The experimental setup is identical to that of a normal guided reaction described in Section 4.4.1 (see Fig. 4.8). Automatic dual stabilisation was set up specifically for these experiments, but is now in use for all experimental work.

Reactions are carried out in a similar manner to either a room-temperature reaction (see Section 4.3.1) or a guided reaction (see Section 4.4.1). The exception is that they are now performed at laser powers and detunings determined specifically by the desired steady-state electronic state populations. MATLAB scripts based on the OBE treatment outlined in Section 2.6 enable the steady-state population to be calculated based on the measured power and detuning of the 397 nm beam. This determines the 397 nm power and detuning to be used in each measurement, and these are set as described in Section 6.2.1. Across all experimental measurements the 866 nm laser power/attenuation is deliberately chosen to remain constant ($P_{866} \approx 5.2$ mW), although there are small fluctuations due to environmental factors. The 866 nm detuning is stabilised at a wavelength corresponding to $\Delta_{866} = 0$ MHz at the beginning of each measurement.

Given the previously described tendency of the absolute wavelength measured by the wavemeter to drift, several measurements of the position of the atomic resonance relative to the measured laser wavelength are made before and after each measurement. A drift in the measured wavelength during active stabilisation will result in a drift in the detuning from the atomic transition frequency. In the event of a small drift in the detuning over the course of reaction, the mean value of the before and after measurements was used in calculating the final theoretical steady-state populations for that measurement. Power measurements are also taken after every measurement to ensure accurate modelling of the state populations (laser powers can fluctuate during the day by up to $\Delta P_{397} \leqslant 50$ $\mu$W, $\Delta P_{866} \leqslant 200$ $\mu$W,

although typically by lesser amounts).

Given the laser powers and detunings accompanying each separate Coulomb crystal reaction, and a knowledge of how to obtain effective laser intensities using the calibrations outlined earlier in this chapter, we may calculate steady-state electronic state populations for each reaction. In this way we can systematically vary the populations and investigate the effect on the rate constant for the reaction system under study (either using room-temperature neutral reactants or translationally-cold velocity-selected neutral molecules). Figure 6.6 contains plots of the steady-state populations with respect to a change in the 397 nm laser detuning at both high and low 397 nm laser power. Dashed vertical lines indicate our approximate detuning limits: outside of these lines the crystal is prone to melting on the timescale of our experiment due to either inadequate cooling under increased collision rates (introduction of reactant molecules) or due to laser fluctuations which can bring the blue laser frequency too close to the atomic resonance.

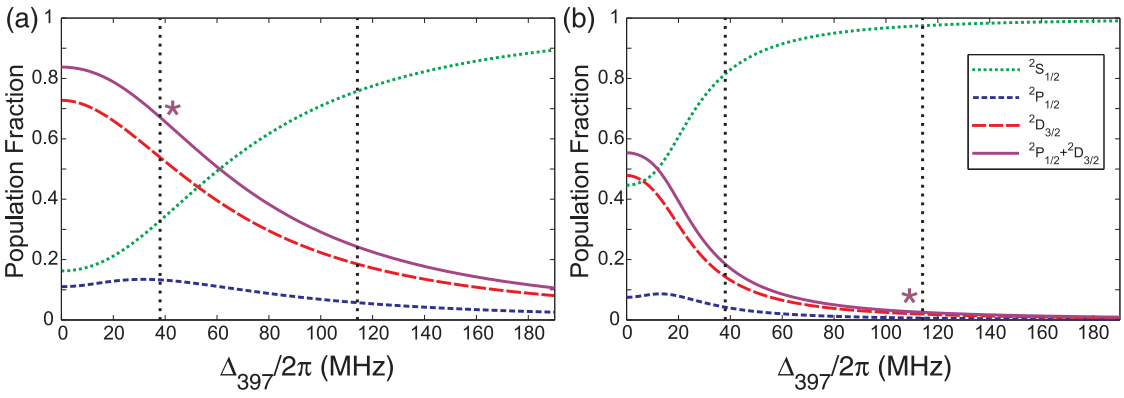


Figure 6.6: Calculation of steady-state electronic state populations (based on the eight-level OBE) at different values of the 397 nm laser detuning $\Delta_{397}$. (a) Shows calculations for the approximate upper bound of our 397 nm laser power, with $P_{397} = 900$ $\mu$W, whilst (b) shows calculations at lower power with $P_{397} = 70$ $\mu$W. In both plots $P_{866} = 5$ mW, $\Delta_{866}/2\pi = 0$ MHz and $\Gamma_{397}/2\pi = \Gamma_{866}/2\pi = 5$ MHz. Both lasers are linearly-polarised and oriented perpendicular to a magnetic field of $B = 1.1$ G.

In order to achieve the very lowest total excited state populations we use low

397 nm laser powers in conjunction with large 397 nm detunings (see the asterisk in Fig. 6.6(b)), and for the largest total excited state populations we must use both a small detuning and a large 397 nm laser power (see the asterisk in Fig. 6.6(a)). For a given shift in the detuning, there will be a greater change in the populations when this occurs at smaller detunings, and larger 397 nm laser power, due to the steeper population gradient there. This will be reflected in a larger relative uncertainty in the total excited state population when the ions are more highly excited (see Figs. 6.7, 6.10 and 6.12), and this uncertainty stems primarily from error in determining the absolute detuning, along with any detuning drifts that may occur during a particular reaction experiment. As can be seen from Fig. 6.6, we can achieve a large range of total excited state populations (0–70% total excited state) by manipulating the blue laser alone. The major contribution to the total excited state population comes from the $^2D_{3/2}$ state, with the $^2P_{1/2}$ state limited to around 10–20% of the total population. The 866 nm repumping laser, maintained at high power and zero detuning, is effectively saturating the 866 nm transition. We can achieve a higher total excited state population through a decrease in the 866 nm laser power and increase of its detuning, however this will result in an increased population of the metastable state relative to the upper excited state. This of course will result in a smaller photon scattering rate on the main cooling transition, leading to less efficient laser cooling and less observed fluorescence. For this reason, and for experimental convenience, we elect to keep the 866 nm transition saturated and the laser parameters constant throughout our experimentation. Additionally, we seek to avoid the dark resonance located near zero detuning, and we are limited in our laser powers in that we wish to avoid stimulated emission dominating over spontaneous emission. Stimulated emission would occur to the same vacuum mode occupied by the laser photons and thus result in inefficient cooling (asymmetric emission), and a reduction in the observed fluorescence (as the photons due to

stimulated emission are not directed towards the CCD camera).

The experimental procedure and determination of rate constants are otherwise identical to the descriptions in Chapter 4. The reactions of $^{40}Ca^{+}$ with $CH_3F$, $CH_2F_2$ and $CH_3Cl$ were studied in this way, and the results are presented in the next section. The ionisation pressure gauge gas sensitivity factors used in the determination of neutral molecule number densities are listed in Table 4.5. The neutral molecular number densities are determined from guided flux measurements as described in Section 4.2.2.

## 6.3 Experimental results

### 6.3.1 Reaction with Fluoromethane

Reactions were performed for the $Ca^{+} + CH_3F \rightarrow CaF^{+} + CH_3$ system, both in the high temperature regime ($\langle E_{\text{coll}} \rangle / k_{\text{B}} = 243$ K via direct admission of room-temperature neutral molecules) and at low collision energies ($\langle E_{\text{coll}} \rangle / k_{\text{B}} = 5$ K via velocity-selection). Rate constants are plotted as a function of the combined excited state population (*i.e.*, the sum of the populations in the $^2P_{1/2}$ and $^2D_{3/2}$ states), calculated through the input of the relevant laser-cooled parameters into the OBE. From these plots (shown in Fig. 6.7), a linear least-squares fitting procedure was used to determine the ground state and combined excited state rate constants.

The rate constants measured for the ground and excited state surfaces in the two energy regimes are listed in Table 6.1 along with other experimental values from the literature, and some predictions obtained through capture theory calculations. Table 6.2 lists the dipole moments, polarisability volumes and interpolated values of C(T) (see Eq. 1.6) for each of the reactant molecules. These values are used in theoretical predictions of the rate constants, and these methods are outlined in

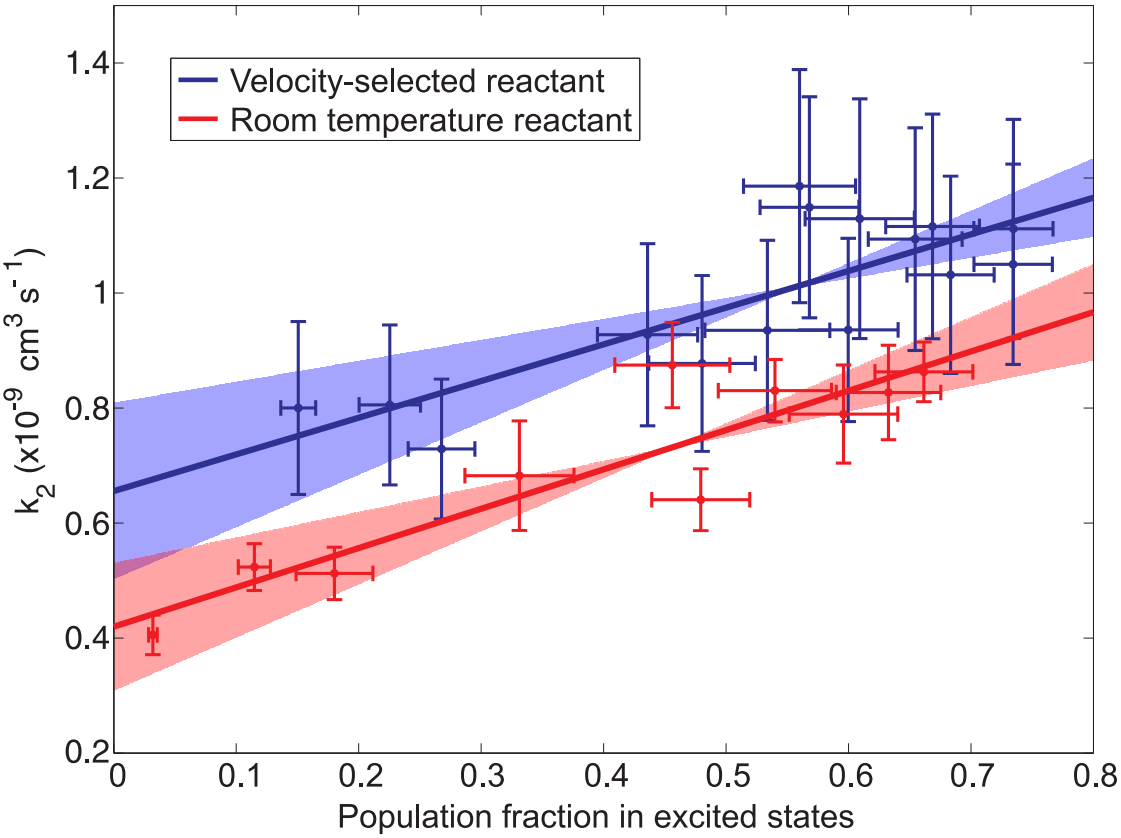


Figure 6.7: Variation of the observed bimolecular rate constant as a function of the total excited state population of $^{40}Ca^+$ for the reaction of $Ca^+ + CH_3F$. Reactions were performed in two collision energy regimes: $\langle E_{coll}\rangle/k_B = 243$ K (room-temperature $CH_3F$ molecules) and $\langle E_{coll}\rangle/k_B = 5$ K (velocity-selected $CH_3F$ molecules). The shaded areas indicate the 95% confidence interval for the corresponding data fit, and are used to calculate the rate constant uncertainties.

Section 1.2.1.

From Table 6.1 we can see that the ADO and ACCSA theories predict a slight increase in the rate constant with respect to Langevin theory. Experimentally, the rate constant determined for the combined excited states of $Ca^+$ appears to agree well with the ACCSA value, while the ground state rate constant is more than a factor of two smaller. Given the uncertainty associated with the measurements, this smaller ground state rate constant is in reasonable agreement with the inductively coupled plasma/selected-ion flow tube (ICP/SIFT) tandem mass spectrometer study of Zhao and coworkers [205]. Both this study and the Fourier-

| $Ca^+ + CH_3F \rightarrow CaF^+ + CH_3$ | | | |
|---|---|---|---|
| Rate Constant ($\times 10^{-9}$ cm$^3$ s$^{-1}$) | T = 5 K | T = 243 K | T = 300 K |
| This work ($^2S_{1/2}$) | 0.66(15) | 0.42(11) | – |
| ($^2P_{1/2}$+$^2D_{3/2}$) | 1.29(12) | 1.10(13) | – |
| FTICR-MS ($^2S_{1/2}$), Harvey *et al.* [204] | – | – | 0.15 |
| ICP/SIFT ($^2S_{1/2}$), Zhao *et al.* [205] | – | – | 0.26 |
| Adiabatic capture ($T_{rot}$ =$T_{trans}$) (ACCSA) | 10.36 | 1.22 | 1.11 |
| Adiabatic capture ($T_{rot}$=300 K) (ACCSA) | 1.85 | 1.14 | 1.11 |
| Average Dipole Orientation (ADO) | – | 1.92 | 1.79 |
| Langevin | 0.87 | 0.87 | 0.87 |

Table 6.1: Comparison between experimental and theoretical rate constants for the $Ca^+$+$CH_3F$→ $CaF^+$+ $CH_3$ reaction. The simple capture theory models that predict the listed theoretical rate constants are outlined in Section 1.2.1.

| Molecule | $\mu$ (D) | $\tilde{\alpha}$ (Å$^3$) | C(T) |
|---|---|---|---|
| $CH_3F$ | 1.85 | 2.540 | 0.2388 (243 K) |
| | | | 0.2319 (300 K) |
| $CH_2F_2$ | 1.97 | 3.200 | 0.2421 (196 K) |
| | | | 0.2285 (300 K) |
| $CH_3Cl$ | 1.87 | 4.416 | 0.2285 (199 K) |
| | | | 0.2122 (300 K) |

Table 6.2: Parameters used in the theoretical calculation of rate constants for $Ca^+$ reactions involving the corresponding molecule.

transform ion cyclotron resonance mass spectrometry (FTICR-MS) experiments by Harvey *et al.* involved $Ca^+$ in the ground state. Thus, with respect to capture theory, it appears that the excited state rate constant is approximately in line with the theoretical values, whilst the ground state rate constant is smaller than might be predicted on the basis of these simple capture theory models.

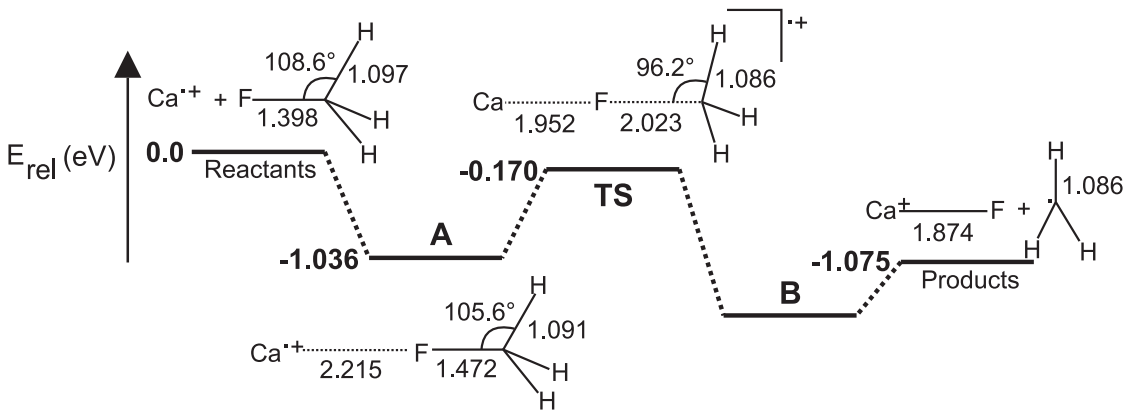


Figure 6.8: Turning point energies and geometries for the $Ca^+ + CH_3F \rightarrow CaF^+ + CH_3$ ground state potential surface, calculated by Harvey [206].

*Ab initio* electronic structure calculations by Harvey *et al.* [204, 206][‡] have provided a possible explanation for this reduction in rate by predicting the existence of a submerged barrier on the $Ca^+ + CH_3F$ ground-state potential surface. As illustrated in Fig. 6.8, this submerged barrier lies 0.17 eV below the energy of the separated reactants. It has been suggested that this type of barrier may arise as a consequence of a strongly avoided crossing at short range between the ground state surface and a reactant ionic state surface [74]. This is illustrated schematically in Fig. 6.9, where the upper state is characterised by charge transfer from the $Ca^+$ ion to the $CH_3F$ molecule. The difference in energy between these states at infinite separation corresponds to the difference of the ionisation energy of $Ca^+$ and the electron affinity[§] of $CH_3F$. It has been noted that the smaller this energy difference (*i.e.*, IE(electron donor) - EA(electron acceptor)), the more strongly avoided the crossing and the shallower the barrier[¶]. In particular, the reactivity of different Lanthanide ions with fluoromethane and other fluorinated hydrocarbons can be

[‡]Where relevant, $Ca^+ + CH_3F$ PES energies from the most recent calculations [206] are assumed to supersede those from earlier work [204].

[§]EA(X) is defined throughout as the energy change for the process $X^- \rightarrow X + e^-$.

[¶]It has been observed for radical-neutral reactions that if this difference is less than 8.75 eV a submerged barrier is likely [74]. However given that IE($Ca^+$) = 11.87 eV [204], and the fact that experimental values for EA($CH_3F$) range between -3.2 and -6.2 eV [207, 208], we note a much larger difference in this ion-molecule reaction (see Fig. 6.9).

shown to correlate with the ionisation energy of the Lanthanide mono-cations, as the bonding in the transition state is similar in all cases [209]; these types of considerations are also present in the analysis of $S_N2$ type reactions [208, 210]. However as we shall observe in the following sections, similar reactivity or barrier height correlations with this energy difference are not as clear given a variation in the neutral reactant rather than the metal cation. As well as possible bonding differences in the transition state, the available experimental and theoretical data on the gas-phase electron affinity of the methyl halides vary widely, hindering analysis in this regard (see Refs. [207, 210] and lastly [208] and references therein). In general the methyl halides appear to have negative electron affinities suggesting that they are unstable with respect to the addition of an electron, which may explain the apparent lack of associated experimental data.

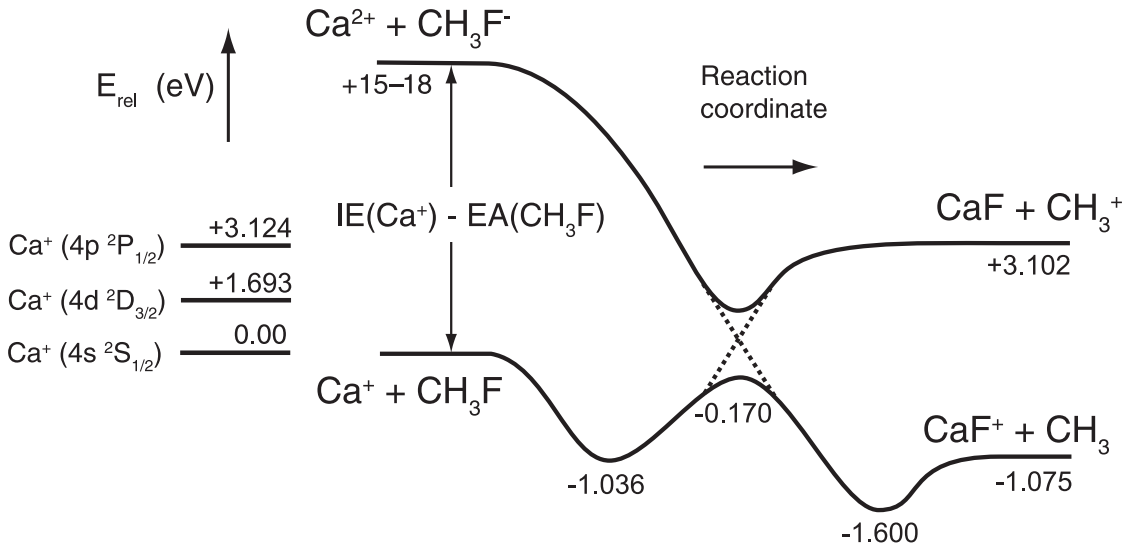


Figure 6.9: Schematic reaction profile for the $Ca^+ + CH_3F \rightarrow CaF^+ + CH_3$ reaction based around PES turning point energies calculated by Harvey [204, 206] and literature data [211].

A similar charge transfer process is invoked in the "harpoon" mechanism believed to govern the reaction between neutral Ca and the methyl halides [71]. However, the reaction between $Ca^+$ and $CH_3F$ is believed to proceed via the formation of an

ion-molecule collision complex whose subsequent progression through the transition state into the product complex (which rapidly decomposes to form the products) is hindered by the dynamical bottleneck of a submerged barrier on the ground state potential surface. Although the reactants have enough energy to overcome the submerged barrier, if the complex lifetime is short a reaction will only occur given an entrance channel trajectory that immediately finds the barrier. If this is not the case, time is spent sampling other regions of the potential surface and the complex can often dissociate before reaction has occurred. Thus, given a spread of initial trajectories on the ground-state potential surface, the submerged barrier suppresses the overall rate constant.

However, in the case of the potential surfaces correlating with the excited states of the $Ca^+$ ion, we see a much faster reaction characterised by a rate constant that is almost a factor of three larger than the ground state rate constant at 243 K. This suggests that the excited state reaction is not limited by the same dynamical bottleneck, and is likely to be happening on a barrierless potential surface. The precise details of the excited state potential energy surface are not known, and further *ab initio* calculations are required for this type of reaction to be understood more fully. However, qualitatively speaking, it has been suggested [43, 74] that the decreased ionisation energy from the 4p and 3d levels of $Ca^+$ leads to a decrease in separation between the valence-bond states illustrated in Fig. 6.9. This could lead to a more strongly avoided crossing which would reduce the height of any submerged barrier. In addition the reduced energy separation would push any avoided crossings to larger reactant separations relative to the ground-state avoided crossing, thus preventing the formation of a near-threshold barrier. An investigation by Harvey *et al.* [204] into the reactions of various transition metal ions with $CH_3F$ leads to similar suggestions.

These trends appear to hold in the case of lower collision energy; however for both ground and excited state reactions there is a slight increase in the rate constant as the collision energy is decreased. This is consistent with the predictions of ACCSA theory, in which the inclusion of the ion-permanent dipole interaction is sufficient to cause an increase of the rate constant at low temperatures, in contrast to Langevin theory. However the main contribution to the increased ACCSA ($T_{rot}$ =$T_{trans}$) rate constant at lower energy arises because at lower energies there is an increasing population of the lower rotational quantum states. At higher rotation energies, the averaging effect of the molecular rotation effectively weakens the interaction between the ion and the molecule and contributes to a smaller rate constant. We recall that the velocity-selected/guided molecules are not rotationally cold. To a first approximation the rotational distribution of molecules exiting the guide is described by a constant value of $T_{rot} = 300$ K. If this is factored into the ACCSA calculation a much more modest increase is observed at lower collision energy (see Table 6.1), which results in better agreement between the theoretical prediction and the measured rate constant value for the excited state. Additionally, within the two transition state model of ion-molecule reactions (discussed in Section 1.2.1), it is often observed that the outer transition state (capture) dominates at lower temperatures [74, 75], and vice-versa. In this context the decreasing importance of the inner transition state (the submerged barrier) at low temperatures correlates with the increased rate constants observed in the lower temperature limit for both high and low electronic excitations. Recent calculations by Sordo *et al.* [212] emphasize the importance of both the inner and outer transition state in determining the kinetics of these types of reaction, with the relative contributions dependent also on the height of the inner barrier.

The replacement of the velocity-selector with the Stark decelerator would allow similar investigations of the rate constant, but with neutral molecules that are

rotationally cold *i.e.*, in specific low energy rotational quantum states. This would allow us to see whether the large enhancement to the rate constant predicted by ACCSA theory for the lowest rotational states is borne out by experiment (although this may not be so pronounced for fluoromethane, given the existence of the aforementioned submerged barrier on the ground potential surface).

### 6.3.2 Reaction with Difluoromethane

In Fig. 6.10, rate constants determined for the reaction of $Ca^+ + CH_2F_2 \rightarrow CaF^+ + CH_2F$ are plotted as a function of the total excited state population. As for fluoromethane, this work was carried out both in the high temperature regime ($\langle E_{\text{coll}} \rangle / k_{\text{B}} = 196$ K via direct admission of room-temperature neutral molecules) and at low collision energies ($\langle E_{\text{coll}} \rangle / k_{\text{B}} = 5$ K via velocity-selection). The rate constants for the ground and combined excited states of $Ca^+$ in each energy regime are listed in Table 6.3 along with other relevant values.

| $Ca^+ + CH_2F_2 \rightarrow CaF^+ + CH_2F$ | | | |
|---|---|---|---|
| Rate Constant ($\times 10^{-9}$ cm$^3$ s$^{-1}$) | T = 5 K | T = 196 K | T = 300 K |
| This work ($^2S_{1/2}$) | <0.04 | <0.03 | – |
| ($^2P_{1/2}$+$^2D_{3/2}$) | 0.41(06) | 1.65(14) | – |
| Adiabatic capture ($T_{\text{rot}} = T_{\text{trans}}$) | 8.65 | 1.20 | 0.98 |
| Adiabatic capture ($T_{\text{rot}}$=300 K) | 1.83 | 1.04 | 0.98 |
| Average Dipole Orientation | – | 2.02 | 1.75 |
| Langevin | 0.88 | 0.88 | 0.88 |

Table 6.3: Comparison between experimental and theoretical rate constants for the $Ca^+ + CH_2F_2 \rightarrow CaF^+ + CH_2F$ reaction. ACCSA and ADO theory rate constants are approximated based on a symmetric top treatment.

In the case of difluoromethane, and within our experimental error, we resolve no

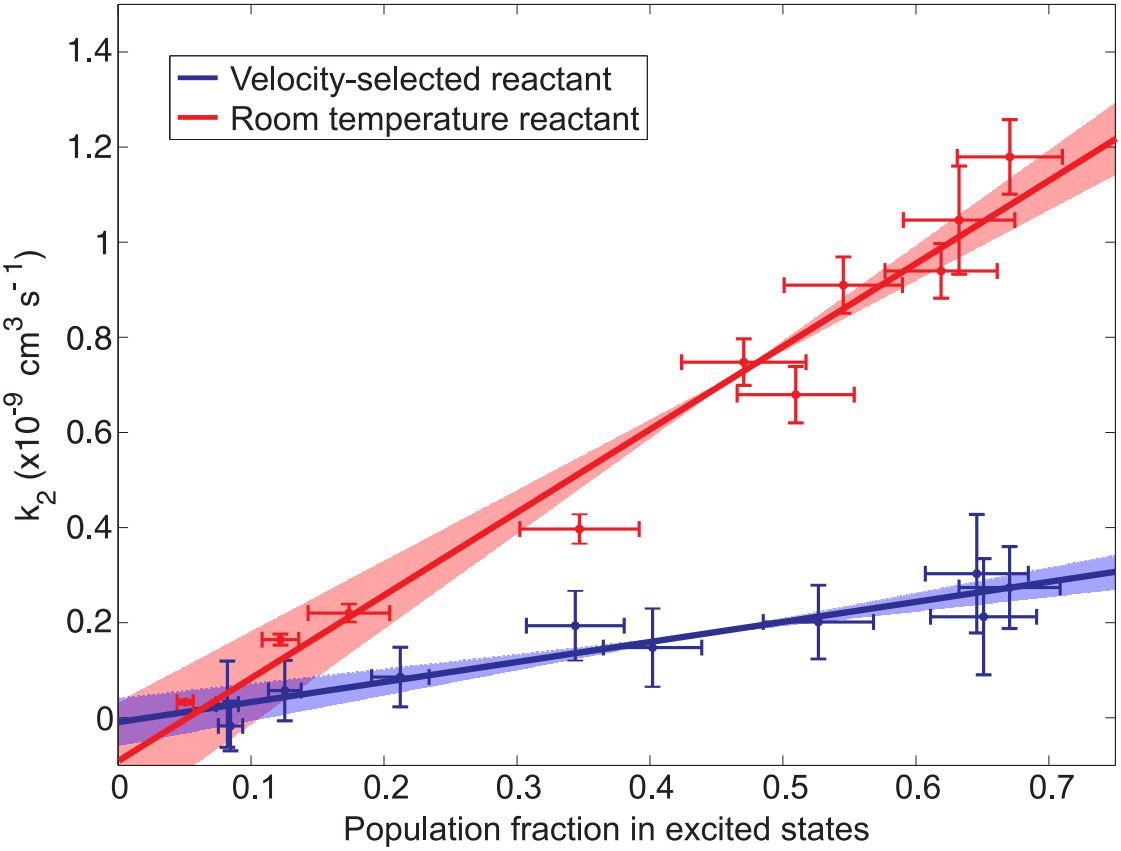


Figure 6.10: Variation of the observed bimolecular rate constant as a function of the total excited state population of $^{40}Ca^{+}$ for the reaction of $Ca^{+}$ + $CH_2F_2$. Reactions were performed in two collision energy regimes: $\langle E_{coll} \rangle / k_B = 196$ K (room-temperature $CH_2F_2$ molecules) and $\langle E_{coll} \rangle / k_B = 5$ K (velocity-selected $CH_2F_2$ molecules). The shaded areas indicate the 95% confidence interval for the corresponding data fit, and are used to calculate the rate constant uncertainties.

measurable reaction from the ground state (as indicated within Fig. 6.10 by the $y$-intercepts of the fitted lines). This implies that $k_2 \lesssim 0.5 \times 10^{-10}$ cm$^3$ s$^{-1}$ for the ground state, as we cannot presently measure rate constants lower than this. Reaction from the combination of the excited states does proceed however, and the rate constant measured at 196 K agrees reasonably well with ADO theory. However the excited state rate constant at low collision energy is almost a factor of four smaller than at room-temperature. Once again, recent *ab initio* electronic structure calculations by Harvey et al. [206] can help to provide some understanding of the reaction dynamics. Density functional theory calcu-

lations using the MPW1K functional and basis sets of (extended) 14s9p/[8s5p] TZV and 6-311+G(d) respectively for $Ca^+$ and C/H/F atoms, predict that the energy of the transition state relative to the separate reactants is +1.4 kcal/mol (or +0.06 eV). The stationary point energies calculated on the ground state potential surface of the $Ca^+ + CH_2F_2$ system suggest the existence of a real barrier. The plot in Fig. 6.11 illustrates that, in contrast to the submerged barrier seen in the fluoromethane reaction, the inner transition state on the ground state surface for the difluoromethane reaction appears to be above the energy of the separated reactants. This represents a transition-state barrier height increase of +0.23 eV or +5.3 kcal/mol between fluoromethane and difluoromethane. Such an increase could occur as the result of a weaker avoided crossing due to an increase in energy separation between the ground state surface and the valence bond state associated with charge transfer from the $Ca^+$ to $CH_2F_2$ (or more generally $H_3C$-X). However, literature values for EA($CH_2F_2$) are not available to the best of our knowledge, hindering this interpretation.

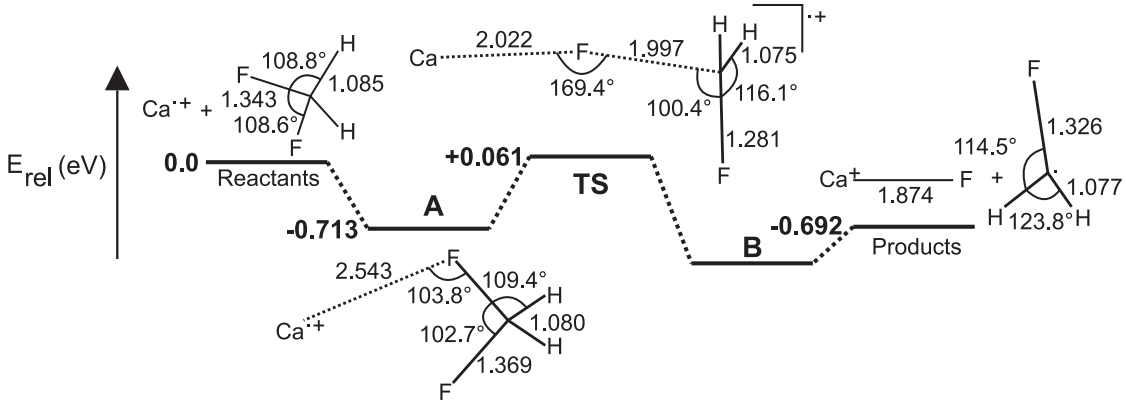


Figure 6.11: Turning point energies and geometries for the $Ca^+ + CH_2F_2 \rightarrow CaF^+ + CH_2F$ ground state potential surface, calculated by Harvey [206].

We might also rationalise the increased barrier height in terms of the bonding in the transition state. Progression from the initial ion-molecule complex to the transition state involves the weakening of the R-X bond (see Fig. 6.11) and the beginning

of Ca-X bond formation. Thus, we might expect the relative difference between these bond energies to provide some understanding of the transition state energy relative to the reactants. Given that the Ca-F bond energy is common to both cases, the relative difference in transition state barrier height can be rationalised in terms of the stronger C-F bonds in difluoromethane (a +4 kcal/mol difference: B(R-F) = 111 kcal/mol for R = $CH_2F$, and 107 kcal/mol for R = $CH_3$ [213]). Following the transition state the Ca-X bond is strengthened in the product ion-molecule complex, which then dissociates to form the products. The observation of a negligible rate constant for the ground state reaction strongly supports the existence of a real barrier on the ground state surface. In the excited states however, there is additional energy available to surmount any barriers, and the reaction may proceed. Additional information about the topology of the excited state potential surfaces is nevertheless desirable, and this would require further electronic structure calculations.

The factor of four difference between the excited state rate constants at 5 K and 196 K is somewhat more challenging to rationalise. The translational energy difference between these two regimes corresponds to about $1.6\times10^{-2}$ eV. If the reaction proceeds via the formation of an ion complex, we might expect this extra translational energy to be distributed into the internal modes of the complex. Given enough time for the redistribution of this internal energy within the complex, it seems unlikely that such a small change in the translational energy of the reactants can result in such a marked variation in rate constant; this may indicate non-statistical behaviour in the reaction dynamics. If this effect is indeed real, then it must depend intimately on the topology of the excited state potential energy surfaces, possibly indicating the presence of a very small barrier. Again, further electronic structure calculations are desirable in this regard. Additionally, little is known about the rotational population distribution of this asymmetric-top

molecule post-velocity-selection. As a result of the very low $CH_2F_2$ flux transmitted by the velocity-selector relative to the other neutral reactants employed here, the relative uncertainty in the $CH_2F_2$ number density at the Coulomb crystal is approximately double that of the other gases. In addition, the low $CH_2F_2$ flux necessitates extrapolation to much lower currents from the Residual Gas Analyser (RGA) for calibration of the number density. It is not known if a linear relationship between reactant pressure (as measured with the ionisation gauge) and RGA current is a good approximation at these very low currents; uncertainty arising from any weakness in this assumption is not accounted for in the error bars in Fig. 6.10. It is important to be mindful of these factors when considering the difference between the rate constants at 5 K and 196 K for this particular reactant.

### 6.3.3 Reaction with Chloromethane

Similar reaction experiments were performed in the case of $Ca^+ + CH_3Cl \rightarrow CaCl^+ + CH_3$, and Fig. 6.12 shows the measured rate constants as a function of the total excited state population. The rate constants for ground and combined excited states in each collision energy regime ($\langle E_{\text{coll}} \rangle / k_{\text{B}} = 5$ and 199 K) are listed in Table 6.4 along with other relevant theoretical values.

In the $Ca^+ + CH_3Cl$ reaction, the observed trends in the rate constants appear similar to the case of fluoromethane: the ground state rate constant is smaller than might be expected in the context of capture theory, yet the excited state rate constants agree well with ADO theory at 199 K, and reasonably well at 5 K with ACCSA theory. Again, *ab initio* electronic structure calculations indicate the existence of a submerged barrier on the ground state potential surface (see Fig. 6.13). Therefore the interpretation of these results broadly mirrors that of the $Ca^+ + CH_3F$ results: the submerged barrier acts as a dynamical bottleneck, suppressing the ground state rate constant. The reduced separation (relative to

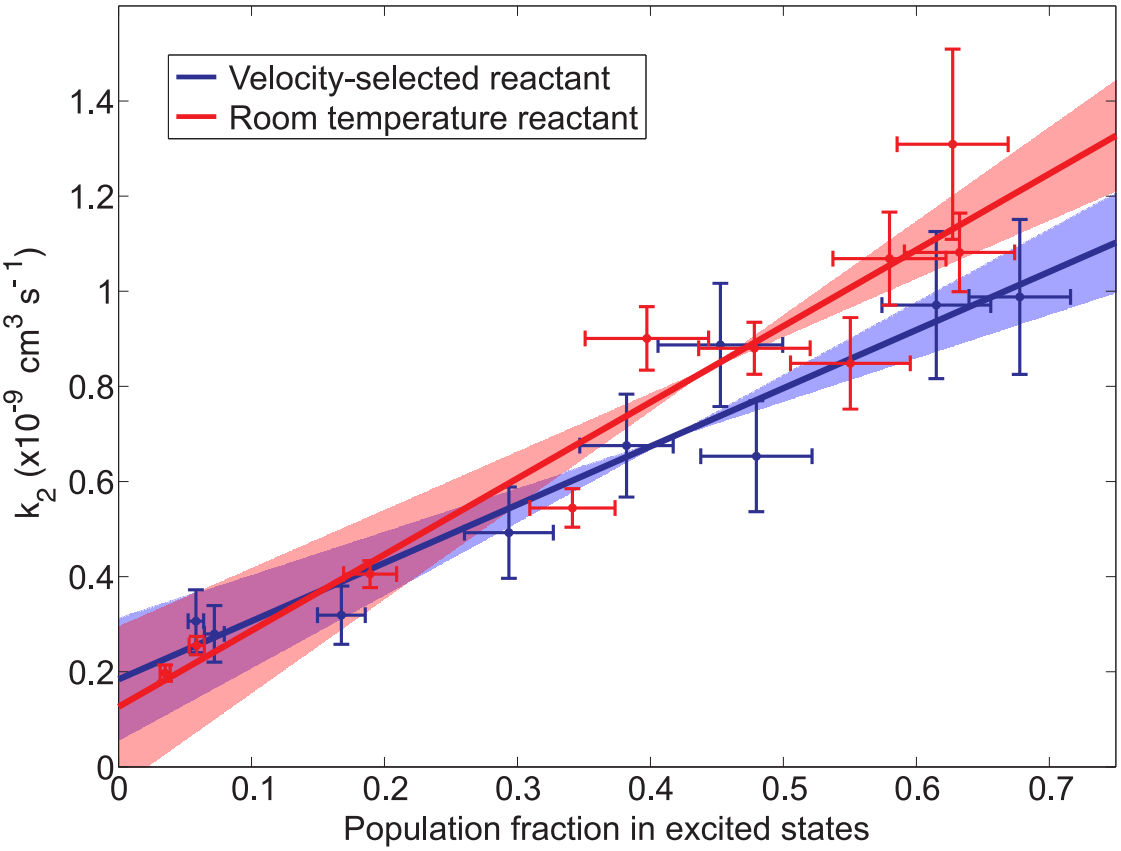


Figure 6.12: Variation of the observed bimolecular rate constant as a function of the total excited state population of $^{40}Ca^{+}$ for the reaction of $Ca^{+}$ + $CH_3Cl$. Reactions were performed in two collision energy regimes: $\langle E_{coll} \rangle / k_B = 199$ K (room-temperature $CH_3Cl$ molecules) and $\langle E_{coll} \rangle / k_B = 5$ K (velocity-selected $CH_3Cl$ molecules). The shaded areas indicate the 95% confidence interval for the corresponding data fit, and are used to calculate the rate constant uncertainties.

the ground state) between the excited state surfaces and the higher energy valence bond state surface corresponding to charge transfer from $Ca^{+}$ to $CH_3Cl$ could result in a stronger avoided crossing that also occurs at larger separations with respect to the entrance channel. This could lead to a reduced submerged barrier height, which agrees with the observation that the reaction on the excited state surfaces appears to proceed in an effectively barrierless manner for the case of chloromethane.

In contrast to the fluoromethane reaction however, there is some small suggestion that the reaction is faster at higher energies, mainly from the combined excited

| $Ca^+ + CH_3Cl \rightarrow CaCl^+ + CH_3$ | | | |
|---|---|---|---|
| Rate Constant ($\times 10^{-9}$ cm$^3$ s$^{-1}$) | T = 5 K | T = 199 K | T = 300 K |
| This work ($^2S_{1/2}$) | 0.18(13) | 0.13(17) | – |
| ($^2P_{1/2}$+$^2D_{3/2}$) | 1.41(18) | 1.73(21) | – |
| Adiabatic capture ($T_{rot}$ =$T_{trans}$) | 9.55 | 1.31 | 1.10 |
| Adiabatic capture ($T_{rot}$=300 K) | 1.73 | 1.14 | 1.10 |
| Average Dipole Orientation | – | 2.06 | 1.81 |
| Langevin | 1.04 | 1.04 | 1.04 |

Table 6.4: Comparison between experimental and theoretical rate constants for the $Ca^+ + CH_3Cl \rightarrow CaCl^+ + CH_3$ reaction.

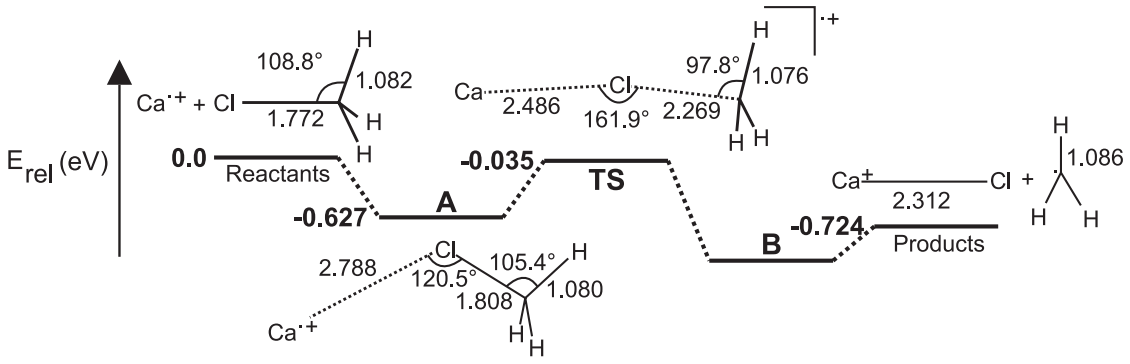


Figure 6.13: Turning point energies and geometries for the $Ca^+ + CH_3Cl \rightarrow CaCl^+ + CH_3$ ground state potential surface, calculated by Harvey [206].

states. However this is less clear cut than in the case of fluoromethane because there appears to be no difference between the measured 5 K or 199 K rate constants within the experimental uncertainty. In addition, the submerged barrier for the $Ca^+ + CH_3Cl$ ground state surface is calculated to be only 0.035 eV below the reactant asymptote whereas the barrier is 0.17 eV below the asymptote on the $Ca^+ + CH_3F$ ground state surface (despite the weaker halomethane bond in the $CH_3Cl$ case: B($H_3C$-X) = 76.7 kcal/mol and 107 kcal/mol for X = Cl and F respectively [213]). This explains the observed decrease in the ground state rate

constant by a factor of three for the $CH_3Cl$ reaction, relative to that of $CH_3F$, in both collision energy regimes.

The difference between these two reaction systems is nevertheless rather small, and we must be conscious of the appreciable uncertainty in the neutral reactant number densities, which stems primarily from the determination of gas sensitivity factors for the ionisation pressure gauge (see Table 4.5). Further investigation would be needed to obtain more accurate measurements of these values (as suggested in the next section), and discussion should strictly be limited to that of large absolute differences in reactivity, or for a given reactant, the relative differences between rate constants in the ground and excited states or at different collision energies. Finally, the MPW1K calculations used for the electronic structure calculations described in this chapter are not accurate enough to predict the barrier heights quantitatively, but the qualitative trend of a predicted increase in barrier height from $CH_3F$ to $CH_3Cl$ to $CH_2F_2$ should be reliable [206].

Further information is also necessary to determine whether it is possible to form the products in the excited state; if this remains energetically unfeasible given the amount of electronic excitation of the reactants, then non-adiabatic surface-hopping effects may be important. Given the exothermicity of the reaction, the formation of the first excited state ($^2A_1$') of the methyl radical is clearly not possible as this state lies at 5.73 eV relative to the methyl ground state [211]. The analogous data does not appear to be available for $CaCl^+$ or $CaF^+$, therefore it is not clear at the current time whether these electronically-excited products can be formed.

### 6.3.4 Summary and further work

In this chapter we have examined the application of the optical Bloch equations to our experiment setup in order to calculate the average steady-state populations of

the electronic quantum states involved with the laser cooling of a $^{40}Ca^{+}$ Coulomb crystal. For three reaction systems, measurements of the rate constants have been performed at collision energies of approximately 5 K and between 196 and 243 K whilst systematically varying the relative state populations. This has allowed us to obtain rate constants involving the ground state and combined excited states of $Ca^{+}$ respectively. Subsequently these rate constant values have been compared, and examined in the context of various ion-molecule capture theories. The roles of both real and submerged barriers on the ground state potential surfaces of these reactions have been highlighted and point to the need for further *ab initio* calculations.

Having carried out this work, a number of possible improvements and refinements to the experimental methods have presented themselves. In the first instance it would prove useful to stabilise the absolute calibration of the High Finesse WS-U wavemeter against a reference. In this way we would hope to avoid the drifts in the laser detunings that represent a major contribution to the error in establishing the average quantum-state populations of the calcium ions in the crystal. Secondly, in order to reduce the error in the absolute rate constant, it would be beneficial to establish the number densities of the various molecular reactants at the ion crystal with reduced uncertainty. This could be achieved by having a full-range calibration of our particular ionisation gauge's response performed (see Ref. [214]) for each gas used in the reaction experiments, over the entire useful pressure range of the gauge. This is the only way to be absolutely sure of the gas sensitivity factors (to within 1–2%) for our ionisation pressure gauge, and would save us relying on published values (or extrapolations) which may differ by 20% or more from the true values for any given gauge [193]. Additionally, the length of time between flux measurement and the reaction experiments (which is brought about by the need to open the vacuum chamber and rearrange the apparatus for each scenario) could

be a handicap if there is any change to the guiding efficiency in the interim. For example, slight breakdowns across the insulators, or gas deposits on the electrode surface can cause very small currents to flow between the electrodes, and it is not known how this affects the magnitude of the guided flux. It would be advantageous to establish some form of flux measurement that could be performed *in situ*, such that neutral molecular number density data could be established over a longer period and associated directly with any reaction work carried out at a particular time.

In principle, it is possible to separate the rate contributions from each of the excited states of the $Ca^{+}$ ions, however there are caveats to consider. Separate measurements of these rate contributions depend on our ability to vary the relative population of the two excited states. According to the eight-level OBE treatment, the population of the $^{2}D_{3/2}$ state dominates over that of the $^{2}P_{1/2}$ state (which is limited to a population fraction of around 0.1–0.2). The relative population difference between the $^{2}D_{3/2}$ and $^{2}P_{1/2}$ states can be increased by reducing the power of (or even chopping) the repumping laser, as well as increasing its detuning, thereby increasing the population of the metastable $^{2}D_{3/2}$ state at the expense of the ground and upper excited state populations. Whilst this would make the combined excited state rate constant tend towards the value of the $^{2}D_{3/2}$ state rate constant, it would also reduce the observed fluorescence and lead to inefficient cooling and therefore crystal instability. Both of these factors make an already challenging experiment more difficult, and this is the primary reason why we have limited the current work and not attempted to separate the contributions of the $^{2}P_{1/2}$ and $^{2}D_{3/2}$ states to the global rate constants. Also, it is likely that the difference in rate constant between the two excited states will not be as great as the rate difference between the ground state and an excited state. Within our current experimental error it is not clear if we could currently resolve this difference.

It has already been experimentally demonstrated that the use of applied magnetic fields and well-defined laser polarisations can afford more refined control over the internal state populations of the laser-cooled ions. For example, methods such as the state-selective shelving of population into specific $m_J$ sub-levels are important in areas such as quantum information processing [102, 175]. The selective population of different quantum states can result in different electron density distributions, and could provide information on orientation-dependent reaction cross-sections. A topic for future study could be the investigation of such alignment effects or vector correlations in reactive collisions.

In general the velocity-selector is a relatively simple cold molecule source in terms of its implementation and operation, and it has the flexibility to guide a fairly wide range of polar species. The velocity-selector's main limitations with respect to reactive collision studies include its (only) partial rovibrational state selectivity [43], the lack of rotational cooling, and the fact that the properties of the effusive source limit the flux and densities of guided molecules. Increasing the source pressure in an effort to increase guided flux eventually results in "boosting" of the velocity distribution, defeating the point of the exercise. This can be mitigated by cooling the source gas to compress the velocity distribution and increase guiding efficiency, but ultimately this is limited by condensation of the molecules inside the effusive nozzle. A future improvement to our velocity-selector would be to follow in the footsteps of van Buuren *et al.* [215, 216] and combine the effusive source with a buffer gas cooling cell containing helium at around 5 K, or neon at around 15 K. This allows effective compression of the velocity distribution prior to guiding, which will increase the eventual density of the guided molecules at the crystal. Additionally, such a method allows the internal degrees of freedom of the guided sample to be effectively cooled. It has also been demonstrated (in formaldehyde) that the tuning of helium atom density near the effusive nozzle allows some control

over the population distribution of the low-lying rotational states, which could be applied in collision studies. The future upgrade of our velocity-selection apparatus in this manner is currently under investigation.

As well as improving the velocity-selector, we are currently attempting to couple the Stark decelerator to the ion trap apparatus as an alternative source of cold neutral molecules. A Stark decelerator provides narrower neutral reactant velocity distributions centred at more precisely tunable velocities than a quadrupole guide velocity-selector. Molecular number densities of Stark decelerated species, expected (on average) to be comparable to those from the guide, will ideally be measurable in between reaction experiments via a REMPI detection scheme involving ionisation lasers coincident with the trap centre. As mentioned previously, further work involving the Stark decelerator as the source of the cold neutral molecules could open up some interesting new possibilities in both reactive and inelastic collision studies. Whilst the molecules exiting the quadrupole guide (in its current state) are still rotationally hot, the same is not true for molecules leaving the Stark decelerator. Owing to the supersonic expansion of the molecular beam, and the state-selectivity of the Stark deceleration, we will be able to produce neutral molecules in both selected and low energy rotational quantum states. This will allow investigation of state-specific rate constants, and in particular the large increases in rate constant predicted by adiabatic capture theories for ion-molecule reactions where the molecule is in low rotational quantum states.

Additionally, there is also the possibility of producing and sympathetically cooling molecular ions in specific quantum states through methods such as multi-photon ionisation — indeed the state-selectivity of the Stark decelerator itself could allow the loading of state-selected molecular ions through photoionisation of state-selected molecules. This ultimately paves the way for the experimental

investigation of fully state-selected chemical reactions. These would involve both reactants in selected quantum states, approaching at tunable collision energies and with an energy resolution far in excess of that possible with the velocity-selector (100 mK energy resolutions have been projected for low rotational states [43], whereas collision energy distributions arising from guided neutrals are typically 10–15 K wide). Thermalisation of the rotational distribution of trapped molecular ion species is expected to occur on a shorter timescale than current reaction experiments; however, this problem could be mitigated by cryogenic cooling of the trap environment (reducing redistribution due to blackbody radiation), working with non-polar molecular ions, or via the implementation of continuous optical rotational-cooling [107, 114].

To date, $ND_3$ has been successfully decelerated in the Stark decelerator, and the installation of a fast-opening mechanical shutter in the beam path has demonstrated the practicality of admitting only the decelerated molecules to the crystal. Work to improve the efficiency of the decelerator and couple it to the ion trap apparatus is currently being performed. Possible initial goals involve the deceleration of $CH_3F$, which would allow direct comparison with the velocity-selected reaction of $Ca^+ + CH_3F \rightarrow CaF^+ + CH_3$. Subsequent ideas include the investigation of reactions such as $ND_3 + Kr^+$ where $Kr^+$ is produced state-selectively via a (2+1) REMPI ionisation scheme, and the study of fully state-selected molecular ion-molecule reactions.

Given that the above possibilities include the study of reactions of state-selected molecular ions in Coulomb crystals, the next chapter presents an investigation of the reaction of sympathetically-cooled molecular ions at low collision energies.

# Chapter 7

# Reaction of sympathetically-cooled molecular ions with translationally-cold neutral molecules

The experimental setup outlined so far can be extended to study a wide range of ion-molecule reactions involving laser-cooled ions such as $Be^+$, $Ca^+$, $Mg^+$ or $Ba^+$, and suitable neutral molecules. However the same setup has the potential to be much more general through the study of reactions involving sympathetically-cooled atomic or molecular ions, whose identity is not restricted by the need for a simple energy level structure as in the case of direct laser cooling. An ideal choice of reaction system would involve a neutral reactant species unreactive with respect to the laser-cooled ions or the reaction product ions. The progress of reaction can be tracked in one of two ways: The most general technique involves the use of resonance excitation mass spectrometry at regular time intervals throughout the reaction. In this way, the changing intensity of a given mass/charge peak is correlated with the changing number of ions of the corresponding species within the crystal. This method has been applied to the study of $H_2^+ + H_2 \rightarrow H_3^+ +$

H using laser-cooled $Be^+$ ions [126]. A slightly less general (but more convenient) choice of reaction system would involve reactant and product ions with masses that lie either side of the mass of the laser-cooled ions. In such a situation, the heavier reactant (or product) ions would lie on the outside of the framework of the laser-cooled ions, while the lighter product (or reactant) ions would lie in the centre. In this case, the relative numbers of reactant and product ions may be differentiated clearly by analysing changes in the imaged fluorescence of the laser-cooled ions; it is this method that we invoke in the current study.

This chapter deals with the first study of this kind to involve translationally-cold ($\sim$5 K) velocity-selected neutral molecules, in what is effectively a proof-of-concept experiment involving the charge transfer reaction between $OCS^+$ and $ND_3$.

## 7.1 Experimental Procedure

In these experiments we begin by loading a $^{40}Ca^+$ Coulomb crystal in the usual manner. Laser-cooling parameters are set in order to provide efficient cooling, but we are not overly concerned about the steady-state quantum populations of the $^{40}Ca^+$ ions, as they are only spectators in the actual reaction. Once a pure $^{40}Ca^+$ crystal is prepared, we begin to leak OCS into the chamber at partial pressures of approximately $1 \times 10^{-8}$ mbar. An additional ionisation laser beam at 280 nm (the frequency doubled output of a pulsed Nd:YAG pumped-dye laser operating at 10 Hz) is focused through a 30 cm focal length lens to the trap centre. Typically the ionising laser beam is admitted at a power of around 0.8–1 mJ per pulse (or 8–10 mW), and for a duration of 5–60 s, although depending on vacuum conditions and OCS partial pressure we have ionised for periods of up to 5 minutes. This beam is aligned perpendicular to the cooling lasers in order that it does not strike the grounded mesh that insulates the trap from the large electric fields of the

quadrupole guide (see Fig. 7.1). Previous attempts to ionise OCS with the ionising laser parallel to the cooling lasers resulted in trap loss of the crystal ions, and this was attributed to photo-ejection of particles from the mesh by the 280 nm beam.

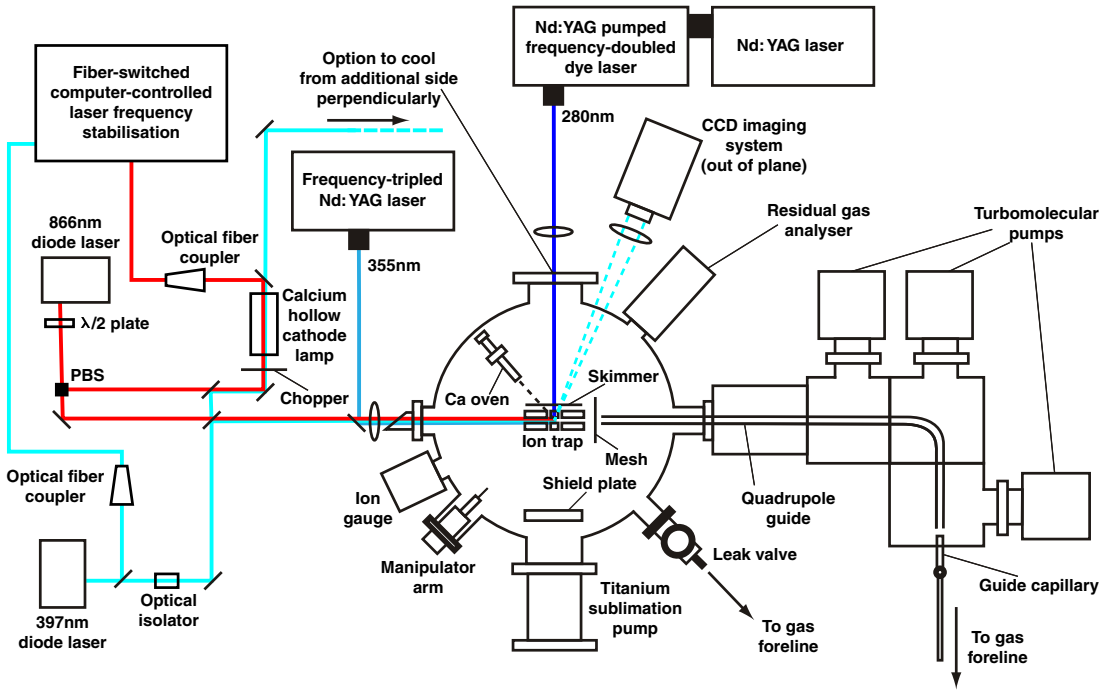


Figure 7.1: Schematic of the experimental apparatus for performing low-temperature sympathetically-cooled ion-molecule reactions with the quadrupole guide velocity-selector. The ionisation beam at 280 nm is included for the purpose of $(2+1)$ Resonance-Enhanced Multiphoton Ionisation of OCS.

The 280 nm beam ionises OCS via $(2+1)$ resonance-enhanced multiphoton ionisation (REMPI) proceeding via the $[^2\Pi_{1/2}]4p\pi;^1\Delta \leftarrow \tilde{X}^1\Sigma^+$ states [217], and this is performed *in situ* such that the $OCS^+$ ions generated are sympathetically-cooled into the existing $^{40}Ca^+$ Coulomb crystal. As the mass of $OCS^+$ (60.07 u) is greater than that of $^{40}Ca^+$ these heavier ions aggregate around a central $^{40}Ca^+$ core in accordance with the inverse mass dependence of the effective radial trapping potential (see Sections 3.4.2 and 2.2.2). In general $OCS^+$ is loaded until a strong flattening of the outer edge of the $Ca^+$ core is observed (see Fig. 7.2(b)), which indicates the presence of a large number of $OCS^+$ ions. At this stage $ND_3$ is introduced to

the crystal, either by admittance of a room-temperature sample through the leak valve, or at low translational energies via guiding with the velocity-selector.

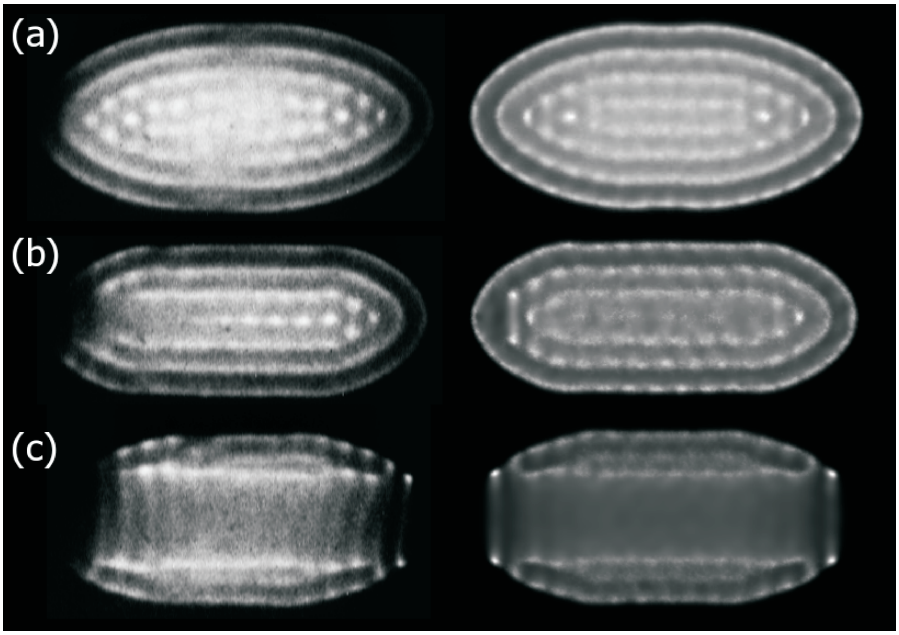


Figure 7.2: Coulomb crystal images observed in the course of the room temperature $OCS^+ + ND_3$ reaction (left) and simulated images (right). In all cases only $Ca^+$ ions are visible, nevertheless observation of distortions in the $Ca^+$ fluorescence allows the determination of the number of dark ions. (a) $Ca^+$ Coulomb crystal before production of $OCS^+$. (b) With sympathetically-cooled $OCS^+$ surrounding the $Ca^+$ core. (c) After reaction with $ND_3$ with $ND_3^+$ product ions in the core.

As the charge-transfer reaction proceeds according to $OCS^+ + ND_3 \rightarrow OCS + ND_3^+$, the $ND_3^+$ product ions are sympathetically-cooled into the crystal. With a mass of 20.06 u, they are lighter than $^{40}Ca^+$ and aggregate closer to the trap axis, displacing the $^{40}Ca^+$ ions radially. In the 2D projection of the fluorescence imaged by the camera system this manifests as a splitting apart of the $^{40}Ca^+$ fluorescence, such that a dark core appears to grow over time in the images (see Fig. 7.2(c)). The progress of reaction against time is logged by a sequence of experimental fluorescence images. Comparison of these images with those generated by Molecular Dynamics simulations of multi-component crystals enables the determination of the number of ions of each species present in the crystal at each time interval

recorded in a reaction sequence. This allows the calculation of the rate constant, as detailed in the next section. A better understanding of the structure present in the fluorescence images shown in this chapter may be attained by studying Fig. 3.4 in Section 3.1.2, which shows a simulated image of a tri-component crystal consisting of $Ca^+$, $OCS^+$ and $ND_3^+$, with all the ions made visible.

## 7.2 Determination of rate constants via molecular dynamics simulations

The rate of reaction for $OCS^+ + ND_3 \rightarrow OCS + ND_3^+$ can be expressed as

$$\frac{\mathrm{d}n_{\mathrm{ND_3^+}}}{\mathrm{d}t} = -\frac{\mathrm{d}n_{\mathrm{OCS^+}}}{\mathrm{d}t} = k_2 \; n_{\mathrm{OCS^+}} \; n_{\mathrm{ND_3}}, \tag{7.1}$$

where $k_2$ is the bimolecular rate constant for the reaction. The analysis is more sensitive to the appearance of the dark core due to the lighter product ion generation, than to the loss of edge distortion of the $^{40}Ca^+$ fluorescence due to depletion of the heavier reactant ions, therefore we treat the equation in terms of $\frac{\mathrm{d}n_{\mathrm{ND_3^+}}}{\mathrm{d}t}$. We express the number of $OCS^+$ ions remaining in the crystal as $n_{\mathrm{OCS^+}} = n_{\mathrm{OCS^+}}(0) - n_{\mathrm{ND_3^+}}$ which means that

$$\frac{\mathrm{d}n_{\mathrm{ND_3^+}}}{\mathrm{d}t} = k_2 \; n_{\mathrm{ND_3}} \left( n_{\mathrm{OCS^+}}(0) - n_{\mathrm{ND_3^+}} \right). \tag{7.2}$$

This expression can then be integrated to obtain

$$n_{\mathrm{ND_3^+}}(t) = n_{\mathrm{OCS^+}}(0) \left( 1 - e^{-k_2 n_{\mathrm{ND_3}} t} \right) = n_{\mathrm{OCS^+}}(0) \left( 1 - e^{-k_1 t} \right), \tag{7.3}$$

where $k_1$ is analogous to the pseudo-first-order rate constant described in Section 4.3.2 for the direct reaction of $^{40}Ca^+$. Molecular Dynamics simulations are performed for 5–6 images per reaction sequence, allowing $n_{\mathrm{ND_3^+}}(t)$ data to be compiled. We assume that the final value of $n_{\mathrm{ND_3^+}} = n_{\mathrm{OCS^+}}(0)$, which is reasonable as the

crystal structure is observed to remain static once all the $OCS^+$ ions have been reacted away. There may still be heavier dark impurities present, and these are assumed merely to spectate. In general we assume that there are no competing reactions occurring that would interchange any heavier or lighter impurities (with respect to the mass of $^{40}Ca^+$). We may then perform a non-linear least-squares fit to these data using the functional form described in Eq. 7.3 to recover $k_1$ the pseudo-first-order rate constant. This, in conjunction with a knowledge of the $ND_3$ number density at the position of the crystal when guiding (see Section 4.2.2), or when admitting neutral reactant to the chamber through the leak valve, allows us to recover the bimolecular rate constant $k_2$.

A typical reaction sequence is illustrated in Fig. 7.3, where both experimental and simulated images are compared. A composition change of just two ions (lighter than $^{40}Ca^+$) produces an observable difference in the simulated images. In general our sensitivity to the number of lighter ions is maximised with smaller numbers of $^{40}Ca^+$ ions in the crystal, and at lower values of $V_{RF}$ where the relative change in the width of the dark core upon the addition of lighter ions is amplified.

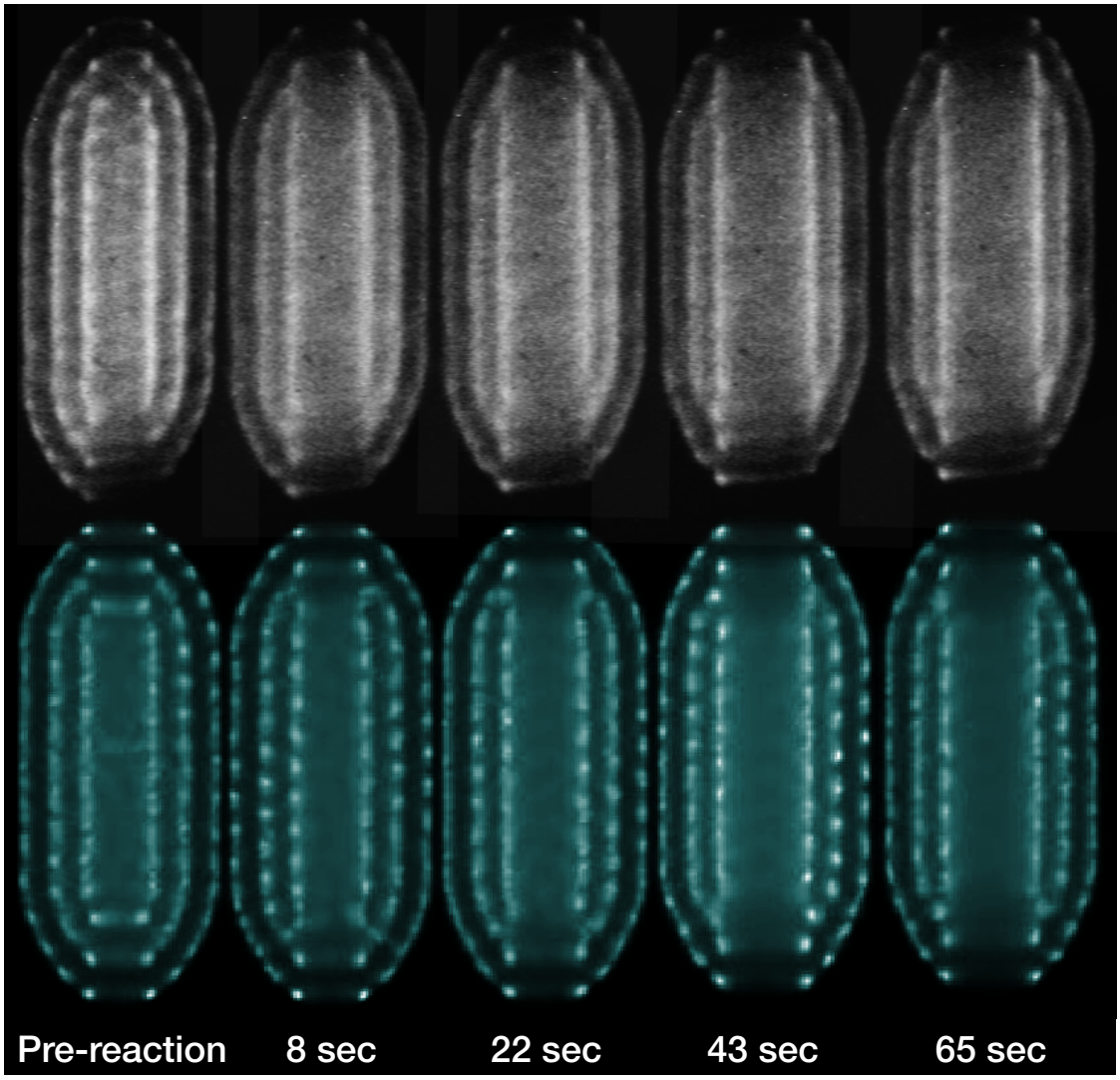


Figure 7.3: Top row: An $\langle E_{\rm coll}\rangle/k_{\rm B} = 337$ K reaction sequence, with images recorded at intervals over the course of 65 seconds. Bottom row: Simulations performed in the analysis, determining the addition of 41 ions lighter than $Ca^+$ over the corresponding time. Simulated images are superimposed on experimental images to determine the best fit.

## 7.3 Experimental results

A number of guided reactions were performed using $V_{\text{quad}} = \pm 3$ kV, which, given crystal sizes similar to those shown in Fig. 7.3, results in average $OCS^+/ND_3$ collision energies of approximately $\langle E_{\text{coll}} \rangle / k_{\text{B}} = 8$ K*. A similar number of reactions were carried out using room-temperature samples of $ND_3$ admitted through the leak valve (resulting in an average collision energy of $\langle E_{\text{coll}} \rangle / k_{\text{B}} = 337$ K as discussed in Section 4.3.3). Table 7.1 summarises the values of the rate constants obtained in these two collision energy regimes, along with a previous experimental value from the literature.

| $OCS^+ + ND_3 \rightarrow OCS + ND_3^+$ | | | |
|---|---|---|---|
| Rate Constant ($\times 10^{-9}$ cm$^3$ s$^{-1}$) | T = 8 K | T = 300 K | T = 337 K |
| This work ($\pm 3$ kV) | 2.0(5) | – | 1.8(2) |
| SIFT, Lindinger *et al.* [218] | – | 2.3* | – |
| Average Dipole Orientation | – | 1.79 | 1.73 |
| Langevin | 1.05 | 1.05 | 1.05 |

Table 7.1: Comparison between experimental and theoretical rate constants for the $OCS^+ + ND_3 \rightarrow OCS + ND_3^+$ reaction. Values marked with an asterisk refer to the non-deuterated case.

We do not resolve a measurable difference between the rate constants measured at average collision energies of $\langle E_{\text{coll}} \rangle / k_{\text{B}} = 8$ and 337 K. Given the experimental uncertainty there appears to be a reasonable level of agreement between our measured rate constants and the previous experimental value at 300 K. There also

*These calculations were carried out in a manner analogous to those detailed in Section 4.4.3. It is worth noting that the reaction of molecular ions lighter than the laser-cooled ions can result in average collision energies much less than 8 K, as ions nearer the trap axis have much lower effective kinetic energies. For example, simulations for reaction of $ND_3$ with $ND_3^+$ (with $Ca^+$ spectating) suggest that $\langle E_{\text{coll}} \rangle / k_{\text{B}} \approx 1$ K at $V_{\text{quad}} = \pm 3$ kV.

| $\mu$ (D) | $\tilde{\alpha}$ (Å$^3$) | C(T) |
|---|---|---|
| 1.50 | 3.0 | 0.2098 (300 K)<br>0.2047 (337 K) |

Table 7.2: Parameters used in the theoretical calculation of rate constants for the $OCS^+ + ND_3$ reaction.

appears to be an acceptable level of agreement between our experimental values and the ADO theory rate constants.

## 7.4 Improvements and further work

Several challenging aspects were uncovered in the course of these experiments, mainly regarding attempts to cleanly load $OCS^+$ ions into the crystal. Often we appeared to be introducing lighter impurities (presumed to be $S^+$) into the crystal either instead of, or along with heavier ions (presumably $OCS^+$). Additionally we were not originally able to verify the exact mass of the species involved in this study through the single-ion mass spectrometry techniques described in Chapter 5. Difficulties in both the attempted single $OCS^+$ ion studies in Chapter 5 and the bulk reaction studies in this chapter may have arisen due to the fact that the apparatus was not fully optimised to carry out these experiments. The clean addition of molecular ions to the crystal should be a relatively simple endeavour; we are confident that a small number of optimisations can drastically increase the ease with which both single-ion and bulk crystal reaction experiments involving sympathetically-cooled ions may be performed.

For the most part, the proposed optimisations for experiments involving the reaction of large numbers of sympathetically-cooled molecular ions are similar to those proposed for single molecular ion experiments (described at the end of Chapter 5). The addition of a beam dump for the 280 nm ionising laser inside the chamber

would prevent the relatively high energy beam striking surfaces that have calcium or other species deposited on them. During these experiments our ionising beam struck the stainless steel plate shielding the main chamber from the titanium sublimation pump, and this plate was also struck by the beam of calcium from the oven. In theory any ions generated from this plate should not be able to penetrate back inside the ion trap, but if any stray reflections were incident with the inner surfaces of the trap electrodes, ion impurities could be generated (this may explain the appearance of additional $Ca^+$ ions when ionising with the calcium oven off). Also, a calcium oven shutter would be a welcome addition to the experimental setup. This would speed up loading attempts as the oven could be left on at a lower current, eradicating the time spent waiting for it to reach a steady operating temperature. In particular, the ability to detect the molecular ions during their generation inside the trap would also help by allowing us to verify that the production of molecular ions is optimised. These steps, along with a good deal of care when aligning and focusing the molecule-ionising laser should result in stronger reproducibility when loading crystals of a particular composition.

At the time of writing, work in the area of molecular ion-molecule reactions continues in anticipation of the coupling of the Stark decelerator to the ion trap. This new combined apparatus will indeed have the capability to detect molecular ions formed inside the trapping region via Resonantly-Enhanced MultiPhoton Ionisation (REMPI). This can be achieved by applying a static voltage to the trap electrodes such that any molecular ions formed by REMPI inside the trap will be accelerated into a field-free time-of-flight tube and onto an MCP detector, allowing a time-of-flight mass spectrum to be generated.

# Chapter 8

# Conclusions

## 8.1 Summary

This thesis has detailed the first coupling of a quadrupole velocity-selector to an ion trap apparatus; this was carried out in order to study ion-molecule reactions at low temperatures. Initially, this required the construction of a new apparatus for trapping and laser-cooling atomic ions to very low kinetic energies, whereupon a phase change to an ordered lattice-like structure occurs. The resultant system is characterised by strongly localised ions, with secular temperatures in the millikelvin regime, that persist in the trap for many hours. These ions can act as a heat bath and, through the Coulomb interaction, are able to translationally cool a sample of molecular ions introduced into the trap. Through this sympathetic-cooling, molecular ions may be cooled to the translational temperature of the laser-cooled ions and incorporated into the crystal structure. Single and multi-component Coulomb crystals have been explored experimentally and through the use of Molecular Dynamics simulations. These cold crystallised atomic or molecular ions may be reacted with a slow beam of neutral polar molecules, produced by a quadrupole guide velocity-selector, as originally developed by Rempe *et al.* [46]. The velocity-selector acts as a low-pass kinetic energy filter, and selectively

retains the low energy fraction of the Maxwell-Boltzmann velocity distribution of a room-temperature gas sample. The slow-moving molecular flux from the guide has been characterised at a range of operating voltages for all the reactant molecules employed in this work. The measured velocity distributions show that the mean speeds and translational temperatures of guided samples are tunable over a small range through a variation of the guide voltage. In general, the most-probable translational kinetic energies of molecules generated by the guide are found in the range $E_{\rm kin}/k_{\rm B}$ = 1–2 K. The velocity-selector is mounted such that translationally cold neutral molecules are guided directly into the laser-cooled ion ensemble.

By imaging the spontaneous fluorescence emitted by the laser-cooled ions as a function of time, the progress of various reactions may be followed with exceptional sensitivity; even a single reactive collision can be detected. The sympathetic-cooling of product ions has also been demonstrated, and the accumulation of product ions over minutes or hours allows practical use of the very low number densities of slow moving neutral molecules (between $\sim$2$\times$10$^4$ and 7 $\times$ 10$^6$ cm$^{-3}$) produced by the velocity-selector. Using the new setup, a range of chemical reactions have been studied at collisional temperatures approaching 1 K. These include the reactions of $Ca^+$ with $CH_3F$, $CH_2F_2$ and $CH_3Cl$, as well as the charge transfer reaction of $OCS^+$ with $ND_3$. This latter reaction represents a proof-of-principle experiment for the low temperature study of ion-molecule reactions involving sympathetically-cooled molecular ions and using a combined velocity-selector/ion trap apparatus. For each system, analogous reactions have also been performed at average collision energies between $\langle E_{\rm coll}\rangle/k_{\rm B}$ = 196–337 K (depending on reaction system) to allow a direct comparison with the low energy results. Using the methods outlined in Chapters 4 and 7, bimolecular rate constants have thus been obtained for all systems in two collision energy regimes. These values have been compared with those obtained from various capture theories and, for the reactions of $Ca^+$ with

the aforementioned halomethanes, analysed in the context of *ab initio* electronic structure calculations.

In the case of the direct reactions of $Ca^+$, a dependence of the rate constant on the extent of the electronic excitation of the laser-cooled ions has been demonstrated, and the relationship between this excitation and the laser-cooling parameters has been modelled within an appropriate theoretical framework. Manipulation of the laser-cooling parameters has allowed the separation of the contributions to the global rate constant from the ground ($^2S_{1/2}$) and combined excited states ($^2P_{1/2}$, $^2D_{3/2}$) of $Ca^+$, and this has allowed us to infer information regarding the reaction potential surfaces. In the reactions of $Ca^+$ with $CH_3F$ and $CH_3Cl$, ground state rate constants were measured to be smaller than might be expected from capture theories. This provides evidence for the existence of a submerged barrier on the ground state potential energy surface. Such a below-threshold barrier, which has been suggested to arise from an avoided crossing with a higher energy potential surface, can act as a dynamical bottleneck leading to a suppressed ground state rate constant. This is in agreement with *ab initio* calculations for both the $CH_3F$ and $CH_3Cl$ systems and, furthermore, the small increase in submerged barrier height when moving from $CH_3F$ to $CH_3Cl$ can be seen to correlate with the observation of a slight reduction in the ground state rate constant. Rate constants for the combined excited states ($^2P_{1/2}$ + $^2D_{3/2}$) are in reasonable agreement with capture theory and, relative to the ground state, the enhancement in rate is believed to occur due to a reduced submerged barrier height on the excited state potential surfaces. This reduction is suggested to be a consequence of the smaller energy difference between the excited state surfaces and the higher-energy valence bond state surface described by charge transfer from $Ca^+$ to the halomethane; this may result in a more strongly avoided crossing which would reduce the barrier height and mitigate the dynamical bottleneck. In the case of $Ca^+ + CH_2F_2$ the rate of reaction

from the ground state is too small to be measured with the current resolution, suggesting the existence of a real barrier on the ground state potential surface. This is supported by *ab initio* calculations which show the energy of the inner transition state to be above the asymptotic reactant energy by approximately 0.06 eV. The rate of reaction from the combined excited states at 196 K agrees well with simple capture theories, however at lower collision energy the rate constant still appears suppressed below capture theory predictions by a factor of approximately 3–4. This latter observation remains unexplained at the present time, but may indicate the presence of a small barrier on the excited state surface for this reaction.

In support of each of these direct reaction studies, we have demonstrated the identification of the sympathetically-cooled product ions through single-ion resonance-excitation mass spectrometry. This technique, originally developed by Drewsen and coworkers [104, 105], involves the excitation of oscillatory ion motion via the frequency-scanning of an additional radiofrequency field (or similar modulation of the radiation pressure). When the space-charge drag effects encountered with multiple ions are removed (through the sympathetic-cooling of a single atomic or molecular ion by a single laser-cooled atomic ion) the motional mode frequencies may be related directly to the mass/charge ratios of the constituent ions. Given a knowledge of the parameters for a pure two-ion $Ca^+$ crystal, this allows accurate identification of the sympathetically-cooled ions. In this manner, we have demonstrated the production of sympathetically-cooled $CaX^+$ ions in the reactions of $Ca^+$ with the aforementioned halomethanes. Attempts to confirm the identity of the non-fluorescing ions in the $OCS^+ + ND_3$ reaction were hampered by problems with reproducibility in the number of ions loaded, and the generation of extra $Ca^+$ or non-fluorescing ions.

## 8.2 Future work

The velocity-selector can be used to produce a range of translationally-cold neutral polar molecules, given a strong enough Stark effect. This means that the study of further systems such as $Ca^+ + CH_3NO_2$, $CH_3CHO$ or $CH_3CN$ is possible. Increasing the bend radius of the guide would also allow the guiding of molecules with larger mass or smaller effective dipole moments. This may enable the efficient production of slow moving HDO molecules, for example, and in conjunction with single-ion mass spectrometry would enable a measurement of the branching ratio of $Ca^+ + HDO \rightarrow CaOH^+(CaOD^+) + D(H)$. Considered improvements to the velocity-selector centre primarily on the addition of a helium buffer gas cell close to the effusive nozzle. This method, which has recently been demonstrated experimentally by Rempe and coworkers [216], results in an increase in the guided flux and, more importantly, causes a large decrease in the number of populated rotational states. For example, in the case of formaldehyde, Rempe *et al.* demonstrated that control over the rotational populations was possible through variation of the helium atom density near the effusive nozzle [215]. This may have some interesting applications in future collision studies and this approach is currently being pursued in our laboratory.

Various incremental improvements to the ion trap apparatus are also envisaged. The addition of irises inside the UHV chamber itself have already been shown to drastically reduce the stray light that creates background noise in the fluorescence imaging. This enables clearer imaging of $Ca^+$ ions, which is especially important for the optimal performance of single-ion mass spectrometry studies. The introduction of a beam dump to the chamber will, we hope, reduce the problems encountered with the pure production of molecular ions. Addition of an oven shutter will hopefully minimise the deposition of calcium on various surfaces, as well

as speed up the repeated loading of the ion trap. An awareness of the problems associated with switching the identity of the gas that is admitted through our leak valve has also prompted the idea of a dual leak valve setup, whereby each gas is admitted through a separate leak valve (when high pressure valve purging is not an option). Together, these improvements should increase the efficiency with which we can carry out ion-molecule reaction studies involving molecular ions, and facilitate the verification of reaction pathways via single-ion resonance-excitation mass spectrometry. Another possible option to consider could be the use of higher-multipole ion traps [219]. These trapping configurations result in steeper potentials and larger field-free trapping regions. Ions confined in a multipole trap are expected to have a narrower kinetic energy distribution (which would improve the collision energy resolution in any associated reactive scattering studies) and be less susceptible to the ion heating generated by background collisions in high radiofrequency field regions. However, the generation of Coulomb crystals in these traps is a relatively recent development (*e.g.*, octupole traps [220]), and it remains to be seen how applicable these trap designs are.

Work to combine an ion-trap with a Stark decelerator is already being carried out in our laboratory. This will enable the production of translationally and internally cold packets of quantum state-selected neutral molecules, at a tunable final velocity and with a narrow velocity distribution, which can be focused into a Coulomb crystal. Such a combined apparatus would allow ion-molecule reactive collision studies to be carried out with greater collision energy resolution than the current velocity-selector/ion trap apparatus, and bring us one step closer to the goal of fully quantum state-selected reactions at tunable collision energies.

As mentioned in Chapter 4, a 131-stage Stark decelerator has already been assembled and tested by decelerating $ND_3$ molecules seeded in Xenon (see Fig. 4.7).

Additionally, a fast-opening mechanical shutter has now been implemented and tested, and this will enable the selective admission of only decelerated molecules to the ion trap chamber. Further refinements are desirable in order to enable the study of ion-molecule collisions. Three-dimensional focusing of the decelerated packets is necessary to enable the efficient transfer of the decelerated molecules into the ion trap, and increase the density of the molecular sample at the crystal. Practical work with $ND_3$ has demonstrated the feasibility of this plan through the combination of transverse focusing using hexapole electrode arrangements, and longitudinal focusing using a buncher (an additional set of electrode pair stages positioned a short distance after the decelerator's final stages). Initially, operation of the Stark decelerator/ion trap apparatus as a time of flight mass spectrometer is also envisaged. In order to confirm the production of particular molecular ions, a molecular beam will be sent through the Stark decelerator apparatus and ionised in the position of the ion trap centre. Large static voltages applied to the ion trap electrodes will accelerate molecular ions formed at the position of the trap centre through a time-of-flight tube and onto an MCP detector. In this way, we hope to optimise the production of molecular ions and the performance of the Stark decelerator. Additionally, the possibility of ejecting trapped ions onto the MCP detector is being explored. This may allow the (albeit destructive) characterisation of the number of trapped ions at a particular mass/charge ratio in a bulk crystal. Finally, the high translational energy resolution afforded by the decelerator also introduces the possibility of studying reactive resonances in state-selected ion-molecule reactions at higher collision energies, with $E_{\mathrm{coll}}/k_{\mathrm{B}} \approx 100$–$200$ K.

The experiments described in this thesis are some of the first to capitalise on the development of cold atomic and molecular sources for the study of ion-molecule reactive collisions at collision energies of $E_{\mathrm{coll}}/k_{\mathrm{B}} < 10$ K. However, further improvements in the field of cold matter are required before the study of *ultracold*

chemical reactions becomes a reality for more than a highly exclusive set of systems, such as those involving laser-cooled alkali atoms. In this regard, perhaps the most exciting recent studies are those of Jin, Ye and coworkers [98], who have succeeded in performing true ultracold reaction studies with KRb molecules, formed from the association of ultracold laser-cooled atoms in a magnetic trap. As well as improvements to methods for the translational cooling of atomic and molecular samples, the manipulation and cooling of internal states — for example those of sympathetically-cooled molecules in ion traps — is likely to be of paramount importance for low-energy chemistry studies. In this respect, advances in all-optical rotational cooling techniques such as those demonstrated by the groups of Drewsen and Schiller [107, 114] are likely to be invaluable tools for future work involving state-selected chemical reactions. These methods provide a continuous cooling of the rotational energy distribution, whereas methods such as state-selective photoionisation (*e.g.*, REMPI) can be hampered by blackbody-radiation-induced rotational re-thermalisation*. The refinement of techniques for producing cold matter should benefit a host of fields, and assist in many applications in fundamental physics, high resolution spectroscopy and quantum information processing. Ultimately these advances may also provide the tools for investigations where more refined control exists over the nature of a chemical collision, thereby enabling a richer understanding of fundamental chemical dynamics.

*However this could be mitigated to some extent by cryogenically cooling the apparatus or using non-polar molecular ions.

# Appendices

# Appendix A

# A brief derivation of the harmonic pseudopotential

Given the adiabatic approximation to the motion of an ion in a stable trapped trajectory, the ion's secular motion can be interpreted within the context of a time-independent effective potential, $V^*$. This can greatly simplify further analysis and aid efficient simulations.

In order to derive the form of this pseudopotential, we start by assuming a quasistationary electric field $E(r,t)$ composed of the static field, $E_{\mathrm{s}}(r)$, and time-dependent part, $E_0(r)cos(\Omega t+\delta)$. $E_0(r)$ is the field amplitude, $\Omega = 2\pi f$ is a fixed angular frequency and the phase is denoted $\delta$. It can be shown that the inclusion of relativistic effects, along with a magnetic field term, proves unnecessary in the case of atomic or molecular ions in small or negligible magnetic fields [82]. Non-relativistic motion of a particle with charge $q$ travelling in the above electric field (and in the effective absence of a magnetic field) is given by the differential equation

$$m\ddot{r} = qE_0(r)\cos(\Omega t+\delta) + qE_{\mathrm{s}}(r) \tag{A.1}$$

For simplicity the static field is set to zero and the phase shift $\delta$ eliminated via

a shift in the time origin. Direct solution is possible in a homogeneous field (for which $E_0$ is independent of $r$), yielding for the particle's position the expression

$$r(t) = r(0) - a\cos(\Omega t) \tag{A.2}$$

which corresponds to the particle oscillating about the point $r(0)$. Inserting this expression into Eq. A.1 gives the following expression for the amplitude, $a$, of the oscillation:

$$a = \frac{qE_0}{m\Omega^2}. \tag{A.3}$$

With an inhomogeneous field, where there is a dependence of the field on the position $r$, an analytical solution is often impossible, with numerical integration often the sole path to determining the particle orbit. However if the field is only weakly inhomogeneous the solution can be assumed to deviate only slightly from the homogeneous case. The amplitude of oscillation remains almost the same, but the charge experiences a varying field strength during oscillation which mainly results in a slow drift in the average position. By making further assumptions it is possible to derive an approximate analytical expression analogous to Eq. A.1 but for the case of an inhomogeneous RF field.

First we assume that the field is a smooth continuous function of $r$ and that the amplitude of the oscillation, $a$, is kept small by a high enough RF frequency. In aiming to find a solution to Eq. A.1 we posit a solution which is the combination of a smooth drift term $R_0(t)$ with a high frequency oscillation term $R_1(t)$:

$$r(t) = R_0(t) + R_1(t) \tag{A.4}$$

with

$$R_1(t) = -a(t)\cos(\Omega t). \tag{A.5}$$

Using a Taylor expansion for the electric field $E_0(r)$ leads to

$$E_0(R_0 - a\cos\Omega t) \approx E_0(R_0) - (a\cdot\nabla)E_0(R_0)\cos\Omega t + \ldots, \tag{A.6}$$

and we truncate the expansion at two terms assuming a slow spatial variation of $E_0$. In addition, the assumption of slow time variation in $a$ and $R_0$ implies $\dot{a} \ll \Omega a$ and $\ddot{R}_0 \ll \Omega \dot{R}_0$. Thus, neglecting these smaller time derivatives in the substitution of Eqs. A.4 and A.6 into Eq. A.1 leads to

$$m\ddot{R}_0 + m\Omega^2 a(t)\cos\Omega t = qE_0(R_0)\cos\Omega t - q[a(t)\cdot\nabla]E_0(R_0)\cos^2\Omega t. \tag{A.7}$$

The assumption that the oscillation amplitude changes in time only due to the motion along $R_0$ allows $a(t)$ to be replaced with $a(R_0)$ and substituted using Eq. A.3. This allows the cancellation of the $\cos\Omega t$ terms, which in conjunction with the substitution of $\cos^2\Omega t$ with its average value $\frac{1}{2}$, yields:

$$m\ddot{R}_0 = -\frac{q^2}{2m\Omega^2}[E_0(R_0)\cdot\nabla]E_0(R_0). \tag{A.8}$$

Applying the vector analysis relation

$$(E_0\cdot\nabla)E_0 = \frac{1}{2}\nabla E_0^2 - E_0\times(\nabla\times E_0) = \frac{1}{2}\nabla E_0^2, \tag{A.9}$$

which relies upon $\nabla\times E_0 = 0$ or the vanishing of $E_0$ under rotation for quasistatic fields, leads to

$$m\ddot{R}_0 = -\frac{q^2}{4m\Omega^2}\nabla E_0^2. \tag{A.10}$$

This equation of motion takes into account the time-averaged nature of the oscillating field. The charged particle experiences a force due to the field gradient, or inhomogeneity of the field, whose strength and direction is determined by the gradient of $E_0^2$.

The last step is to incorporate the force due to the electrostatic potential, denoted $qE_s(r)$ in Eq. A.1, using $E_s = -\nabla\Phi_s$. This yields

$$m\ddot{R}_0 = -\frac{q^2}{4m\Omega^2}\nabla E_0^2 - q\nabla\Phi_s \tag{A.11}$$

which, using $ma = F = -\nabla V^*(R_0)$, leads to the expression for the time-independent effective potential or pseudopotential, and the associated equation of motion for

the smooth trajectory:

$$V^*(R_0) = \frac{q^2 E_0^2}{4m\Omega^2} + q\Phi_s \tag{A.12}$$

$$m\ddot{R}_0 = -\nabla V^*(R_0). \tag{A.13}$$

The faster oscillating motion that may be superimposed on this smooth trajectory, can be described via insertion of $E_0(R_0)$ into Eqs. A.5 and A.3 by

$$R_1(t) = -\frac{qE_0(R_0)}{m\Omega^2}\cos(\Omega t). \tag{A.14}$$

Integrating equation A.13 gives us

$$\frac{1}{2}m\dot{R}_0^2 + \frac{q^2 E_0^2}{4m\Omega^2} + q\Phi_s = E_m, \tag{A.15}$$

which shows the total energy $E_m$ to be constant during the ion's motion, with the first term representing the kinetic energy associated with the secular motion, and the third term the electrostatic potential energy. The second term can be shown to represent the time-averaged kinetic energy of the fast-oscillating micromotion, by substituting the derivative of Eq. A.14, into $\frac{1}{2}m\dot{R}_1^2$ and taking the time-average, with the value of $\frac{1}{2}$ substituted for $\sin^2\Omega t$ :

$$\left\langle \frac{1}{2}m\dot{R}_1^2 \right\rangle = \frac{q^2 E_0^2}{4m\Omega^2}. \tag{A.16}$$

In essence what this means is that in the pseudopotential, $V^*$, the kinetic energy associated with the faster micromotion is treated as an effective potential energy. The total energy is constant, and transferred between the kinetic energy associated with the secular motion, this effective potential energy and the electrostatic potential energy (assuming a stable trajectory).

# Appendix B

# Introduction to the density operator

## B.1 Statistical mixtures of states

The dynamical behaviour of a quantum system, disregarding decoherence effects, may be described by the time-dependent Schrödinger equation:

$$|\dot{\psi}\rangle = -iH|\psi\rangle, \tag{B.1}$$

where $H$ is the Hamiltonian operator of the system whose state is described by the vector $|\psi\rangle$. Given a pure state (or a superposition of pure states), the expectation value of an observable operator $A$ is determined by:

$$\langle A\rangle = \langle\psi|A|\psi\rangle. \tag{B.2}$$

However, an ensemble of laser-cooled ions, each of which may either be in the electronic state denoted by $|1\rangle$, $|2\rangle$ or $|3\rangle$ at a particular time, represents a *statistical mixture* of pure states. Such as mixed state may be written

$$|\psi\rangle = \rho_1|1\rangle + \rho_2|2\rangle + \rho_3|3\rangle, \tag{B.3}$$

with

$$\sum_k \rho_{\mathrm{k}} = 1, \tag{B.4}$$

where $\rho_{\mathrm{k}}$ is the fraction of ions in state $|k\rangle$. An equivalent system would be a single ion that exists with a certain probability in one of the three states, and in this case the $\rho_{\mathrm{k}}$ terms in equation B.3 represent the probability of that ion being in the state $|k\rangle$. There is no state vector $|\psi\rangle$ that can adequately describe a system like this and still satisfy equation B.2, despite the fact that the statistical behaviour of the observable $A$ of such a system may in fact be completely determined. Any measurement of a system such as this must result in a sum of eigenvalues weighted by the various probabilities, which is to say

$$\langle A\rangle = \rho_1 a_1 + \rho_2 a_2 + \rho_3 a_3, \tag{B.5}$$

and, given Eq. B.3, this clearly does not arise from $\langle A\rangle = \langle\psi|A|\psi\rangle$ .

This description must not be confused with a linear superposition of states:

$$|\psi\rangle = \sum_k c_{\mathrm{k}}|k\rangle, \tag{B.6}$$

in which a system exists instantaneously as a linear combination of pure states (which is itself a pure state). Such a state vector does satisfy equation B.2 — for example, with k over the range 1–2 (and $|k\rangle$ not necessarily orthogonal),

$$\begin{aligned}\langle A\rangle &= \langle\psi|A|\psi\rangle \\ &= (\langle 1|c_1^* + \langle 2|c_2^*)|A|(c_1|1\rangle + c_2|2\rangle) \\ &= |c_1^*|^2 A_{11} + |c_2^*|^2 A_{22} + c_1^* c_2 A_{12} + c_2^* c_1 A_{21}.\end{aligned} \tag{B.7}$$

Thus, for such a linear combination, any single measurement of an observable (given $|k\rangle$ as eigenvectors) has a probability $|c_k^2|$ of returning the eigenvalue associated with the state $|k\rangle$. However, this is not equivalent to the system having the probability $|c_k^2|$ of being in state $|k\rangle$. The presence of the cross terms represents interference between the states in the linear combination and these are very important in quantum mechanics. This is why it is generally impossible to represent

a statistical mixture of states, as described by equation B.3, by an "average state vector", or superposition of the $|k\rangle$ states. When we perform a probability weighted sum we do not obtain these interference terms. The solution to this quandary is not the use of an "average state vector", but rather an "average operator", the density operator $\hat{\rho}$.

### The density operator

Density operator formalism is equally applicable to systems described by a pure state, or a statistical mixture of states. The coefficient terms, $c_{\mathrm{i}}^{*}c_{\mathrm{j}}$, that appear in the expectation value (Eq. B.7) for a pure system, are simply the matrix elements of the density operator, $\hat{\rho}(t)$, which is defined as:

$$\hat{\rho}(t) = |\psi(t)\rangle\langle\psi(t)|. \tag{B.8}$$

The density operator can be represented as a matrix in a given basis, and the elements of the density matrix are these coefficient terms, $c_{\mathrm{i}}^{*}c_{\mathrm{j}}$, according to:

$$\rho_{ij}(t) = \langle i|\hat{\rho}(t)|j\rangle = c_{\mathrm{i}}^{*}c_{\mathrm{j}}. \tag{B.9}$$

Therefore, the trace of the density matrix must equal unity in a normalised system in accordance with

$$\sum_{n} |c_{\mathrm{n}}(t)|^2 = \sum_{n} \rho_{\mathrm{nn}}(t) = Tr\rho(t) = 1. \tag{B.10}$$

Additionally the expectation value of an observable operator is defined for a linear combination as:

$$\begin{aligned}
\langle A\rangle &= \Big\langle \sum_{i} c_i\phi_i|A| \sum_{j} c_j\phi_j \Big\rangle \\
&= \sum_{i,j} c_i^{*}c_j\langle\phi_i|A|\phi_j\rangle = \sum_{i,j}\rho_{ji}A_{ij} \\
&= \sum_{i,j}\langle\phi_j|\rho|\phi_i\rangle\langle\phi_i|A|\phi_j\rangle = \sum_{j}(\rho A)_{jj} \\
&= Tr(\rho A).
\end{aligned} \tag{B.11}$$

The time evolution of the operator $\rho(t)$ can be generated via the Schrödinger equation according to:

$$\begin{aligned}\dot{\rho}(t) &= |\dot{\psi}(t)\rangle\langle\psi(t)| + |\psi(t)\rangle\langle\dot{\psi}(t)| \\ &= \frac{1}{i\hbar}H(t)|\psi(t)\rangle\langle\psi(t)| - \frac{1}{i\hbar}|\psi(t)\rangle\langle\psi(t)|H(t) \\ &= \frac{1}{i\hbar}[H(t), \rho(t)], \end{aligned} \tag{B.12}$$

which is otherwise known as the quantum mechanical Liouville equation.

Applying the density operator formalism to the statistical mixture of states, described by Eq. B.3, the density matrix operator may be defined as:

$$\hat{\rho} = \sum_{a,b=1,2,3} \rho_{\mathrm{ab}}|a\rangle\langle b|. \tag{B.13}$$

The matrix elements $\rho_{11}$, $\rho_{22}$ and $\rho_{33}$ correspond to the expectation values for finding the ion in the corresponding states $|1\rangle$, $|2\rangle$ or $|3\rangle$ and therefore

$$Tr(\hat{\rho}) = \rho_{11} + \rho_{22} + \rho_{33} = 1. \tag{B.14}$$

In a pure state, one of these diagonal elements is 1 and the others are 0; in a mixed state, more than one diagonal element is non-zero. The off-diagonal matrix elements represent the interference effects that can occur between the states when they comprise a linear superposition. A non-zero off-diagonal element means that a certain coherence exists between the two states that are involved, and for this reason these elements are generally referred to as *coherences*.

The density matrix formalism allows us to describe the state of a system which is a statistical mixture quantum mechanically. Given an appropriate Hamiltonian, the Liouville equation governs the evolution of the density matrix.

# Appendix C

# Transformations of the Hamiltonian matrix

The transformation of the Hamiltonian matrix under the operator $U$, where $UU^\dagger = U^\dagger U = 1$ may be understood as follows:

When a quantum mechanical state $|\psi\rangle$ is transformed with the operator $U$ according to

$$|\psi'\rangle = U|\psi\rangle, \tag{C.1}$$

the corresponding transformation for the Hamiltonian matrix can be written as follows:

$$\begin{aligned}
\hat{H}'|\psi'\rangle &= i\hbar\frac{\mathrm{d}|\psi'\rangle}{\mathrm{d}t} \\
&= i\hbar\frac{\mathrm{d}(U|\psi\rangle)}{\mathrm{d}t} = i\hbar UU^\dagger\frac{\mathrm{d}(U|\psi\rangle)}{\mathrm{d}t} \\
&= i\hbar U\left(\frac{\mathrm{d}(U^\dagger U|\psi\rangle)}{\mathrm{d}t} - \frac{\mathrm{d}U^\dagger}{\mathrm{d}t}U|\psi\rangle\right) \\
&= U\left(\hat{H}U^\dagger U|\psi\rangle - i\hbar\frac{\mathrm{d}U^\dagger}{\mathrm{d}t}U|\psi\rangle\right) \\
\hat{H}'|\psi'\rangle &= \underbrace{\left(U\hat{H}U^\dagger - i\hbar U\frac{\mathrm{d}U^\dagger}{\mathrm{d}t}\right)}_{\hat{H}'}U|\psi\rangle.
\end{aligned} \tag{C.2}$$

Thus two equivalent results are available:

$$\begin{aligned} \hat{H}' &= \left( U\hat{H}U^{\dagger} - i\hbar U\frac{\mathrm{d}U^{\dagger}}{\mathrm{d}t} \right) \\ &= \left( U\hat{H}U^{\dagger} + i\hbar\frac{\mathrm{d}U}{\mathrm{d}t}U^{\dagger} \right). \end{aligned} \tag{C.3}$$

In the case of the transformation of Eq. 2.57 into Eq. 2.58 (transformation to a reference frame rotating at the atomic transition frequency), additional simplification of the transformed Hamiltonian $\hat{\overline{\mathbf{H}}}_{12}$ is possible, using:

$$H = H_{\mathrm{atom}} + H_{12} \tag{C.4}$$

$$U = e^{iH_{atom}t/\hbar} \tag{C.5}$$

via

$$\begin{aligned} \overline{H}'_{12} &= UHU^{\dagger} + i\hbar\frac{\mathrm{d}U}{\mathrm{d}t}U^{\dagger} \\ &= U(H_{\mathrm{atom}} + H_{12})U^{\dagger} + i\hbar(\frac{i}{\hbar}UH_{\mathrm{atom}})U^{\dagger} \\ &= UH_{\mathrm{atom}}U^{\dagger} + UH_{12}U^{\dagger} - UH_{\mathrm{atom}}U^{\dagger} \\ &= UH_{12}U^{\dagger}. \end{aligned} \tag{C.6}$$

Also, using the expression

$$H_{atom} = \hbar\omega_1|1\rangle\langle 1| + \hbar\omega_2|2\rangle\langle 2| \tag{C.7}$$

and setting the zero point of the energy arbitrarily at $\omega_1$ such that

$$H_{atom} = \hbar\omega_{12}|2\rangle\langle 2|. \tag{C.8}$$

we obtain the final operator U for the required transformation as

$$U = e^{i\omega_{12}t|2\rangle\langle 2|}. \tag{C.9}$$

# Appendix D

# Formation of the Liouvillian matrix and solution of the OBE

The evolution of the density matrix is governed by Eq. 2.75, reproduced here along with other relevant equations for convenience:

$$\dot{\rho} = -\frac{i}{\hbar}\left(\widetilde{H}\rho - \rho\widetilde{H}^{*}\right) + \sum_{\mathrm{m}} \hat{C}_{\mathrm{m}}\rho\hat{C}_{\mathrm{m}}^{\dagger}. \tag{D.1}$$

$$\widetilde{H} = \left(H - \frac{i\hbar}{2}\sum_{\mathrm{m}} \hat{C}_{\mathrm{m}}^{\dagger}\hat{C}_{\mathrm{m}}\right). \tag{D.2}$$

The objective is the numerical solution of the evolution of the density matrix, and by taking advantage of the linearity of this equation with respect to the elements of the density matrix we may rewrite it as a system of linear equations in matrix form according to:

$$\dot{\rho}_{\mathrm{i}} = \sum_{\mathrm{j}} \mathbf{M}_{\mathrm{ij}}\rho_{\mathrm{j}} \tag{D.3}$$

with

$$\rho^{\mathrm{T}} = [\rho_{11}, \rho_{12}, \rho_{13}, ..., \rho_{32}, \rho_{33}]. \tag{D.4}$$

We can determine the form of the Liouvillian matrix, **M**, by considering the evolution of the elements of the density matrix.

$$\begin{aligned}
\dot{\rho}_{\mathrm{ab}} &= -\frac{i}{\hbar}\langle a|\left(\widetilde{H}\rho-\rho\widetilde{H}^{\dagger}\right)|b\rangle+\langle a|\sum_{\mathrm{m}}\hat{C}_{\mathrm{m}}\rho\hat{C}_{\mathrm{m}}^{\dagger}|b\rangle \\
&= -\frac{i}{\hbar}\left(\sum_{\mathrm{j}}\widetilde{H}_{\mathrm{aj}}\rho_{\mathrm{jb}}-\sum_{\mathrm{k}}\rho_{\mathrm{ak}}\widetilde{H}_{\mathrm{kb}}^{\dagger}\right)+\sum_{\mathrm{m}}\sum_{\mathrm{jk}}\langle a|\hat{C}_{\mathrm{m}}|j\rangle\langle j|\rho|k\rangle\langle k|\hat{C}_{\mathrm{m}}^{\dagger}|b\rangle \\
&= -\frac{i}{\hbar}\left(\sum_{\mathrm{jk}}\widetilde{H}_{\mathrm{aj}}\delta_{\mathrm{kb}}\rho_{\mathrm{jk}}-\sum_{\mathrm{jk}}\widetilde{H}_{\mathrm{kb}}^{\dagger}\delta_{\mathrm{aj}}\rho_{\mathrm{jk}}\right)+\sum_{\mathrm{m}}\sum_{\mathrm{jk}}(\hat{C}_{\mathrm{m}})_{\mathrm{aj}}\rho_{\mathrm{jk}}(\hat{C}_{\mathrm{m}}^{\dagger})_{\mathrm{kb}} \\
&= \sum_{\mathrm{jk}}\left(-\frac{i}{\hbar}\left(\widetilde{H}_{\mathrm{aj}}\delta_{\mathrm{kb}}-\widetilde{H}_{\mathrm{kb}}^{\dagger}\delta_{\mathrm{aj}}\right)+\sum_{\mathrm{m}}(\hat{C}_{\mathrm{m}})_{\mathrm{aj}}(\hat{C}_{\mathrm{m}}^{\dagger})_{\mathrm{kb}}\right)\rho_{\mathrm{jk}}. \qquad \text{(D.5)}
\end{aligned}$$

This can be expressed as

$$\dot{\rho}_{\mathrm{ab}}=\sum_{\mathrm{jk}}M_{\mathrm{ab,jk}}\rho_{\mathrm{jk}}, \qquad \text{(D.6)}$$

where **M** is the $N^2\times N^2$ Liouvillian matrix determined by

$$M_{\mathrm{ab,jk}}=-\frac{i}{\hbar}\left(\widetilde{H}_{\mathrm{aj}}\delta_{\mathrm{kb}}-\widetilde{H}_{\mathrm{kb}}^{\dagger}\delta_{\mathrm{aj}}\right)+\sum_{\mathrm{m}}(\hat{C}_{\mathrm{m}})_{\mathrm{aj}}(\hat{C}_{\mathrm{m}}^{\dagger})_{\mathrm{kb}}. \qquad \text{(D.7)}$$

Concise MATLAB code for the formation of this matrix can be found in D.1.

# D.1 MATLAB code for solution of the OBE

## D.1.1 Calculation of Rabi frequency from laser intensity

The expressions that relate the Rabi frequency to the experimentally determined laser intensity, transition wavelength and spontaneous decay rate were obtained for the three-level treatment from pg. 50 of Ref. [175], and for the eight-level treatment from pg. 27 of Ref. [174]. The difference in the two expressions stems from a different definition of the Rabi frequency in either derivation. For simplicity both expressions are included in the code below, however in practice this code should be duplicated into rabi.m (three-level) and rabi8.m (eight-level) with the appropriate expressions used in each case. These two functions are called from the SIMPOP scripts that solve the OBE.

```
%% Function to calculate Rabi frequency
function omega = rabi(I,which)%3-level
function omega = rabi8(I,which)%8-level
%I = Intensity in Wm^-2
%which = 1 for 397 nm, 2 for 866 nm
c = 299792458; % M/s
h = 6.626068e-34; hbar = h/(2*pi);

switch which
    case 1 %397 nm laser
        wl = 396.847e-9;
        lt = 7.7e-9; %natural lifetime
    case 2 %866 nm laser
        wl = 866.214e-9;
        lt = 94.3e-9; %natural lifetime
end

g = 1/lt; %Spontaneous decay rate in Hz
omega = sqrt((3 * I * wl^3 * g)/(4 * pi^2 * c * hbar));%3-level
omega = sqrt((3 * I * wl^3 * g)/(16 * pi^2 * c * hbar));%8-level
omega = omega/(1e6); % Angular Mhz
```

### D.1.2 Formation of the three-level Liouvillian matrix

This code forms the $9 \times 9$ Liouvillian matrix which is used to propagate the three-level density matrix. It accepts the Rabi frequencies, detunings and linewidths of both cooling lasers, along with the natural lifetimes of the two transitions. This function is called from the SIMPOP codes that solve the OBE.

```
%% Formation of Liouvillian Matrix
% Density matrix treatment of 3 level atom
% in the absence of a magnetic field
function M=M3(O12,O23,D1,D2,l1,l2,g1,g2)

I=eye(3);

% Coherent hamiltonian
H=[  D1    O12/2    0
   O12/2     0   O23/2
     0     O23/2   D2];
% Relaxation terms
R = zeros(3,3); R(2,2) = g1 + g2;
R(1,1) = 2*l1; R(3,3) = 2*l2;
% Feeding terms dp_ab = <a|Ldamp|b>
F = zeros(9,9);
F(1,1) = 2*l1; F(9,9) = 2*l2;
F(1,5) = g1; F(9,5) = g2;

H = H - (i/2)*R; % Form effective Hamiltonian
M = -i*(kron(H,I) - kron(I,H')); % Form Liouville matrix
M = M + F; %Add feeding terms
```

### D.1.3 Formation of the eight-level Liouvillian matrix

This code forms the $64 \times 64$ Liouvillian matrix which is used to propagate the eight-level density matrix. It accepts the Rabi frequencies, detunings and linewidths of both cooling lasers, along with the natural lifetimes of the two transitions. This function is called from the SIMPOP codes that solve the OBE.

```
%% Formation of Liouvillian Matrix
% Density matrix treatment of 8 level atom in a magnetic field
function L=M8(O1,O2,D1,D2,l1,l2,g1,g2,u,alpha)

gS=2; gP=2/3; gD=4/5; % Lande factors
c=cos(alpha); s=sin(alpha); w3=3^0.5; E=eye(8);
ii=(1:8)'*ones(1,8); i1=reshape(ii',1,64); % first index
i2=reshape(ii,1,64); % second index
H=diag([D1,D1,0,0,D2,D2,D2,D2]+...
     0.5*u*[-gS,gS,-gP,gP,-3*gD,-gD,gD,3*gD]);
HSP=-O1/w3*[ -c s ; s c ];
HDP=-O2/2/w3*[ w3*s 0 ; 2*c s ; -s 2*c ; 0 -w3*s ];
H(1:2,3:4)=HSP; H(3:4,1:2)=HSP'; H(5:8,3:4)=HDP; H(3:4,5:8)=HDP';
% Relaxation
C1=(2/3*g1)^0.5*E(:,1)*E(4,:);
C2=(2/3*g1)^0.5*E(:,2)*E(3,:);
C3=(1/3*g1)^0.5*(E(:,1)*E(3,:)-E(:,2)*E(4,:));
C4=(1/2*g2)^0.5*E(:,5)*E(3,:)+(1/6*g2)^0.5*E(:,6)*E(4,:);
C5=(1/6*g2)^0.5*E(:,7)*E(3,:)+(1/2*g2)^0.5*E(:,8)*E(4,:);
C6=(1/3*g2)^0.5*(E(:,6)*E(3,:)+E(:,7)*E(4,:));
C7=(2*l1)^0.5*(E(:,1)*E(1,:)+E(:,2)*E(2,:));
C8=(2*l2)^0.5*(E(:,5)*E(5,:)+E(:,6)*E(6,:)+...
                              E(:,7)*E(7,:)+E(:,8)*E(8,:));
CC=(C1'*C1+C2'*C2+C3'*C3+C4'*C4+C5'*C5+C6'*C6+C7'*C7+C8'*C8);
% Form effective Hamiltonian and Liouvillian
H=H-i/2*CC; L = -i*(kron(H,E) - kron(E,H'));
% Add feeding terms
L=L+C1(i1,i1).*C1(i2,i2); L=L+C2(i1,i1).*C2(i2,i2);
L=L+C3(i1,i1).*C3(i2,i2); L=L+C4(i1,i1).*C4(i2,i2);
L=L+C5(i1,i1).*C5(i2,i2); L=L+C6(i1,i1).*C6(i2,i2);
L=L+C7(i1,i1).*C7(i2,i2); L=L+C8(i1,i1).*C8(i2,i2);
```

### D.1.4 Basic steady-state solution of the three-level OBE

This code is called for a single coordinate in detuning space and calculates the steady-state solutions to the three-level OBE; it returns the $Ca^+$ population fractions as a percentage. It accepts the effective areas that relate the measured laser powers to the effective laser intensities at the crystal; variation of these factors allows the fitting of simulated to experimental spectra. Other scripts generate these spectra, or deal with convolutions to account for non-zero axial ion velocities and laser frequency fluctuations. In general these other scripts all call SIMPOP in order to get the underlying populations over the required range of detuning coordinates.

```
function [sim_Fint_out]=SIMPOP(P,detb,detr,effarea,opswitch)
% Program to calculate the steady state populations of a
% trapped three level atom in interaction with two
% coherent light fields.

P397 = P(1); %W
P866 = P(2); %W
A397 = effarea(1)*1e-6; %mm^2 -> m^2 Eff. area @ 397 nm
A866 = effarea(2)*1e-6; %mm^2 -> m^2 Eff. area @ 866 nm
l1 = 5500; % Linewidth of 397nm Diode Laser (kHz)
l2 = 5500; % Linewidth of 866nm Diode Laser (kHz)

%% Constants
c = 299792458; %ms^-1
g1 = 1e-6/7.7e-9;%Ca+ P->S Decay Constant MHz
g2 = 1e-6/94.3e-9;%Ca+ P->D Decay Constant MHz

%% Inline Function Declaration
gendet = @(w) c .* (1./(w(1).*1e-9) - ...
              1./((w(1).*1e-9) + (w(2).*1e-15)));

%% Generation of Rabi Frequencies from Laser Power Data
I12 = P397/A397; %Wm^-2
I32 = P866/A866; %Wm^-2
O12 = rabi(I12,1);
O23 = rabi(I32,2);
```

```
%% Detuning calculations
% Detuning may either be input as single value (Hz)
% or a single value (fm) with a measured zero-detuning
% position (nm) such that the conversion to Hz is done
% automatically. In either case det12/det32 are
% produced in Hz at this stage.

if length(detb)~=2; det12 = detb;
else; det12 = gendet(detb); end;
if length(detr)~=2  det32 = detr;
else; det32 = gendet(detr); end;

%Detunings converted to angular Mhz
D1 = 2*pi*1e-6.*det12;
D2 = 2*pi*1e-6.*det32;

%Laser Linewidths
l1 = 2*pi*1e-3.*l1; %Laser linewidths, input in khz
l2 = 2*pi*1e-3.*l2; %and converted to angular MHz
%% ++++++
% For comparison with Hilmar Oberst's PhD Thesis (Barium)
% O12 = 10*2*pi;
% O23 = 5*2*pi;
% l1=50*1e-3*2*pi;
% l2=50*1e-3*2*pi;
% D1 = -20*2*pi;
% g1 = 15.1*2*pi; %Ba
% g2 = 5.3*2*pi; %Ba
%++++++
%----------------------
%% MAIN STEADY STATE CALCULATION
%In the steady state,  L*rho = 0
%To enforce the correct normalisation we replace
%one equation with the normalisation condition:
%rho(1)+rho(5)+rho(9)=1  (or Tr(rho)=1 when rho is 3x3)

L = M3(O12,O23,D1 ,D2 ,l1,l2,g1,g2);
L(1,:) = 0; L(1,1) = 1; L(1,5) = 1; L(1,9) = 1;
x = zeros(9,1); x(1) = 1;

rhoss = L\x;
```

```
popss = diag(real(reshape(rhoss,3,3)));

N1 = popss(1)*100; % Populations converted to a percentage
N2 = popss(2)*100;
N3 = popss(3)*100;
Espop = N2+N3; % Total excited state populations

%% Designate output
switch opswitch
    case 1
        sim_Fint_out = [N2];
    case 2
        sim_Fint_out = [N1;N2;N3];
    case 3
        sim_Fint_out = [Espop];
end
```

### D.1.5 Steady-state solution of the three-level OBE with non-zero axial crystal temperature and independently fluctuating laser frequencies

This code performs convolutions of the $Ca^+$ state populations using: (a) a Gaussian function whose FWHM is determined by T, the temperature associated with the axial motion of ions in the crystal, (b) Gaussian functions that reflect the distribution of frequencies of the cooling lasers about their feedback-stabilised mean values.

```
function [sim_Fint_out] = SIMPOP_conv_ilf(P, ...
              det_b, det_r, effarea, opswitch, T, freqfwhm)
% Program to calculate the steady state populations at a
% given set of experimental parameters, including
% convolutions due to doppler width and independent
% fluctuations in both laser frequencies.

if (length(det_b)>2) || (length(det_r)>2)
    disp('This function is built for a single ...
                              value of blue/red detunings');
    return
end
% Initial parameters
fwhm_b = freqfwhm(1);
fwhm_r = freqfwhm(2);
%Convolution axis angle, defined from X-axis:
theta = atan(396.95865e-9/866.4513e-9);
npt = 41;
stm = 4;
%[npt stm] = [41 4] accurate to 3 dec.pl. in pop. frac.

% Inline Function Declarations
c = 299792458; %ms^-1
gendet = @(w) c .* (1./(w(1).*1e-9) - ...
                         1./((w(1).*1e-9) + (w(2).*1e-15)));
% Detuning conversion if necessary
if length(det_b) > 1; det_b = gendet(det_b); end;
```

```
if length(det_r) > 1; det_r = gendet(det_r); end;

% Blue fluc Gaussian parameters
sigma_b = fwhm_b/(2*sqrt(2*log(2)));
a_b =1/(sigma_b*sqrt(2*pi)); %normalisation factor
% Red fluc Gaussian parameters
sigma_r = fwhm_r/(2*sqrt(2*log(2)));
a_r =1/(sigma_r*sqrt(2*pi)); %normalisation factor
% Tz Gaussian parameters
fwhm_Tzb= (7.16e-7*c/396.95865e-9) * sqrt(T/40.08);
fwhm_Tzr= (7.16e-7*c/866.4513e-9) * sqrt(T/40.08);
fwhm_Tz = sqrt(fwhm_Tzb^2 + fwhm_Tzr^2);
sigma_Tz = fwhm_Tz/(2*sqrt(2*log(2)));
a_Tz =1/(sigma_Tz*sqrt(2*pi)); %normalisation factor

% Determine detuning grid, centred on experimental laser
% detunings. Grid extent determined by stm*sigma
% truncation of the convolution Gaussian that gives the
% largest kernel size, with all Gaussians centred on the
% experimental detuning values.
% 4*sigma is a good approximation for a Gaussian falling
% to zero (stm stands for 'sigma truncation multiplier').
kernel_width =  max([(2*stm*sigma_b) ...
                     (2*stm*sigma_Tz*acos(theta))] ); %Hz
kernel_height = max([(2*stm*sigma_r)...
                     (2*stm*sigma_Tz*asin(theta))] ); %Hz

detgrid_b = det_b + [-kernel_width/2 : ...
                  kernel_width/(npt-1) : kernel_width/2];
detgrid_r = det_r + [-kernel_height/2 : ...
                  kernel_height/(npt-1) : kernel_height/2];
[BDET,RDET] = meshgrid(detgrid_b,detgrid_r);

% Fill state populations matrix
POP = zeros(npt,npt,3);
for i = 1:npt
   for j = 1:npt
      POP(i,j,(1:3))=SIMPOP(P,BDET(i,j),RDET(i,j),effarea,2);
   end
end

% Form Gaussians for laser fluctuations
```

```
gauss_b = a_b*exp(-((detgrid_b-det_b).^2)./(2.*sigma_b.^2));
gauss_r = a_r*exp(-((detgrid_r-det_r).^2)./(2.*sigma_r.^2));
%Convolute with laser fluctuation Gaussians
sim1_convol = conv2(gauss_b,gauss_r',POP(:,:,1),'same');
sim2_convol = conv2(gauss_b,gauss_r',POP(:,:,2),'same');
sim3_convol = conv2(gauss_b,gauss_r',POP(:,:,3),'same');
%Normalise convoluted fits at each point
sum = 1e-2.*(sim1_convol + sim2_convol + sim3_convol);
sim1_convol = sim1_convol./sum;
sim2_convol = sim2_convol./sum;
sim3_convol = sim3_convol./sum;

%Form 1D Tz Convolution axis at theta to x-axis,
%centred on origin with width 2*stm*sigma_Tz
% Get detuning spacing based on npts along axis
ddet = (2*stm*sigma_Tz)/(npt-1);
% Get detunings along the axis
detgrid_b_Tz=ddet.*((-(npt-1)/2):1:((npt-1)/2)).*cos(theta);
detgrid_r_Tz=ddet.*((-(npt-1)/2):1:((npt-1)/2)).*sin(theta);
Tz_axis_det=-ddet*((npt-1)/2):ddet:ddet*((npt-1)/2);

% Center convolution axis on desired detunings
detgrid_b_Tz = detgrid_b_Tz + det_b;
detgrid_r_Tz = detgrid_r_Tz + det_r;
% 2D Interpolate the axis values
POP_axis_Tz = zeros(npt,3);
POP_axis_Tz = [
[interp2(BDET,RDET,sim1_convol,detgrid_b_Tz,detgrid_r_Tz)];
[interp2(BDET,RDET,sim2_convol,detgrid_b_Tz,detgrid_r_Tz)];
[interp2(BDET,RDET,sim3_convol,detgrid_b_Tz,detgrid_r_Tz)]
];
% Form Gaussian and convolute
gauss_Tz = a_Tz*exp(-(Tz_axis_det.^2)./(2.*sigma_Tz.^2));
sim1_convol_final = convn(gauss_Tz ,POP_axis_Tz(1,:),'same');
sim2_convol_final = convn(gauss_Tz ,POP_axis_Tz(2,:),'same');
sim3_convol_final = convn(gauss_Tz ,POP_axis_Tz(3,:),'same');

%Normalise convoluted fits
sum = 1e-2.*(sim1_convol_final + sim2_convol_final ...
                                        + sim3_convol_final);
sim1_convol_final = sim1_convol_final./sum;
sim2_convol_final = sim2_convol_final./sum;
```

```
sim3_convol_final = sim3_convol_final./sum;

%Interpolate level populations based on the fact that the
%requested value is at zero on the convolution axis
N1 = interp1(Tz_axis_det,sim1_convol_final,0,'linear');
N2 = interp1(Tz_axis_det,sim2_convol_final,0,'linear');
N3 = interp1(Tz_axis_det,sim3_convol_final,0,'linear');
Espop = N2+N3;

%% Designate Output
switch opswitch
    case 1
    sim_Fint_out = [N2];
    case 2
    sim_Fint_out = [N1;N2;N3];
    case 3
    sim_Fint_out = [Espop];
end
```

### D.1.6 Basic steady-state solution of the eight-level OBE

This code is called for a single coordinate in detuning space and calculates the steady-state solutions to the eight-level OBE; it returns the $Ca^+$ population fractions as a percentage. It accepts the effective areas that relate the estimated laser intensity to the effective laser intensity at the crystal, along with additional experimental parameters as commented in the code, and variation of these factors allows the fitting of simulated to experimental spectra.

```
function [sim_Fint_out] = SIMPOP8(P, detb, detr, u, alpha,...
                                                  effarea, opswitch)
% Program to calculate the steady state populations of a trapped
% Ca+ ion in interaction with two coherent light fields, assuming
% 8 sub-levels. Calculations are made with the assumption that
% the magnetic field is perpendicular to the propagation
% direction of the lasers at angle alpha to their polarisations.

%% USER DATA
P397 = P(1); %W or Js^-1
P866 = P(2); %W or Js^-1
A397 = effarea(1)*1e-6; %mm^2 -> m^2 Eff. area @ 397 nm
A866 = effarea(2)*1e-6; %mm^2 -> m^2 Eff. area @ 866 nm
l1 = 5000; % Linewidth of 397nm Diode Laser (kHz)
l2 = 5000; % Linewidth of 866nm Diode Laser (kHz)

%% Constants
c = 299792458; %ms^-1
wl12 = 396.95865e-9; % m
wl32 = 866.4513e-9; % m
g1 = 1e-6/7.7e-9;%Ca+ P->S Decay Constant MHz
g2 = 1e-6/94.3e-9;%Ca+ P->D Decay Constant MHz

%% Inline Function Declaration
gendet = @(w) c.*(1./(w(1).*1e-9) - 1./((w(1).*1e-9) +...
                                        (w(2).*1e-15)));

%% Generation of Rabi Frequencies from Laser Power Data
I12 = P397/A397; %Wm^-2
```

```
I32 = P866/A866; %Wm^-2
O12 = rabi8(I12,1);
O23 = rabi8(I32,2);

%% Detuning calculations
% Detuning may either be input as single value (Hz) or a
% single value (fm) with a measured zero-detuning position (nm)
% such that the conversion to Hz is done automatically.
% In either case det12/det32 are produced in Hz at this stage.
if length(detb)~=2; det12=detb; else; det12=gendet(detb); end;
if length(detr)~=2; det32=detr; else; det32=gendet(detr); end;

%% Conversion/Consolidation of Data with units of Frequency
%Detunings converted to angular Mhz
D1 = 2*pi*1e-6.*det12;
D2 = 2*pi*1e-6.*det32;
%Laser Linewidths
l1 = 2*pi*1e-3.*l1; %Laser linewidths input in USER DATA in khz
l2 = 2*pi*1e-3.*l2; %and converted to angular Mhz
%% ++++++
% For comparison with Hilmar Oberst's PhD Thesis (Barium)
% O12 = 12*2*pi;
% O23 = 10*2*pi;
% l1=50*1e-3*2*pi;
% l2=50*1e-3*2*pi;
% D1 = 10*2*pi;
% D2 = 0;
%
% g1 = 15.1*2*pi; %Ba
% g2 = 5.3*2*pi; %Ba
%++++++
%----------------------
%----------------------
%% MAIN STEADY STATE CALCULATION
%In the steady state,  L*rho = 0
%To enforce the correct normalisation we replace
%one equation with the normalisation condition

L = M8(O12,O23,D1,D2,l1,l2,g1,g2,u,alpha);

L(1,:) = 0;
L(1,1:9:64) = 1;
```

```
x = zeros(64,1); x(1) = 1;
rhoSS = L\x;

popSS = diag(real(reshape(rhoSS,8,8)));
popSS = 100.*popSS./sum(popSS);

N1 = (popSS(1) + popSS(2));
N2 = (popSS(3) + popSS(4));
N3 = (popSS(5) + popSS(6) + popSS(7) + popSS(8));
Espop = N2+N3;

%% Designate output
switch opswitch
    case 1
        sim_Fint_out = [N2];
    case 2
        sim_Fint_out = [N1;N2;N3];
    case 3
        sim_Fint_out = [Espop];
    case 4
        sim_Fint_out = [N1;N2;N3;popSS];
    case 5
        sim_Fint_out = [N1;N2;N3;I12;I32];
    case 6
        sim_Fint_out = [N2/100 N3/100];
end
```

# Appendix E

# Coulomb crystal $^{40}Ca^{+}$ volume analysis

Given the assumption that $^{40}Ca^{+}$ density is constant in large enough crystals ($\geqslant$100 ions), the rate of decrease of the volume occupied by these ions is proportional to the reaction rate (see Section 4.3.2). In order to measure the core volume from experimental fluorescence images, a custom MATLAB script and accompanying GUI (see Fig. E.1) were developed to process sequences of experimental images as efficiently as possible. Automatic processing of these images can be problematic given appreciable stray light in the image. In the end a hybrid automatic/manual method was relied upon, which involved some automatic fitting that could be manually adjusted.

Measurement of the volume of a pure crystal (or $^{40}Ca^{+}$ core in a bi-component crystal involving heavier non-fluorescing ions) can be achieved in the following way. Firstly, the user loads and rotates the experimental image to ensure that the $z$-axis is vertical. Two methods are available for obtaining a volume measurement, and these are termed elliptical fitting and perimeter fitting. Elliptical fitting involves

the simple manual scaling of an overlaid ellipse such that it coincides with the outline of a pure crystal, or such that a flattened core fits within its overall envelope. The volume of the ellipsoid defined by a $\pi$ rotation of this ellipse around the $z$-axis is then given by $\frac{4}{3}\pi ab^2$, where $2a$ and $2b$ are the lengths of the crystal axes parallel and perpendicular to the $z$-axis respectively. In the case of a pure crystal this should be an accurate measure of the volume, but if heavier dark ions are present the perimeter fitting should be used instead. Nevertheless in this latter case, the elliptical fit can often be useful as a guide for perimeter point placement should the tips of the crystal be obscured.

The perimeter fit is performed in the following manner. The user designates the vertical extents of the crystal and proceeds to place additional points along each edge. Alternatively, by setting intensity thresholds the user can automatically fit points to the left and right side of the crystal simultaneously. The script then performs a spline fit for each side of the crystal and this fit may then be refined further until the perimeter overlaid on the image tightly fits the core edges (see Fig. E.1). Assuming cylindrical symmetry about the $z$-axis, the volume is calculated via numerical quadrature using disk integration (volume of a solid of revolution). Each infinitesimal disk at a given point along the $z$-axis has a diameter defined by the width of the perimeter fit at that point. This general method could easily be extended to calculate the volume of the $^{40}Ca^{+}$ fraction of a crystal with lighter impurities also, although typically MD simulations are relied upon more heavily in this instance. Once a final value for the volume is arrived at, the script will append the result to a text file along with the time of the image and with upper and lower error bounds on the volume (error bounds can be visually verified through the GUI). The program also displays the fluorescence profiles along either axis of the crystal and, for the elliptical fit, displays ion numbers based on the fluid model number density equation outlined in Section 2.4.1.

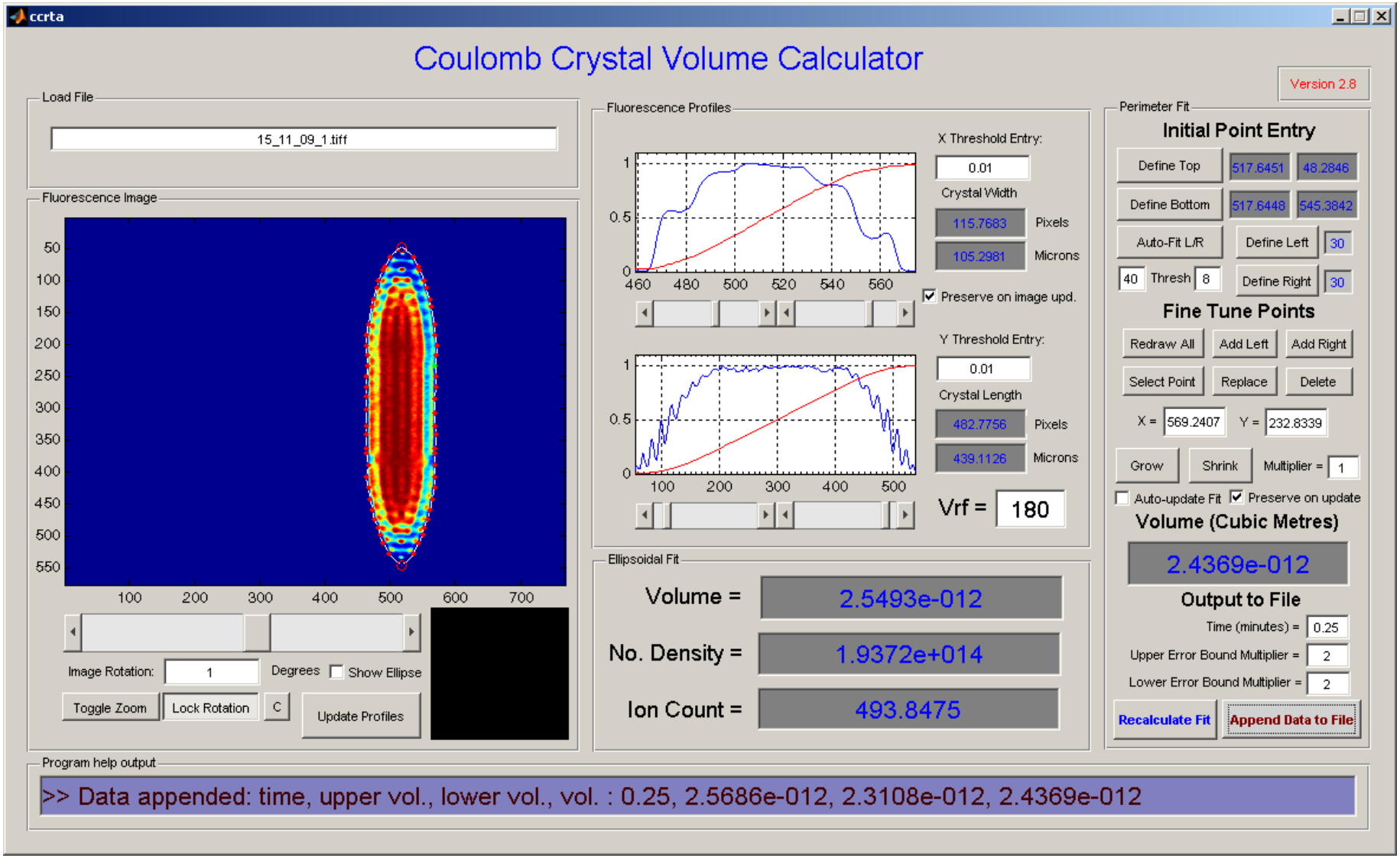


Figure E.1: GUI from the MATLAB script written to facilitate volume calculation for the $Ca^+$ crystal fraction; a perimeter fit is currently displayed.

# Appendix F

# Fluorescence spectra of Coulomb crystals in Gaussian intensity profiles

In Chapter 6 we make the assumption that our laser intensities are well-modelled by a constant mean intensity, thus ignoring any spatial inhomogeneity at the scale of the Coulomb crystal. Whilst this is likely to be a good assumption for the broader 866 nm beam, the 397 nm beam waist is only slightly wider than a typical crystal — a slight misalignment of the beam will leave part of the crystal dark. Given that our diode laser beams do not have a constant transverse intensity profile, some of the ions in the crystal will be experiencing an intensity that could differ quite considerably from the mean. The effect of a variation in the laser intensities on the steady-state quantum state populations (and therefore any fluorescence excitation spectra) is clearly non-linear over a large enough range of intensities (see Fig. F.1). Therefore we need to be sure, given the parameters of our laser beams and the dimensions of a typical Coulomb crystal, that the range of intensities experienced by ions in the crystal is narrow enough to allow the assumption of constant average beam intensities (and therefore a constant average Rabi frequency associated with each laser). In considering this we must be mindful of the fact that

some of the experimental fluorescence spectra were recorded at $V_{\mathrm{RF}} = 110$ V in order to facilitate recrystallisation, whereas reactions are typically performed at $V_{\mathrm{RF}} = 180$ V: At lower RF trapping voltages the crystals will expand to larger radial extent, and sample more of the cross-sectional area of each laser. In this Appendix, we explore these factors through a combination of OBE and molecular dynamics simulations. For computational convenience the investigation is based on the three-level OBE framework, however the conclusions are expected to be valid in the eight-level case (see Appendix G and in particular Fig. G.4).

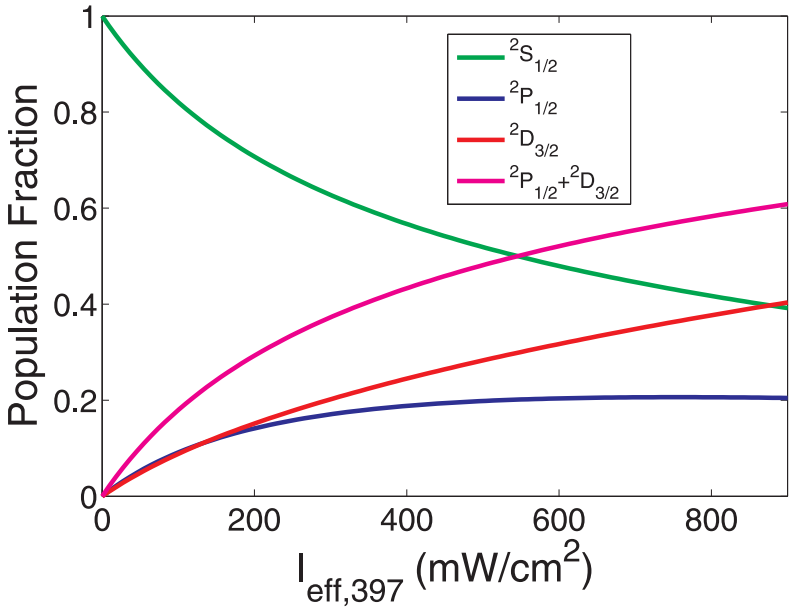


Figure F.1: $Ca^+$ electronic quantum state populations calculated with the three-level OBE as a function of 397 nm laser intensity. Other simulation parameters are as follows: $I_{\mathrm{eff,866}} = 437.7$ mW/cm$^2$, $\Delta_{397}/2\pi = 20$ MHz, $\Delta_{866}/2\pi = 0$ MHz, $\Gamma_{397}/2\pi = \Gamma_{866}/2\pi = 6$ MHz.

The transverse laser intensities at the crystal are approximated with a 2D Gaussian function centred on the beam axis (the trap $z$-axis):

$$f_G(x, y) = Ae^{-\left(\frac{x^2}{2\sigma_x^2} + \frac{y^2}{2\sigma_y^2}\right)}. \tag{F.1}$$

where $\sigma_x$ and $\sigma_y$ are the standard deviations in $x$ and $y$, related to the full-width at half-maxima in each axis by $\mathrm{FWHM} = 2\sqrt{2\ln 2}\sigma$. These standard deviations

allow both the determination of the beam dimensions and, by equating the volume under the 2D Gaussian, $2\pi A\sigma_x\sigma_y$, to the total measured power, the scaling factor $A$. MD simulations can be performed involving crystals typical with regard to the reaction experiments; the resulting crystal structures can then be situated in the Gaussian intensity profile which models each laser. MATLAB scripts allow the interpolation of the laser intensities experienced by each ion and histograms are formed of the 397 nm and 866 nm laser intensity combinations experienced by all ions in the crystal. For each 397 nm/866 nm intensity combination a separate spectral simulation is run, and then by performing a weighted sum the total fluorescence spectrum for the whole crystal can be generated (hereafter referred to as the weighted spectra). At the same time a single spectral simulation can be run at the mean intensity experienced by the ions in the crystal (referred to as the mean spectrum). This mean intensity is analogous to the constant effective intensity determined for each laser by calculating $I_{\text{eff}} = P_{\text{meas}}/A_{\text{eff}}$ (see Eq. 6.11).

Using these methods, weighted spectra can be fit to the experimental spectra purely by adjusting the dimensions of the two Gaussian intensity profiles which model the effective laser intensities (through $\sigma_x$ and $\sigma_y$ for both 397 nm and 866 nm beams). In achieving a fit we have effectively calibrated our experimental beam sizes. In doing so the following values were obtained: 397 nm $\sigma_x = 178.3$ $\mu$m $\sigma_y = 89.3$ $\mu$m, 866 nm $\sigma_x = 1.9$ mm $\sigma_y = 0.9$ mm. Figure F.2 shows the structures obtained by molecular dynamics simulations for an 800 ion crystal at both $V_{\text{RF}} =$ 110 V and 180 V, with $U_{\text{end}} = 4$ V in both cases; included are the $x$ and $y$ Gaussian intensity profiles of both lasers as determined from these spectral fits (which are in reasonable agreement with estimated measurements). Clearly the 866 nm intensity is effectively constant at the crystal scale, but the 397 nm is less clear cut. Figure F.3 shows histograms of the effective 397 nm laser intensities interpolated for the ions in each crystal at both high and low 397 nm power. It

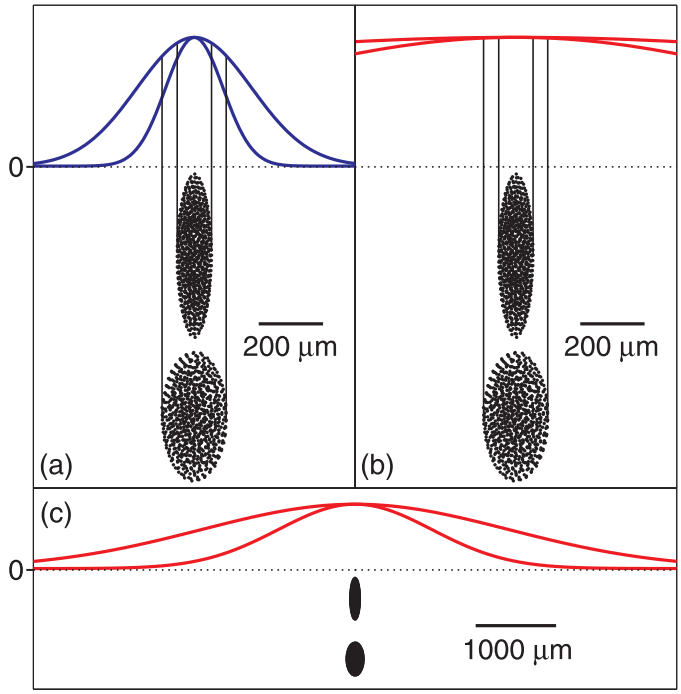


Figure F.2: Simulated tranverse Gaussian intensity profiles of: (a) 397 nm laser beam, (b–c) 866 nm laser beam. These dimensions were obtained by varying the intensity profile widths, at constant total power, until simulated weighted sum fluorescence spectra matched with experiment. The broader profile in each panel corresponds to the long axis of the elliptical beam and the narrower profile to the short axis. MD simulations of an 800 ion crystal are superimposed at $V_{\mathrm{RF}} = 180$ V (top crystal) and $V_{\mathrm{RF}} = 110$ V (bottom crystal).

can be seen that a slightly wider range of effective intensities is experienced by the crystal at $V_{\mathrm{RF}} = 110$ V, and at higher versus lower 397 nm laser power, $P_{397}$. Given laser beam and crystal dimensions typical of our experiments, we observe only a weak dependence of the state populations (and therefore fluorescence spectra) on $V_{\mathrm{RF}}$, stemming from its effect on the radial ion distribution in the intensity field. Smaller values of $V_{\mathrm{RF}}$ (or larger crystals) mean that the ions extend out further radially towards lower laser intensity, and the mean effective intensity drops slightly given a constant beam dimension and power. In the range $V_{\mathrm{RF}} = 110$–$180$ V this effect appears negligible with respect to our experimental noise, and mean spectra that differ only in $V_{\mathrm{RF}} = 110$–$180$ V are identical on the scale plotted in Fig. F.4.

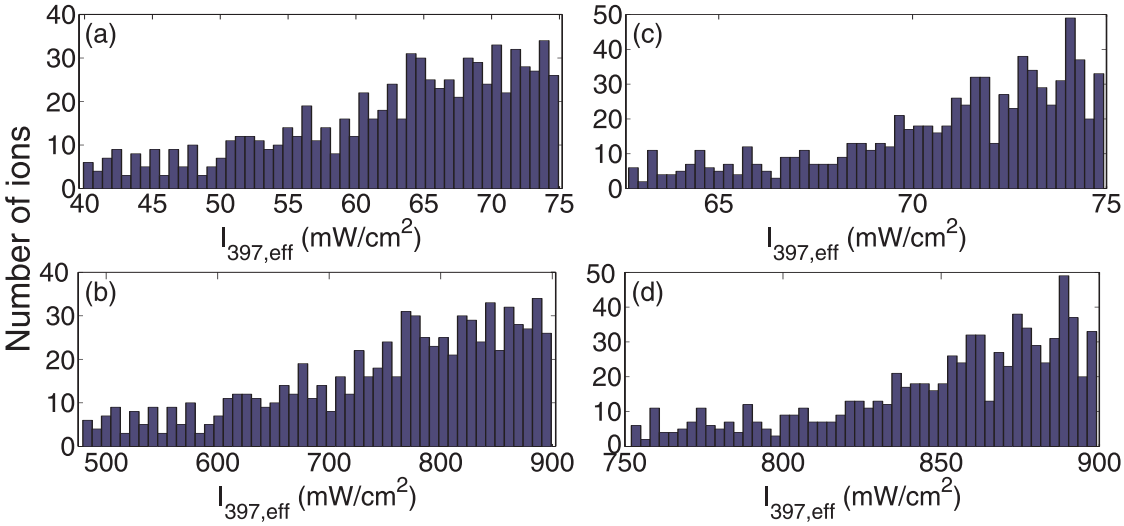


Figure F.3: Histograms of the effective 397 nm laser intensities experienced by the ions in crystals at different values of $P_{397}$ and $V_{\mathrm{RF}}$. These parameters are as follows: (a) $V_{\mathrm{RF}} = 110$ V $P_{397} = 75$ $\mu$W, (b) $V_{\mathrm{RF}} = 110$ V $P_{397} = 900$ $\mu$W, (c) $V_{\mathrm{RF}} = 180$ V $P_{397} = 75$ $\mu$W, (d) $V_{\mathrm{RF}} = 180$ V $P_{397} = 900$ $\mu$W. At lower $V_{\mathrm{RF}}$, and/or at higher $P_{397}$ the range of effective intensities increases. As $V_{\mathrm{RF}}$ decreases, the mean intensity decreases as the ions spread out radially toward lower intensity regions of the laser field.

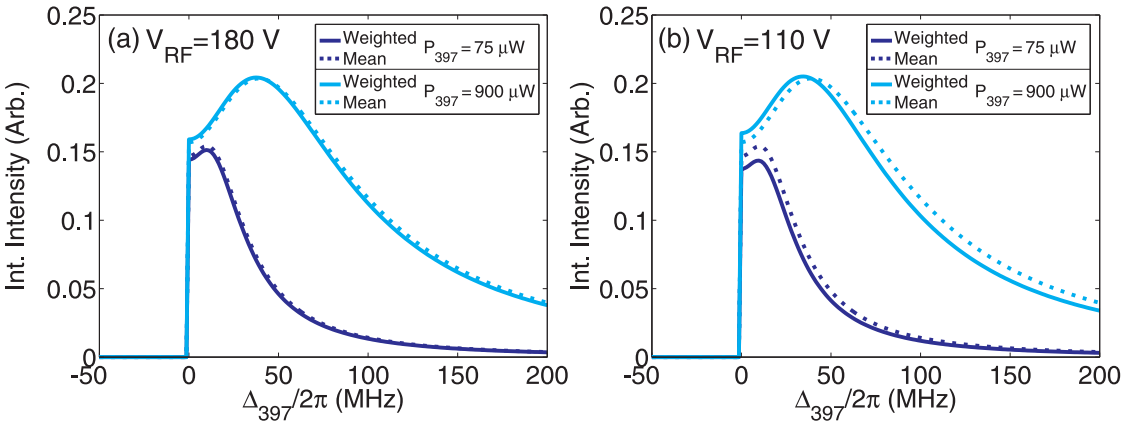


Figure F.4: Simulated fluorescence spectra generated by scanning $\Delta_{397}$ at $\Delta_{866} = 0$ MHz for high and low $P_{397}$ values at (a) $V_{\mathrm{RF}} = 180$ V, (b) $V_{\mathrm{RF}} = 110$ V. Note that in all these simulations $P_{866} = 5$ mW which is in keeping with the power used for all experimentation. The resulting fluorescence intensities are scaled to correspond exactly to the population fraction in the $^2\mathrm{P}_{1/2}$ state, except at $\Delta_{397} < 0$ where the crystal melts and intense fluorescence is lost. The mean spectra calculated at the same power, but different voltages, are virtually identical on this scale.

We now examine whether a single spectrum at the mean intensity is a good approximation of a full weighted spectrum. Figure F.4 shows comparisons between weighted and mean spectra at different 397 nm laser powers for each value of $V_{\mathrm{RF}}$. A single simulation run at the mean intensity is a good approximation to the full weighted spectrum at $V_{\mathrm{RF}} = 180$ V for both indicated values of $P_{397}$ (see Fig. F.4(a)). These powers represent the extremities of the 397 nm powers used in our reaction experiments, which are carried out at $V_{\mathrm{RF}} = 180$ V. However, the weighted and mean spectra start to deviate slightly at $V_{\mathrm{RF}} = 110$ V at either value of $P_{397}$. For example, Fig. F.4(b) shows a peak difference in the steady-state $^2\mathrm{P}_{1/2}$ population of about 1% between the mean and weighted spectra. Some of the $A_{\mathrm{eff}}$ calibrations were made at $V_{\mathrm{RF}} = 110$ V due to the fact that a lower radial trapping voltage facilitates recrystallisation. This is of practical use when a PMT is being used to collect the ion fluorescence rather than a CCD camera system. In the fitting process, simulated spectra are scaled in intensity to the peaks of the experimental spectra. This operation results in an even closer match between weighted and mean spectra and therefore calibration of the effective laser areas, $A_{\mathrm{eff}}$, as described in Chapter 6, will be negligibly affected by a different $V_{\mathrm{RF}}$ within the range 110–180 V. Overall, for our experimental parameters, these calculations demonstrate the validity of using constant effective areas, $A_{\mathrm{eff}}$, to relate the measured laser powers to the effective laser intensities (as summarised by Eq. 6.11). It has been demonstrated that, given our experimental configuration, experimental fluorescence spectra may be well-modelled by assuming constant average laser intensities. This means that we can avoid any explicit treatment of spatial inhomogeneity in the laser intensities at the scale of a typical Coulomb crystal.

However, if the intensity gradient throughout the crystal does become too large, a weighted spectrum will strongly deviate from a spectrum calculated at the mean intensity. This can occur if the dimensions of the crystal are beginning to match

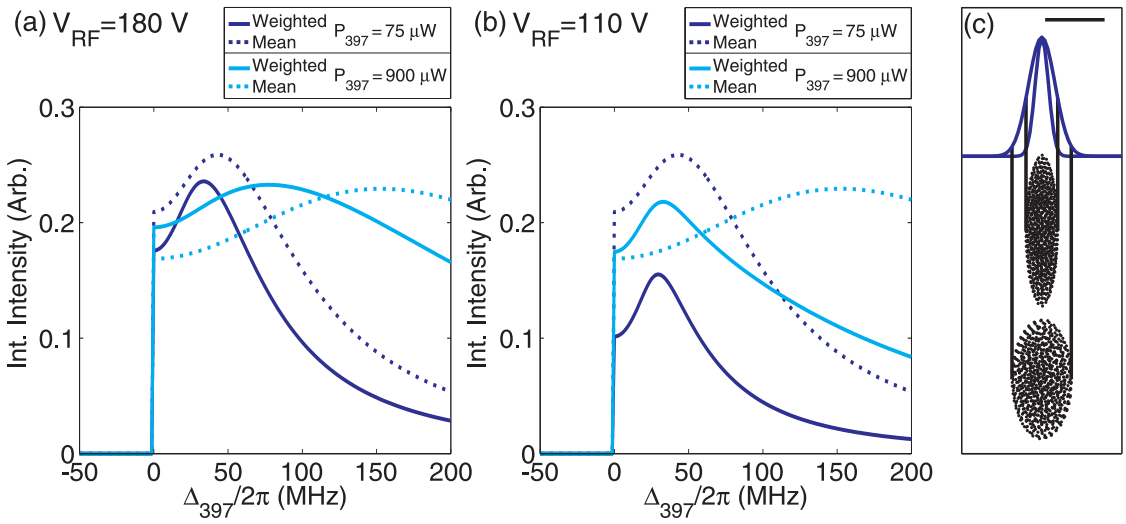


Figure F.5: Simulated fluorescence spectra generated by scanning $\Delta_{397}$ at $\Delta_{866} = 0$ MHz for high and low $P_{397}$ values at (a) $V_{\mathrm{RF}} = 180$ V, (b) $V_{\mathrm{RF}} = 110$ V. The intensities are scaled to correspond exactly to the population fraction in the $^2\mathrm{P}_{1/2}$ state, except at $\Delta_{397} < 0$ where the crystal melts and intense fluorescence is lost. (c) Illustrates the 397 nm transverse intensity distributions for these simulations. The scale reference line at the top of the figure is 200 $\mu$m in length, and the crystals were simulated at $V_{\mathrm{RF}} = 180$ V (top) and $V_{\mathrm{RF}} = 110$ V (bottom). Both 397 nm and 866 nm lasers have had their dimensions quartered versus those shown in Fig. F.2, and therefore $\sigma_x$ and $\sigma_y$ are a quarter of the values quoted in the text. When the dimension of the crystal begins to exceed the beam widths the mean spectrum is a poor approximation of the weighted sum spectrum in both magnitude and overall form.

or exceed that of the beam diameter, and reflects the non-linear response of the quantum state populations to the laser intensities. The calculations shown in Fig. F.5(a–b) are analogous to those performed for Fig. F.4, but involve laser beams of one quarter the dimension at the same total powers; Fig. F.5(c) illustrates the transverse intensities for the 397 nm beam relative to the same crystals used in Fig. F.2. The weighted sum spectra deviate strongly from the mean spectra because the intensity gradient experienced by the ions is sufficiently large to expose the non-linear dependence of the quantum state populations to the laser intensities. There is both a deviation in intensity and the form of these spectra suggesting that the mean is a poor approximation of the weighted spectrum in this limit. Therefore,

in this regime, any effective laser cross-sectional areas, $A_{\text{eff}}$, calibrated using fits of mean simulated spectra to experimental fluorescence spectra would be expected to be erroneous.

Ultimately, we conclude that, given our particular laser systems and within the $P_{397}$, $P_{866}$ and $V_{\text{RF}}$ ranges used in our reaction experiments, it is valid to relate the total beam powers of each laser to the effective laser intensities via the constant effective cross-sectional areas, $A_{\text{eff;397}}$ and $A_{\text{eff;866}}$.

# Appendix G

# Comparison of results based on three- and eight-level OBE simulations

This Appendix contains a number of figures intended to allow the comparison of various results produced through the use of the three- and eight-level OBE treatments. Whilst the eight-level treatment is believed to be a better model of the experiment, and is therefore relied upon in the determination of the rate constant results discussed in Chapter 6, it can be seen in Table G.1 that, ultimately, there are not significant differences between the final rate constants predicted using either of these two frameworks. This is because, given the experimental parameters, the variation of the $Ca^+$ total excited state population as a function of the 397 nm laser detuning does not differ markedly between the three- and eight-level treatments. However, as shown in Fig. G.3, the eight-level treatment does predict a larger contribution to the total excited state population from the metastable $^2D_{3/2}$ state — such a difference between these two models would be important if attempting to separate the relative contributions of the $^2P_{1/2}$ and $^2D_{3/2}$ states to any combined

excited state rate constants.

## G.1 Fluorescence spectra fits based on the three-level OBE treatment

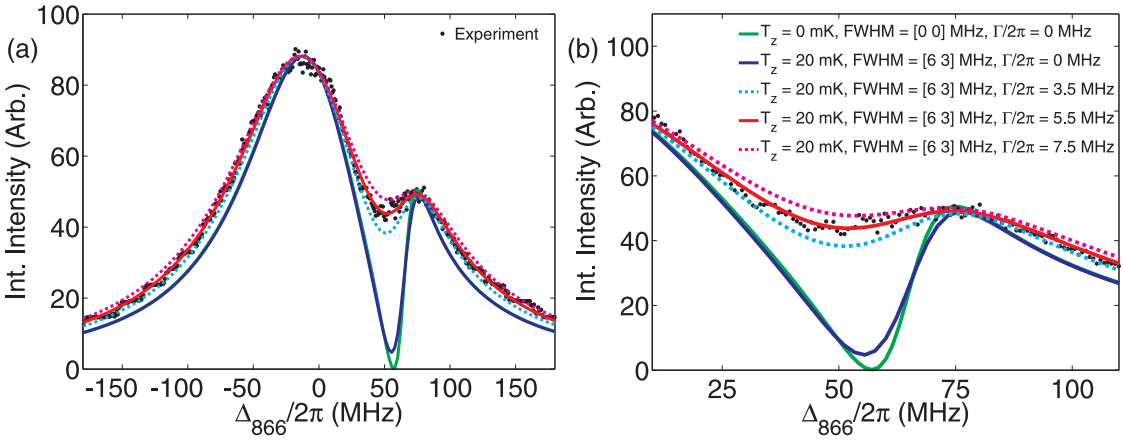


Figure G.1: Linewidth determination using the three-level OBE treatment (to be compared with Fig 6.3). (a) Simulated fluorescence spectra superimposed on an experimental scan, with (b) zoomed in around the dark resonance. Both frequency fluctuations and non-zero axial ion velocities are simulated, and laser linewidths are then determined by matching the spectra around the dark resonance.
Experimental parameters are as follows:
$P_{397} = 673\ \mu$W, $P_{866} = 5.310$ mW, $\Delta_{397}/2\pi = 57.06$ MHz or 30 fm.
Additional fitting parameters:
$A_{\text{eff;}397} = 0.11(2)$ mm$^2$, $A_{\text{eff;}866} = 11.4(11)$ mm$^2$.

For the three-level treatment, the average laser linewidths, determined by the fitting of simulated fluorescence lineshapes to multiple experimental spectra, were determined to be $\Gamma_{397}/2\pi = \Gamma_{866}/2\pi = 6(1)$ MHz (as opposed to 5(1) MHz using the eight-level framework). For example, for the spectrum shown in Fig. G.1, the most accurate fit around the dark resonance is provided by $\Gamma_{397}/2\pi = \Gamma_{866}/2\pi = 5.5$ MHz, where both 397 nm and 866 nm laser linewidths are assumed equal. Using the three-level treatment, effective laser cross-sectional areas were determined by fitting simulated fluorescence lineshapes to the same experimental data as for the

eight-level treatment (see Fig. G.2); these effective areas were determined to be $A_{\text{eff;397}} = 0.11(2)$ mm$^2$, $A_{\text{eff;866}} = 11.4(11)$ mm$^2$. Note that whilst these values produce an excellent fit to the data, $A_{\text{eff;866}} = 11.4(11)$ mm$^2$ is deemed to be a somewhat unrealistic value considering the partial focussing of the 866 nm laser beam.

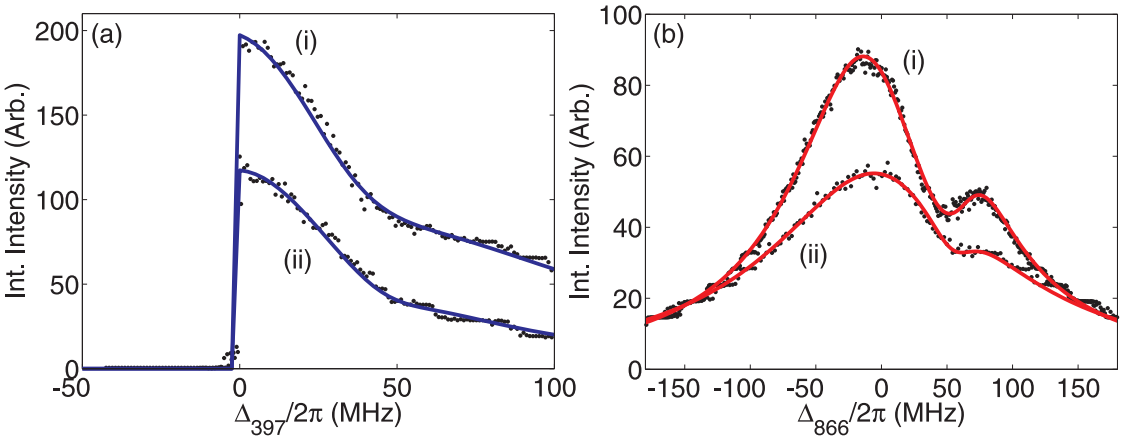


Figure G.2: Three-level OBE simulations overlaid across experimental fluorescence excitation spectra at the upper and lower bounds of the 397 nm laser powers used in the reaction experiments (to be compared with Fig. 6.4). Panel (a) shows 397 nm detuning scans with $\Delta_{866}/2\pi = 40$ MHz, whilst panel (b) shows 866 nm detuning scans with $\Delta_{397}/2\pi = 57$ MHz.
Laser powers are as follows:
(a): (i) $P_{397} = 600$ $\mu$W, $P_{866} = 5.2$ mW, (ii) $P_{397} = 220$ $\mu$W, $P_{866} = 5.3$ mW,
(b): (i) $P_{397} = 670$ $\mu$W, $P_{866} = 5.3$ mW, (ii) $P_{397} = 220$ $\mu$W, $P_{866} = 5.3$ mW.
Fitting parameters are as follows:
$A_{\text{eff;397}} = 0.11(2)$ mm$^2$, $A_{\text{eff;866}} = 11.4(11)$ mm$^2$, $T_z = 20$ mK,
FWHM(397)=6 MHz, FWHM(866)=3 MHz, $\Gamma_{397} = \Gamma_{866} = 6(1)$ MHz.

## G.2 Comparison of state populations and rate constants predicted by the three- and eight-level OBE treatments

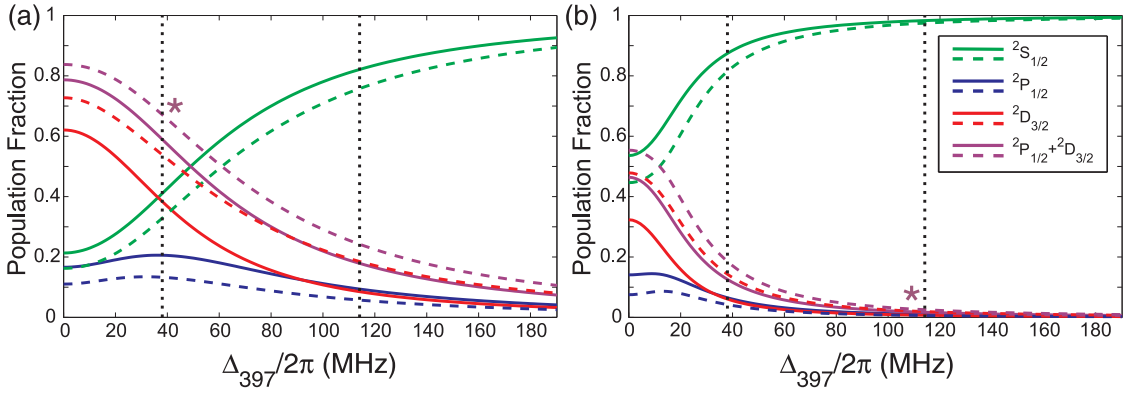


Figure G.3: Comparision of the $Ca^+$ state populations predicted by the three- and eight-level OBE treatments. Populations are plotted as a function of the 397 nm laser detuning and calculated at the upper and lower bounds of the 397 nm laser power used in the reaction experiments: Panel (a) $P_{397} = 900$ $\mu$W, panel (b) $P_{397} = 70$ $\mu$W. In these calculations the 866 nm laser power and detuning are constant at values of $P_{866} = 5$ mW and $\Delta_{866}/2\pi = 0$ MHz respectively.
Solid lines represent solutions from the three-level OBE using the parameters: $\Gamma_{397} = \Gamma_{866} = 6$ MHz, $A_{\text{eff;}397} = 0.11(2)$ mm$^2$, $A_{\text{eff;}866} = 11.4(11)$ mm$^2$.
Dashed lines represent solutions from the eight-level OBE using the parameters: $\Gamma_{397} = \Gamma_{866} = 5$ MHz, $A_{\text{eff;}397} = 0.055(3)$ mm$^2$, $A_{\text{eff;}866} = 1.90(3)$ mm$^2$, $B = 1.1$ G, $\alpha = \pi/2$.
Note that whilst the total excited state populations are similar, the eight-level treatment predicts a much greater contribution from the metastable $^2D_{3/2}$ state. The three-level treatment predicts similar populations for the $^2D_{3/2}$ and $^2P_{1/2}$ states at larger 397 nm laser detunings, and this would seem to be incorrect based on a simple degeneracy argument.

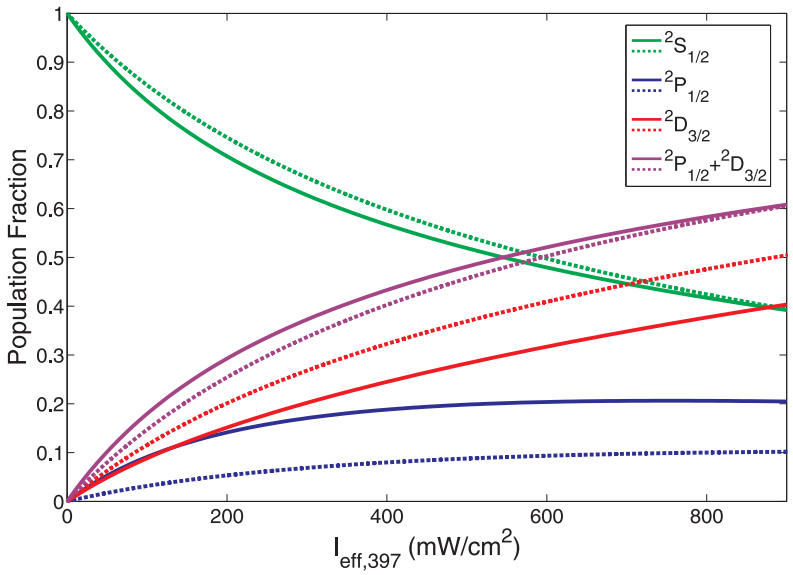


Figure G.4: $Ca^+$ state populations calculated as a function of the 397 nm laser intensity, $I_{397}$, using both the three- and eight-level OBE treatments. In these calculations the 397 nm laser detuning is kept constant at a value of $\Delta_{397}/2\pi =$ 20 MHz and the 866 nm laser intensity and detuning are also constant at values of $I_{\text{eff},866} = 437.7$ mW/cm$^2$ and $\Delta_{866}/2\pi = 0$ MHz respectively.
Solid lines represent solutions from the three-level OBE using the parameters: $\Gamma_{397} = \Gamma_{866} = 6$ MHz.
Dashed lines represent solutions from the eight-level OBE using the parameters: $\Gamma_{397} = \Gamma_{866} = 5$ MHz, $B = 1.1$ G, $\alpha = \pi/2$.
Over the range of effective 397 nm laser intensities used in our experiments (based on measured laser powers and calibrated effective areas), predictions of the total excited state population do not differ markedly between the three- and eight-level OBE treatments. This suggests that the assumptions drawn in Appendix F using the three-level OBE treatment also hold in the case of the eight-level treatment.

| Reactant: | $CH_3F$ | | $CH_3Cl$ | | $CH_2F_2$ | |
|---|---|---|---|---|---|---|
| Rate Constant ($\times 10^{-9}$ cm$^3$ s$^{-1}$) | 5 K | 243 K | 5 K | 199 K | 5 K | 196 K |
| **3-level OBE:** ($^2S_{1/2}$) | 0.70(14) | 0.45(11) | 0.23(13) | 0.17(16) | <0.06 | <0.06 |
| ($^2P_{1/2}$+$^2D_{3/2}$) | 1.38(16) | 1.20(18) | 1.63(26) | 2.02(27) | 0.48(09) | 1.93(14) |
| **8-level OBE:** ($^2S_{1/2}$) | 0.66(15) | 0.42(11) | 0.18(13) | 0.13(17) | <0.04 | <0.03 |
| ($^2P_{1/2}$+$^2D_{3/2}$) | 1.29(12) | 1.10(13) | 1.41(18) | 1.73(21) | 0.41(06) | 1.65(14) |
| ACCSA ($T_{rot}$ =$T_{trans}$) | 10.36 | 1.22 | 9.55 | 1.31 | 8.65 | 1.20 |
| ACCSA ($T_{rot}$=300 K) | 1.85 | 1.14 | 1.73 | 1.14 | 1.83 | 1.04 |
| ADO | – | 1.92 | – | 2.06 | – | 2.02 |
| Langevin | 0.87 | 0.87 | 1.04 | 1.04 | 0.88 | 0.88 |

Table G.1: Comparison between experimental rate constants obtained using either the three-level or eight-level OBE treatments in the determination of the $Ca^+$ state populations. Reactions include those of $Ca^+$ with translationally-cold (guided), and room-temperature (admitted via leak valve) samples of $CH_3F$, $CH_3Cl$ and $CH_2F_2$. Relevant theoretical values are also included as per Chapter 6. It can be seen that the corresponding rate constants do not vary significantly between the three- and eight-level treatments given the specified uncertainties. Nevertheless, for reasons discussed primarily in Section 2.6 and Chapter 6, greater confidence is associated with those rate constants based on the eight-level OBE treatment

.

# References


[1] R. V. Krems, W. C. Stwalley, and B. Friedrich, eds., *Cold Molecules: Theory, Experiment, Applications*. CRC Press, 2009.

[2] R. Sahai and L. A. Nyman, "The boomerang nebula: The coldest region of the universe," *Astrophys. J.*, vol. 487, pp. L155–L159, 1997.

[3] E. Herbst and T. J. Millar, "The chemistry of cold interstellar cloud cores." Chapter 1 in: Low temperatures and cold molecules, World Scientific Publishing, ed. by Ian W. M. Smith, ISBN 978-1-84816-209-9, pp. 121-174 (2008).

[4] A. Gutberlet, G. Schwaab, Ö. Birer, M. Masia, A. Kaczmarek, H. Forbert, M. Havenith, and D. Marx, "Aggregation-induced dissociation of $HCl(H_2O)_4$ below 1 K: The smallest droplet of acid," *Science*, vol. 324, no. 5934, pp. 1545–1548, 2009.

[5] I. W. M. Smith, A. M. Sage, N. M. Donahue, E. Herbst, and D. Quan, "The temperature-dependence of rapid low temperature reactions: experiment, understanding and prediction," *Faraday Discuss.*, vol. 133, pp. 137–156, 2006.

[6] I. M. W. Smith, "Reactions at very low temperatures: Gas kinetics at a new frontier," *Angew. Chem. Int. Ed.*, vol. 45, pp. 2842–2861, 2006.

[7] S. Y. T. van de Meerakker, N. Vanhaecke, M. P. J. van der Loo, G. C. Groenenboom, and G. Meijer, "Direct measurement of the radiative lifetime of vibrationally excited OH radicals," *Phys. Rev. Lett.*, vol. 95, no. 1, p. 013003, 2005.

[8] B. Hansmann and B. Abel, "Kinetics in cold laval nozzle expansions: From atmospheric chemistry to oxidation of biomolecules in the gas phase," *Chem. Phys. Chem.*, vol. 8, pp. 343–356, 2007.

[9] X. Gu, S. Kim, R. I. Kaiser, A. M. Mebel, D. Liang, and Y. L. Yung, "Chemical dynamics of triacetylene formation and implications to the synthesis of polyynes in titans atmosphere," *Proc. Nat. Acad. Sci. U.S.A*, vol. 106, pp. 16078–16083, 2009.

[10] V. Batteiger, S. Knünz, M. Herrmann, G. Saathoff, H. A. Schüssler, B. Bernhardt, R. H. T. Wilken, T. W. Hänsch, and T. Udem, "Precision spectroscopy of the 3s-3p fine-structure doublet in $Mg^+$," *Phys. Rev. A*, vol. 80, p. 022503, 2009.

[11] H. S. Margolis, "Frequency metrology and clocks," *J. Phys. B: At. Mol. Opt. Phys.*, vol. 42, p. 154017, 2009.

[12] D. J. Wineland, J. C. Bergquist, D. Bebland, J. J. Bollinger, F. C. Cmz, W. M. Itano, B. M. Jelenkovid, B. E. King, D. M. Meekhof, J. D. Miller, C. Monroe, M. Rauner, and J. N. Tan, "Application of laser-cooled ions to frequency standards and metrology," *Proc. 1995 Freq. Stand. Metrology Symp.*, pp. 11–19, 1995.

[13] E. R. Hudson, H. J. Lewandowski, B. C. Sawyer, and J. Ye, "Cold molecule spectroscopy for constraining the evolution of the fine structure constant," *Phys. Rev. Lett.*, vol. 96, no. 14, p. 143004, 2006.

[14] M. T. Murphy, V. V. Flambaum, S. Muller, and C. Henkel, "Strong limit on a variable proton-to-electron mass ratio from molecules in the distant universe," *Science*, vol. 320, no. 5883, pp. 1611–1613, 2008.

[15] J. J. Hudson, B. E. Sauer, M. R. Tarbutt, and E. A. Hinds, "Measurement of the electron electric dipole moment using YbF molecules," *Phys. Rev. Lett.*, vol. 89, p. 023003, 2002.

[16] M. Quack, J. Stohner, and M. Willeke, "High-resolution spectroscopic studies and theory of parity violation in chiral molecules," *Annu. Rev. Phys. Chem.*, vol. 59, pp. 741–76, 2008.

[17] A. Micheli, G. K. Brennen, and P. Zoller, "A toolbox for lattice-spin models with polar molecules," *Nat. Phys.*, vol. 2, pp. 341–347, 2006.

[18] D. DeMille, "Quantum computation with trapped polar molecules," *Phys. Rev. Lett.*, vol. 88, p. 067901, 2002.

[19] H. Häffner, W. Hänsel, C. F. Roos, J. Benhelm, D. C. al kar, M. Chwalla, T. Körber, U. D. Rapol, M. Riebe, P. O. Schmidt, C. Becher, O. Gühne, W. Dür, and R. Blatt, "Scalable multiparticle entanglement of trapped ions," *Nature*, vol. 438, p. 643, 2005.

[20] K. V. Kheruntsyan, M. K. Olsen, and P. D. Drummond, "Einstein-Podolsky-Rosen correlations via dissociation of a molecular Bose-Einstein condensate," *Phys. Rev. Lett.*, vol. 95, no. 15, p. 150405, 2005.

[21] M. G. Moore and A. Vardi, "Bose-enhanced chemistry: Amplification of selectivity in the dissociation of molecular Bose-Einstein condensates," *Phys. Rev. Lett.*, vol. 88, p. 160402, 2002.

[22] V. V. Flambaum and J. S. M. Ginges, "Resonance reactions and enhancement of weak interactions in collisions of cold molecules," *Phys. Rev. A*, vol. 74, p. 025601, 2006.

[23] L. Santos, G. V. Shlyapnikov, P. Zoller, and M. Lewenstein, "Bose-Einstein condensation in trapped dipolar gases," *Phys. Rev. Lett.*, vol. 85, pp. 1791–1794, 2000.

[24] T. Lahaye, T. Koch, B. Fröhlich, M. Fattori, J. Metz, A. Griesmaier, S. Giovanazzi1, and T. Pfau, "Strong dipolar effects in a quantum ferrofluid," *Nature*, vol. 448, pp. 672–675, 2007.

[25] J. M. Doyle, B. Friedrich, J. Kim, and D. Patterson, "Buffer-gas loading of atoms and molecules into a magnetic trap," *Phys. Rev. A*, vol. 52, no. 4, pp. R2515–R2518, 1995.

[26] J. Stuhler, P. O. Schmidt, S. Hensler, J. Werner, J. Mlynek, and T. Pfau, "Continuous loading of a magnetic trap," *Phys. Rev. A*, vol. 64, p. 031405, 2001.

[27] M. H. Anderson, J. R. Ensher, M. R. Matthews, C. E. Wieman, and E. A. Cornell, "Observations of Bose-Einstein condensation in a dilute atomic vapor," *Science*, vol. 269, pp. 198–201, 1995.

[28] K. B. Davis, M. O. Mewes, M. R. Andrews, N. J. van Druten, D. S. Durfee, D. M. Kurn, and W. Ketterle, "Bose-Einstein condensation in a gas of sodium atoms," *Phys. Rev. Lett.*, vol. 75, p. 3969, 1995.

[29] D. S. Durfee and W. Ketterle, "Experimental studies of Bose-Einstein condensation," *Optics Express*, vol. 2, no. 8, pp. 299–313, 1998.

[30] S. N. Bose, "Plancks gesetz und lichtquantenhypothese," *Zeit. Physik.*, vol. 26, no. 1, pp. 178–181, 1924.

[31] A. Einstein, "Quantentheorie des einatomigen idealen gases," *Sitzungsberichte der Preussischen Akademie der Wissenschaften, Physik-Mathematik*, pp. 3–14, 1925.

[32] B. K. Stuhl, B. C. Sawyer, D. Wang, and J. Ye, "A magneto-optical trap for polar molecules," *Phys. Rev. Lett.*, vol. 101, p. 243002, 2008.

[33] M. D. D. Rosa, "Laser-cooling molecules - concept, candidates, and supporting hyperfine-resolved measurements of rotational lines in the A-X(0,0) band of CaH," *Eur. Phys. J. D*, vol. 31, p. 395, 2004.

[34] E. S. Shuman, J. F. Barry, D. Glenn, and D. DeMille, "Radiative force from optical cycling on a diatomic molecule," *Phys. Rev. Lett.*, vol. 103, p. 223001, 2009.

[35] J. T. Bahns, W. C. Stwalley, and P. L. Gould, "Laser cooling of molecules: A sequential scheme for rotation, translation, and vibration," *J. Chem. Phys.*, vol. 104, p. 9689, 1996.

[36] M. Viteau, A. Chotia, M. Allegrini, N. Bouloufa, O. Dulieu, D. Comparat, and P. Pillet, "Optical pumping and vibrational cooling of molecules," *Science*, vol. 321, no. 5886, pp. 232–234, 2008.

[37] M. Viteau, A. Chotia, D. Sofikitis, M. Allegrini, N. Bouloufa, O. Dulieu, D. Comparat, and P. Pillet, "Broadband lasers to detect and cool the vibration of cold molecules," *Faraday Discuss.*, vol. 142, pp. 257–270, 2009.

[38] F. Robicheaux, "A proposal for laser cooling of OH molecules," *J. Phys. B: At. Mol. Opt. Phys.*, vol. 42, p. 195301, 2009.

[39] M. Greiner, C. A. Regal, and D. S. Jin, "Emergence of a molecular Bose-Einstein condensate from a Fermi gas," *Nature*, vol. 426, pp. 537–540, 2003.

[40] M. Zwierlein, C. A. Stan, C. H. Schunck, S. F. Raupach, S. Gupta, Z. Hadzibabic, and W. Ketterle, "Observation of Bose-Einstein condensation of molecules," *Phys. Rev. Lett.*, vol. 91, no. 25, p. 250401, 2003.

[41] J. Fuchs, G. J. Duffy, G. Veeravalli, P. Dyke, M. Bartenstein, C. J. Vale, P. Hannaford, and W. J. Rowlands, "Molecular Bose-Einstein condensation in a versatile low power crossed dipole trap," *J. Phys. B: At. Mol. Opt. Phys.*, vol. 40, pp. 4109–4118, 2007.

[42] H. L. Bethlem, G. Berden, and G. Meijer, "Decelerating neutral dipolar molecules," *Phys. Rev. Lett.*, vol. 83, no. 8, pp. 1558–1561, 1999.

[43] M. T. Bell, *Cold Chemistry in the Gas Phase using Velocity Selection and Molecular Deceleration*. PhD thesis, University of Oxford, 2008.

[44] P. Barker and M. Shneider, "Slowing molecules by optical microlinear deceleration," *Phys. Rev. A*, vol. 66, no. 6, p. 065402, 2002.

[45] S. Y. T. van de Meerakker, B. G. Sartakov, A. P. Mosk, R. T. Jongma, and G. Meijer, "Optical pumping of metastable NH radicals into the paramagnetic ground state," *Phys. Rev. A*, vol. 68, no. 3, p. 032508, 2003.

[46] S. A. Rangwala, T. Junglen, T. Rieger, P. W. H. Pinkse, and G. Rempe, "Continuous source of translationally cold dipolar molecules," *Phys. Rev. A.*, vol. 67, p. 043406, 2003.

[47] M. S. Elioff, J. J. Valentini, and D. W. Chandler, "Subkelvin cooling NO molecules via "billiard-like" collisions with argon," *Science*, vol. 302, no. 5652, pp. 1940–1943, 2003.

[48] M. S. Elioff, J. J. Valentini, and D. W. Chandler, "Formation of NO(j'=7.5) molecules with sub-kelvin translational energy via molecular beam collisions with argon using the technique of molecular cooling by inelastic collisional energy-transfer," *Eur. Phys. J. D*, vol. 31, p. 385, 2004.

[49] D. J. Larson, J. C. Bergquist, J. J. Bollinger, W. M. Itano, and D. J. Wineland, "Sympathetic cooling of trapped ions: A laser-cooled two-species nonneutral ion plasma," *Phys. Rev. Lett.*, vol. 57, no. 1, pp. 70–73, 1986.

[50] K. Mølhave and M. Drewsen, "Formation of translationally cold $MgH^+$ and $MgD^+$ molecules in an ion trap," *Phys. Rev. A.*, vol. 62, p. 011401, 2000.

[51] A. Bertelsen, I. S. Vogelius, S. Jørgensen, R. Kosloff, and M. Drewsen, "Photodissociation of cold $MgH^+$ ions," *Eur. Phys. J. D*, vol. 31, pp. 403–408, 2004.

[52] A. Ostendorf, C. B. Zhang, M. A. Wilson, D. Offenberg, B. Roth, and S. Schiller, "Sympathetic cooling of complex molecular ions to millikelvin temperatures," *Phys. Rev. Lett.*, vol. 97, p. 243005, 2006.

[53] B. Roth, P. Blythe, H. Daerr, L. Patacchini, and S. Schiller, "Production of ultracold diatomic and triatomic molecular ions of spectroscopic and astrophysical interest," *J. Phys. B: At. Mol. Opt. Phys.*, vol. 39, pp. S1241–S1258, 2006.

[54] B. Roth, A. Ostendorf, H. Wenz, and S. Schiller, "Production of large molecular ion crystals via sympathetic cooling by laser-cooled $Ba^+$," *J. Phys. B: At. Mol. Opt. Phys*, vol. 38, pp. 3673–3685, 2005.

[55] M. T. Bell and T. P. Softley, "Ultracold molecules and ultracold chemistry," *Mol. Phys.*, vol. 107, no. 2, pp. 99–132, 2009.

[56] L. D. Carr, D. DeMille, R. V. Krems, and J. Ye, "Cold and ultracold molecules: Science, technology, and applications," *New J. Phys.*, vol. 11, p. 055049, 2009.

[57] D. G. Truhlar, B. C. Garrett, and S. J. Klippenstein, "Current status of transition-state theory," *J. Phys. Chem.*, vol. 100, pp. 12771–12800, 1996.

[58] D. Skouteris, D. E. Manolopoulos, W. Bian, H. J. Werner, L. H. Lai, and K. Liu, "van der Waals interactions in the Cl + HD reaction," *Science*, vol. 286, no. 5445, pp. 1713–1716, 1999.

[59] N. Balakrishnan, "On the role of van der Waals interaction in chemical reactions at low temperatures," *J. Chem. Phys.*, vol. 121, p. 5563, 2004.

[60] R. V. Krems, "Molecules near absolute zero and external field control of atomic and molecular dynamics," *Int. Rev. Phys. Chem.*, vol. 24, no. 1, pp. 99–118, 2005.

[61] S. Y. T. van de Meerakker and G. Meijer, "Collision experiments with Stark-decelerated beams," *Faraday Discuss.*, vol. 142, pp. 113–126, 2009.

[62] D. C. Clary, "Fast chemical reactions: theory challenges experiment," *Ann. Rev. Phys. Chem*, vol. 41, pp. 61–90, 1990.

[63] T. Su, E. C. F. Su, and M. T. Bowers, "Ion-polar molecule collisions. Conservation of angular momentum in the average dipole orientation theory. The AADO theory," *J. Chem. Phys.*, vol. 69, p. 2243, 1978.

[64] T. Su and M. T. Bowers, "Ion-polar molecular collisions: the average quadrupole orientation theory," *Int. J. Mass Spectrom.*, vol. 17, no. 3, pp. 309–319, 1975.

[65] J. Troe, "Statistical adiabatic channel model for ion-molecule capture processes," *J. Chem. Phys.*, vol. 87, p. 2773, 1987.

[66] T. Stoecklin, D. C. Clary, and A. Palma, "Rate constant calculations for ion-symmetric top and ion-asymmetric top reactions," *J. Chem. Soc. Faraday Trans*, vol. 88, no. 7, pp. 901–908, 1992.

[67] D. C. Clary, "Calculations of rate constants for ion-molecule reactions using a combined capture and centrifugal sudden approximation," *Mol. Phys.*, vol. 54, no. 3, pp. 605–618, 1985.

[68] M. Ramillon and R. McCarroll, "Adiabatic capture models for fast chemical reactions," *J. Chem. Phys.*, vol. 101, p. 8697, 1994.

[69] E. I. Dashevskaya, A. I. Maergoiz, J. Troe, I. Litvin, and E. E. Nikitin, "Low-temperature behavior of capture rate constants for inverse power potentials," *J. Chem. Phys.*, vol. 118, no. 16, pp. 7313–7320, 2003.

[70] E. I. Dashevskaya, I. Litvin, E. E. Nikitin, and J. Troe, "Low temperature capture of open shell dipolar molecules by ions: the capture of rotationally selected NO(21/2, j) by $C^+$," *Phys. Chem. Chem. Phys.*, vol. 9, pp. 1559–1567, 2007.

[71] A. J. H. M. Meijer, G. C. Groenenboom, and A. van der Avoird, "Semiclassical calculations on the energy dependence of the steric effect for the reaction $Ca(^1D)+CH_3F(jkm=111) \rightarrow CaF+CH_3$," *J. Chem. Phys.*, vol. 105, no. 6, pp. 2247–2262, 1996.

[72] J. F. Castillo and D. E. Manolopoulos, "Quantum mechanical angular distributions for the F+HD reaction," *Faraday Discuss.*, vol. 110, pp. 119–138, 1998.

[73] R. T. Skodje, D. Skouteris, D. E. Manolopoulos, S. H. Lee, F. Dong, and K. Liu, "Resonance-mediated chemical reaction: F + HD $\rightarrow$ HF + D," *Phys. Rev. Lett.*, vol. 85, no. 6, p. 1206, 2000.

[74] H. Sabbah, L. Biennier, I. R. Sims, Y. Georgievskii, S. J. Klippenstein, and I. W. M. Smith, "Understanding reactivity at very low temperatures: The reaction of oxygen atoms with alkenes," *Science*, vol. 317, pp. 102–105, 2007.

[75] Y. Georgievskii and S. J. Klippenstein, "Strange kinetics of the $C_2H_6$ + CN reaction explained," *J. Phys. Chem. A*, vol. 111, pp. 3802–3811, 2007.

[76] E. E. Greenwald, S. W. North, Y. Georgievskii, and S. J. Klippenstein, "A two transition state model for radical-molecule reactions: A case study of the addition of OH to $C_2H_4$," *J. Phys. Chem. A*, vol. 109, pp. 6031–6044, 2005.

[77] H. Böhringer and F. Arnold, "Temperature dependence of three-body association reactions from 45 to 400 K. the reactions $N_2^+ + 2N_2 \rightarrow N_4^+ + N_2$ and $O_2^+ + 2O_2 \rightarrow O_4^+ + O_2$," *J. Chem. Phys.*, vol. 77, no. 11, p. 5534, 1982.

[78] A. Canosa, F. Goulay, I. R. Sims, and B. R. Rowe, "Gas phase reactive collision at very low temperatures: Recent experimental advances and perspectives." Chapter 2 in: Low temperatures and cold molecules, World Scientific Publishing, ed. by Ian W. M. Smith, ISBN 978-1-84816-209-9, pp. 121-174 (2008).

[79] S. E. Barlow, G. H. Dunn, and M. Schauer, "Radiative association of $CH_3^+$ and $H_2$ at 13 K," *Phys. Rev. Lett.*, vol. 52, no. 11, pp. 902–905, 1983.

[80] D. Gerlich, "The study of cold collisions using ion guides and traps." Chapter 3 in: Low temperatures and cold molecules, World Scientific Publishing, ed. by Ian W. M. Smith, ISBN 978-1-84816-209-9, pp. 121-174 (2008).

[81] D. Gerlich and G. Borodi, "Buffer gas cooling of polyatomic ions in rf multielectrode traps," *Faraday Discuss.*, vol. 142, pp. 57–72, 2009.

[82] D. Gerlich, "Inhomogeneous rf fields: a versatile tool for the study of processes with slow ions." in Advances in Chemical Physics: State-selected and state-to-state ion molecule reaction dynamics Vol. LXXXII, John Wiley and Sons, New York (1992).

[83] D. Gerlich, E. Herbst, and E. Roue, "$H_3^+ + HD \leftrightarrow H_2D^+ + H_2$: low-temperature laboratory measurements and interstellar implications," *Planetary and Space Science*, vol. 50, p. 1275, 2002.

[84] O. Asvany, I. Savić, S. Schlemmer, and D. Gerlich, "Variable temperature ion trap studies of $CH_4^+ + H_2$, HD and $D_2$: negative temperature dependence and significant isotope effects," *Chem. Phys.*, vol. 298, p. 97, 2004.

[85] G. Scoles, *Atomic and Molecular Beam Methods*, vol. 1. Oxford University Press, 1988.

[86] U. Erlekam, M. Frankowski, G. von Helden, and G. Meijer, "Cold collisions catalyse conformational conversion," *Phys. Chem. Chem. Phys.*, vol. 9, pp. 3786–3789, 2007.

[87] L. K. Randeniya, X. Zeng, and M. A. Smith, "Low-temperature $NO^+$ ion-molecule reactions in a nitric oxide expansion," *Chem. Phys. Lett.*, vol. 147, p. 346, 1988.

[88] S. R. Mackenzie and T. P. Softley, "New experimental method for studying state-selected ion-molecule reactions," *J. Chem. Phys.*, vol. 101, p. 10609, 1994.

[89] I. R. Sims, "Experimental investigation of neutral-neutral reactions and energy transfer at low temperatures." Proceedings of the International Astronomical Union, 1, pp doi:10.1017/S1743921306007083, 2005.

[90] I. R. Sims and I. M. W. Smith, "Gas-phase reactions and energy transfer at very low temperatures," *Ann. Rev. Phys. Chem.*, vol. 46, pp. 109–138, 1995.

[91] I. R. Sims and I. W. M. Smith, "Rate constants for the radical-radical reaction between CN and $O_2$ at temperatures down to 99 K," *Chem. Phys. Lett.*, vol. 151, pp. 481–484, 1988.

[92] M. Hawley, T. L. Mazely, L. K. Randeniya, R. S. Smith, X. K. Zeng, and M. A. Smith, "A free jet flow reactor for ion molecule reaction studies at very low energies," *Int. J. Mass Spectrom. Ion Processes*, vol. 97, pp. 55–86, 1990.

[93] M. Hawley and M. A. Smith, "Ion chemistry at extremely low temperatures: a free jet expansion approach," *Adv. Gas Phase Ion Chem.*, vol. 1, pp. 167–202, 1992.

[94] M. A. Smith, C. Y. Ng, T. Bauer, and I. Powis, *Ion molecule reaction dynamics at very low temperatures*. John Wiley and Sons Ltd, New York, 1994.

[95] D. Gerlich, "Guided ion beams, rf ion traps, and merged beams: state specific ion-molecule reactions at mev energies." XVIII. International Conference on Physics of Electronic and Atomic Collisions, T. Andersen, T. Fastrup, B.; Folkmann, F.; Knudsen, H. (Eds.), AIP, New York, pp. 607-622 (1993).

[96] J. J. Gilijamse, S. Hoekstra, S. Y. T. van de Meerakker, G. C. Groenenboom, and G. Meijer, "Near-threshold inelastic collisions using molecular beams with a tunable velocity," *Science*, vol. 313, no. 5793, pp. 1617–1620, 2006.

[97] S. Y. T. van de Meerakker, H. L. Bethlem, and G. Meijer, "Manipulation of molecules with electric fields." Chapter 9 in: Low temperatures and cold molecules, World Scientific Publishing, ed. by Ian W. M. Smith, ISBN 978-1-84816-209-9, pp. 121-174 (2008).

[98] S. Ospelkaus, K.-K. Ni, D. Wang, M. H. G. de Miranda, B. Neyenhuis, G. Quéméner, P. S. Julienne, J. L. Bohn, D. S. Jin, and J. Ye, "Quantum-state controlled chemical reactions of ultracold KRb molecules," *Science*, vol. 327, no. 5967, pp. 853–857, 2010.

[99] C. A. Regal, C. Ticknor, J. L. Bohn, and D. S. Jin, "Creation of ultracold molecules from a Fermi gas of atoms," *Nature*, vol. 424, pp. 47–50, 2003.

[100] M. T. Bell, A. D. Gingell, S. Willitsch, and T. P. Softley, "Chemical applications of laser- and sympathetically-cooled ions in ion traps," *Phys. Chem. Chem. Phys.*, vol. 10, p. 7228, 2008.

[101] D. J. Wineland and H. Dehmelt, "Proposed $10^{14}\Delta\nu < \nu$ frequency resolution laser fluorescence spectroscopy on $Tl^+$ mono-ion oscillator," *Bull. Am. Phys. Soc.*, vol. 20, p. 637, 1975.

[102] P. Staanum, *Quantum Optics with Trapped Calcium Ions*. PhD thesis, University of Aarhus, 2004.

[103] B. Roth, C. J. Koelemeij, H. Daerr, and S. Schiller, "Rovibrational spectroscopy of trapped molecular hydrogen ions at millikelvin temperatures," *Phys. Rev. A*, vol. 74, no. 4, p. 040501, 2006.

[104] M. Drewsen, A. Mortensen, R. Martinussen, P. Staanum, and J. L. Sørensen, "Nondestructive identification of cold and extremely localized single molecular ions," *Phys. Rev. Lett*, vol. 93, p. 243201, 2004.

[105] K. Højbjerre, D. Offenberg, C. Z. Bisgaard, H. Stapelfeldt, P. F. Staanum, A. Mortensen, and M. Drewsen, "Consecutive photodissociation of a single complex molecular ion," *Phys. Rev. A*, vol. 77, p. 030702, 2008.

[106] T. Baba and I. Waki, "Cooling and mass-analysis of molecules using laser cooled atoms," *Jpn. J. Appl. Phys.*, vol. 35, pp. 1134–1137, 1996.

[107] P. F. Staanum, K. Højbjerre, P. S. Skyt, A. K. Hansen, and M. Drewsen, "Rotational laser cooling of vibrationally and translationally cold molecular ions," *Nat. Phys.*, vol. 6, pp. 271–274, 2010.

[108] S. Vogelius, L. B. Madsen, and M. Drewsen, "Rotational cooling of molecular ions through laser-induced coupling to the collective modes of a two-ion Coulomb crystal," *J. Phys. B: At. Mol. Opt. Phys.*, vol. 39, pp. S1267–S1280, 2006.

[109] A. Bertelsen, S. Jørgensen, and M. Drewsen, "The rotational temperature of polar molecular ions in Coulomb crystals," *J. Phys. B: At. Mol. Opt. Phys.*, vol. 39, pp. L83–L89, 2006.

[110] I. S. Vogelius, L. B. Madsen, and M. Drewsen, "Rotational cooling of molecules using lamps," *J. Phys. B: At. Mol. Opt. Phys.*, vol. 37, p. 4571, 2004.

[111] I. S. Vogelius, L. B. Madsen, and M. Drewsen, "Blackbody-radiation-assisted laser cooling of molecular ions," *Phys. Rev. Lett.*, vol. 89, p. 173003, 2002.

[112] I. S. Vogelius, L. B. Madsen, and M. Drewsen, "Rotational cooling of heteronuclear molecular ions with $^1\Sigma$ , $^2\Sigma$ , $^3\Sigma$ , and $^2\Pi$ electronic ground states," *Phys. Rev. A.*, vol. 70, p. 053412, 2004.

[113] K. Højbjerre, A. K. Hansen, P. S. Skyt, P. F. Staanum, and M. Drewsen, "Rotational state resolved photodissociation spectroscopy of translationally and vibrationally cold $MgH^+$ ions: toward rotational cooling of molecular ions.," *New Jour. Phys.*, vol. 11, p. 055026, 2009.

[114] T. Schneider, B. Roth, H. Duncker, I. Ernsting, and S. Schiller, "All-optical preparation of molecular ions in the rovibrational ground state," *Nat. Phys.*, vol. 6, pp. 275–278, 2010.

[115] P. Herskind, A. Dantan, M. B. Langkilde-Lauesen, A. Mortensen, J. L. Sørensen, and M. Drewsen, "Loading of large ion Coulomb crystals into a linear Paul trap incorporating an optical cavity," *Appl. Phys. B*, vol. 93, pp. 373–379, 2008.

[116] A. Dantan, M. Albert, J. P. Marler, P. F. Herskind, and M. Drewsen, "Large ion Coulomb crystals: A near-ideal medium for coupling optical cavity modes to matter," *Phys. Rev. A*, vol. 80, p. 041802, 2009.

[117] A. Dantan, M. Albert, J. P. Marler, P. F. Herskind, and M. Drewsen, "Realization of collective strong coupling with ion Coulomb crystals in an optical cavity," *Nat. Phys.*, vol. 5, pp. 494–498, 2009.

[118] G. Rempe, "Atoms in an optical cavity: quantum electrodynamics in confined space," *Contemp. Phys.*, vol. 34, no. 3, pp. 119–129, 1993.

[119] P. Maunz, T. Puppe, I. Schuster, N. Syassen, P. W. H. Pinkse, and G. Rempe, "Cavity cooling of a single atom," *Nature*, vol. 428, pp. 50–52, 2004.

[120] M. Keller, B. Lange, K. Hayasaka, W. Lange, and H. Walther, "Deterministic cavity quantum electrodynamics with trapped ions," *J. Phys. B: At. Mol. Opt. Phys.*, vol. 36, pp. 613–622, 2003.

[121] M. Keller, B. Lange, K. Hayasaka, W. Lange, and H. Walther, "Continuous generation of single photons with controlled waveform in an ion-trap cavity system," *Nature*, vol. 431, pp. 1075–1078, 2004.

[122] L. Hornekær, *Single and multi-species Coulomb Ion Crystals: Structures, Dynamics and Sympathetic Cooling.* PhD thesis, University of Aarhus, 2000.

[123] M. Drewsen, L. Hornekær, N. Kjærgaard, K. Mølhave, A. M. Thommesen, Z. Videsen, A. Mortensen, and F. Jensen, "Ion Coulomb crystals and some applications." Non-neutral Plasma Physics IV, edited by F. Anderegg, C. F. Driscoll, and L. Schweikhard, AIP Conf. Proc. No. 606 AIP, Melville, NY, 2002.

[124] M. Drewsen, I. Jensen, J. Lindballe, N. Nissen, R. Martinussen, A. Mortensen, P. Staanum, and D. Voigt, "Ion Coulomb crystals: a tool for studying ion processes," *Int. J. Mass. Spectrom.*, vol. 229, pp. 83–91, 2003.

[125] B. Roth, P. Blythe, H. Wenz, H. Daerr, and S. Schiller, "Ion-neutral chemical reactions between ultracold localized ions and neutral molecules with single-particle resolution," *Phys. Rev. A*, vol. 73, no. 4, p. 042712, 2006.

[126] B. Roth and S. Schiller, "Sympathetically cooled molecular ions: from principles to first applications." in "Cold Molecules", R. Krems, B. Friedrich, and W. Stwalley, eds., Taylor and Francis (2009).

[127] B. Roth, D. Offenberg, C. B. Zhang, and S. Schiller, "Chemical reactions between cold trapped $Ba^+$ ions and neutral molecules in the gas phase," *Phys. Rev. A*, vol. 78, no. 4, p. 042709, 2008.

[128] P. F. Staanum, K. Højbjerre, R. Wester, and M. Drewsen, "Probing isotope effects in chemical reactions using single ions," *Phys. Rev. Lett.*, vol. 100, p. 243003, 2008.

[129] T. Baba and I. Waki, "Chemical reaction of sympathetically laser-cooled molecular ions," *J. Chem. Phys.*, vol. 116, pp. 1858–1861, 2002.

[130] D. Offenberg, C. Wellers, C. B. Zhang, B. Roth, and S. Schiller, "Measurement of small photodestruction rates of cold, charged biomolecules in an ion trap," *J. Phys. B: At. Mol. Opt. Phys.*, vol. 42, p. 035101, 2009.

[131] M. T. Bell, A. D. Gingell, J. M. Oldham, T. P. Softley, and S. Willitsch, "Cold reactive collisions between laser-cooled ions and velocity-selected neutral molecules," *Phys. Rev. Lett.*, vol. 100, p. 043203, 2008.

[132] H. J. Metcalf and P. van der Straten, *Laser Cooling and Trapping.* Springer, 1999.

[133] E. Fisher, "Die dreidimensionale stabilisierung von ladungstragern in einem vierpolfeld," *Z. Phys.*, vol. 156, pp. 1–26, 1959.

[134] D. A. Church, "Storage-ring ion trap derived from the linear quadrupole radio-frequency mass filter," *J. Appl. Phys.*, vol. 40, pp. 3127–3134, 1969.

[135] H. G. Dehmelt, "Radiofrequency spectrocopy of stored ions: I storage," *Adv. At. Mol. Phys.*, vol. 3, pp. 53–72, 1967.

[136] J. D. Prestage, G. J. Dick, and L. Maleki, "New ion trap for frequency standard applications," *J. Appl. Phys.*, vol. 66, pp. 1013–1017, 1989.

[137] W. Paul, H. P. Reinhard, and U. von Zahn, "Das electrische massenfilter als massen spektrometer und isotopentrenner," *Z. Phys.*, vol. 152, pp. 143–182, 1958.

[138] W. Paul, "Electromagnetic traps for charged and neutral particles," *Angew. Chem.*, vol. 29, p. 739, 1990.

[139] J. R. Gibson and S. Taylor, "Numerical investigation of the effect of electrode size on the behaviour of quadrupole mass filters," *Rapid Commun. Mass Spectrom.*, vol. 40, p. 2001, 1960.

[140] M. Drewsen and A. Bröner, "Harmonic linear Paul trap: Stability diagram and effective potentials," *Phys. Rev. A*, vol. 62, p. 045401, 2000.

[141] R. Takai, K. Nakayama, W. Saiki, K. Ito, and H. Okamoto, "Nonlinear resonance effects in a linear Paul trap," *J. Phys. Soc. Jpn.*, vol. 76, p. 014802, 2007.

[142] K. Mølhave, "Construction of and experiments with a linear Paul trap," Master's thesis, University of Aarhus, 2000.

[143] C. S. Adams and E. Riis, "Laser cooling and manipulation of neutral particles." to appear in "The New Optics", Cambridge University Press.

[144] C. S. Adams and E. Riis, "Laser cooling and trapping of neutral particles," *Prog. Quant. Electron.*, vol. 21, no. 1, pp. 1–79, 1997.

[145] D. Leibfried, R. Blatt, C. Monroe, and D. J. Wineland, "Quantum dynamics of single trapped ions," *Rev. Mod. Phys.*, vol. 75, 2003.

[146] S. Chu, "Nobel lecture: The manipulation of neutral particles," *Rev. Mod. Phys.*, vol. 70, no. 3, pp. 685–706, 1998.

[147] W. D. Phillips, "Nobel lecture: Laser cooling and trapping of neutral atoms," *Rev. Mod. Phys.*, vol. 70, no. 3, 1998.

[148] J. Dalibard and C. Cohen-Tannoudji, "Laser cooling below the doppler limit by polarization gradients: simple theoretical models," *J. Opt. Soc. Am. B*, vol. 6, no. 11, 1989.

[149] D. J. Wineland, J. Dalibard, and C. Cohen-Tannoudji, "Sisyphus cooling of a bound atom," *J. Opt. Soc. Am. B*, vol. 9, no. 1, pp. 32–42, 1989.

[150] A. Aspect, E. Arimondo, R. Kaiser, N. Vansteenkiste, and C. Cohen-Tannoudji, "Laser cooling below the one-photon recoil energy by velocity-selective coherent population trapping," *Phys. Rev. Lett.*, vol. 61, no. 7, p. 826, 1988.

[151] M. Kasevich and S. Chu, "Laser cooling below a photon recoil with three-level atoms," *Phys. Rev. Lett.*, vol. 69, pp. 1741–1744, 1992.

[152] P. Herskind, *Cavity Quantum Electrodynamics with Ion Coulomb Crystals.* PhD thesis, University of Aarhus, 2008.

[153] J. Emsley, *The Elements.* Oxford University Press, 1995.

[154] H. M. van Horn, "Dense astrophysical plasmas," *Science*, vol. 252, pp. 384–389, 1991.

[155] M. Bonitz, V. S. Filinov, V. E. Fortov, P. R. Levashov, and H. Fehske, "Crystallization in two-component Coulomb systems," *Phys. Rev. Lett.*, vol. 95, p. 235006, 2005.

[156] L. Segretain, "Three-body crystallisation diagrams and the cooling of white dwarfs," *Astron. Astrophys.*, vol. 310, p. 485, 1996.

[157] E. Wigner, "On the interaction of electrons in metals," *Phys. Rev.*, vol. 46, p. 1002, 1934.

[158] C. C. Grimes and G. Adams, "Evidence for a liquid-to-crystal phase transition in a classical, two-dimensional sheet of electrons," *Phys. Rev. Lett.*, vol. 42, pp. 795–798, 1979.

[159] V. V. Deshpande and M. Bockrath, "The one-dimensional Wigner crystal in carbon nanotubes," *Nature Physics*, vol. 4, p. 314, 2008.

[160] U. Frölich, B. Roth, and S. Schiller, "Ellipsoidal Coulomb crystals in a linear radio-frequency trap," *Physics of Plasmas*, vol. 12, no. 7, p. 073506, 2005.

[161] W. L. Slattery, G. D. Doolen, and H. E. DeWitt, "Improved equation of state for the classical one-component plasma," *Phys. Rev. A*, vol. 21, p. 2087, 1980.

[162] E. L. Pollock and J. P. Hansen, "Statistical mechanics of dense ionized matter. II. Equilibrium properties and melting transition of the crystallized one-component plasma," *Phys. Rev. A*, vol. 8, no. 6, pp. 3110–3122, 1973.

[163] R. Hasse and J. P. Schiffer, "The structure of the cylindrically confined Coulomb lattice," *Ann. Phys.*, vol. 203, no. 2, pp. 419–448, 1990.

[164] D. J. Wineland, J. C. Bergquist, W. M. Itano, J. J. Bollinger, and C. H. Manney, "Atomic-ion Coulomb clusters in an ion trap," *Phys. Rev. Lett.*, vol. 59, no. 26, pp. 2935–2938, 1987.

[165] F. Diedrich, E. Peik, J. M. Chen, W. Quint, and H. Walther, "Observation of a phase transition of stored laser-cooled ions," *Phys. Rev. Lett.*, vol. 59, no. 26, pp. 2931–2934, 1987.

[166] C. B. Zhang, D. Offenberg, B. Roth, M. A. Wilson, and S. Schiller, "Molecular-dynamics simulations of cold single-species and multispecies ion ensembles in a linear Paul trap," *Phys. Rev. A*, vol. 76, no. 1, p. 012719, 2007.

[167] L. Turner, "Collective effects on equilibria of trapped charged plasmas," *Physics of Fluids*, vol. 30, no. 10, pp. 3196–3203, 1987.

[168] H. E. Dubin and T. M. ONeil, "Trapped nonneutral plasmas, liquids, and crystals (the thermal equilibrium states)," *Rev. Mod. Phys.*, vol. 71, no. 1, pp. 87–172, 1999.

[169] A. Mortensen, *Aspects of Ion Coulomb Crystal based Quantum Memory for Light*. PhD thesis, University of Aarhus, 2005.

[170] L. Hornekær, N. Kjærgaard, A. M. Thommesen, and M. Drewsen, "Structural properties of two-component Coulomb crystals in linear Paul traps," *Phys. Rev. Lett.*, vol. 86, no. 10, pp. 1994–1997, 2001.

[171] J. M. Oldham, "Ultracold ion-molecule reactions: Simulations of Coulomb crystals," Master's thesis, University of Oxford, 2007.

[172] T. Matthey, "Protomol md simulation package." http://protomol.sourceforge.net/.

[173] T. Matthey, *Framework Design, Parallelization and Force Computation in Molecular Dynamics*. PhD thesis, University of Bergen, 2002.

[174] H. Oberst, *Resonance Fluorescence of single Barium ions*. PhD thesis, University of Innsbruck, 1999.

[175] M. McDonnell, *Two-photon readout methods for an ion trap quantum information processor*. PhD thesis, University of Oxford, 2003.

[176] D. F. V. James, "Quantum dynamics of cold trapped ions with application to quantum computation," *Appl. Phys. B*, vol. 66, pp. 181–190, 1998.

[177] M. Schubert, I. Siemers, R. Blatt, W. Neuhauser, and P. E. Toschek, "Transient internal dynamics of a multilevel ion," *Phys. Rev. A*, vol. 52, no. 4, pp. 2994–3006, 1995.

[178] K. Mølmer, Y. Castin, and J. Dalibard, "Monte Carlo wave-function method in quantum optics," *J. Opt. Soc. Am. B*, vol. 10, pp. 524–538, 1993.

[179] A. Mortensen, E. Nielsen, T. Matthey, and M. Drewsen, "Observation of three-dimensional long-range order in small ion Coulomb crystals in an rf trap," *Phys. Rev. Lett.*, vol. 96, no. 10, p. 103001, 2006.

[180] T. B. Mitchell, J. J. Bollinger, D. H. E. Dubin, X.-P. Huang, W. M. Itano, and R. H. Baughman, "Direct observations of structural phase transitions in planar crystallized ion plasmas," *Science*, vol. 282, pp. 1290–1293, 1998.

[181] W. M. Itano, J. J. Bollinger, J. N. Tan, B. Jelenkovic, X.-P. Huang, and D. J. Wineland, "Bragg diffraction from crystallized ion plasmas," *Science*, vol. 279, pp. 686–689, 1998.

[182] J. N. Tan, J. J. Bollinger, B. Jelenkovic, and D. J. Wineland, "Long-range order in laser-cooled, atomic-ion Wigner crystals observed by bragg scattering," *Phys. Rev. Lett.*, vol. 75, no. 23, pp. 4198–4201, 1995.

[183] M. A. van Eijkelenborg, M. E. M. Storkey, D. M. Segal, and R. C. Thompson, "Sympathetic cooling and detection of molecular ions in a Penning trap," *Phys. Rev. A.*, vol. 60, pp. 3903–3910, 1999.

[184] S. Schiller and C. Lämmerzahl, "Molecular dynamics simulations of sympathetic crystallisation of molecular ions," *Phys. Rev. A*, vol. 68, p. 053406, 2003.

[185] D. Offenberg, C. B. Zhang, C. Wellers, B. Roth, and S. Schiller, "Translational cooling and storage of protonated proteins in an ion trap at subkelvin temperatures," *Phys. Rev. A*, vol. 78, p. 061401, 2008.

[186] E. Teloy and D. Gerlich, "Integral cross sections for ion-molecule reactions. I. The guided beam technique," *Chem. Phys.*, vol. 4, p. 417, 1974.

[187] K. Højbjerre, A. K. Hansen, P. S. Skyt, P. F. Staanum, and M. Drewsen, "Rotational state resolved photodissociation spectroscopy of translationally and vibrationally cold $MgH^+$ ions: toward rotational cooling of molecular ions," *New Journal of Physics*, vol. 11, p. 055026, 2009.

[188] T. Junglen, T. Rieger, S. A. Rangwala, P. W. H. Pinkse, and G. Rempe, "Slow ammonia molecules in an electrostatic quadrupole guide," *Eur. Phys. J. D*, vol. 31, no. 2, pp. 365–373, 2004.

[189] M. T. Bell, A. D. Gingell, J. M. Oldham, T. P. Softley, and S. Willitsch, "Ion-molecule chemistry at very low temperatures: cold chemical reactions between Coulomb-crystallized ions and velocity-selected neutral molecules," *Faraday Discuss.*, vol. 142, pp. 73–91, 2009.

[190] C. E. Heiner, H. L. Bethlem, and G. Meijer, "Molecular beams with a tunable velocity," *Phys. Chem. Chem. Phys.*, vol. 8, pp. 2666–2676, 2006.

[191] S. Y. T. van de Meerakker, P. H. M. Smeets, N. Vanhaecke, R. T. Jongma, and G. Meijer, "Deceleration and electrostatic trapping of OH radicals," *Phys. Rev. Lett.*, vol. 94, no. 2, p. 023004, 2005.

[192] M. T. Bell. Private Communication, 2009-2010.

[193] Stanford Research Systems, "Gas correction factors for Bayard-Alpert ionization gauges." www.thinkSRS.com.

[194] R. L. Summers, "Empirical observations on the sensitivity of hot cathode ionization type vacuum gages." Glenn Research Center, NASA, 1969.

[195] B. Roth, P. Blythe, and S. Schiller, "Motional resonance coupling in cold multi-species Coulomb crystals," *Phys. Rev. A*, vol. 75, no. 2, p. 023402, 2007.

[196] T. Baba and I. Waki, "Laser-cooled fluorescence mass spectrometry using laser-cooled barium ions in a tandem linear ion trap," *J. Appl. Phys.*, vol. 89, pp. 4592–4598, 2001.

[197] K. Blaum, "High-accuracy mass spectrometry with stored ions," *Phys. Rep.*, vol. 425, no. 1, pp. 1–78, 2006.

[198] S. Rainville, J. K. Thompson, and D. E. Pritchard, "An ion balance for ultra-high-precision atomic mass measurements," *Science*, vol. 303, p. 334, 2004.

[199] P. F. Staanum, K. Højbjerre, and M. Drewsen, *Chapter 10 in Practical Aspects of Trapped Ion Mass Spectrometry.* Taylor and Francis, 2010.

[200] D. Kielpinski, B. E. King, C. J. Myatt, C. A. Sackett, Q. A. Turchette, W. M. Itano, C. Monroe, and D. J. Wineland, "Sympathetic cooling of trapped ions for quantum logic," *Phys. Rev. A*, vol. 61, p. 032310, 2000.

[201] H. Ellman (Toptica Photonics). Private Communication, 2009.

[202] W. Demtröder, *Laser Spectroscopy.* Springer, 2nd ed., 1996.

[203] R. Loudon, *The Quantum Theory of Light.* Oxford University Press, 3rd ed., 2000.

[204] J. N. Harvey, D. Schröder, W. Koch, D. Danovich, S. Shaik, and H. Schwarz, "Electron-transfer reactivity in the activation of organic fluorides by bare metal monocations," *Chem. Phys. Lett.*, vol. 278, pp. 391–397, 1997.

[205] X. Zhao, G. K. Koyanagi, and D. K. Bohme, "Reactions of methyl fluoride with atomic transition-metal and main-group cations: gas-phase room-temperature kinetics and periodicities in reactivity," *J. Chem. Phys. A*, vol. 110, no. 36, pp. 10607–10618, 2006.

[206] J. N. Harvey. Private Communication, 2009-2010.

[207] D. Zhang, C. Liu, and S. Bi, "Density functional studies of the reactions of lanthanide monocations with fluoromethane: C-F bond activation and electron-transfer reactivity," *J. Phys. Chem. A*, vol. 106, pp. 4153–4157, 2002.

[208] M. N. Glukhovtsev, A. Pross, and L. Radom, "Gas-phase identity $S_N2$ reactions of halide anions with methyl halides: A high-level computational study," *J. Am. Chem. Soc.*, vol. 117, pp. 2024–2032, 1995.

[209] H. H. Cornehl, G. Hornung, and H. Schwarz, "Gas-phase reactivity of lanthanide cations with fluorocarbons: C-F versus C-H and C-C bond activation," *J. Am. Chem. Soc.*, vol. 118, pp. 9960–9965, 1996.

[210] J. R. Mathis, R. Bianco, and J. T. Hynes, "On the activation free energy of the $Cl^-$ + $CH_3Cl$ $S_N2$ reaction in solution," *J. Mol. Liquids*, vol. 61, pp. 81–101, 1994.

[211] P. J. Linstrom and W. G. Mallard, "NIST chemistry webbook," *NIST Standard Reference Database Number 69*, 2008.

[212] A. Varela-Alvarez, V. M. Rayon, P. Redondo, C. Barrientos, and J. A. Sordo, "Gas-phase reaction between calcium monocation and fluoromethane: Analysis of the potential energy hypersurface and kinetics calculations," *J. Chem. Phys.*, vol. 131, p. 144309, 2009.

[213] G. Glockler, "Carbon-halogen bond energies and bond distances," *J. Chem. Phys.*, vol. 63, no. 6, pp. 828–832, 1959.

[214] Stanford Research Systems, "SRS Bayard-Alpert gauge calibration service." www.thinkSRS.com.

[215] M. Motsch, M. Schenk, L. D. van Buuren, M. Zeppenfeld, P. W. H. Pinkse, and G. Rempe, "Internal-state thermometry by depletion spectroscopy in a cold guided beam of formaldehyde," *Phys. Rev. A*, vol. 76, p. 061402, 2007.

[216] L. D. van Buuren, C. Sommer, M. Motsch, S. Pohle, M. Schenk, J. Bayerl, P. W. H. Pinkse, and G. Rempe, "Electrostatic extraction of cold molecules from a cryogenic reservoir," *Phys. Rev. Lett.*, vol. 102, p. 033001, 2009.

[217] W. J. Buma, C. R. Scheper, C. A. de Lange, R. A. Morgan, A. J. Orr-Ewing, D. Ascenzi, and M. N. R. Ashfold, "Resonance enhanced multiphoton ionization spectroscopy of carbonyl sulphide," *J. Chem. Phys.*, vol. 105, no. 6, pp. 2141–2152, 1996.

[218] D. Smith, N. G. Adams, and W. Lindinger, "Reactions of the $HnS^+$ ions (n=0 to 3) with several molecular gases at thermal energies," *J. Chem. Phys.*, vol. 75, p. 3365, 1981.

[219] K. Okada, K. Yasuda, T. Takayanagi, M. Wada, S. Ohtani, and H. A. Schuessler, "Crystallization of $Ca^+$ ions in a linear rf octupole ion trap," *Phys. Rev. A*, vol. 75, p. 033409, 2007.

[220] K. Okada, T. Takayanagi, M. Wada, S. Ohtani, and H. A. Schuessler, "Observation of ion Coulomb crystals in a cryogenic linear octupole rf ion trap," *Phys. Rev. A*, vol. 80, p. 043405, 2009.